COMMUNICATIONS OF THE GEOLOGICAL SURVEY OF NAMIBIA

Volume 29

MINISTRY OF INDUSTRIES, MINES
AND ENERGY

2026

GEOLOGICAL SURVEY OF NAMIBIA
MINISTRY OF MINES AND ENERGY

Deputy Permanent Secretary: Gloria Simubali

COMMUNICATIONS OF THE GEOLOGICAL SURVEY OF NAMIBIA

VOLUME 29

Reviewers: P. Hielscher, A. B. Müller, U. M. Schreiber

Manuscript handling: U. M. Schreiber

Obtainable from
Geological Survey of Namibia
Private Bag 13297, Windhoek, Namibia
and
https://www.mme.gov.na/publications/?designation=gsn

ISSN 1026-2954

COMMUNICATIONS OF THE GEOLOGICAL SURVEY OF NAMIBIA

VOLUME 29
2026

CONTENTS

Original papers/Reviews:

Reports:

Cover image: View of the Schwarzrand escarpment with three diatreme pipes of the Kainab Alkaline Province in the foreground (farm Garub 266, Garub valley, Great Karas Mountains; photo: L. Kemmler)

Communications of the Geological Survey of Namibia, ***29*** *(2026), 1-42*

Revisiting the Alnöitic Tuffisite Diatremes in the Kainab Alkaline Province, Southern Namibia

Lorenz Kemmler[1,2*], R. Johannes Giebel[2,3], Benjamin F. Walter[1], Michael A. W. Marks[1], Paul H. Macey[4], Gregor Markl[1]

[1]Eberhard Karls University Tübingen, Department of Petrology and Mineral Resources, Schnarrenbergstraße 94-96, 72074 Tübingen, Germany
[2]Technische Universität Berlin, Department of Applied Geochemistry, Ernst-Reuter-Platz 1, 10587 Berlin, Germany
[3]University of the Free State, Department of Geology, 250 Nelson-Mandela-Drive, Bloemfontein 9300, South Africa
[4]University of Cape Town, Department of Geological Sciences, 13 University Avenue South, Rondebosch 7701, South Africa

*Corresponding author: <lorenz.kemmler@gmail.com>

Abstract :- This study examines carbonate-bearing diatremes, dykes, and sills of the Kainab Alkaline Province in the Garub valley, southern Namibia. The valley hosts some 100 genetically related magmatic bodies covering ~3000 km² and marking the north-eastern extent of the Kuboos-Bremen Line, a NE-SW-trending line of Pan-African intrusive complexes extending over 270 km from South Africa into Namibia. To study the petrogenesis of the rocks, a combination of petrography, whole-rock geochemistry, micro-X-ray fluorescence, scanning electron microscopy and stable isotope analysis, were employed.

The studied samples feature macrocrystic phlogopite and diopside, along with bleached xenoliths of gneiss and sandstone, set in a fine-grained groundmass of dolomite, albite, and quartz, with minor modal amounts of magnetite, rutile, and apatite. Some samples contain phlogopite, diopside, clinochlore, calcite, and baryte, an unusual assemblage in ultramafic and carbonatitic rocks. The diatremes and dykes are surrounded by metasomatic halos, characterised by bleached wall-rock gneiss, enriched in Na (albitisation). Concurrently, the intrusives themselves were contaminated by the wall rock, thereby assimilating Si, Al and K. Mineral assemblages formed under explosive, hypabyssal conditions (fluidisation), as indicated by rock textures. These assemblages comprise a mixture of xenocrystic material, magmatic phases, and hydrothermal products, which is supported by textural evidence and stable isotope data.

This unique suite of rocks is classified as hypabyssal dolomite silico-carbonatite with a distinct ultramafic lamprophyre affinity. Trace element ratios, together with literature data, suggest a carbonated garnet peridotite melt source, partially molten due to asthenospheric upwelling. Two distinct melt types were identified: an ultramafic melt (Type 1: diopside, phlogopite, dolomite) and a carbonatitic melt (Type 2: dolomite, albite, apatite, magnetite), both of which have been preserved in pelletal lapilli within halos of relatively uncontaminated melt. Derived from the same source, these melts probably resulted from liquid immiscibility. The emplacement of these diatremes occurred in the early Cambrian, probably along pre-existing Tonian NNE-trending brittle structures which were reactivated during the regional-scale crustal warping in advance of the evolving Damara and Gariep orogens.
.

Keywords :- Carbonatite, Great Karas Mountains, Volcanism, Pan-African, Fluids

Introduction

Carbonatites, kimberlites, and ultramafic lamprophyres (UMLs) are commonly associated with each other (e. g. Smith *et al*., 2013; Mattsson *et al*., 2019; Tappe *et al*., 2017; Dongre and Tappe, 2019) and originate from mantle sources, although their exact compositions and depths are still under debate (e. g. Rock, 1986; Tappe *et al.,* 2006; Yaxley *et* *al*., 2021). This implies a shared origin of these rocks from deep-seated, volatile-rich magmas (Tappe *et al*., 2006; Foley *et al*., 2019), likely derived from low-degree partial melting of carbonated peridotite in a depleted mantle, possibly influenced by phlogopite-rich metasomes (Downes *et al*., 2005; Prokopyev *et al*., 2020). Both, garnet and spinel peridotite are considered viable sources (Dasgupta *et al*., 2009; Yaxley *et al*., 1991), and are commonly found in UMLs (Tappe *et al*., 2005). These melts may rise rapidly through the lithosphere - within 10 hours to 2 days (Sparks *et al*., 2006) - via volatile exsolution and fractional crystallisation (Giuliani *et al*., 2020). As SiO_2 increases, CO_2 solubility decreases, triggering fluid exsolution and accelerating magma ascent (Russel *et al*., 2012, 2019), which results in typically explosive emplacement. Thus, kimberlites and, less commonly, UMLs and carbonatites form hypabyssal intrusions (dykes, sills) and volcanoclastic pipes (diatremes) containing abundant country rock xenoliths, mantle-derived xenoliths and magmaclasts (Smith *et al*., 2018). The partial melting, giving rise to these rather exotic rocks, may be triggered by asthenospheric upwelling or mantle plumes (Bell and Tilton, 2001; Davies and Rawlinson, 2014). The relationship between kimberlites and carbonatites remains under dispute. Some models propose that ascending carbonatite melts assimilate mantle material, thus becoming enriched in SiO_2 and evolving into hybrid magmas resembling kimberlites (Kjarsgaard *et al*., 2009; Kamenetsky, 2016).

The ~100 diatremes and associated intrusions (dykes and sills) of the Kainab Alkaline Province (KAP) in southern Namibia were initially described by Verwoerd (1967), and subjected to more detailed investigations by Schreuder (1975). These two studies remain the only comprehensive assessments of the site to date. However, the rocks remain poorly understood, including their proper classification. Various authors have proposed affinities with carbonatites, kimberlites, lamprophyres or olivine melilitites, underscoring the petrological and genetic complexity of these bodies (Schreuder, 1975; Spriggs, 1988; Verwoerd, 1993; Miller, 2012). The intrusive mode is referred to as tuffisite diatremes (Schreuder, 1975), but peperites have been proposed as well (Verwoerd, 1967). Recent advances in the understanding of carbonatite-related systems, alongside improved analytical techniques and geodynamic models, provide a timely opportunity to reassess this enigmatic occurrence. This contribution aims to identify the processes involved during volcanism in the KAP, the nature of the parental magma and, finally, to propose a revised classification of this occurrence. In addition, the genetic link of these diatremes with the contemporaneous intrusive complexes of the Kuboos-Bremen Line (Reid, 1991) is evaluated, as recent dating shows that not all initially proposed intrusives are related in age (Zech *et al*., 2025). To further put the KAP field into context, its carbonatitic characteristics are examined and compared with neighbouring and analogous carbonatite occurrences such as Mickberg, Weltevrede, Gross Brukkaros, and Marinkas Quelle.

The Garub intrusives share key characteristics with ultramafic lamprophyres, which typically contain macrocrysts of phlogopite and olivine. These rocks are further classified into three types: alnöite (melilite-bearing), aillikite (carbonate-rich), and damtjernite (containing nepheline and/or alkali feldspar; Rock, 1986; Tappe *et al*., 2005).

Carbonatites are igneous rocks with ≥25–50 vol.% primary carbonate minerals (Le Maitre *et al*., 2002; Mitchell, 2005; Tappe *et al*., 2025), which are classified by the dominant carbonate into calcite-, dolomite-, ankerite-/siderite- (“ferro-”) and nyerereite-/gregorite- (“natro-“) carbonatites (Yaxley *et al*., 2022). They occur in extrusive, intrusive, and carbothermal forms, commonly associated with ultramafic or alkaline rocks (Woolley and Kjarsgaard, 2008; Schmidt *et al*., 2024). Carbonatite genesis remains debated, with hypotheses including mantle-derived primary carbonate melts, residual melts from fractional crystallisation of carbonate-bearing silicate melts, and products of silicate-carbonate immiscibility (Yaxley *et al*., 2021; Schmidt *et al*., 2024). Many intrusive types represent cumulates or evolved melts (Veksler *et al*., 1998; Kamenetsky *et al*., 2021), modified by fluid interaction, creating high-salinity brines (Prokopyev *et al*., 2016; Anenburg *et al*., 2021; Walter *et al*., 2021). Carbonatite magmas and associated fluids alter host rocks, forming fenites characterised by albite, orthoclase, aegirine, and amphibole (Le Bas, 2008; Elliot *et al*., 2018). Interaction with crustal material may also produce Fe-Mg silicates such as olivine, clinopyroxene, and mica (Giebel *et al*., 2019; Vasyukova and Williams-Jones, 2022).

Kimberlites are deep-origin volcanic rocks (150–250 km) known for transporting diamonds and mantle materials rapidly to the surface (Haggerty, 1994; Sparks, 2013). They typically contain olivine macrocrysts (20–30 vol.%) set in a matrix of olivine, spinel, phlogopite, perovskite, apatite, monticellite, and calcite, along with late-stage carbonates and serpentinite. Accessory macrocrysts may include pyrope, ilmenite, Cr-diopside, and diamonds (Mitchell *et al.*, 2019; Sparks *et al.*, 2006).

Geological Setting

Regional Geology

The Kainab Alkaline Province (KAP; formerly referred to as the Garub intrusions or the Grünau Alkaline Province; Schreuder, 1975; Winter and Rikhotso, 1998) bodies are hosted within rocks of the Namaqua–Natal Metamorphic Province (NNMP), a polyphase Mesoproterozoic (~1.35-1.0 Ga) orogenic belt that extends from eastern South Africa to the central Namibian coastline (e. g. Bial *et al.*, 2016; Macey *et al.*, 2022; Fig.1). In southern Namibia, the NNMP is subdivided into three NW-trending tectonic domains. The Palaeoproterozoic (1.91-1.86 Ga) arc-related (meta-)volcanic and (meta-)plutonic rocks of the Richtersveld Subprovince are tectonically overlain by Mesoproterozoic metapelitic granulites and granitic orthogneisses (~1.22-1.16 Ga), and late- to post-tectonic granitoids (~1.12-1.08 Ga) of the Kakamas Domain (Fig.1). The Richtersveld Subprovince and Kakamas Domain are separated by the Lower Fish River-Onseepkans Thrust Zone, a ~50km-wide, low-angle tectonic damage zone consisting of slices of both the Richtersveld Subprovince and the Kakamas Domain, interlayered with exotic sheets of 1.81 Ga and ~1.31-1.26 Ga orthogneisses. The main NW-trending regional penetrative gneissic foliation resulting from isoclinal folding and thrusting during the main Namaqua Orogeny (~1.20-1.12 Ga) was refolded into large, kilometre-scale dome- and basin folds, and subsequently reworked along major, discrete, subvertical NW-trending transcurrent shear zones (~1.0-0.96 Ga) intruded by coeval leucogranite and pegmatite (Macey *et al.*, 2022 and references within).

Extension of the Namaqua (Kalahari Craton) crust in the mid-Tonian led to the emplacement of granitic to syenitic plutons, plugs and ring complexes (and volcanic equivalents) of the Richtersveld Igneous Suite (903–771 Ma, Frimmel *et al.*, 2001; Zech *et al.*, 2025), and the intrusion of the ~150 km-wide NNW to NNE-striking Gannakouriep mafic dyke swarm (~790 Ma, Rioux *et al.*, 2010) that extends for more than 300 km from Kleinzee in South Africa to north of Grünau in Namibia. Continued extension resulted in the development of a basin into which the Gariep Supergroup (mostly arenite, mudstone and diamictite) was deposited (e. g. Frimmel, 2008). Tectonic inversion and the closure of the Gariep Basin during the assembly of Gondwana began approximately 555 Ma ago, resulting in the formation of the southeast-vergent, greenschist-facies Gariep fold-and-thrust belt, which was thrust over the NNMP. The crustal flexure in the foreland of the developing Gariep Orogen formed basins into which the late Ediacaran to Cambrian Nama Group sediments were deposited onto NNMP basement rocks (~555–500 Ma; e. g. Allsopp *et al.*, 1979; Saylor *et al.*, 2005; Nelson *et al.*, 2022).

The Kuboos-Bremen Suite, a NE-trending line of Cambrian granitic, syenitic and carbonatite plutons, ring complexes, plugs, breccias, and dykes intruded the NNMP basement and Nama Group at the end of the Gariep Orogeny (Fig. 1A; e. g. Reid, 1991; Zech *et al.*, 2025). Following a period of stability, the NE-striking Karasburg graben developed in southern Namibia as a fault-bounded peripheral basin to the developing main Karoo basin, into which the Carboniferous Dwyka Group (comprising shales and diamictite) and Permian Ecca Group (mudstone, siltstone, sandstone) were deposited unconformably on top of the NNMP and Nama Group. Post-Karoo dolerites intruded during the Jurassic break-up of Eastern Gondwana (~185 Ma; Siedner and Mitchell, 1976).

Several phases of brittle tectonics have occurred since the end of the Namaqua Orogeny, with post-Gannakouriep faults and fractures controlled by pre-existing Namaquan (NW-trending) and Gariepian (N- to NE-trending) structures (e. g. Muir *et al*, 2023).

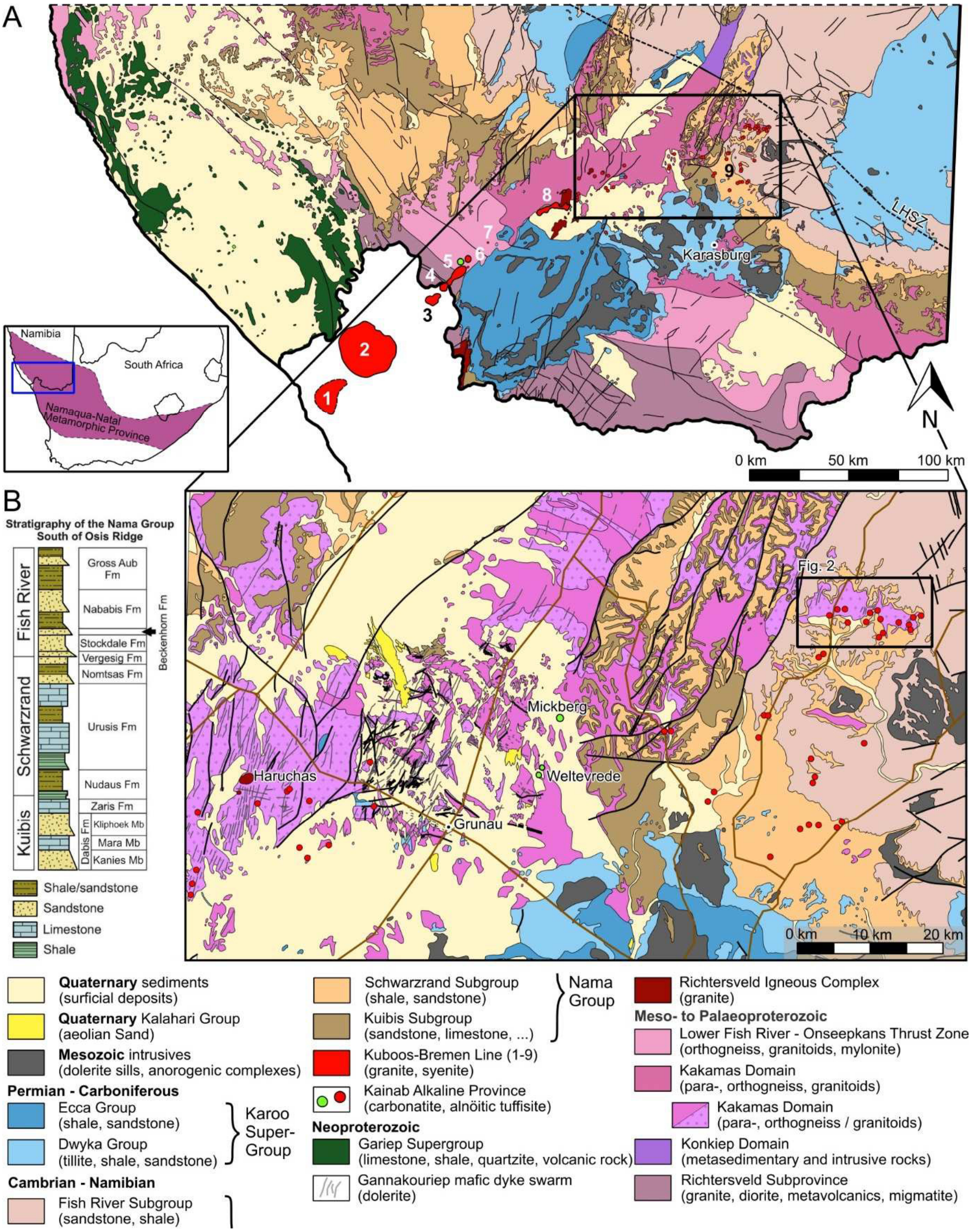

Figure 1. A) Regional geological map of southern Namibia, featuring intrusive complexes of the Kuboos-Bremen Line (1-9; Appendix 1) - bottom left: extent of the NNMP; GIS data obtained from Geological Survey of Namibia, KBL locations after Reid (1991); B) Geological map of the Kainab Alkaline Province showing intrusive locations (red dots), confirmed carbonatite occurrences (after Schreuder 1975, green dots); left: stratigraphy of the Nama Group in southern Namibia (adapted from Walter *et al*., 2023; originally from Germs,1983)

Kuboos-Bremen Line (KBL) and Kainab Alkaline Province (KAP)

The KBL was first described by Söhnge and De Villiers (1948) and is composed of nine intrusive complexes extending over 270 km from the Atlantic Coast in South Africa to the Grünau area (Reid, 1991; Fig. 1A). From SW to NE these include the Swartbank, Kuboos and Tatasberg complexes in South Africa, as well as the Namibian Grootpenseiland, Marinkas Quelle, Kanabeam intrusive complexes, the Mt. Ai-Ais breccia pipe, the Bremen igneous centres and the Kainab Alkaline Province (KAP; Appendix 1). While granites and quartz-syenites dominate in the southwest (Swartbank, Kuboos, and Tatasberg), syenites and foid-syenites become increasingly prominent towards the northeast (Grootpenseiland, Marinkas Quelle and Kanabeam). Marinkas Quelle and the much smaller Mickberg and Weltevrede bodies of the KAP are currently the only recognised carbonatite occurrences of the KBL (Verwoerd, 1993). The KBL cuts across several Precambrian tectonic boundaries, intruding the Namaqua domains, the Gariep Belt, and the overlying Nama Group. Radiometric age data for the different complexes of the KBL range from ~536 to 492 Ma, indicating intrusion during the Pan-African orogeny (Allsopp *et al*., 1979; Smithies, 1991; Zech *et al*., 2025).

Being part of the KBL, the KAP comprises about 100 diatremes, dykes and sills of carbonate-rich mafic alkaline rocks within an ENE-trending zone extending from farm Garub 266 to the Dreikopf Hills west of the Bremen Complex (Fig. 1B). They were discovered during regional mapping from 1938 to 1939 by J. T. Wessels (unpublished) and first described by Verwoerd (1967), later by Schreuder (1975) and briefly mentioned in an unpublished prospecting report (Winter and Rikhotso, 1998), which represent the only studies of the KAP to date. Subsequent publications largely rely on Schreuder's findings with only limited new additions (e. g. Verwoerd, 1993; Miller, 2012). In the central part of the KAP (10 and 20 km northeast of Grünau) two carbonatite occurrences are recognised: 1) Weltevrede , composed of two breccia plugs of variable carbonate contents, with cross-cutting ankeritic carbonatite dykes (Walter *et al*., 2025), and 2) Mickberg, a 100 m tall double-crested hill, composed of Namaqua gneiss, intruded and brecciated by ankeritic carbonatite (Schreuder, 1975).

The largest concentration of carbonate-bearing eruptives of the Kainab Alkaline Province is situated on farm Garub 266, within an erosional window/valley traversed by the predominantly dry Kainab River drainage. This valley, which is located 80 km north of Karasburg at an elevation of approximately 1200 m within the Great Karas Mountains, hosts around 60 mapped KAP occurrences. These are distributed along the farm road that traverses the valley in an E-W direction (Fig. 2; Verwoerd, 1967). The valley floor consists of medium-grained gneisses of the Kakamas Domain (Schreuder, 1975; Macey *et al*., 2022), likely belonging to the Narries Group (granulitic metapelite) and/or Eendoorn Suite (garnet-bearing augen gneiss) that have been dated between 1220 and 1190 Ma (Nordin, 2009; Macey *et al*., 2022). Within the Garub valley, there are no significant mapped structures except for the NW-SE striking gneissic foliation and roughly SSW-NNE striking Gannakouriep doleritic dykes (Fig. 2). About 6 km to the north, the Lord Hill-Excelsior Shear Zone (LH-ESZ) separates the Kakamas Domain from the Konkiep Domain (Macey *et al*., 2022). West of the valley lies a series of five NNE-SSW striking faults that have been interpreted as reverse faults (Schreuder, 1975). An angular unconformity separates the Kakamas Domain from the overlying late Neoproterozoic to early Cambrian Nama Group, which is subdivided into the Kuibis, Schwarzrand, and Fish River Subgroups (Germs, 1983). Although the Kuibis Subgroup is well developed elsewhere within the KAP, it is absent in the Garub valley. The Schwarzrand Subgroup comprises a succession of greyish-green quartzite, sandstone, sandy shale, siltstone, and brown and yellow weathering dolomitic limestone (Fig. 3D; Schreuder, 1975; Spiering *et al*., 2023). The Schwarzrand Subgroup in the Garub valley is significantly thinner (80 m) than in other regions (Schreuder, 1975). Eight volcanic ash beds from the Schwarzrand Subgroup (~125 km SW of the Garub valley) have been dated by U-Pb zircon methods and yield ages from about 545 Ma at the base to about 539 Ma at the top (Nelson *et al*., 2022; Linnemann *et al*., 2019). The Fish River Subgroup conformably overlies the Schwarzrand Subgroup and forms the capping strata of the

Great Karas Mountains, east of the aforementioned reverse faults. It is typically red to purple in colour and composed of sandstones and shales (Geyer, 2005). The whole sedimentary cover reaches a thickness of around 130 m.

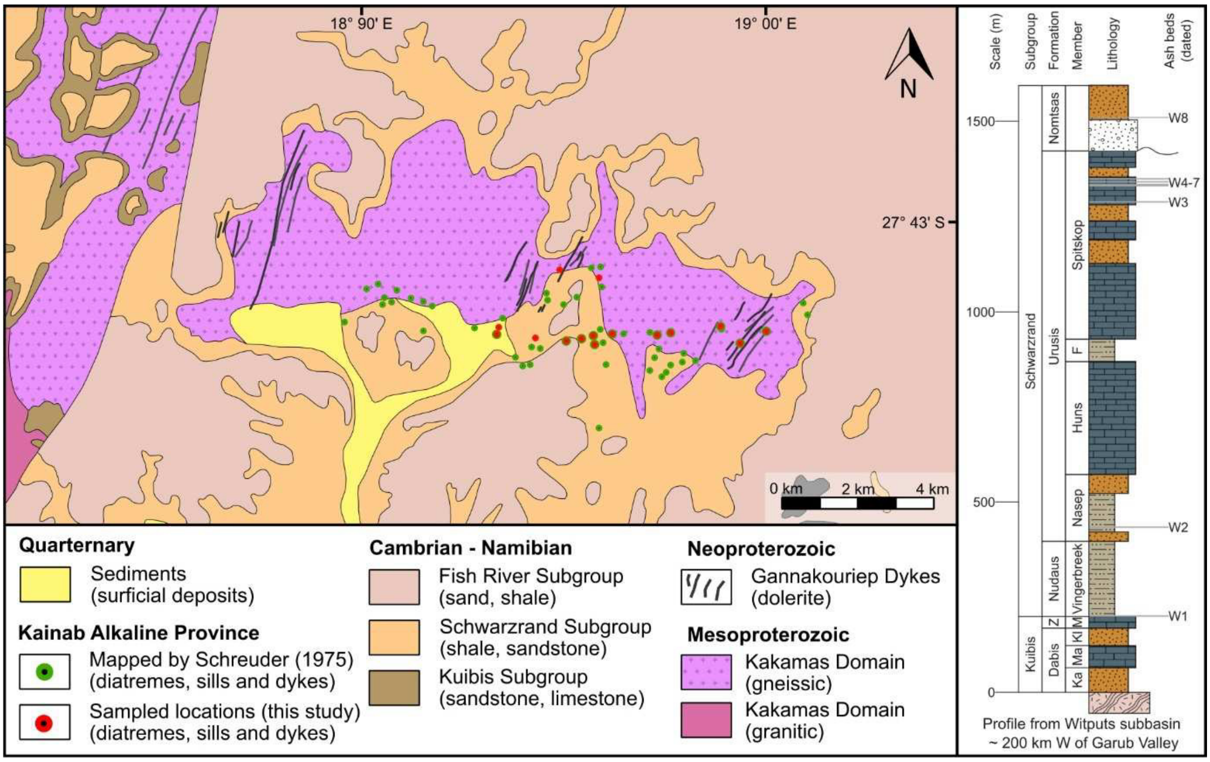

Figure 2. Geological map of the Garub valley with intrusive locations mapped by Schreuder (1975; green) and locations of occurrences sampled during this study (red); on the right is a stratigraphic profile of the Schwarzrand Subgroup from the Witsputs Subbasin around 200 km west of the Garub valley including dated ash beds W1-W8 (Spiering *et al*., 2023). Please note that this profile has a thickness of around 1500 m while the Schwarzrand Subgroup is only around 80 m thick within the Garub valley, where it nevertheless has a correlating stratigraphy.

Igneous rocks of the KAP include diatremes, dykes, and sills (Schreuder, 1975), with the latter two often emanating from the former (Fig. 3E). The diatremes have diameters of up to 50 m (Figs 3A-B) and may be composed of multiple generations of diatreme facies, indicated by different colours, textures, and xenolith types and abundance (Fig. 3H). Xenoliths are commonly fist-sized but range from <1 mm to tens of centimetres (Fig. 3F). They are either of sedimentary (Schwarzrand Subgroup) or metamorphic (Namaqua basement gneisses) origin, with the latter type often being bleached (Figs 3F-G). The dykes typically appear as brown or dark-brown ridges, are up to about 5 m wide, can be traced for up 500 m, and are usually directly associated with the diatreme bodies (Fig. 3E). Some dykes are controlled by joints or foliation in the wall rock, while others are randomly oriented and sinuous. The sills are typically emplaced above or below limestone layers of the Schwarzrand Subgroup (Fig. 3D). They vary in thickness, ranging from a few centimetres to two metres, commonly exhibiting a lenticular shape. The oldest determined age from a pyroclastic sill in the eastern Garub valley is 491 ± 8 Ma (Rb-Sr analyses on whole rock and biotites; Allsopp *et al*., 1979). Biotite Ar-Ar dating on lamprophyric carbonate dykes yield ages of 523 and 527±2 Ma (Zech *et al*., 2025), confirming previous Ar-Ar (514–524 Ma) ages on biotite from dykes outcropping ~30 km south of the Garub valley (Spriggs, 1988).

At its eastern extent, the Garub valley hosts an abandoned lead-fluorite mine, which is believed to have operated between 1922 and 1939 (Schreuder, 1975, and references therein). The deposit is situated at the contact between Namaqua basement gneiss and a tuffisite diatreme, with a nearby associated dolerite dyke. In addition to fluorite, minor amounts of Pb-, Fe-, Cu- and Ag-sulfides, along with their supergene reaction products, as well as baryte, calcite, and quartz, have been reported. Walter *et al*. (2024) suggest that the fluorite deposit is unlikely to have formed as a direct result of diatreme magmatism. Instead, the diatreme probably served as a fluid migration pathway or structurally weak zone that facilitated the deposit's formation during Mesozoic times (Walter *et al*., 2024).

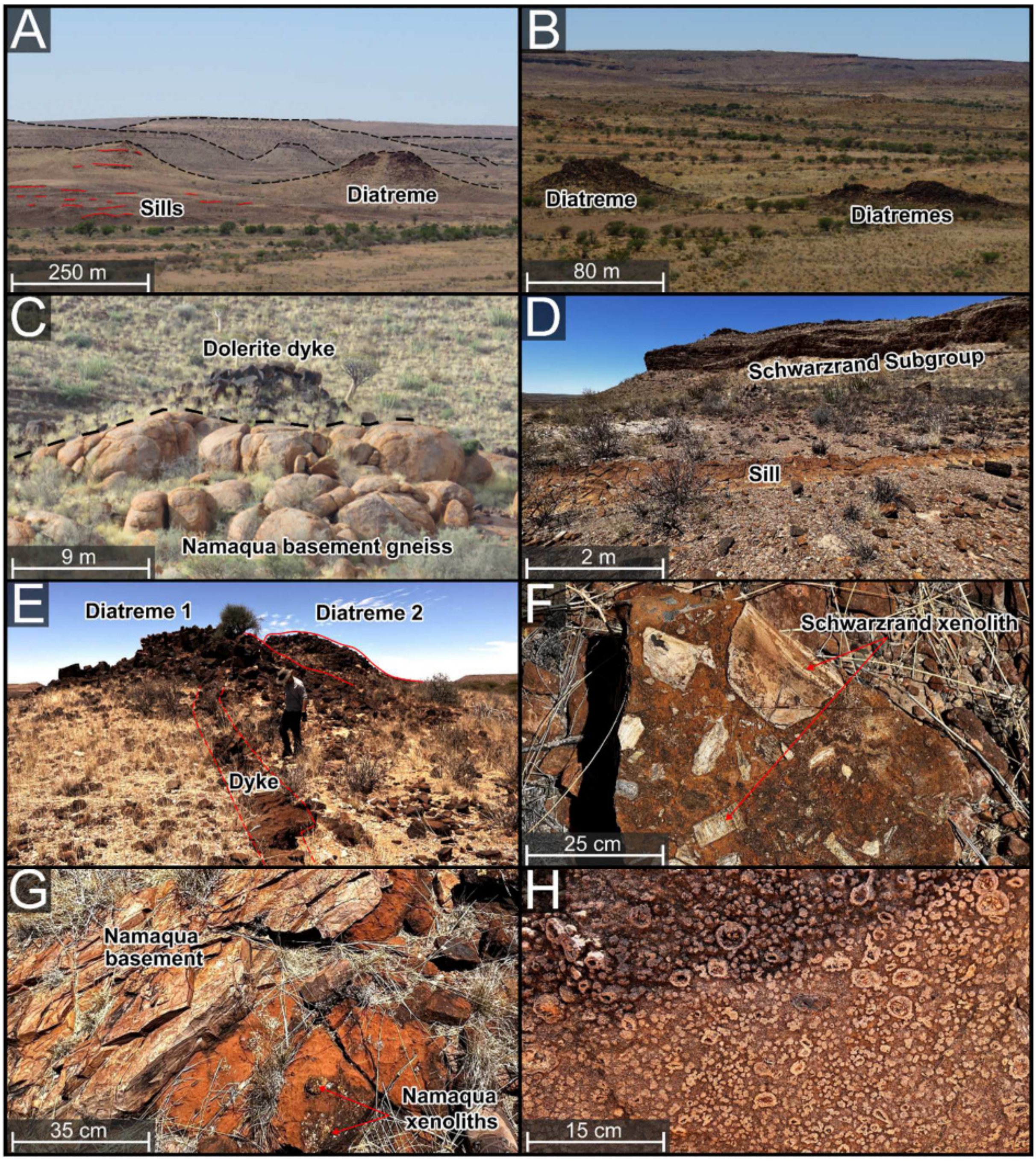

Figure 3. A) View of two large diatremes with small dykes to the left (marked in red) and the Nama escarpment in the background; B) Three medium-sized diatremes, two of which are adjacent, with escarpments in the background; C) Spherically weathered Namaqua gneiss/granite with dark doleritic dyke in the background; D) Schwarzrand escarpment featuring alternating limestone and sandstone, with a small sill in the foreground; E) Small diatreme with a cross-cutting dyke; F) Block of diatreme breccia containing xenoliths of various sizes and types; G) Outcropping of xenolith-rich diatreme breccia next to Namaqua basement; H) Spherical textures in a diatreme locally containing xenoliths (sample GRB039)

Sample Material and Analytical Methods

A total of 50 fist-sized rock samples were collected, representing 15 diatremes and associated dykes and sills and their country rocks (Appendix 2). Several of the diatreme samples are rich in xenoliths of Namaqua gneisses (Figs 4B, D-F & H) or, in some cases, of sedimentary rocks of the Schwarzrand Subgroup (Figs 4B-C).

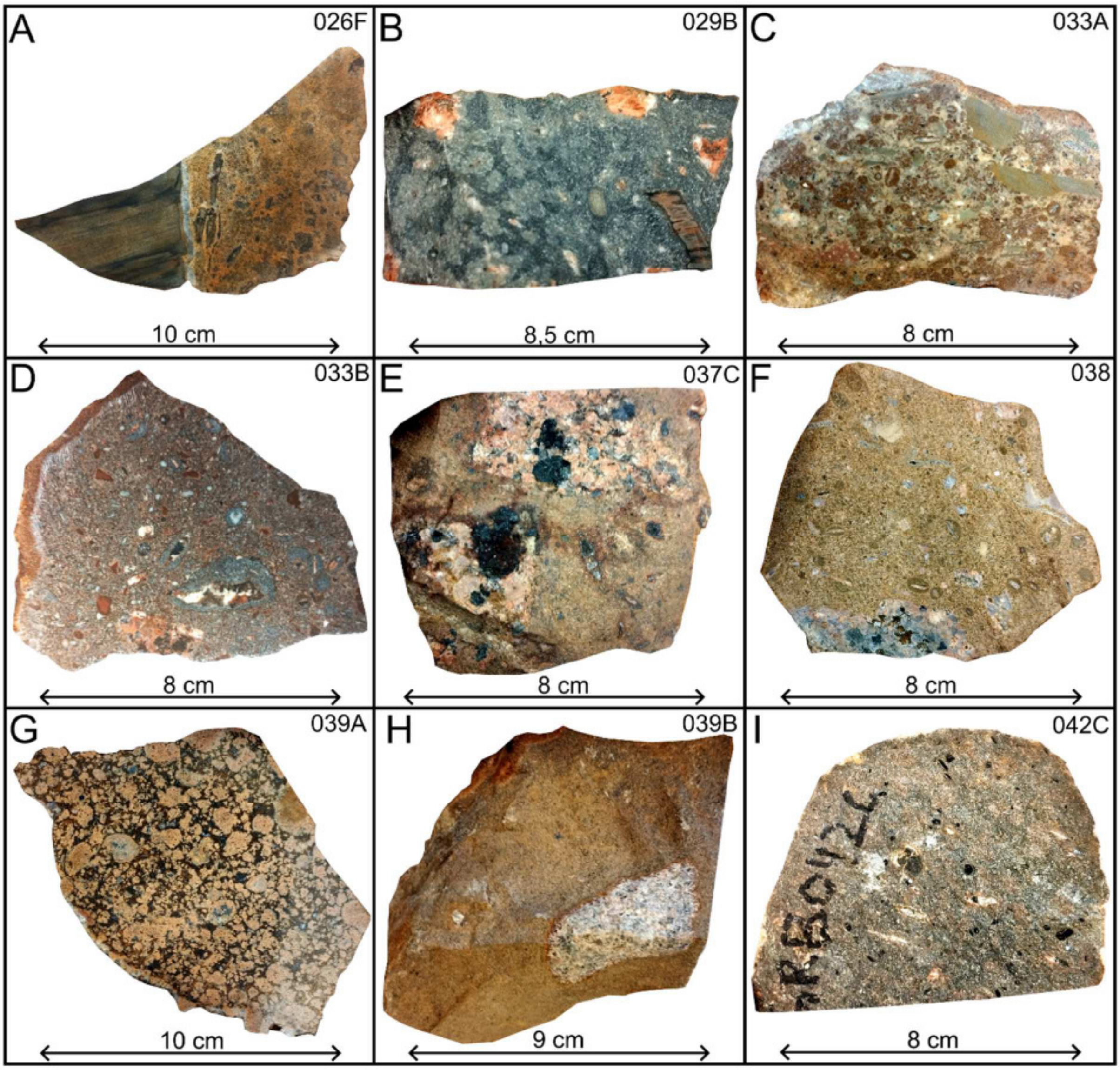

Figure 4. Montage of selected samples showcasing their diversity: A) Contact between Schwarzrand limestone and diatreme; B) Grey matrix diatreme with Schwarzrand Subgroup and Namaqua gneiss xenoliths, exhibiting slight globular textures; C) Strongly brecciated diatreme with multiple xenolith types of various sizes; D) Similar brecciation but with a differently coloured matrix and circular grey zones around the xenoliths; E) Large, bleached xenoliths of gneiss within diatreme facies; F) Altered large xenolith in a matrix hosting smaller clasts surrounded by darker, rounded rims; G) Dark-brown matrix with lighter-brown globules, some of which contain clasts; H) Large bleached gneissic xenolith within a xenolith-free matrix; I) Greyish matrix containing black phlogopite and small clasts

For petrographic study, thin sections of 40 samples were investigated by transmitted and reflected light microscopy, and by micro-x-ray fluorescence analysis (M4 Tornado by Bruker) at the mineralogical and geochemical micro-analytical laboratory (MAGMA-Lab) of the Department of Applied Geochemistry (Technische Universität Berlin, Germany). The latter was equipped with a Rh tube, run with 50 kV using a beam current of 600 µA with a beam diameter of 20 µm. The measuring point distance was 20 µm, with a measuring time of 30 ms per analysis spot using the area mode. Scanning electron microscopy (SEM) analysis was conducted at the Department of Geosciences, Universität Tübingen (Germany) with two tabletop instruments (Phenom XL and TM3030+) run with an acceleration voltage of 15 kV at the BSE mode using a focused beam.

Whole-rock major and minor element geochemistry was determined on 35 samples by wavelength dispersive XRF (S8 Tiger, Bruker) on fused beads (Li-tetraborate/-metaborate: sample ratio = 2:1) at the MAGMA-Lab. Element concentrations were quantified using the GeoQuant calibration package (Bruker). The loss on ignition (LOI) was determined as the percentage weight difference between the dried (105°C for 24 hours) and annealed sample powder (1200°C for 3 hours). LOI was accounted for in the XRF quantification; the mean total XRF sums (oxides plus LOI) ranged between 99 to 101 wt.% for most samples, with a few exceptions at 95 and 105 wt.%. Since the LOI values were not used as weathering indicators, no further corrections were applied. Calibration was conducted using 32 standards, with defined lower and upper limits for element concentrations.

Total sulfur and total carbon analyses were carried out with the Carbon-Sulfur-Analyser CS-2000 (ELTRA) at the Laboratory for Environmental and Raw Materials Analysis (LERA, Karlsruhe Institute for Technology, Germany). The accuracy (<0.2 %) and reproducibility (<6 %) was checked by correlation with certified reference materials (steel, bariumsulfate). Trace element and REE were determined by ICP-MS (iCAP, Thermo Fisher Scientific; LERA) after HNO_3-HF-$HClO_4$-HCl acid digestion of powdered sample material (100 mg). For complete silicate decomposition, the pre-oxidised sample was digested with HF and $HClO_4$ in a sealed Teflon vessel at 120 °C for 16 hours. After evaporation, it was re-dissolved in HNO_3 and HCl, purified by triple evaporation, and finally dissolved in 50 ml of ultrapure water. The precision of the ICP-MS measurement was in the range of 1 %. Measurement quality was checked regularly, with 5 µg/l standard element solutions. The precision and the accuracy of the whole process, including acid digestion, was monitored by inserting certified reference materials CRM-Sy2 and GRE03 (High-Purity standards, Inc.) into the measurement sequence at ten sample intervals (SD is between 1 % and 8 % for most elements).

Stable isotope ($\delta^{13}C$, $\delta^{18}O$) analyses were also conducted on seven samples from the Garub valley and six samples from the wider Kainab Alkaline Province (LERA). Carbonate-rich samples (0–80% calcite, 20–100% dolomite/ankerite) were analysed for stable isotope ratios ($\delta^{13}C$, $\delta^{18}O$) using a GasBench II gas chromatography system (Thermo Fisher Scientific). Sample sizes were adjusted to ensure a carbonate signal >40 µg C, and samples were ground to µm-sized fractions for full reaction with phosphoric acid. Following Al-Aasm *et al.* (1990) and Baudrand *et al.* (2012), carbonates were analysed without prior separation, leveraging their different reaction rates: calcite reacted at 25 °C for 2 hours, while residual carbonates reacted at 50 °C for 24 hours after an intermediate flushing step. Samples were reacted in Gas Bench II vials at 25 and 50 °C, flushed with He, and injected with acid. The evolved CO_2 was analysed by Delta V Advantage IRMS, with each sample measured ten times. Accuracy was assessed using in-house Carrara marble and certified standards (NBS-18, IAEA CO-1). Dolomite and ankerite data were corrected according to Kim *et al.* (2015). Replicate analysis confirmed a precision of ±0.05 ‰ for $\delta^{13}C$ and $\delta^{18}O$.

Petrography

Wall Rocks

Namaqua samples (GRB037B, GRB 040C, GRB041A) are porphyroblastic garnet gneisses (Kakamas Domain) comprising quartz, alkali feldspar, plagioclase, garnet (almandine), biotite, muscovite and sillimanite, with minor amounts of rutile, zircon, and monazite. Most feldspars are turbid, elongated alkali feldspars with perthitic textures, along with smaller, more circular grains of albite-oligoclase, often containing biotite inclusions. The rock also contains heavily serpentinised minerals, displaying an oil film-like colour with iron-rich phases remaining in the cracks. Muscovite is slightly bent and often associated with biotite and sillimanite (Fig. 5H). Garnets frequently contain inclusions of quartz and biotite. Gneissic xenoliths or direct contacts with the diatremes are heavily altered, featuring albite, quartz, and serpentinised and chloritised minerals. Since xenocrystals from the Namaqua wall rocks are often present in significant proportions in the diatremes, they are included in the paragenetic sequence to indicate alteration reactions (Fig. 6).

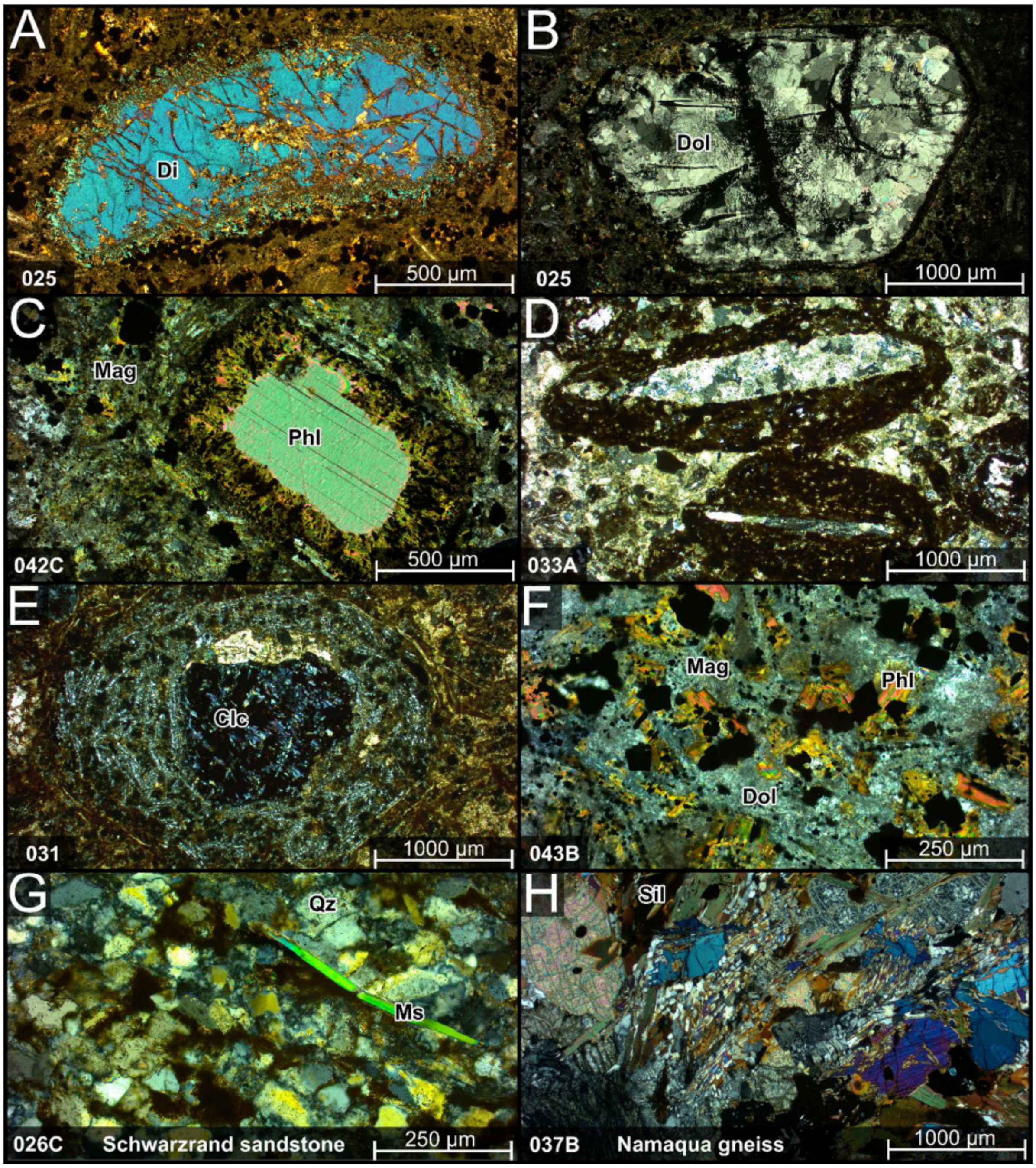

Figure 5. Photomicrographs of selected minerals, textures and lithologies: A) Altered diopside with blue interference colours; B) Spherical rims composed of multiple equigranular dolomites, likely of replacive origin; C) Phlogopite macrocrysts with zone of alteration; D) Two pelletal lapilli in matrix containing elongated xenolith surrounded by a dark halo; E) Heavily chloritised phenocryst with anomalous blue interference colours, featuring a spherical rim and prevalent black iron phases; F) Phlogopite-rich matrix along with magnetite, dolomite, and albite; G) Fine-grained sandstone from the Schwarzrand Subgroup, composed of quartz with minor muscovite; H) Gneissic Namaqua basement, consisting of quartz, plagioclase, perthitic K-feldspar, minor sillimanite, and biotite, along with rounded, serpentinised (?) grains with high interference colours

Samples of the Schwarzrand Subgroup include limestone (GRB026B, GRB029A) and quartzitic sandstone (GRB026C, GRB026F). The micritic dolomitic limestone features areas of light, transparent dolomite and brownish regions, reflecting small-scale stratigraphic variations. They contain carbonate veins and pockets of larger, optically clear calcite, with zones of oxidation, forming brown, colloform-like rims emanating from these veins. Other minerals are not present in observable quantities. The sandstones are fine-grained, predominantly composed of angular quartz with minor feldspar, some displaying pericline twinning (Fig. 5G). Infrequent muscovite and occasional zircon may be present. Macroscopic bedding structures may occur (Fig. 7D), while thin veins of quartz may cross-cut the strata. Occasional sandstone xenoliths within the diatreme are angular and do not show any reactive halos opposed to the Namaqua wall rock (Fig. 8C).

Diatreme Facies

Samples from diatremes, dykes, and sills are similar optically, petrographically and geochemically, but have varying amounts of xenoliths, phenocrysts, and globular textures, which are used to discriminate rock types.

Most samples feature a matrix of calcite or iron-bearing dolomite, with variable amounts of albite/oligoclase, magnetite, rutile, quartz, clinochlore and phlogopite (Figs 5F & 9E). Dolomite appears as enclosed remnants within magnetite or phlogopite and as larger matrix-forming grains. Small anhedral or acicular albite/oligoclase grains may form tangentially around clasts of various compositions (Fig. 5E). Phlogopite is partially replaced by albite, which is also interstitial to dolomite (Fig. 9E). Small books of clinochlore frequently exhibit anomalous blue interference colours near or within altered xenolith remains (Fig. 5E). Small, evenly dispersed, typically euhedral rutile is often accompanied by magnetite. Subordinate euhedral apatite and, in some samples, baryte are also present, with tiny euhedral apatite crystals within phlogopite. Minor ilmenite, euhedral pyrite, and uncommon chalcopyrite occur locally (Figs 9C-E). A paragenetic sequence is divided into a basement section (Namaqua) and a magmatic and hydrothermal stage (diatreme facies; Fig. 6).

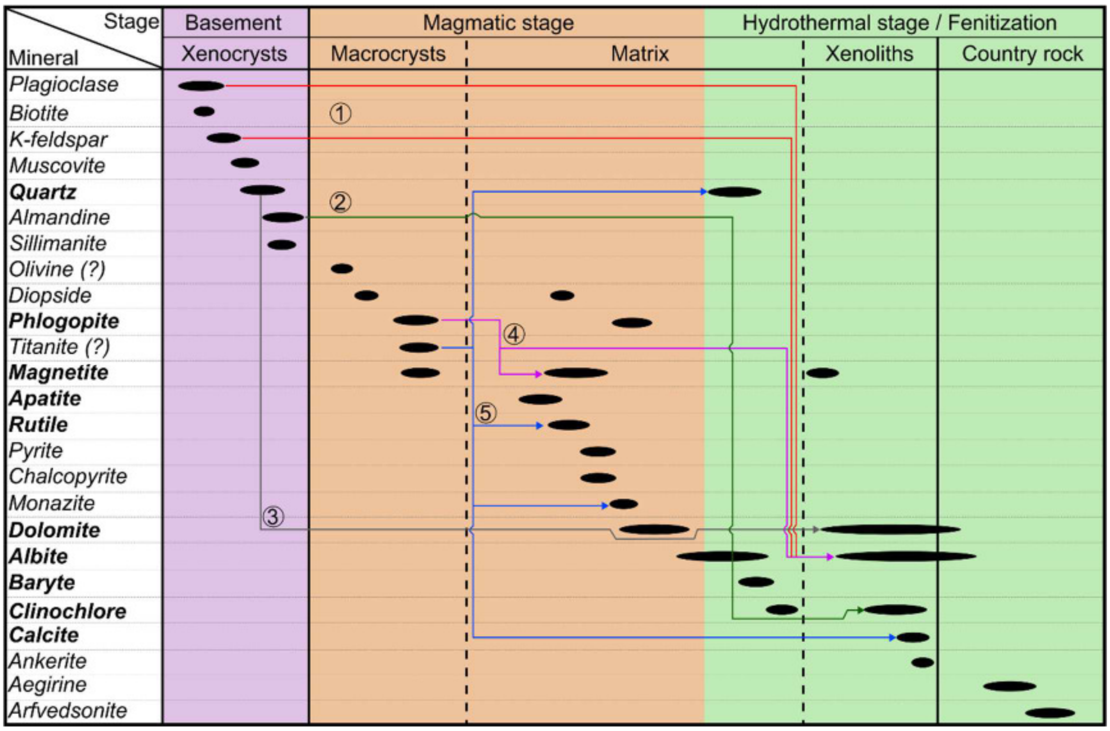

Figure 6. Paragenetic sequence of the Namaqua gneissic basement, the KAP intrusives (including macrocrysts and matrix), embedded Namaqua xenoliths, and the fenitised country rock (macroscopic contact samples): the sequence includes a magmatic stage and a hydrothermal stage, with a continuous transition between them. Minerals that constitute most of the intrusive samples are shown in bold type, while altered and now unidentifiable minerals are identified by a question mark (?). Alteration reactions and replacements are indicated by arrows with corresponding numbers, which are explained in the discussion.

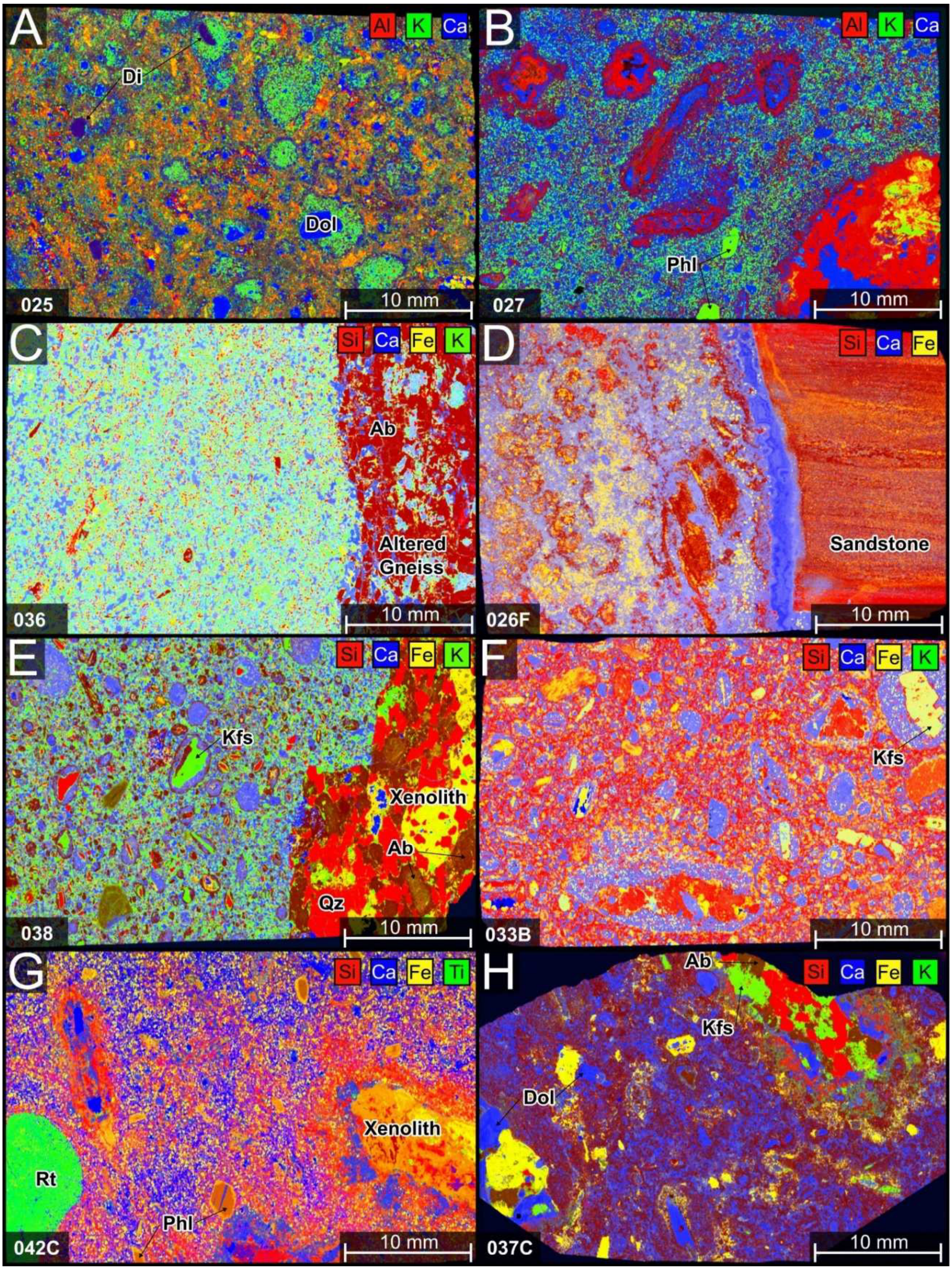

Figure 7. Selection of µXRF elemental mappings, showing KAP intrusives of various texture: A) Carbonate-poor matrix hosting diopside, dolomite and phlogopite macrocrysts, surrounded by K-enriched halos; B) Carbonate-rich and phlogopite phenocryst-bearing sample, hosting altered xenoliths now composed of albite, dolomite and some clinochlore; C) K-enriched matrix in contact with altered basement gneiss, composed of albite, dolomite and remains of K-feldspar; D) Altered xenoliths in a carbonate matrix in direct contact with Schwarzrand sandstone, with a later calcite veinlet (blue) along the contact; E) K-enriched matrix hosting lithic fragments (albite to K-feldspar) surrounded by a carbonate halo, and a large, altered basement gneiss xenolith; F) Lithic fragments (monomineralic, xenoliths) surrounded by carbonate halos in a Si-rich matrix; G) Rounded rutile macrocryst, phlogopite phenocrysts and altered xenoliths in a carbonate-bearing matrix; H) Variably altered granitic basement xenoliths hosted in a dolomite - albite matrix

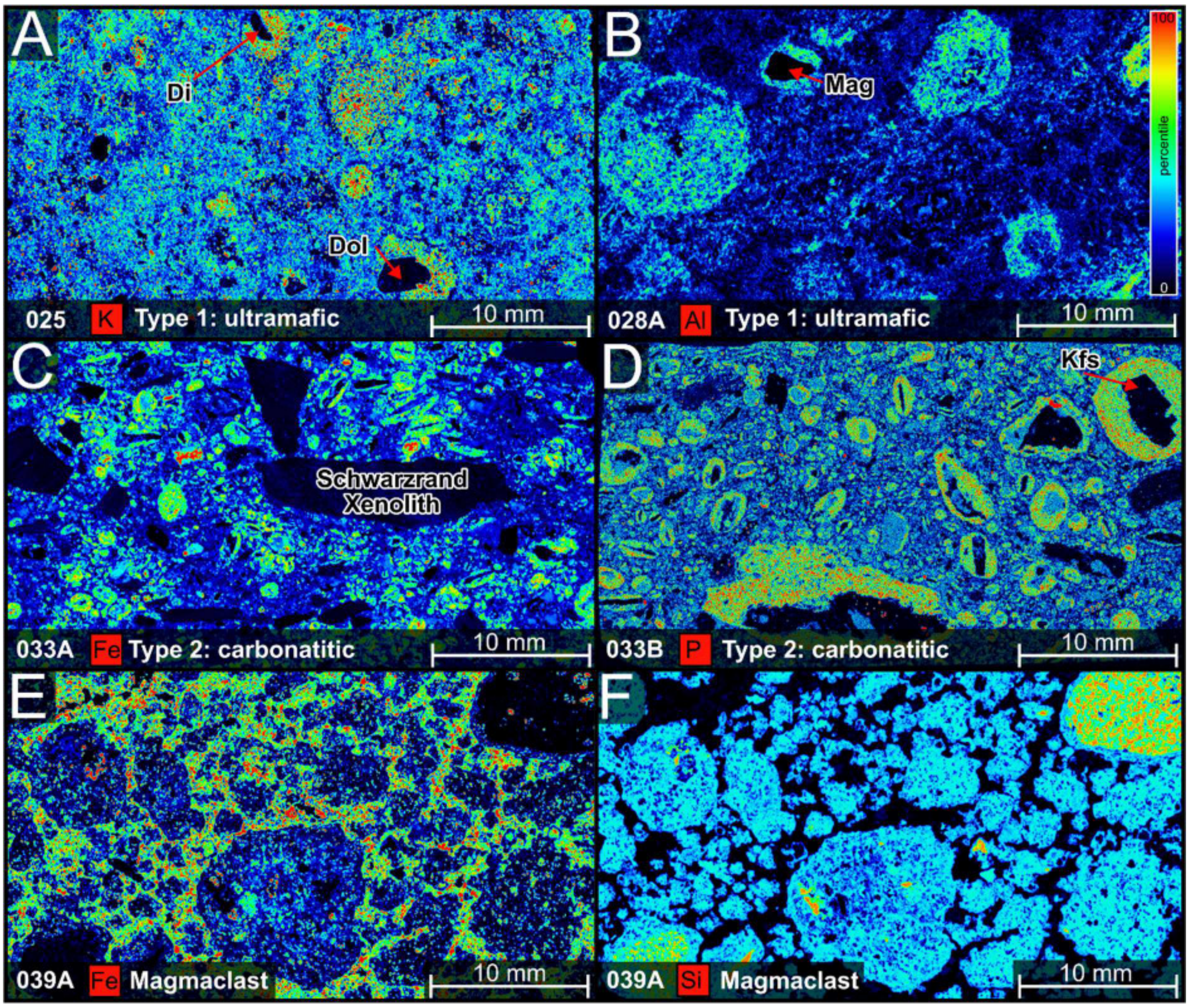

Figure 8. Representative intensity element mappings (percentile value distribution) of two types of pelletal lapilli, based on different halo compositions (derived from the globular sample GRB039A): A) Type 1 ("ultramafic") halos with elevated K concentrations; B) Type 1 with elevated Al concentrations; C) Type 2 ("carbonatitic") with elevated Fe contents. D) Type 2 with elevated P contents; E) Elevated Fe contents in the matrix surrounding the globules; F) Si contents, revealing rounded xenoliths with a rim and other, xenolith-free globules of similar composition

Phenocryst-Rich Varieties

Phenocrysts are mainly phlogopite (~ 1-5 mm), in some samples they make up up to 5 vol. % (Fig. 4I); commonly they have rounded rims due to alteration or partial resorption. The degree of alteration varies, but it is typically characterised by a dark band (Fig. 5C). This band contains subhedral magnetite, and albite surrounded by phlogopite (Fig. 9D). Small euhedral apatite crystals are present near the contact with unaltered matrix, still within the alteration zone (Fig. 9D).

Locally phenocrystic diopside is present, showing strong alteration especially along cleavage planes (Figs 5A and 7A). Surrounding the phenocrysts is later anhedral diopside and dolomite, as well as euhedral magnetite (Fig. 9C). These phenocrysts may be surrounded by globular structures with elevated levels of K, Ca, and Mn (Fig. 8A).

Other common components are carbonate “phenocrysts” of either dolomite or calcite, which may exhibit a superordinate crystal habit (e. g. pseudohexagonal). Unlike the matrix carbonates they are optically clear and composed of multiple equigranular mineral grains (Fig. 5B). They are either intergrown with opaque Fe-oxide or surrounded by an opaque seam. A singular, large (1.5 cm) titanium-rich macrocryst (Fig. 7G) comprises small, anhedral rutile crystals with interstitial calcite, albite and quartz with minor Ce-rich monazite, exhibiting a symplectitic texture. Phenocrysts of hornblende and a single kelyphitic garnet were documented by Schreuder (1975). Additionally, Winter and Rikhotso (1998) reported garnet, clinopyroxene, spinel, and ilmenite from the KAP, although they did not petrographic context or specific sample locations. It is to be noted that none of these minerals were identified in the current samples collected from the Garub valley.

Subvolcanic Breccia Characteristics (GRB027, 037C, 033)

In these xenolith-rich samples most clasts are derived from the gneissic basement (Figs 7B, E, G & H), but locally sandstone clasts derived from the Schwarzrand Subgroup are present (Figs 4B–C & 8C). Other xenoliths, e. g. mantle debris are absent, or at least untraceable. Additional common breccia constituents include xenocrysts, such as common alkali feldspar with partial albitisation, less frequent albite clasts, one angular magnetite as well as some undulous quartz clasts (Figs 8A & D). These clasts are commonly surrounded by a rounded halo or seam, which is distinguishable from the matrix by its contrasting colour (Figs 5D & 8A-D) or texture by displaying tangentially aligned lath-shaped albite or carbonate (more detail below). The less affected gneissic xenoliths are mostly composed of quartz and K-feldspar, with cracks filled by albite (Fig. 7H). Albite also appears to traverse around dolomite clasts, like the caulking of a sediment. More altered xenoliths appear to contain dolomite (dark-blue, Ca-mapping), likely replacing earlier constituents. In places, quartz and K-feldspar is still present, along with more common albite and dolomite (Figs 7B & E). Halos around these xenoliths are characterised by Fe-oxides and albite (Fig. 7H). Strongly altered gneissic xenoliths are composed of albite with interstitial dolomite seemingly replacing albite (Figs 7B & E). Smaller xenoliths have well-defined optical edges, but their elemental content transitions diffusely as albite crystallises beyond the original xenolith margins (Fig. 7B).

Globular Textural Features

Another distinctive feature of the diatreme samples is the common presence of globular textures (Figs 4B & G). They are spherical structures of hypabyssal material, reaching up to 100 mm in diameter, and referred to as pelletal lapilli, “well-rounded clasts consisting of an inner ‘seed’ particle with a complex rim, thought to represent quenched juvenile melt”, that formed within the diatreme (Gernon *et al*., 2012). Some of these pelletal lapilli contain xenoliths, while others contain xenocrysts; some samples contain phenocrysts derived from the basement gneiss (Fig. 7E). Several pelletal lapilli seem to lack seed fragments. The pelletal lapilli present in the Garub valley diatremes can make up more than 35 vol.% of the rock. The circular reaction rims have contrasting compositions to the matrix (Figs 7A & E-F) and were previously described as ankeritisation (Schreuder, 1975). Elemental mappings reveal that these seams are predominantly composed of Ca-carbonates and, to a lesser extent, Mg and Fe. Small apatite, rutile, and magnetite are present, along with larger hematite (bladed texture) and rutile farther away from the K-feldspar.

Based on these observations two types of pelletal lapilli can be distinguished. Type 1 lapilli occur in only two samples (GRB025, GRB028A). They have an "ultramafic" character, with macrocryst kernels or seeds of diopside, dolomite, and magnetite, surrounded by a halo of diopside, dolomite, and some euhedral (microcrystic?) magnetite, pyrite, and rutile (Fig. 13D). The elliptical halo is visible in qualitative µXRF element mappings of K or Al, which are elevated compared to the matrix (Figs 8A-B) More common are type 2 pelletal lapilli, which have a "carbonatitic" character. These commonly contain kernels derived from basement gneiss, and occur as xenoliths or xenocrystic K-feldspar, albite, or quartz, surrounded by a halo dominated by dolomite, with lesser albite, magnetite, rutile, and apatite (Fig. 13E). The halo is chemically distinct from the matrix, particularly in terms of Fe and P content, which are especially prominent in samples GRB033A and B (Figs 8C-D).

Sample GRB039A is notable for its unique texture, featuring globular structures differing from the pelletal lapilli (Figs 8E & F) and closely resembling magmaclasts, which are also referred to as globular (melt) segregations (Scott Smith *et al*., 2018). It contains two well-rounded, fine-grained xenoliths composed mainly of albite, quartz, rutile, and minor baryte and Fe-oxide. These xenoliths are encased in a fine-grained seam primarily made up of albite, with lesser amounts of rutile, dolomite, and minor apatite. In all other magmaclasts, xenoliths are missing, but their mineral composition is the same as that of the seam. All globules are embedded in a "matrix" composed of alternating layers of calcite and ankerite, which may grow euhedrally into former open spaces. One distinct section of the sample displays relatively euhedral mineral assemblages, which are typically smaller and unevenly dispersed (Fig. 9A-B).

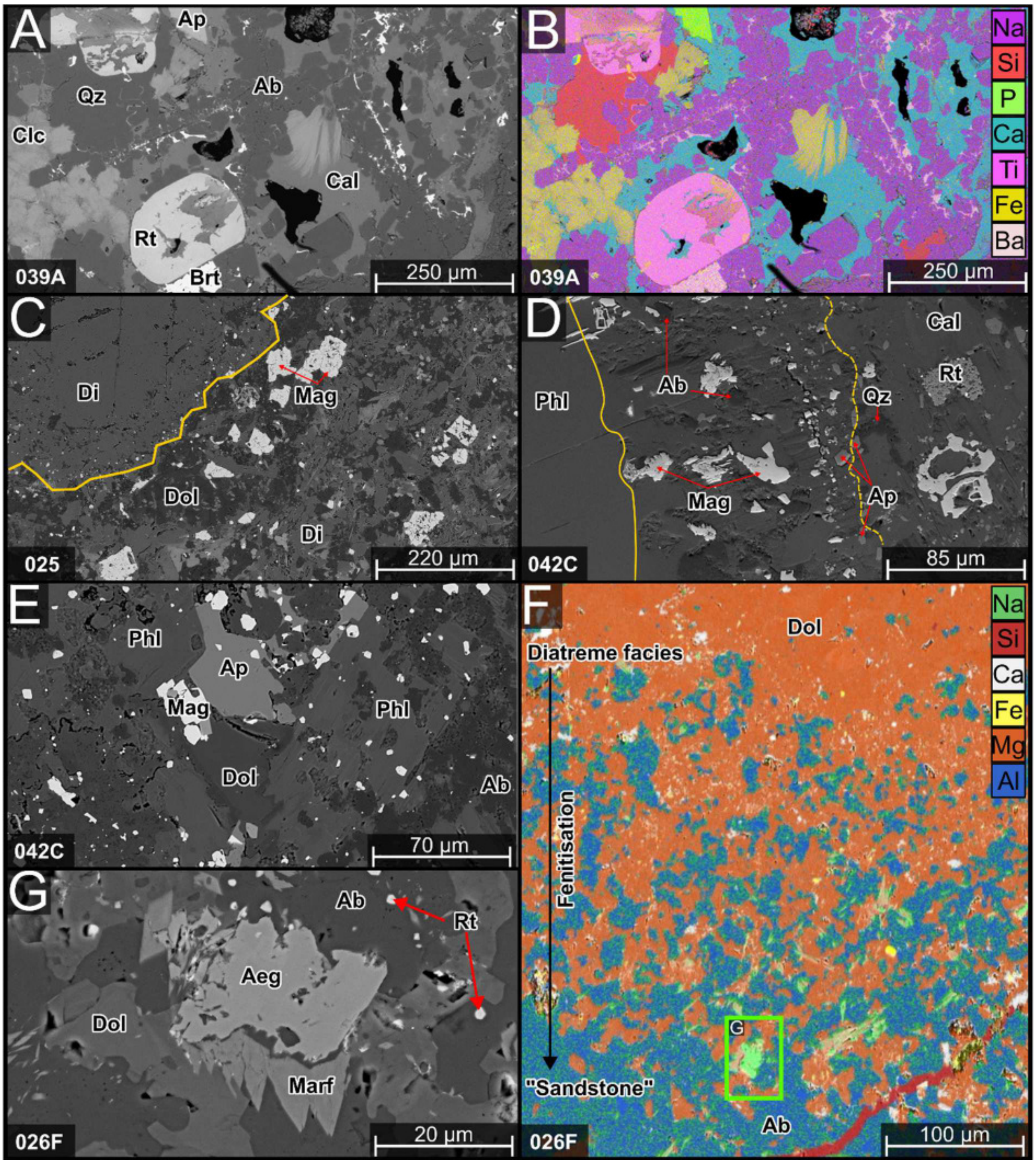

Figure 9. Selected back-scattered electron (BSE) images and EDX *(*energy dispersive X-ray) elemental mappings: A) BSE image of a euhedral assemblage comprising apatite, rutile, albite, and clinochlore, surrounded by interstitial calcite and quartz; B) Corresponding EDX mapping illustrating paragenetic relationships; C) Altered diopside phenocryst at the contact between diopside and its immediate surroundings; D) Phlogopite phenocryst with an alteration rim, as indicated by yellow lines; E) Close-up of the phlogopite-bearing matrix; F) EDX mapping of the direct contact between the diatreme facies and the Schwarzrand Subgroup, showing extensive fenitisation through a compilation of various elements: dolomite (orange), calcite (white), albite (greenish blue), and quartz (red). Location of the close-up BSE image is indicated by the green rectangle. G) Aegirine and magnesio-arfvedsonite surrounded by dolomite and albite

Wall rock contact alteration and fenitisation

To investigate contact relationships in detail and metasomatic interactions (fenitisation), multiple samples were selected from the contact between the Namaqua basement / Schwarzrand sandstone and the KAP intrusives (Figs 7C & D). Although metasomatic halos are not as prominent compared to intrusive carbonatite complexes, bleached basement is common a couple of metres around KAP diatremes. The contact between the diatremes and Schwarzrand sediments appears sharper than the contacts with the Namaqua basement. On sample scale, the Namaqua - KAP intrusive contact is characterised by elevated K contents within the aphanitic matrix, as indicated by elemental mappings (Fig. 7C). In contrast, the basement or basement-derived xenoliths exhibit K-feldspar variably replaced by albite or, in some cases, consist solely of albite (Figs 7B & C). This implies sodium enrichment in the wall rock and a corresponding potassium enrichment within the diatremes. Sample GRB026F shows a sharp contact between a dyke and Schwarzrand sandstone (7D). BSE imaging and EDX mapping (Fig. 9F) reveals that the diatreme at the top of the image, composed of dolomite (orange) and interstitial calcite (white), transitions to albite-dominated sandstone (blue) at the bottom with green spots of aegirine and a quartz vein (red). High resolution BSE imagery reveals the presence of aegirine and magnesio-arfvedsonite with a characteristic wedge shape (Fig. 9G), and sodic metasomatism emanating from the intruding dyke. Scattered, relatively small rutile is also present.

Whole Rock Analysis and Geochemistry

For this study, 35 whole-rock analyses were conducted on selected samples from the Garub valley. The results of these analyses are presented in appendices 3-5. Please note that the diatreme facies samples commonly contain clasts and xenoliths of various lithologies, which implies significant contamination of the original magma. Therefore, all whole rock data should be interpreted with this potential contamination in mind.

Major Elements

The binary diagrams in Figure 10 reveal several notable features. The samples from the Garub valley closely align with those from the broader KAP analysed by Schreuder (1975). It is interesting that the fenitisation of the gneissic basement is also evident from the chemical data. Some basement samples show a loss of SiO_2 (up to 20 wt.%) and Fe_2O_3, concomitant with a gain of CaO and Na_2O. The behaviour of the alkalis is particularly interesting as it complements earlier insights into the character of the fenitisation, with two distinct tendencies observed: the basement gneiss becomes enriched in Na_2O and depleted in K_2O (almost 4 wt.%; Fig. 10C-D), clearly showing a sodic fenitising character. Similarly, one of the two siltstone samples follows this gain and loss trend.

Analysed KAP rocks vary significantly in K_2O content and do not accurately plot within the ultramafic lamprophyre field as defined by Rock (1986; Fig. 10D). The distinction between ultramafic and calc-alkaline lamprophyres can be made using TiO_2 content, with a threshold of 2.5 wt.% (Rock, 1986). Nearly all diatreme samples fall just above this value, which is characteristic of ultramafic lamprophyres.

When compared to similar occurrences of diatreme-hosted ultramafic intrusives, such as Aillik Bay (Canada; Tappe *et al.*, 2006) and Gross Brukkaros (Walter *et al.*, 2023), or carbonatites and aillikites from the Batain Nappes diatremes (Oman; Nasir *et al.*, 2011), the chemistry of the analysed rocks most closely resembles aillikites and damtjernites. There is a notable overlap in SiO_2 vs CaO and SiO_2 vs TiO_2 ratios (Figs 10A & F), but a significant discrepancy in the Al_2O_3 vs MgO bivariation (Fig. 10G). The ultramafic lamprophyre (UML) suite, including some primary silicocarbonatites from the Beara Peninsula (Ireland; Moore *et al.*, 2022), also shares similar compositional traits. The diatreme or dyke-hosted carbonatites and the KAP intrusives exhibit a close chemical affinity, more particularly overlapping with Garub valley samples of lower SiO_2 content.

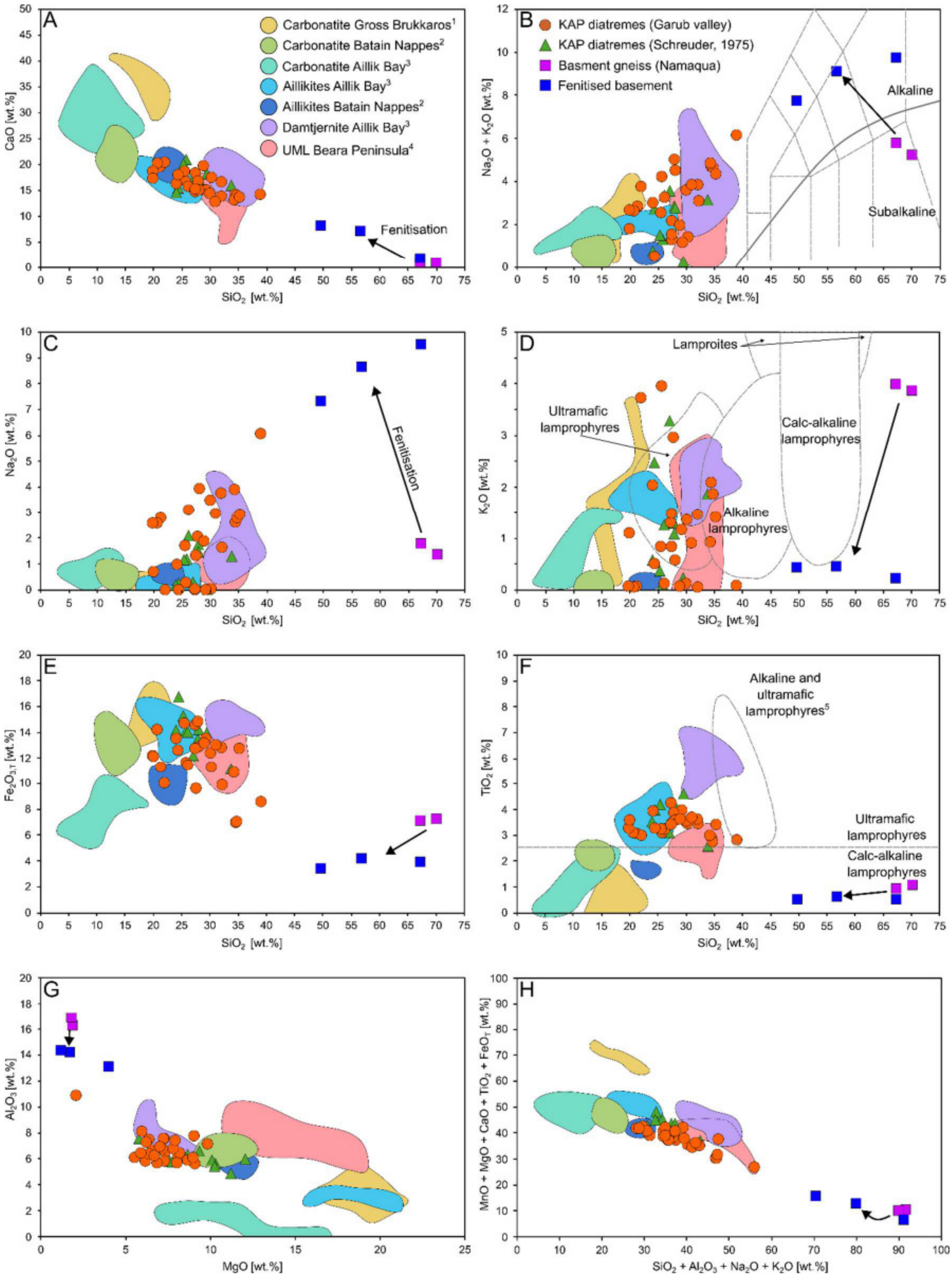

Figure 10. Binary plots illustrating the composition of present KAP samples, previous KAP data (Schreuder, 1975), basement gneiss, fenitised basement, Gross Brukkaros carbonatitic diatremes (Walter *et al*., 2023), carbonatites/aillikites from Batain Nappes diatremes (Nasir *et al*., 2011), carbonatites, aillikites and damtjernite from Aillik Bay (Tappe *et al*., 2006) and silicocarbonatite and lamprophyre from Ireland (Moore *et al*., 2022). Arrows indicate chemical changes due to fenitisation. A-F) Major element vs SiO_2 plots: B) classical TAS discrimination, D) discrimination after Rock (1986); F) mafic and calc-alkaline distinctions after Rock (1986) / alkaline and ultramafic lamprophyre fields after Krmíček and Chalapathi Rao (2022); G) Al_2O_3 vs MgO plot; H) plot of elements compatible in carbonatite vs carbonated-silicate melts

Differences within the KAP intrusive rocks based on factors such as emplacement mode (diatreme, dyke, or sill), country rock type, texture, and appearance were considered to identify chemical groupings, but this approach has not been particularly successful. To compare the Garub intrusives with other ultramafic rocks worldwide, a database comprising 3857 carbonatite analyses (DIGIS Team, 2025), 1821 kimberlite samples, and 324 ultramafic lamprophyres (Giuliani *et al*., 2025) was used. The analysed KAP diatreme samples, with an average of ca. 28.1 wt.% SiO_2, are akin to the average compositions of ultramafic lamprophyres and kimberlites, while carbonatites typically contain less than 10 wt.% SiO_2.The average CaO content of 16.4 wt.% is generally higher than that of ultramafic lamprophyres and kimberlites, which hover around 10 wt.%, while in carbonatites Ca typically is the most abundant element. Na_2O contents of up to 6 wt.% are relatively high, and are usually found only in extrusive carbonatites such as Oldoinyo Lengai (Tanzania), rarely in ultramafic lamprophyres or kimberlites. Potassium contents, with an average of ~1.2 wt.%, are scattered and fall within the range of other ultramafics.

Fe content (Fe_2O_3total) is slightly higher than in kimberlites, with an average of ~11.9 wt.%. TiO_2, averaging 3.4 wt.%, is even more elevated compared to kimberlites, and also unusually high relative to carbonatites. In contrast, MgO, averaging 7.2 wt.%, is very low compared to kimberlites and ultramafic lamprophyres, but falls within the range of carbonatites. Other major elements, such as Mn_2O_3 (average of 0.3 wt.%) and P_2O_5 (average of 1.2 wt.%), and loss on ignition (average of 20.5 wt.%), are detailed in appendices 3-5.

The classical definition scheme for carbonatites proposed by Gittins and Harmer (1997) was employed, given the significant carbonate component in the magmatic rocks. This approach indicates that the KAP rocks are ferrocarbonatites to ferruginous calcio-carbonatites. When considering the potential influence of other Ca-, Mg-, or Fe-bearing minerals, such as Fe oxides or phlogopite, the data points do not represent the carbonate fraction. Thus, it is assumed that they fall a bit farther away from the FeO/MnO end member, between the ferruginous calcio-carbonatite and magnesio-carbonatite field, only taking the carbonate composition into account.

As the KAP rocks have been previously described as ultramafic lamprophyres or alnöitic tuffisites, a second classification scheme after Rock (1986) is deemed appropriate (Fig. 11A). This scheme is based on MgO, FeO_T, and Al_2O_3 content ratios and places the Garub rocks within the alnöite and aillikite fields. Other occurrences of UMLs and carbonatite plot nearby, but have higher MgO contents, although they still lie within the above fields (Fig. 11A).

Trace Elements

Primitive mantle-normalised REE patterns (Fig. 11B) demonstrate that the Garub intrusives are compositionally similar, though slightly enriched in LREE relative to the REE-depleted Nama Group host rocks, which exhibit a negative Europium (Eu) anomaly. This anomaly also appears in the basement gneiss and its fenitised equivalent. The unfenitised basement is richer in HREE than the KAP suite, while one fenite sample is LREE-enriched but nearly HREE-devoid. Calcite carbonatites from Dicker Willem show similar REE trends, with Garub valley samples overlapping the lower part.

On a Sm vs La/Yb plot, these samples lie just above the UML field (Rock, 1986), due to elevated Sm levels (Fig. 11C). Sm/Yb vs La/Yb trends align with partial melting (~7%) of carbonated garnet peridotite (Fig. 11D), diverging from pure garnet or spinel peridotite sources with lower Ta/Yb. The Ce/Pb vs Sm/Nd plot (Fig. 11E) suggests crustal assimilation during melt ascent. High Ce/Pb implies an asthenospheric source; lower values indicate upper/middle crustal contamination. While such trace element ratios are typically applied to basaltic systems, their application to UMLs yields useful, though simplified, insights into mantle processes. Radiogenic isotope studies remain essential for definitive source interpretations.

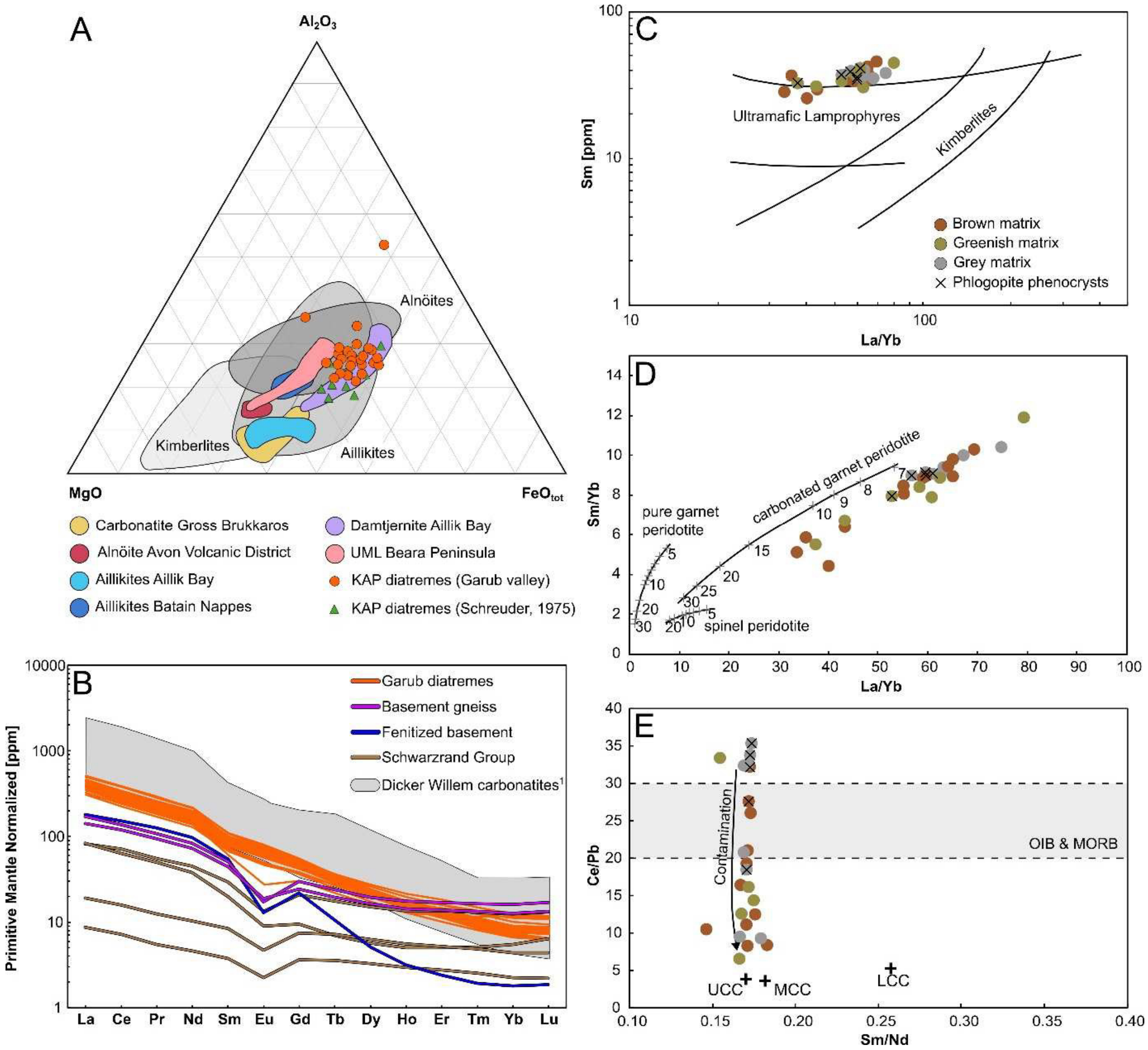

Figure 11. A) Classification for kimberlites, aillikites and alnöites following Rock (1986); comparative data are from carbonatitic diatremes from Gross Brukkaros (Walter *et al*., 2023), alnöites from the Avon Volcanic District (Shavers *et al*., 2016), aillikites and damtjernite from Aillik Bay (Tappe *et al*., 2006), aillikites from Batain Nappes diatremes (Nasir *et al*., 2011) and silicocarbonatite and lamprophyre from Ireland (Moore *et al*., 2022); B) Primitive mantle-normalised rare earth element (REE) plot after Sun and McDonough (1989) of the Garub intrusive suite including Namaqua basement gneiss, fenitised basement, and Nama Group host rocks (brown). For reference, values for the Dicker Willem calcite carbonatites (grey) are shown, representing a classical REE-barren carbonatite (unpublished data); C) Sm vs La/Yb plot after Rock (1986) showing fields for kimberlites and ultramafic lamprophyres; D) Sm/Yb vs La/Yb plot showing melting curves calculated for spinel peridotite, garnet peridotite and carbonated garnet peridotite, with numbers representing the degree of partial melting (adapted from Yu *et al*., 2015); E) Sm/Nd vs Ce/Pb plot showing ranges of typical OIB and MORB Ce/Pb ratios, and depleted mantle ratios (Hofmann *et al*., 1986), together with average upper continental crust (UCC), middle continental crust (MCC) and lower continental crust (LCC) (from Rudnick and Gao, 2003; diagram adapted from Yu *et al*., 2015)

Stable Isotopes

Carbon and oxygen isotope data of the Garub valley samples, along with six measurements from other KAP occurrences, are plotted together with data from various kimberlites, carbonatites, and ultramafic lamprophyres (Fig. 12). The Garub valley diatremes develop towards heavier isotopic ratios ($\delta^{18}O$, 15.1 to 19.5; $\delta^{13}C$, -4.1 to -0.84 ‰; Appendix 6) that align well with the Rayleigh (high temperature) fractionation or metasedimentary contamination trend (Deines, 1989). Data for Nama Group carbonates show characteristic values for limestone with an average of around 23.0 ‰ (δ^{18}O) and 1.6 ‰ (δ^{13}C) situated atop of this trajectory (Ries *et al*., 2009). Isotopic data for the gneissic basement is lacking, but δ^{18}O values for granitic to gneissic basement rock (e. g. Archaean crust) are generally around 10 ‰, and are unlikely to cause contamination (Harris *et al*., 2015, and references therein). The studied samples also show heavier carbon and oxygen isotopes compared to primitive igneous carbonatites (PIC; Taylor *et al*., 1967; Keller and Hoefs, 1995), to which aillikites from Aillik Bay (Canada) and some unevolved carbonatites belong (Fig. 12). The Garub valley samples display an increase of up to 10‰ in δ^{18}O and up to 4‰ in δ^{13}C relative to aillikite and some carbonatites. More evolved carbonatites (fractionated) as well as kimberlites from Udachnaya East (Siberia) and damtjernites from Chuktukon (Siberia), share a similar range of isotopic values. One measurement from the Gross Brukkaros carbonatite falls between the Garub valley diatremes and the broader KAP data, exhibiting relatively heavy δ^{18}O (> 25 ‰) and low δ^{18}C (< -4 ‰) values. These samples potentially follow the low temperature/hydrothermal alteration trend or the degassing trajectory away from the Garub valley trend, probably because of the hypabyssal emplacement mode and subsequent degassing and alteration. Sample GRB039A (globular textures) from the Garub valley shares these characteristics with the KAP samples.

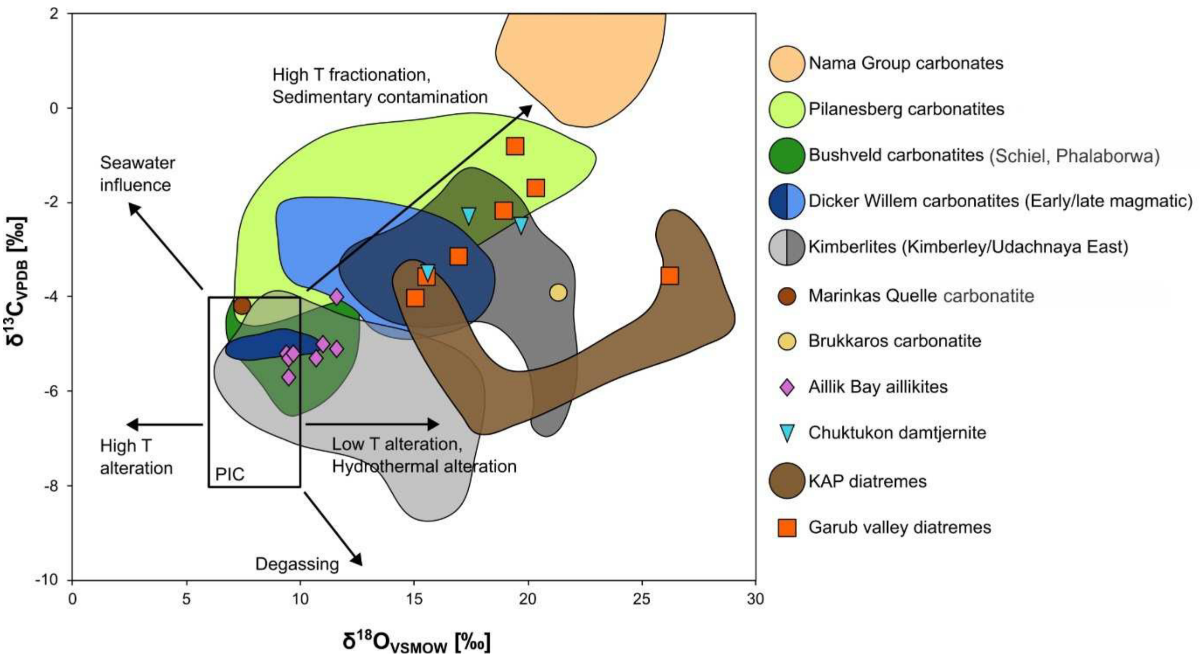

Figure 12. Carbon and oxygen isotope diagram displaying the Primary Igneous Carbonatite (PIC) field, based on Taylor *et al*. (1967) and Keller and Hoefs (1995), with arrows indicating processes that shift isotope ratios, following Deines (1989); also shown are data from the Nama Group sediments (Ries *et al*., 2009), Marinkas Quelle carbonatite (Horstmann and Verwoerd, 1997), Brukkaros carbonatite (Horstmann and Verwoerd, 1997), Pilanesberg carbonatites (Glenover, Nooitgedacht, Goudini, Kruidfontein, Bulhoek, Tweerivier, Stukpan, Spitskop, and Derdepoort; Horstmann and Verwoerd, 1997), Bushveld carbonatites (Schiel, Horstmann and Verwoerd, 1997; Phalaborwa, Munro and Harris, 2023), Dicker Willem (Reid and Cooper, 1992), kimberlites (Giuliani *et al*., 2014), aillikite from type locality Aillik Bay (Tappe *et al*., 2006), damtjernite from the Chuktukon Complex (Siberia; Doroshkevich *et al*., 2019) for comparison with the Kainab Alkaline Province (KAP) and Garub valley diatremes.

DISCUSSION

Classification of the Garub valley diatremes: kimberlites, ultramafic lamprophyres, or carbonatites?

The KAP diatremes have been variously described as alnöitic tuffisites and lamprophyric carbonate rocks (Schreuder, 1975), carbonatites of uncertain affinity (Verwoerd, 1993), olivine melilitites (Spriggs, 1988), or para-kimberlite (Winter and Rikhotso, 1998), underscoring the petrological and genetic complexity of these bodies. The common occurrence of phlogopite and less frequent diopside macrocrysts are characteristic of ultramafic lamprophyres as well as of kimberlites. In addition, although olivine has not been found in the studied samples, it may have been originally present, as indicated by pseudomorphic replacements by chlorite (Fig. 5E; Schreuder, 1975). The reported mineral data of garnet, spinel, clinopyroxene and ilmenite (Winter and Rikhotso, 1998), and a described kelyphitic garnet and rare augite (Schreuder, 1975) point towards mantle derived rocks for the KAP, although in the Garub valley samples none of these minerals have been observed apart from one rutile macrocryst and some clinopyroxene (Fig. 7G). The absence of these mantle-derived macrocrysts is atypical for mantle derived rocks (Tappe *et al*., 2005). Especially the presence of abundant interstitial quartz (matrix) throughout most samples complicates their proper classification and indicates that the Garub valley diatremes do not represent pristine mantle-derived rocks, but have undergone modification/contamination.

One distinguishing feature is the presence of local groundmass clinopyroxene in the samples, which excludes their classification as kimberlites or ultrapotassic orangeites (Tappe *et al*., 2005). Furthermore, the studied samples also are chemically distinct from kimberlites, as they display, on average, a relatively low Mg content of 7.2 wt.%, while kimberlites are generally richer in this element.

The Al_2O_3–FeO–MgO discrimination diagram (Fig. 11A; Rock, 1986) suggests that the KAP rocks are chemically related to ultramafic alnöites or aillikites. According to Tappe *et al*. (2005), three end members describe the petrographic and compositional continuum of ultramafic lamprophyres: alnöite (characterised by essential groundmass melilite), aillikite (characterised by essential primary carbonate), and damtjernite (characterised by essential groundmass nepheline and/or alkali feldspar). The KAP intrusives exhibit characteristics of both aillikite and damtjernite, being carbonate-rich and containing abundant albite/oligoclase. Evidence of melilite is solely based on the assumption that lath-shaped carbonates or feldspars are pseudomorphs after melilite (Schreuder, 1975). As no relics of melilite were found during this study, and laths of calcite or dolomite can be primary in carbonatites and aillikites (Tappe *et al*., 2006), the classification of the KAP diatremes as alnöites is rejected here. Similarly, in the Gardar alkaline igneous province (Greenland), the interpretation of carbonates as pseudomorphs after melilite has been questioned, leading to the rejection of a prior classification as alnöites (Upton *et al*., 2006).

Due to intense interaction and modification during emplacement, likely influenced by the presence of silicic xenoliths and other lithic fragments, the original composition of these rocks is cryptic. When accounting for significant Si and Al input from contamination and considering an originally higher Na content (subsequently depleted by fenitisation), an original carbonatitic character appears plausible. Based on µXRF mappings, a primary carbonate content of 30–50 vol.% is suggested, which may have been even higher if xenocrystic material is excluded. This would classify most samples as carbonatites, while the prevalence of dolomite over calcite and the high silica content (>20 wt.% SiO_2) further classifies these rocks as dolomitic silico-carbonatites (Le Maitre, 2002; Mitchell, 2005; Yaxley *et al*., 2022; Tappe *et al*., 2025).

However, due to their ultramafic character, particularly the presence of phlogopite macrocrysts, classification as aillikite-damtjernite (transition) is also possible. Since damtjernites have been considered gangue equivalents to carbonatites (Kapustin, 1981), the authors interpret the Garub valley rocks as hypabyssal dolomite silico-carbonatites with a distinguished UML affinity. A smooth transition between these rock types is possible.

Origin of Textures and their Implications

Magmaclasts as evidence for carbo(hydro) thermal fluids?

These segregations can resemble pelletal lapilli in their petrographic features, but are generally coarser and often lack a macrocrystal core (Clement, 1982). Where abundant, they give the rock a pseudo-conglomeritic appearance (Fig. 3H). They are believed to form due to surface tension in boiling magma within near-surface hypabyssal environments, as proposed by Clement (1982) and Mitchell (1986). The term "globular segregations," initially introduced by Clement and Skinner (1985), has evolved into the descriptive term "magmaclasts", now widely accepted (Webb and Hetman, 2021). The origin of these textures, involving the interplay of explosive emplacement, magma fragmentation, and physical aspects such as pipe or diatreme geometry, is diversely discussed and interpreted (Scott Smith *et al.*, 2018; Webb and Hetman, 2021 and references therein).

The observed globular texture in the samples closely resembles magmaclasts, with uniform rims encompassing rounded xenoliths to distinguish them from resorbed xenoliths or breccias. Additionally, the curvilinear edges with sharp transitions to the calcite and siderite matrix (as seen in Figs 8E-F) and the abundance of vesicles (shown in Figs 9A-B) point to a magmaclastic origin rather than a brecciated one. The magmaclasts are surrounded by euhedral calcite and interposed bands of ankerite, thought to have precipitated from a carbo(hydro)thermal fluid, either derived from a late pulse associated with the earlier ascending melt or, more plausibly, exsolved from the freshly contaminated melt. The mineral assemblage of the magmaclasts (Figs 9A-B) is interpreted to consist of microcrysts of apatite, rutile, and magnetite, surrounded by calcite, albite, and clinochlore with some baryte, which are all minerals commonly associated with hydrothermal regimes. However, as these magmaclasts are separated from the matrix and differ in containing silicate phases, they represent a transitional stage between hydrothermal and magmatic conditions. This could arguably be labelled as the brine-melt stage (Walter *et al.*, 2021). Evidence pointing towards a hydrothermal regime are also the elevated $\delta^{18}O$ values of the carbonates, which is attributed to the common dolomite and ankerite matrix (Fig. 12). Quartz cannot form in carbonatites under typical magmatic conditions (>400°C) due to the low silica activity in carbonatitic systems at high temperatures (Massuyeau *et al.*, 2015). However, at lower temperatures, such as those found under hydrothermal conditions, silica buffering ceases, allowing quartz to become stable (Yaxley *et al.*, 2022). It is believed that during the adiabatic cooling of the brine-melt upon partial vaporisation (eruption), silica buffering decreases abruptly, facilitating the immediate formation of quartz (Walter *et al.*, 2023).

Pelletal lapilli as evidence for two types of melt

Pelletal lapilli are primary magmatic constituents, not rounded xenolithic clasts, and are characteristic of diatreme rocks, indicative of diatreme environments (Mitchell, 1995). Although originally described in kimberlites, they are also present in melilitites, orangeite, or, more rarely, in carbonatite diatremes (e. g. Carnevale and Zanon, 2024). Rocks containing pelletal lapilli derive from CO_2–rich magmas (Mitchell, 1995) and are believed to form by rapid expulsion of dissolved volatiles (Clement, 1982) or by interaction with groundwater (Mitchell, 1986). As suggested by Gernon *et al.* (2012) their formation can be explained by gas jets caused by strong degassing, lifting and coating nearby particles with a low-viscosity melt (Fig. 13).

In the studied rocks, the seed materials are commonly alkali feldspar (probably derived from basement gneisses), but also xenoliths (Figs 7E-F). Some kernels appear to have been altered to carbonate, veiling their original composition. The rims of the kernels vary, but tiny (<50 µm) dolomite, rutile, magnetite, and apatite crystals are present throughout, indicating high-temperature formation (Prokopyev *et al.*, 2023). The absence of accretionary lapilli and glassy or bread-crust surfaces suggests high-temperature, mostly "dry" eruption conditions (Lloyd and Stoppa, 2003), pointing to the rapid expulsion of dissolved volatiles rather than an interaction with groundwater. This is in accordance with the stable isotope data, in which there seem to be no evidence of alteration due to meteoric water, but rather evidence pointing towards degassing (Fig. 12).

Two distinct types of pelletal lapilli,

with distinct mineral seeds and "halos" have been encountered. Accordingly, two discrete environments are assumed for their formation, differing both in location and melt composition. The location, in terms of relative depth within a diatreme system (Fig. 13A), varies as type 1 pelletal lapilli are found in xenolith-barren samples. This suggests either a sub-explosive level (root zone) or, more likely, a less violent emplacement lacking strong brecciation and associated CO_2 exsolution. This aligns with the differing types of kernels, interpreted to be mantle-derived diopside and magnetite, along with dolomite probably replacing original olivine and diopside (Figs 5A-B, 7A, 8A-B & 13D). Thus, type 1 pelletal lapilli indicate an essentially ultramafic and uncontaminated silicate melt (no basement fragments present), allowing the formation of later diopside around diopside macrocrysts.

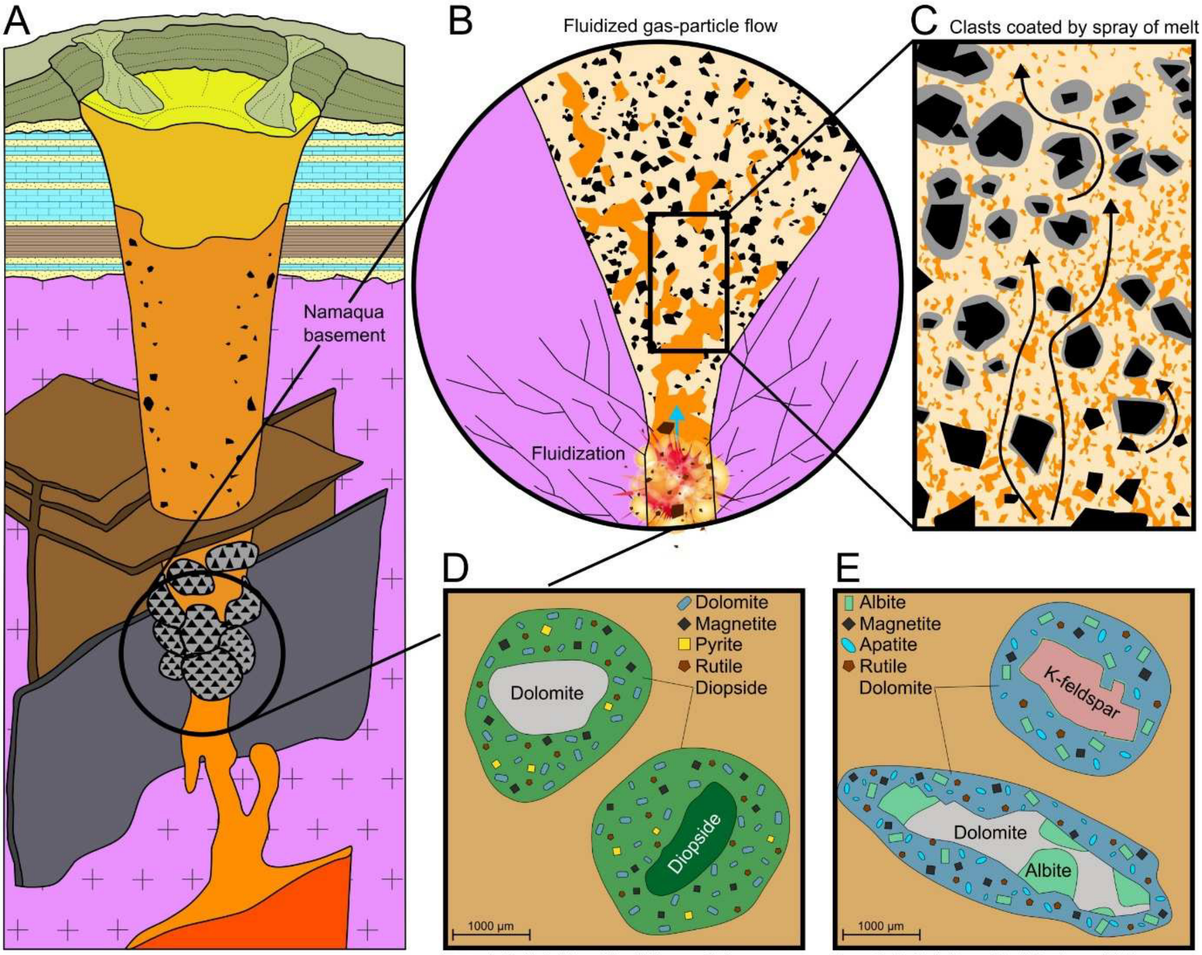

Type 1 Pelletal Lapilli - "Ultramafic"

Type 2 Pelletal Lapilli - "Carbonatitic"

Figure 13. Schematic illustration depicting the formation of pelletal lapilli within diatremes in the Garub valley: A) Cross-section of a diatreme adapted from Mitchell (1986) reflecting the local geology; B) Closer view of the lower diatreme facies, illustrating the explosive emplacement of a mingled, CO_2-exsolving melt (fluidised gas-particle flow); C) This process leads to the formation of pelletal lapilli, which are lithic fragments coated by sprayed melt-particles during their turbulent, fluidised ascent. D) Type 1 ultramafic pelletal lapilli, consisting of a phenocryst kernel surrounded by a halo rich in diopside and dolomite, with minor amounts of magnetite, pyrite, and rutile (sketch based on sample GRB025); E) Type 2 carbonatitic pelletal lapilli featuring xenolith and xenocryst kernels from the surrounding Namaqua basement, encased in a halo primarily composed of dolomite and albite, along with apatite, magnetite, and rutile (sketch based on sample GRB033B)

Type 2 pelletal lapilli are typically found in samples that are rich in basement fragments, which almost all serve as seeds (Figs 5D, 7E-F, 8C-D, 13E). Xenoliths from the Schwarzrand Subgroup show no reaction, likely because they were a late addition to the already formed pelletal lapilli. The melt had probably already reacted with these xenoliths (resorption, Fig. 15), overcoming the chemical gradient between the ultramafic melt and the felsic xenoliths. Consequently, the emplacement level of this sample should be significantly above the site of explosion (also indicated by the relatively small size of pelletal lapilli). In contrast, the pelletal lapilli with larger and solely gneissic xenoliths/xenocrysts with halos, probably solidified at deeper levels closer to the explosion. This variation is likely due to different velocities of the kernels being sprayed by the melt, with larger particles moving upward more slowly, allowing for size-based sorting within a single diatreme. Since halos of type 2 pelletal lapilli are practically devoid of silicate minerals (apart from minor albite), the melt spraying the lithic fragments probably was of a carbonatitic character. Thus, these halos provide evidence of a carbonatitic melt before intensive contamination or leaching of the basement introduced significant amounts of Si, Al, and other felsic-typical elements.

In summary, these two pelletal lapilli types indicate the presence of two distinct melts that formed the Garub intrusives. As the matrices of most samples are quite similar, they are believed to represent the resulting, heavily contaminated melt after the explosive emplacement level, probably affected by successive hydrothermal fluids. This process resulted in relatively uniform whole-rock compositions throughout the numerous intrusives of the Garub valley.

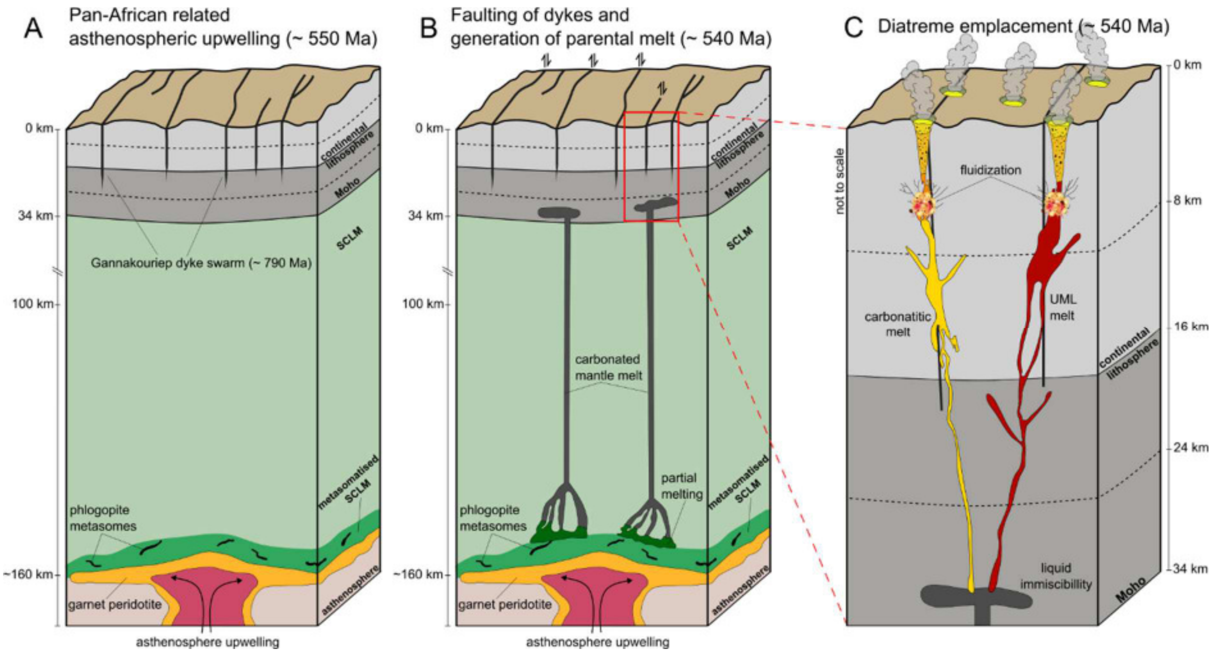

Figure 14. Schematic illustration depicting the assumed stages leading to diatreme formation in the Garub valley. The process is shown by means of cross-sections extending to the asthenosphere (not to scale), including asthenospheric upwelling, phlogopite metasomes, and partial melting: A) llustrates the Pan-African related asthenospheric upwelling; B) Partial melting generates a mantle-derived carbonated peridotite melt ascending through the SCLM (subcontinental lithospheric mantle).; C) Further ascent of a now immiscible mantel melt (carbonatite - yellow; UML - red) along pre-existing faulted dykes to shallow crustal levels and subsequent fluidisation, resulting in diatreme eruptions in the Garub valley

Deciphering the Magmatic Evolution and Origin

Mantle Source of the Primary Melt?

At Garub, primitive ultramafic lamprophyres (type 1 pelletal lapilli) likely represent carbonated mantle melts from depleted sources. At adiabatic temperatures, carbonatites cannot form in the asthenosphere, as the mantle adiabat exceeds the solidus of carbonated peridotite by 200–300 °C (Dasgupta *et al*., 2013). At 5–7 GPa, carbon exists as diamond, graphite, or alloy—not carbonate. During upwelling, garnet releases Fe^{3+}, oxidising carbon to CO_2, lowering the solidus by ~400 °C and producing carbonated silicate melts (Walter, 1998; Schmidt *et al.*, 2024). These melts are therefore carbonated silicates, not pure carbonatites. To produce the chemical characteristics observed in the Garub diatremes (high Ti, Fe, and Na) and explain the presence of phlogopite and diopside phenocrysts, partial flux-melting of phlogopite-ilmenite metasomes within the cratonic mantle is assumed (Pilbeam *et al.*, 2024). Accordingly, Nd-Hf isotope data from Labrador aillikites result from interactions between an asthenospheric carbonate-rich silicate melt and melts from K-rich metasomes in the cratonic mantle lithosphere (Tappe *et al.*, 2008). Evidence pointing towards a garnet peridotite mantle source includes the reported presence of a garnet phenocryst with a kelyphitic rim (Schreuder, 1975), believed to form around mantle garnets during their ascent (Obata, 2011). Limited mineral data report lherzolitic garnets, garnet-peridotite derived clinopyroxenes and mantle-derived spinels from the Kainab Alkaline Province (Winter and Rikhotso, 1998). Supporting this are Sm/Yb vs La/Yb ratios, suggesting a carbonated garnet peridotite source with around 6-7 % partial melting (Fig. 10D; Yu *et al.*, 2015). Negative εHf(t) values measured in the central part of the Kuboos-Bremen Line of intrusives (0 to –5; Grootpenseiland-Marinkas Quelle, Kanabeam, Bremen Complexes) are believed to result from partial melting of a metasomatised lithospheric mantle (Zech *et al.*, 2025). This would likely be similar to the Garub valley diatremes, but to confirm a mantle source, εHf-εNd isotopic values or the presence of unaltered "fresh" mantle material, such as olivines or lherzolitic xenoliths, as reported from kimberlites, are needed (e. g. Grégoire *et al.*, 2005).

Emplacement Mechanism of the Diatremes

The rapid ascent of carbonatitic and kimberlitic melts, is believed to be driven by the violent exsolution of CO_2, causing fracturing of the wall rock and creating pathways for the melt to ascend (e. g. Walter *et al.*, 2021; Russell *et al.*, 2012). The degassing of CO_2 can be explained by two main factors: decompression with decreasing depth and the decreasing solubility of CO_2 as SiO_2 content increases (~18-32 wt.%; Russel *et al.*, 2012). The disaggregation and dissolution (assimilation) of mantle debris increase SiO_2 content in the ascending melt, coupled with a drastic decrease in CO_2 solubility, thus propelling the magma through the upper mantle (Russell *et al.*, 2012). These factors can work together, creating a self-sustaining cycle that accelerates the ascent to potentially supersonic speeds (Walter *et al.*, 2021).

The primary mantle-derived melts that formed the Garub diatremes likely ascended in a similar way but underwent some modification. Assimilation of crustal material, as implied by Ce/Pb vs Sm/Nd ratios (Fig. 11E), thus facilitated the rapid ascend of the melt. At one point, the primary carbonated silicate melt began to segregate into a carbonatitic and residual silicate fraction (liquid immiscibility; e. g. Berndt and Klemme, 2022), corresponding to the two melts inferred from the two types of pelletal lapilli present (see above). This immiscibility probably occurred under crustal conditions, after the differentiation of primitive carbonated silicate melts to alkali contents exceeding 10 wt% (Brooker and Kjarsgaard, 2011; Schmidt *et al.*, 2024). Unlike primary melts from carbonated mantle, liquid immiscibility in natural CO_2-bearing silicate melts creates carbonatitic melts with high alkali contents (8–25 wt% $Na_2O + K_2O$), accounting for the formation of fenites (Schmidt *et al.*, 2024).

The carbonatitic melt and the residual silicate melt then further ascended to shallow crustal levels until fluidisation facilitated explosive emplacement. Evidence for a phreatomagmatic emplacement (e. g. Brukkaros), such as quenched magma (glassy textures) or abundant vesicles is lacking (Kurszlaukis and Lorenz, 1997), while fluidisation is supported by the presence of pelletal lapilli. The carbonatitic melt probably suffered a more violently explosive emplacement, as these samples usually contain higher amounts and larger xenoliths of Namaqua basement material. Increased explosive power could be attributed to the rapid bleaching of basement xenoliths, causing rapid CO_2 exsolution (SiO_2 contamination). This process is summarised schematically in Figure 15.

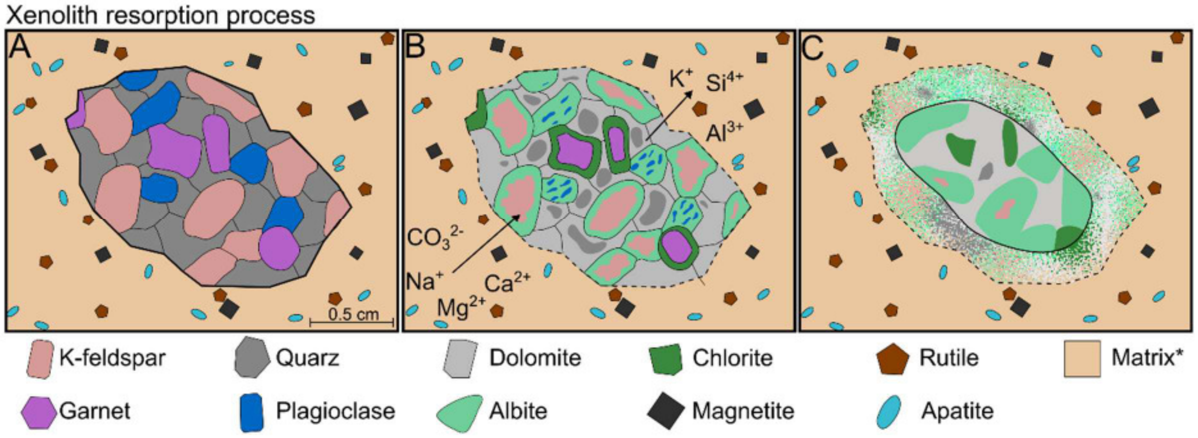

Figure 15. Schematic illustration depicting the stages of resorption of a gneissic Namaqua xenolith, composed of quartz, plagioclase, K-feldspar, and garnet (simplified composition), entrained in the diatreme-forming melt; the melt is represented by the typical observed matrix (*consisting of dolomite, albite, magnetite, rutile, and apatite). The illustration is based on elemental mappings from xenolith-rich samples (Fig. 7). A) Unaffected angular xenolith; B) Progressive albitisation, initially affecting plagioclase, followed by K-feldspar; garnet undergoes chloritisation, while quartz is replaced by dolomite. Elemental transfer between the melt and xenolith is indicated; C) Further resorption results in the shrinking of the now rounded xenolith. The halo comprises a very fine-grained mixture of K-feldspar, albite, quartz, dolomite, and chlorite.

Metasomatic Processes

Textures, mineral assemblages, and stable isotopes suggest the presence of a hydrothermal phase or overprint, which has caused alterations in the diatremes. These effects will be unravelled in the following discussion.

Xenolith Resorption

The common granitic to gneissic, frequently bleached Namaqua xenoliths, which are found in the diatreme samples, exhibit various degrees of alteration (Figs 4H & 7B, E & H), which can be so extensive that the xenoliths come to resemble the mineral composition of the matrix, including dolomite and albite. Such alteration and progressive resorption of xenoliths are commonly observed features, particularly in carbonatites (e. g. Giebel *et al.*, 2019; Walter *et al.*, 2022). Accordingly, the alteration and subsequent resorption of xenoliths are believed to result from three likely simultaneous processes, as illustrated in the paragenetic sequence (Fig. 6; numbered arrows corresponding to the processes): 1) albitisation, 2) chloritisation, and 3) dolomitisation.

Albitisation appears to be quite extensive, observable in both the host rocks and the diatreme samples. During albitisation of non-diatreme components, first plagioclase, then K-feldspar is replaced by albite. This order of replacement has been observed elsewhere (e. g. Kaur *et al.*, 2012) and is indicated by the presence of plagioclase in the country rock but not within the diatreme, with K-feldspar present in both. The presence of albite in the diatreme matrix is more difficult to explain, as it has a similar paragenetic character to dolomite, implying simultaneous crystallisation (e. g. Fig. 9E). Albite has been reported to be a major constituent (up to 65 vol. %) in the carbonatite breccia from Swartbooisdrif, and there is believed to be of hydrothermal origin pre-dating or synchronous to the carbonatite emplacement (Drüppel *et al.*, 2005).

The presence of chlorite group minerals (Figs 5E & 9B) in approximately half of the diatreme samples suggests a hydrous regime for their formation, as chloritisation is a typical reaction process in hydrothermal environments (e. g. Parneix *et al.*, 1985). There are two groups of chlorites: type 1 - trioctahedral, probably an alteration product of ultramafic minerals (Shirozu, 1978), and type 2 - dioctahedral, which could represent a primary (synmagmatic?) hydrothermal constituent. For type 2 chlorite, Al could be provided by the alteration of plagioclase to albite, while Fe and Mg are present in common garnets (almandine-pyrope) from the country rock. These elements are also available from the melt. Type 1 chlorite is likely a result of post-eruptive alteration due to intruding groundwater along the diatremes.

The observed transformation of quartz into dolomite within resorbed xenoliths is probably a magmatic process, as quartz within the surrounding wall rock is only partially affected by alteration. Since carbonatitic melts have very low viscosities (Dobson *et al.*, 1996), they can behave similar to a fluid and can also act as a metasomatic agents (Vasyukova and Williams-Jones, 2022). However, this is strictly a magmatic replacement and not metasomatism.

Xenolith resorption is envisioned to transform a fresh, angular gneissic fragment into a smaller, rounded (resorbed) xenolith with a fine-grained halo of tiny minerals from the original xenolith and the melt (Figs 15A-C). Elemental transfer is believed to cause an enrichment in Na, Mg, Ca, and CO_3 and a release of K, Si, and Al. This is supported by increased modal albite within the xenolith compared to pre-alteration modal plagioclase and K-feldspar.

Fenitisation

Fenitisation is partially observed at the Garub diatremes, as noted by Schreuder (1975). In the studied samples it can be categorised into two groups based on host rock type. Within the gneissic Namaqua host rock it is more pronounced due to its coarser texture and mineral composition, which is more susceptible to fenitisation (e. g. feldspar, quartz). In the Nama host rock fenitisation is observed in samples with direct contact relationships (GRB026F) to the diatreme. Evidence for fenitisation include the high abundance of albite/oligoclase in the Namaqua basement, along with turbid K-feldspars exhibiting perthite textures. Small biotite grains may also be of metasomatic origin. Fenitisation of the Schwarzrand sediments is less prominent. Where the diatreme is in direct contact with the Nama host rock, SEM analysis reveals abundant albite, as well as minor aegirine and magnesio-arfvedsonite, typical of sodic fenites (Fig. 9G; Elliott *et al.*, 2018). The lack of evidence for potassic fenitisation at the Garub diatremes does not necessarily imply it did not occur.

Spatial and temporal variations in fenites are influenced by temperature, pressure, and CO^2 content of the fenitising fluid (Rubie and Gunter, 1983). K is more mobile at lower temperatures, forming shallower potassic fenites, while sodium is lost from fluids at deeper levels (>600°C), creating deeper sodic fenites (Elliot *et al.*, 2018). The presence of K-feldspar rimmed by albite (Ruri Hills, Kenya and Koga, Pakistan), along with K-feldspar-rich fenite cut by albite veins (Bayan Obo, China; Le Bas, 2008), shows that sodic fenitisation can also follow potassic fenitisation.

The high abundance of K-feldspar in the Namaqua basement gneiss, would balance any potential chemical gradient, making a potassic fenitisation less prominent, while the low Na content in the basement gneiss creates a high gradient, allowing for more intense sodic fenitisation. However, it is believed that a major potassic fenitising fluid was not involved; rather, a highly sodic fluid led to the release of K, as indicated by the moderate albitisation of K-feldspar in the basement. The released K is probably available to form the non-macrocrystal phlogopite present in the matrix of some samples (Figs 7C, E & H).

The hydrothermal overprint, evidenced by the abundant albite within the diatremes and the wall rock, is most likely due to the same fluid expelled from the carbonatitic melt during its ascent and emplacement. The presence of abundant gneissic xenoliths and the high levels of Si and Al contamination made the carbonatitic, tuffisitic rock equally susceptible to metasomatism. Since multiple pulses of sodic aqueous fluids are typical (Elliot *et al.*, 2018), these fluids would be capable of fenitising both the wall rock and diatreme rocks, predominantly through albitisation. To gain a better understanding of these fluids, further studies are necessary.

Age and Geological Setting

The age of 491 ± 8 Ma, derived from Rb-Sr analyses on whole rock and biotite, can be considered as a lower limit (Allsopp *et al.*, 1979). Recent biotite Ar-Ar dating yields ages of 523 and 527 (±2) Ma (Zech *et al.*, 2025), corroborating earlier Ar-Ar ages ranging from 514 to 524 Ma (Spriggs, 1988). These Ar-Ar ages were determined from KAP rocks approximately 30 km south of the Garub valley and may not necessarily reflect the exact age of the intrusives within the Garub valley itself. For instance, the Hegau-Urach (Germany) volcanic region hosts numerous ultramafic volcanics across a comparable area, exhibiting age spans of 19–12 Ma (Urach) and 15–9 Ma (Hegau) of continuous volcanic activity (Binder *et al.*, 2023). Therefore, it is likely that the KAP encompasses ages spanning several million years, similar to the KBL, which does not show any age progression tracks, but rather an age range of approximately 70 million years (Zech *et al.*, 2025 and references therein).

The Great Karas Mountains, in which the Garub valley is located, are characterised by an extensive sedimentary cover of Fish River Subgroup (Fig. 1B), apparently barren of KAP intrusions. This implies that the Garub valley diatremes erupted through the Schwarzrand Subgroup (dated from 545.27 ± 0.11 Ma to 538.58 ± 0.19 Ma; Nelson *et al.*, 2022; Linnemann *et al.*, 2019), forming sills and pipes, but did not penetrate the Fish River Subgroup, which in turn argues for emplacement prior to the deposition of the Fish River Subgroup.

The most plausible stratigraphic age is associated with the Nomtsas Formation, specifically the ash bed W8 (538.58 ± 0.19 Ma; Linnemann *et al.*, 2019), which unconformably overlies the Urusis Formation (Fig. 2).

Within a similar time frame, the Pan-African orogenies led to the formation of the Damara, Kaoko and Gariep Belts (e. g. Miller, 1983; Gray *et al.*, 2006; Frimmel, 2008). The latter extends along the coast of southern Namibia (Fig. 1A), approximately 200 km west of the Garub valley. It has a collision-related metamorphic age of around 550-540 Ma (Frimmel and Frank, 1998). The Nama Group, interpreted as foreland basin sediments resulting from orogenic crustal thickening and subsequent erosion (Germs, 1983), indicates that the KAP intrusives were emplaced within the farther field of influence of this orogeny. This aligns with the fact that 75% of all carbonatites have erupted within 600 km of craton edges or within 2200 km of orogenic events (Humphreys-Williams and Zahirovic, 2021), both of which applies to the KAP intrusives.

Trigger for Emplacement

The intrusive complexes along the Kuboos–Bremen Line do not align with existing regional Namaquan or Gariepian geological structures. Instead, they cross-cut established boundaries leaving their tectonic emplacement mechanism poorly understood (Zech *et al.*, 2025). Their formation likely resulted from far-field effects associated with the contemporaneous Pan-African orogenies, which may also apply locally within the KAP. A plausible scenario is that asthenospheric upwelling along the KBL caused the magmatism, possibly related to the syn-convergent extension during intracontinental orogeny as, for instance, proposed for the Heping pluton in China (Xie *et al.,* 2020).

A major NNE-trending reverse fault system traversing the Great Karas Mountains (Karasburg graben shoulder) lies immediately to the west of the Garub valley (Fig. 1A), while approximately 20 km northeast of the valley, the NE-trending Trans-Kalahari Lineament, a deep-seated, crustal-scale fault, intersects the SE-trending Lord Hill-Excelsior shear zone, which forms the northern boundary of the Namaquan Kakamas Domain (Corner, 2000; Macey *et al*., 2022). Although diatremes of the Kainab Alkaline Province were rarely emplaced along these major structures (Fig. 1), satellite imagery reveals smaller fault systems and dykes within the Garub valley (Fig. 2).

Examination of magnetic imagery from the Grünau area reveals that the western KAP intrusions are frequently located on NNE-trending magnetic lineaments that represent dolerite dykes of the Gannakouriep swarm. Geophysical data for the eastern KAP has not been studied. During regional mapping by the Geological Survey of Namibia and Council for Geoscience (South Africa) faults were observed that formed along and reworked the Gannakouriep dykes (e. g. Macey *et al.*, 2020). The mapping also revealed that faults were active during Nama Group deposition, with blind faults that displaced lower Nama Group units overlain by younger, unaffected Nama sediments. Ar-Ar dating of the NNE-striking Oup fault SE of the Garub valley revealed an age of about 512 Ma (Büttner *et al.*, 2013), confirming faulting was active during Nama times. Given that Garub bodies intruded during the deposition of the Nama Group, and apparently along reworked Tonian dykes, we hypothesise that pre-existing deep Gannakouriep structures, reactivated during the development of the Nama Basin, provided the pathways for the emplacement of the diatreme-forming melts (Fig. 14).

Conclusions

The classification of the KAP rocks is complicated by their tuffisitic nature and contamination, which obscure the original melt composition. The examined rocks exhibit traits of both ultramafic and carbonatitic types in terms of emplacement style, texture, mineralogy, and alteration effects. While they are best described as carbonatitic, strict classification remains to be solved, with a focus on understanding their formative processes rather than rigid nomenclature.

Mineralogically, the Garub valley rocks include dolomite, albite, phlogopite, quartz, magnetite, rutile, apatite, clinochlore, calcite, and baryte, indicating both magmatic and hydrothermal origins. Stable isotope data confirm significant hydrothermal influence. Two distinct melt types are inferred: a diopside-bearing ultramafic melt and a silicate-free carbonatitic melt, likely derived from the first. Syn-magmatic hydrothermal fluids caused extensive albitisation and fenitisation, with diagnostic minerals like aegirine and arfvedsonite. Additional hydrothermal phases suggest carbonatitic influence but lack ore elements.

Country-rock xenolith resorption involved both magmatic and hydrothermal processes, introducing elements like Na, Mg, Ca, and C into xenoliths while releasing Si, Al, and K into the melt, contributing to contamination. Despite variations among diatremes, geochemical data indicate a common mantle source, with melt generated probably from carbonated garnet peridotite. Phlogopite, diopside, and ilmenite phenocrysts suggest a metasomatised subcontinental lithospheric mantle source.

An emplacement age of approximately 540 Ma is proposed, possibly along pre-existing Tonian Gannakouriep dykes, reactivated during the development of the Nama Basin in the foreland of the evolving Gariep and Damara Orogens.

Acknowledgements

The authors would like to thank Axel Müller for reviewing this article and providing insightful comments. Appreciation is also extended to Ute Schreiber for editorial guidance. Thanks are given to Cordelia Lange for her assistance in facilitating the measurement of sample compositions, as well as to Elisabeth Eiche, Tobias Kluge, Maya Denker, and Claudia Mössner for conducting the whole rock and isotope analyses. The authors would also like to thank Jorge Arthuzzi for joining the fieldwork and providing valuable field observations and insights. This study was supported by DFG (Deutsche Forschungsgemeinschaft) grants WA3116/14-1, GI1499/5-1, and MA 2563-25.

References

Al-Aasm, I. S., Taylor, B. E. and South, B. 1990. Stable isotope analysis of multiple carbonate samples using selective acid extraction. *Chemical Geology: Isotope Geoscience section,* **80**, 119–125.

Allsopp, H. L., Kostlin, E. O., Welke, H. J., Burger, A. J., Kröner, A. and Blignault, H. J. 1979. Rb-Sr and U-Pb geochronology of late Precambrian-early Palaeozoic igneous activity in the Richtersveld (South Africa) and southern South West Africa. *Transactions of the Geological Society of South Africa*, **82**, 185–204.

Anenburg, M., Broom-Fendley, S. and Chen, W. 2021. Formation of Rare Earth Deposits in Carbonatites. *Elements*, **17**, 327–332.

Baudrand, M., Aloisi, G., Lécuyer, C., Martineau, F., Fourel, F., Escarguel, G., Blanc-Valleron, M.-M., Rouchy, J.-M. and Grossi, V. 2012. Semi-automatic determination of the carbon and oxygen stable isotope compositions of calcite and dolomite in natural mixtures. *Applied Geochemistry,* **27**, 257–265.

Bell, K. and Tilton, G. R. 2001. Nd, Pb and Sr Isotopic Compositions of East African Carbonatites: Evidence for Mantle Mixing and Plume Inhomogeneity. *Journal of Petrology*, **42**, 1927–1945.

Berndt, J. and Klemme, S. 2022. Origin of carbonatites—liquid immiscibility caught in the act. *Nature Communications,* **13**, https://doi.org/10.1038/s41467-022-30500-7

Bial, J., Büttner, S. and Appel, P. 2016. Timing and conditions of regional metamorphism and crustal shearing in the granulite facies basement of south Namibia: Implications for the crustal evolution of the Namaqualand metamorphic basement in the Mesoproterozoic. *Journal of African Earth Sciences,* **123**, 145–176.

Binder, T., Marks, M. A. W., Gerdes, A., Walter, B. F., Grimmer, J., Beranoaguirre, A., Wenzel, T. and Markl, G. 2023. Two distinct age groups of melilitites, foidites, and basanites from the southern Central European Volcanic Province reflect lithospheric heterogeneity. *International Journal of Earth Sciences,* **112**, 881–905.

Brooker, R. A. and Kjarsgaard, B. A. 2011. Silicate–Carbonate Liquid Immiscibility and Phase Relations in the System SiO_2 – Na_2O - Al_2O_3 – CaO - CO_2 at 0.1 – 2.5 GPa with Applications to Carbonatite Genesis. *Journal of Petrology*, **52**, 1281–1305.

Büttner, S. H., Sherlock, S., Fryer, L., Lodge, J., Diale, T., Kazondunge, R. and Macey, P. 2013. Controls of host rock mineralogy and H_2O content on the nature of pseudotachylyte melts: Evidence from Pan-African faulting in the foreland of the Gariep Belt, South Africa. *Tectonophysics,* **608**, 552–575.

Carnevale, G. and Zanon, V. 2024. Characterisation of Pelletal Lapilli in Explosive Melilitite–Carbonatite Eruptions: An Example from Mt. Vulture Volcano (Southern Italy). *Geosciences*, **14(12)**, https://doi.org/10.3390/geosciences14120349

Clement, C. 1982. *A comparative geological study of some major kimberlite pipes in the Northern Cape and Orange Free State*. Ph.D. thesis, University of Cape Town, South Africa, 451 pp.

Clement, C. R. and Skinner, E. M. W. 1985. A textural-genetic classification of kimberlites. *South African Journal of Geology*, **88**, 403–409.

Corner, B. 2000. Crustal framework of Namibia derived from magnetic and gravity data. *Communications of the Geological Survey of Namibia,* **12**, 15–22.

Dasgupta, R., Hirschmann, M. M., McDonough, W. F., Spiegelman, M. and Withers, A. C. 2009. Trace element partitioning between garnet lherzolite and carbonatite at 6.6 and 8.6 GPa with applications to the geochemistry of the mantle and of mantle-derived melts. *Chemical Geology*, **262**, 57–77.

Dasgupta, R., Mallik, A., Tsuno, K., Withers, A. C., Hirth, G. and Hirschmann, M. M. 2013. Carbon dioxide-rich silicate melt in the Earth's upper mantle. *Nature*, **493**, 211–215.

Davies, D. R. and Rawlinson, N. 2014. On the origin of recent intraplate volcanism in Australia. *Geology*, **42**, 1031–1034.

Deines, P. 1989. Stable isotope variations in carbonatites, 301–359. *In*: In Bell, K. (Ed.) *Carbonatites: Genesis and Evolution*. Unwin Hyman, London, UK, 618 pp.

DIGIS Team 2025. *GEOROC Compilation: Rock Types*. Georg-August Universität Göttingen, Germany, https://doi.org/10.25625/2JETOA

Dobson, D. P., Jones, A. P., Rabe, R., Sekine, T., Kurita, K., Taniguchi, T., Kondo, T., Kato, T., Shimomura, O. and Satoru Urakawa, S. 1996. In-situ measurement of viscosity and density of carbonate melts at high pressure. *Earth and Planetary Science Letters*, **143**, 207–215.

Dongre, A. and Tappe, S. 2019. Kimberlite and carbonatite dykes within the Premier diatreme root (Cullinan Diamond Mine, South Africa): New insights to mineralogical-genetic classifications and magma CO_2 degassing. *Lithos*, **338–339**, 155–173.

Doroshkevich, A. G., Chebotarev, D. A., Sharygin, V. V., Prokopyev, I. R. and Nikolenko, A. M. 2019. Petrology of alkaline silicate rocks and carbonatites of the Chuktukon massif, Chadobets upland, Russia: Sources, evolution and relation to the Triassic Siberian LIP. *Lithos*, **332–333**, 245–260.

Downes, H., Balaganskaya, E., Beard, A., Liferovich, R. and Demaiffe, D. 2005. Petrogenetic processes in the ultramafic, alkaline and carbonatitic magmatism in the Kola Alkaline Province: A review. *Lithos,* **85**, 48–75.

Drüppel, K., Hoefs, J. and Okrusch, M. 2005.

Fenitizing Processes Induced by Ferrocarbonatite Magmatism at Swartbooisdrif, NW Namibia. *Journal of Petrology*, **46**, 377–406.

Elliott, H. A. L., Wall, F., Chakhmouradian, A. R., Siegfried, P. R., Dahlgren, S., Weatherley, S., Finch, A. A., Marks, M. A. W., Dowman, E. and Deady, E. 2018. Fenites associated with carbonatite complexes: A review. *Ore Geology Reviews*, **93**, 38–59.

Foley, S. F., Yaxley, G. M. and Kjarsgaard, B. A. 2019. Kimberlites from source to surface: insights from experiments. *Elements*, **15**, 393–398.

Frimmel, H. E. 2008. The Gariep Belt. *In*: Miller, R. McG. (Ed.). *The Geology of Namibia*, Vol. **2**, chapter 14, 40 pp. Geological Society of Namibia, Windhoek.

Frimmel, H. E. and Frank, W. 1998. Neoproterozoic tectono-thermal evolution of the Gariep Belt and its basement, Namibia and South Africa. *Precambrian Research*, **90**, 1–28.

Frimmel, H. E., Zartman, R. E. and Späth, A. 2001. The Richtersveld Igneous Complex, South Africa: U-Pb Zircon and Geochemical Evidence for the Beginning of Neoproterozoic Continental Breakup. *The Journal of Geology*, **109**, 493–508.

Germs, G. J. B. 1983. Implications of a sedimentary facies and depositional environmental analysis of the Nama Group in South West Africa/Namibia, 89–114. *In*: Miller, R. McG. (Ed.), Evolution of the Damara Orogen of South West Africa/ Namibia. *Special Publications of the Geological Society of South Africa*, **11**, 515 pp.

Gernon, T. M., Brown, R. J., Tait, M. A. and Hincks, T. K. 2012. The origin of pelletal lapilli in explosive kimberlite eruptions. *Nature Communications*, **3**, https://doi.org/10.1038/ncomms1842

Geyer, G. 2005. The Fish River Subgroup in Namibia: stratigraphy, depositional environments and the Proterozoic–Cambrian boundary problem revisited. *Geological Magazine*, **142**, 465–498.

Giebel, R. J., Parsapoor, A., Walter, B. F., Braunger, S., Marks, M. A. W., Wenzel, T. and Markl, G. 2019. Evidence for Magma–Wall Rock Interaction in Carbonatites from the Kaiserstuhl Volcanic Complex (Southwest Germany). *Journal of Petrology*, **60**, 1163–1194.

Gittins, J. and Harmer, R. E. 1997. What is ferrocarbonatite? A revised classification. *Journal of African Earth Sciences*, **25**, 159–168.

Giuliani, A., Phillips, D., Kamenetsky, V. S., Fiorentini, M. L., Farquhar, J. and Kendrick, M. A. 2014. Stable isotope (C, O, S) compositions of volatile-rich minerals in kimberlites: A review. *Chemical Geology*, **374–375**, 61–83.

Giuliani, A., Pearson, D. G., Soltys, A., Dalton, H., Phillips, D., Foley, S. F., Lim, E., Goemann, K., Griffin, W. L. and Mitchell. R. H. 2020. Kimberlite genesis from a common carbonate-rich primary melt modified by lithospheric mantle assimilation. *Science Advances*. **6(17)**, https://doi.org/10.1126/ sciadv.aaz0424

Giuliani, A., Dalton, H. and Pearson, D. G. 2025. Kimberlites: The deepest geochemical probes of Earth, 159–230. *In*: Anbar, A. and Weis, D. (Eds) *Treatise on Geochemistry*, Elsevier, Amsterdam, Netherlands.

Gray, D. R., Foster, D. A., Goscombe, B., Passchier, C. W. and Trouw, R. A. J. 2006. ^{40}Ar/^{39}Ar thermochronology of the Pan-African Damara Orogen, Namibia, with implications for tectonothermal and geodynamic evolution. *Precambrian Research*, **150**, 49–72.

Grégoire, M., Tinguely, C., Bell, D. R. and Le Roex, A. P. 2005. Spinel lherzolite xenoliths from the Premier kimberlite (Kaapvaal craton, South Africa): Nature and evolution of the shallow upper mantle beneath the Bushveld complex. *Lithos*, **84**, 185–205.

Haggerty, S. E. 1994. Superkimberlites: A geodynamic diamond window to the Earth's core. *Earth and Planetary Science Letters*, **122**, 57–69.

Harris, C., Le Roux, P., Cochrane, R., Martin, L., Duncan, A. R., Marsh, J. S., Le Roex, A. P. and Class, C. 2015. The oxygen isotope composition of Karoo and Etendeka picrites: High δ^{18}O mantle or crustal contamination? *Contributions to Mineralogy and Petrology*, **170**, 8.

Hofmann, A. W., Jochum, K. P., Seufert, M. and White, W. M. 1986. Nb and Pb in oceanic basalts: new constraints on mantle evolution. *Earth and Planetary Science Letters*, **79**, 33–45.

Horstmann, U. E. and Verwoerd, W. J. 1997. Carbon and oxygen isotope variations in southern African carbonatites. *Journal of African Earth Sciences*, **25**, 115–136.

Humphreys-Williams, E. R. and Zahirovic, S. 2021. Carbonatites and Global Tectonics. *Elements*, **17**, 339–344.

Kamenetsky, V. S. 2016. Comment on: "The ascent of kimberlite: Insights from olivine" by Brett *et al*., 2015 [*Earth Planet. Sci. Lett*., **424**, 119–131]. *Earth and Planetary Science Letters*, **440**, 187–189.

Kamenetsky, V. S., Doroshkevich, A. G., Elliott, H. A. L. and Zaitsev, A. N. 2021. Carbonatites: Contrasting, Complex, and Controversial. *Elements*, **17**, 307–314.

Kapustin, Y. L. 1981. Damkjernites—dike equivalents of carbonatites. *International Geology Review*, **23**, 1326–1334.

Kaur, P., Chaudhri, N., Hofmann, A. W., Raczek, I., Okrusch, M., Skora, S. and Baumgartner, L. P. 2012. Two-Stage, Extreme Albitization of A-type Granites from Rajasthan, NW India. *Journal of Petrology*, **53**, 919–948.

Keller, J. and Hoefs, J. 1995. Stable Isotope Characteristics of Recent Natrocarbonatites from Oldoinyo Lengai, 113-123. *In*: Bell, K. and Keller, J. (Eds) *Carbonatite Volcanism: Oldoinyo Lengai and the Petrogenesis of Natrocarbonatites*. Springer, 210 pp.

Kim, S.-T., Coplen, T. B. and Horita, J. 2015. Normalization of stable isotope data for carbonate minerals: Implementation of IUPAC guidelines. *Geochimica et Cosmochimica Acta*, **158**, 276–289.

Kjarsgaard, B. A., Pearson, D. G., Tappe, S., Nowell, G. M. and Dowall, D. P. 2009. Geochemistry of hypabyssal kimberlites from Lac de Gras, Canada: Comparisons to a global database and applications to the parent magma problem. *Lithos*, **112**, 236–248.

Krmíček, L. and Chalapathi Rao, N. V. 2022. Lamprophyres, lamproites and related rocks as tracers to supercontinent cycles and metallogenesis. *In*: Krmíček, L. and Chalapathi Rao, N. V. (Eds), Lamprophyres, Lamproites and Related Rocks: Tracers to Supercontinent Cycles and Metallogenesis. *Geological Society, London, Special Publications*, **513**, 1-16.

Kurszlaukis, S. and Lorenz, V. 1997. Volcanological features of a low-viscosity melt: the carbonatitic Gross Brukkaros Volcanic Field, Namibia. *Bulletin of Volcanology*, **58**, 421–431.

Le Bas, M. J. 2008. Fenites associated with carbonatites. *The Canadian Mineralogist*, **46**, 915–932.

Le Maitre, R. W., Streckeisen, A., Zanettin, B., Le Bas, M. J., Bonin, B. and Bateman, P. (Eds) 2002. *Igneous Rocks: A Classification and Glossary of Terms*. Cambridge University Press, Cambridge, UK, 236 pp.

Linnemann, U., Ovtcharova, M., Schaltegger, U., Gärtner, A., Hautmann, M., Geyer, G., Vickers-Rich, P., Rich, T., Plessen, B., Hofmann, M., Zieger, J., Krause, R., Kriesfeld, L. and Smith, J. 2019. New high-resolution age data from the Ediacaran–Cambrian boundary indicate rapid, ecologically driven onset of the Cambrian explosion. *Terra Nova*, **31**, 49–58.

Lloyd, F. and Stoppa, F. 2003. Pelletal Lapilli in Diatremes - Some Inspiration from the Old Masters. *GeoLines*, **15**, 65-71.

Macey, P. H., Minnaar, H., Miller, J. A., Lambert, C. W., Kisters, A. F., Diener, J. F. A, Thomas, R. J., Groenewald, C. A. Indongo, J., Angombe, M., Smith, H., Shifotoka, G., Le Roux. P., and Frei, D. 2020. The Precambrian Geology of the Warmbad region, Southern Namibia, Chapter 8 – Post-Namaqua intrusions and superficial deposits. Unpublished Report Council for Geoscience (South Africa)/Geological Survey of Namibia, 72 pp.

Macey, P. H., Thomas, R. J., Kisters, A. F. M., Diener, J. F. A, Angombe, M., Doggart, S., Groenewald, C. A., Lambert, C. W., Miller, J. A., Minnaar, H., Smith, H., Moen, H. F. G., Muvangua, E., Nguno, A., Shifotoka, G., Indongo, J., Frei, D., Spencer, C., Le Roux. P., Armstrong, R. A. and Tinguely, C. 2022. A continental back-arc setting for the Namaqua belt: Evidence from the Kakamas Domain. *Geoscience Frontiers*, **13,** https://doi.org/10.1016/j.gsf.2022.101408

Massuyeau, M., Gardés, E., Morizet, Y. and Gaillard, F. 2015. A model for the activity of silica along the carbonatite–kimberlite–mellilitite–basanite melt compositional joint. *Chemical Geology*, **418**, 206–216.

Mattsson, H. B., Högdahl, K., Carlsson, M. and Malehmir, A. 2019. The role of mafic dykes in the petrogenesis of the Archean Siilinjärvi carbonatite complex, east-central Finland. *Lithos,* **342–343**, 468–479.

Miller, R. McG. 1983. The Pan-African Damara Orogen of South West Africa/Namibia, 431-515. *In*: Miller, R. McG. (Ed.), Evolution of the Damara Orogen of South West Africa/ Namibia. *Special Publications of the Geological Society of South Africa*, **11**, 515 pp.

Miller, R. McG. 2012. Review of Mesoproterozoic magmatism, sedimentation and terrane amalgamation in southwestern Africa. *South African Journal of Geology*, **115**, 417–448.

Mitchell, R. H. 1986. *Kimberlites. Mineralogy, Geochemistry, and Petrology*. Plenum Press, New York, London, 442 pp.

Mitchell, R. H. 1995. Kimberlites and Orangeites. 1–90. *In*: Mitchell, R. H. (Ed.) *Kimberlites, Orangeites, and Related Rocks*. Springer, New York (USA), 424 pp.

Mitchell, R. H. 2005. Carbonatites and carbonatites and carbonatites. *The Canadian Mineralogist*, **43**, 2049–2068.

Mitchell, R. H., Giuliani, A. and O'Brien, H. 2019. What is a Kimberlite? Petrology and Mineralogy of Hypabyssal Kimberlites. *Elements*, **15**, 381–386.

Moore, K. R., Brady, A. E. and Costanzo, A. 2022. Crystal-Liquid Segregation in Silicocarbonatite Magma Leads to the Formation of Calcite Carbonatite. *Journal of Petrology*, **63**, https://doi.org/10.1093/petrology/egac056

Muir, R. A., Whitehead B. A., New T., Stevens V., Macey P. H., Groenewald C. A., Salomon G., Kahle B., Hollingsworth J., Sloan R. A. 2023. Exceptional Scarp Preservation in SW Namibia Reveals Geological Controls on Large Magnitude Intraplate Seismicity in Southern Africa. *Tectonics* **42**, https://doi.org/10.1029/2022TC007693

Munro, J. and Harris, C. 2023. A High-δ^{18}O Mantle Source for the 2.06 Ga Phalaborwa Igneous Complex, South Africa? *Journal of Petrology*, **64**, https://doi.org/10.1093/petrology/egad063

Nasir, S., Al-Khirbash, S., Rollinson, H., Al-Harthy, A., Al-Sayigh, A., Al-Lazki, A., Theye, T., Massonne, H.-J. and Belousova, E. 2011. Petrogenesis of early cretaceous carbonatite and ultramafic lamprophyres in a diatreme in the Batain Nappes, Eastern Oman continental margin. *Contributions to Mineralogy and Petrology*, **161**, 47–74.

Nelson, L. L., Ramezani, J., Almond, J. E., Darroch, S. A. F., Taylor, W. L., Brenner, D. C., Furey, R. P., Turner, M. and Smith, E. F. 2022. Pushing the boundary: A calibrated Ediacaran-Cambrian stratigraphic record from the Nama Group in northwestern Republic of South Africa. *Earth and Planetary Science Letters*, **580**, https://doi.org/10.1016/ j.epsl.2022.117396

Nordin, F. 2009. *U-Pb dating, Lu-Hf isotopic analyses and geothermobarometry of rocks in the Grünau Terrane and Richtersveld Subprovince, Namaqua Sector, southern Africa*. M. Sc. thesis, University Gothenburg, Sweden, 52 pp.

Obata, M. 2011. Kelyphite and symplectite: textural and mineralogical diversities and universality, and a new dynamic view of their structural formation. *In*: Sharkow, E. (Ed.) *New Frontiers in Tectonic Research - General Problems, Sedimentary Basins and Island Arcs*. InTech, DOI: 10.5772/20265

Parneix, J. C., Beaufort, D., Dudoignon, P. and Meunier, A. 1985. Biotite chloritization process in hydrothermally altered granites. *Chemical Geology*, **51**, 89–101.

Pilbeam, L. H., Nielsen, T. F. D., Waight, T. and Tappe, S. 2024. Links between Calcite Kimberlite, Aillikite and Carbonatite in West Greenland: Numeric Modeling of Compositional Relationships. *Journal of Petrology*, **65**, https://doi.org/10.1093/petrology/egae059

Prokopyev, I. R., Borisenko, A. S., Borovikov, A. A. and Pavlova, G. G. 2016. Origin of REE-rich ferrocarbonatites in southern Siberia (Russia): implications based on melt and fluid inclusions. *Mineralogy and Petrology*, **110**, 845–859.

Prokopyev, I., Starikova, A., Doroshkevich, A., Nugumanova, Y. and Potapov, V. 2020. Petrogenesis of Ultramafic Lamprophyres from the Terina Complex (Chadobets Upland, Russia): Mineralogy and Melt Inclusion Composition. *Minerals*, **10**, https://doi.org/10.3390/min10050419

Prokopyev, I., Doroshkevich, A., Starikova, A., Kovalev, S., Nugumanova, Y. and Izokh, A. 2023. Petrogenesis of juvenile pelletal lapilli in ultramafic lamprophyres. *Scientific Reports*, **13**, https://doi.org/10.1038/s41598-023-32535-2

Reid, D. L. 1991. Alkaline rocks in the Kuboos-Bremen igneous province, southern Namibia: the Kanabeam multiple ring complex. *Communications of the Geological Survey of Namibia*, **7**, 3–13.

Reid, D. L. and Cooper, A. F. 1992. Oxygen and carbon isotope patterns in the Dicker Willem carbonatite complex, southern Namibia. *Chemical Geology,* **94**, 293–305.

Ries, J. B., Fike, D. A., Pratt, L. M., Lyons, T. W. and Grotzinger, J. P. 2009. Superheavy pyrite (δ^{34}Spyr > δ^{34}SCAS) in the terminal Proterozoic Nama Group, southern Namibia: A consequence of low seawater sulfate at the dawn of animal life. *Geology*, **37(8)**, 743-746.

Rioux, M., Bowring, S., Dudás, F. and Hanson, R. 2010. Characterizing the U–Pb systematics of baddeleyite through chemical abrasion: application of multi-step digestion methods to baddeleyite geochronology. *Contributions to Mineralogy and Petrology,* **160**, 777–801.

Rock, N. M. S. 1986. The Nature and Origin of Ultramafic Lamprophyres: Alnöites and Allied Rocks. *Journal of Petrology*, **27**, 155–196.

Rubie, D. C. and Gunter, W. D. 1983. The role of speciation in alkaline igneous fluids during fenite metasomatism. *Contributions to Mineralogy and Petrology*, **82**, 165–175.

Rudnick, R. L. and Gao, S. 2003. Composition of the Continental Crust. *In*: Holland, H. D. and Turekian, K. K. (Eds) *Treatise on Geochemistry,* **3,** Pergamon, Oxford (UK), 64 pp.

Russell, J. K., Porritt, L. A., Lavallée, Y. and Dingwell, D. B. 2012. Kimberlite ascent by assimilation-fuelled buoyancy. *Nature*, **481**, 352–356.

Russell, J. K., Sparks, R. S. J. and Kavanagh, J. L. 2019. Kimberlite Volcanology: Transport, Ascent, and Eruption. *Elements*, **15**, 405–410.

Saylor, B. Z., Poling, J. M. and Huff, W. D. 2005. Stratigraphic and chemical correlation of volcanic ash beds in the terminal Proterozoic Nama Group, Namibia. *Geological Magazine*, **142**, 519–538.

Schmidt, M. W., Giuliani, A. and Poli, S. 2024. The origin of carbonatites—combining the rock record with available experimental constraints. *Journal of Petrology*, **65(10)**, https://doi.org/10.1093/petrology/egae105

Schreuder, C. P. 1975. *Carbonate-bearing eruptives between the Great Karas Mountains and the Bremen igneous complex, South West Africa.* M.Sc. thesis, University of Stellenbosch, South Africa, 66 pp.

Scott Smith, B. H., Nowicki, T. E., Russell, J. K., Webb, K. J., Mitchell, R. H., Hetman, C. M. and Robey, J. v. A. 2018. *A Glossary of Kimberlite and Related Terms.* Scott-Smith Petrology Inc., North Vancouver, Canada, Part 1–144 pp, Part2–59 pp, Part 3–56 pp.

Shavers, E. J., Ghulam, A., Encarnacion, J., Bridges, D. L. and Luetkemeyer, P. B. 2016. Carbonatite associated with ultramafic diatremes in the Avon Volcanic District, Missouri, USA: Field, petrographic, and geochemical constraints. *Lithos*, **248–251**, 506–516.

Shirozu, H. 1978. Chapter 7: Chlorite minerals, 243–264. *In*: Sudo, T. and Shimoda, S. (Eds) Clays and Clay Minerals of Japan, *Developments in Sedimentology*, **26**, Elsevier, Amsterdam, Netherlands.

Siedner, G. and Mitchell, J. G. 1976. Episodic mesozoic volcanism in Namibia and Brazil: A K-Ar Isochron study bearing on the opening of the South Atlantic. *Earth and Planetary Science Letters*, **30**, 292–302.

Smith, C. B., Haggerty, S. E., Chatterjee, B., Beard, A. and Townend, R. 2013. Kimberlite, lamproite, ultramafic lamprophyre, and carbonatite relationships on the Dharwar Craton, India; an example from the Khaderpet pipe, a diamondiferous ultramafic with associated carbonatite intrusion. *Lithos*, **182–183**, 102–113.

Smith, M., Kynicky, J., Chen, X., Wenlei, S., Spratt, J., Jeffries, T., Brtnicky, M., Kopriva, A. and Cangelosi, D. 2018. The origin of secondary heavy rare earth element enrichment in carbonatites: Constraints from the evolution of the Huanglongpu district, China. *Lithos*, **308-309**, 65-82.

Smithies, R. H. 1991. *The geochemical evolution of three alkaline complexes in the Kuboos-Bremen igneous province, southern Namibia. South Africa*. Ph. D. Thesis, Rhodes University, Grahamstown, South Africa, 196 pp.

Söhnge, P. G. and De Villiers, J. 1948. The Kuboos pluton and its associated line of intrusives. *Transactions of the Geological Society of South Africa*, **51**, 1–31.

Sparks, R. S. J. 2013. Kimberlite Volcanism. *Annual Review of Earth and Planetary Sciences*, **41**, 497–528.

Sparks, R. S. J., Baker, L., Brown, R. J., Field, M., Schumacher, J., Stripp, G. and Walters, A. 2006. Dynamical constraints on kimberlite volcanism. *Journal of Volcanology and Geothermal Research*, **155**, 18–48.

Spiering, B. R., Bissick, A., Darroch, S. A. F., Davies, J. H. F. L., Gibson, B. M., Halverson, G. P., Laflamme, M. and Hilgen, F. J. 2023. Initial cyclostratigraphy of the middle Nama Group (Schwarzrand Subgroup) in southern Namibia. *Precambrian Research*, **397**, https://doi.org/10.1016/j.precamres.2023.107200

Spriggs, A. J. 1988. *An isotopic and geochemical study of kimberlites and associated alkaline rocks from Namibia*. Ph.D. thesis, University of Leeds, UK, 308 pp.

Sun, S.-S. and McDonough, W. F. 1989. Chemical and isotopic systematics of oceanic basalts: implications for mantle composition and processes. *In*: Saunders, A.D. and Norry, M. J. (Eds), Magmatism in the Ocean Basins. *Geological Society, London, Special Publications*, **42**, 313–345.

Tappe, S., Foley, S. F., Jenner, G. A. and Kjarsgaard, B. A. 2005. Integrating Ultramafic Lamprophyres into the IUGS Classification of Igneous Rocks: Rationale and Implications. *Journal of Petrology*, **46**, 1893–1900.

Tappe, S., Foley, S. F., Jenner, G. A., Heaman, L. M., Kjarsgaard, B. A., Romer, R. L., Stracke, A., Joyce, N. and Hoefs, J. 2006. Genesis of Ultramafic Lamprophyres and Carbonatites at Aillik Bay, Labrador: a Consequence of Incipient Lithospheric Thinning beneath the North Atlantic Craton. *Journal of Petrology*, **47**, 1261–1315.

Tappe, S., Foley, S. F., Kjarsgaard, B. A., Romer, R. L., Heaman, L. M., Stracke, A. and Jenner, G. A. 2008. Between carbonatite and lamproite—Diamondiferous Torngat ultramafic lamprophyres formed by carbonate-fluxed melting of cratonic MARID-type metasomes. *Geochimica et Cosmochimica Acta*, **72**, 3258–3286.

Tappe, S., Romer, R. L., Stracke, A., Steenfelt, A., Smart, K. A., Muehlenbachs, K. and Torsvik, T. H. 2017. Sources and mobility of carbonate melts beneath cratons, with implications for deep carbon cycling, metasomatism and rift initiation. *Earth and Planetary Science Letters*, **466**, 152–167.

Tappe, S., Beard, C. D., Borst, A. M., Humphreys-Williams, E. R., Walter, B. F. and Yaxley, G. M. 2025. Kimberlite, carbonatite and alkaline magmatic systems: definitions, origins, and strategic mineral resources. EarthArXiv Preprints, https://eartharxiv.org/repository/ view/8658/

Taylor, H. P., Frechen, J. and Degens, E. T. 1967. Oxygen and carbon isotope studies of carbonatites from the Laacher See District, West Germany and the Alnö District, Sweden. *Geochimica et Cosmochimica Acta*, **31**, 407–430.

Upton, B. G. J., Craven, J. A. and Kirstein, L. A. 2006. Crystallisation of mela-aillikites of the Narsaq region, Gardar alkaline province, south Greenland and relationships to other aillikitic–carbonatitic associations in the province. *Lithos*, **92**, 300–319.

Vasyukova, O. V. and Williams-Jones, A. E. 2022. Carbonatite metasomatism, the key to unlocking the carbonatite-phoscorite-ultramafic rock paradox. *Chemical Geology*, **602**, https://doi.org/10.1016/j.chemgeo.2022.120888

Veksler, I. V., Nielsen, T. F. D. and Sokolov, S. V. 1998. Mineralogy of Crystallized Melt Inclusions from Gardiner and Kovdor Ultramafic Alkaline Complexes: Implications for Carbonatite Genesis. *Journal of Petrology*, **39**, 2015–2031.

Verwoerd, W. J. 1967. The carbonatites of South Africa and South West Africa. *Handbook of the Geological Survey of South Africa*, **6**, Government Printer, Pretoria, South Africa, 452 pp.

Verwoerd, W. J. 1993. Update on carbonatites of South Africa and Namibia. *South African Journal of Geology,* **96(3)**, 75–95.

Walter, B. F., Giebel, R. J., Steele-MacInnis, M., Marks, M. A., Kolb, J. and Markl, G. 2021. Fluids associated with carbonatitic magmatism: A critical review and implications for carbonatite magma ascent. *Earth-Science Reviews*, **215**, https://doi.org/10.1016/j.earscirev. 2021.103509

Walter, B., Giebel, R. J., Marlow, A., Siegfried, P., Marks, M., Markl, G., Palmer, M. and Kolb, J. 2022. The Keishöhe carbonatites of southwestern Namibia -the post-magmatic role of silicate xenoliths on REE mobilisation. *Communications of the Geological Survey of Namibia,* **25**, 1–31.

Walter, B. F., Giebel, R. J., Siegfried, P. R., Gudelius, D. and Kolb, J. 2023. The eruption interface between carbonatitic dykes and diatremes – The Gross Brukkaros volcanic field Namibia. *Chemical Geology*, **621**, https://doi.org/10.1016/ j.chemgeo. 2023.121344

Walter, B. F., Giebel, R. J., Arthuzzi, J. C. L., Kemmler, L. and Kolb, J. 2024. Diatreme-hosted fluorite mineralization in S-Namibia

– A tale of cryogenic brine formation and fluid mixing below an unconformity in the context of Pangea rifting. *Journal of African Earth Sciences*, **210**, https://doi.org/10.1016/j.jafrearsci.2023.105154

Walter, B. F., Scharrer, M., Giebel, R. G., Beranoaguirre, A., Arthuzzi, J. C.L., Kemmler, L., Ladisic, A., Dück, S. Marks, M. and Markl, G. 2025. Sideritization and silification of unconformity-related hydrothermal baryte veins near Grünau, south Namibia. *Geochemistry*, **85**, https://doi.org/10.1016/j.chemer.2024.126244

Walter, M. J. 1998. Melting of Garnet Peridotite and the Origin of Komatiite and Depleted Lithosphere. *Journal of Petrology*, **39**, 29–60.

Webb, K. and Hetman, C. 2021. Magmaclasts in kimberlite. *Lithos*, **396–397**, https://doi.org/10.1016/j.lithos.2021.106197

Winter, F. and Rikhotso, C. T. 1998. *A review of kimberlite prospecting by De Beers companies in Namibia during the period 1971 to 1986*. Unpublished Report De Beers Consolidated Mines, 61 pp.

Woolley, A. R. and Kjarsgaard, B. A. 2008. Paragenetic types of carbonatite as indicated by the diversity and relative abundances of associated silicate rocks: evidence from a global database. *The Canadian Mineralogist*, **46**, 741–752.

Xie, Y., Ma, L., Zhao, G., Xie, C., Han, Y., Li, J., Liu, Q., Yao, J., Zhang, Y. and Lu, Y. 2020. Origin of the Heping granodiorite pluton: Implications for syn-convergent extension and asthenosphere upwelling accompanying the early Paleozoic orogeny in South China. *Gondwana Research,* **85**, 149–168.

Yaxley, G. M., Crawford, A. J. and Green, D. H. 1991. Evidence for carbonatite metasomatism in spinel peridotite xenoliths from western Victoria, Australia. *Earth and Planetary Science Letters*, **107**, 305–317.

Yaxley, G. M., Kjarsgaard, B. A. and Jaques, A. L. 2021. Evolution of Carbonatite Magmas in the Upper Mantle and Crust. *Elements*, **17**, 315–320.

Yaxley, G. M., Anenburg, M., Tappe, S., Decree, S. and Guzmics, T. 2022. Carbonatites: classification, sources, evolution, and emplacement. *Annual Review of Earth and Planetary Sciences*, **50(1)**, 261-293.

Yu, X., Chen, L.-H. and Zeng, G. 2015. Growing magma chambers control the distribution of small-scale flood basalts. *Scientific Reports*, **5**, https://doi.org/10.1038/srep16824

Zech, R. F., Onken, C. T., Sartori, G., Simon, S. J., Shipandeni, A., Galli, A., Spikings, R. A. and Schmidt, M. W. 2025. The age and source of Cambrian post-orogenic magmatism in the Kuboos-Bremen Igneous Province (Southern Namibia). *Journal of African Earth Sciences*, **226**, https://doi.org/10.1016/j.jafrearsci.2025.105592

Appendix 1. Sample locations of the Kuboos-Bremen Line intrusives from SE (No 1) to the NW (No. 9) listing main lithologies, age determinations and respective literature references

No.	Locality	Main Lithology	**Age** (Zech et al., 2025)	Literature
1	Swartbank Pluton	Granite	?	Söhnge and De Villiers, 1948
2	Kuboos Pluton	Granite, Syenite	507 Ma (Ar-Ar; Dunn, 2001)	Frimmel, 2000
3	Tatasberg Pluton	Granite	502 Ma (Ar-Ar; Dunn 2001)	Söhnge and De Villiers, 1948
4	Grootpenseiland Complex	Granite, Nepheline syenite, Syenite	501–507 Ma (U-Pb)	Smithies and Marsh, 1996
5	Marinkas Quelle Complex	Granite, Syenite	501–507 Ma (U-Pb)	Smithies and Marsh, 1996
		Carbonatite, Fenite	508–530 Ma (U-Pb)	Smithies and Marsh, 1996
6	Kanabeam Complex	Granite, Nepheline syenite, Syenite, Quartz syenite, Alkali monzonite, Alkali gabbro	500–509 Ma (U-Pb)	Reid, 1991
7	Mt. Ai Ais Breccia Pipe	Alkaline breccia pipes	?	Kröner and Blignault, 1976
8	Younger Bremen Complex	Granite, Nepheline syenite	493 and 496 Ma (U-Pb)	Middlemost, 1967
9	Kainab Alkaline Province	Carbonatite-Melilitite-Lamprophyre swarm	523 and 527 (Ar-Ar)	Schreuder, 1975

Appendix 2. List of all samples from the Garub valley, giving rock type, emplacement mode and coordinates, together with analytical methods used (TS - thin section, WR – whole rock analysis, µXRF – micro X-ray fluorescence, SEM – scanning electron microscopy, CL – cathodoluminescence, SI – stable isotope analysis)

Sample	**Rock type**	**Emplacement mode**	**Locality**		**Analytical methods**
GRB…	(Macroscopic estimate)		Latitude	Longitute	applied
025	Ultramafic	Diatreme	27°27'31.15"S	18°55'58.95"E	TS, WR, µXRF, SEM
026A	Carbonatite breccia	Diatreme	27°27'35.31"S	18°55'58.00"E	TS, WR, SI, µXRF
026B	Limestone	Country rock	27°27'35.31"S	18°55'58.00"E	TS, WR, µXRF
026C	Siltstone	Country rock	27°27'35.31"S	18°55'58.00"E	TS, WR, µXRF
026D	Siltstone + carbonatite	Dyke	27°27'35.31"S	18°55'58.00"E	TS, µXRF
026E	Ultramafic	Dyke	27°27'35.31"S	18°55'58.00"E	TS, WR
026F	Siltstone + carbonatite	Contact	27°27'35.31"S	18°55'58.00"E	TS, WR, µXRF, SEM
027	Carbonatite with granite/gneiss	Diatreme	27°27'38.00"S	18°56'36.60"E	TS, WR, µXRF
028A	Ultramafic	Dyke	27°27'38.69"S	18°56'36.00"E	TS, WR, µXRF, SEM
028B	Ultramafic + carbonatite	Contact	27°27'38.69"S	18°56'36.00"E	TS, µXRF
028C	Carbonatite	Dyke	27°27'38.69"S	18°56'36.00"E	TS, WR, µXRF
029A	Limestone	Country rock	27°27'40.94"S	18°57'05.37"E	TS, WR
029B	ultramafic breccia	Diatreme	27°27'40.94"S	18°57'05.37"E	TS
030	Location only	Unconformity	27°27'40.79"S	18°57'05.02"E	
031	Carbonatite breccia	Pipe	27°27'37.81"S	18°57'18.81"E	TS, WR
032	Location only		27°27'40.72"S	18°57'31.14"E	
033A	Diatreme breccia	Diatreme	27°27'40.72"S	18°57'31.14"E	TS, µXRF, SEM
033B	Diatreme breccia	Diatreme	27°27'40.72"S	18°57'31.14"E	TS, WR, µXRF, CL, SEM
033C	Diatreme breccia	Diatreme	27°27'42.22"S	18°57'31.48"E	TS, WR, SI, µXRF
033D	Diatreme breccia + siltstone	Contact	27°27'42.22"S	18°57'31.48"E	TS, µXRF
034	Location only	Dyke	27°27'35.57"S	18°57'47.77"E	
035A	Diatreme breccia	Diatreme	27°27'35.57"S	18°57'47.77"E	TS, WR
035B	Ultramafic	Diatreme	27°27'35.57"S	18°57'47.77"E	TS, WR
035C	Diatreme breccia	Diatreme	27°27'35.57"S	18°57'47.77"E	TS, WR
036	Diatreme + granite/gneiss	Contact	27°27'35.04"S	18°57'47.13"E	TS, WR, µXRF, SEM
037A	Carbonatite	Dyke	27°27'33.52"S	18°58'30.13"E	TS, WR, EMPA
037B	Garnet bearing gneiss	Country rock	27°27'33.52"S	18°58'30.13"E	TS, WR, µXRF, CL, SEM
037C	Diatreme breccia	Diatreme	27°27'33.52"S	18°58'30.13"E	TS, WR, µXRF, CL, SEM
037D	Dolerite	Dyke	27°27'33.52"S	18°58'30.13"E	
038	Diatreme breccia	Diatreme	27°27'30.73"S	18°58'29.64"E	TS, WR, µXRF, CL, SEM
039A	Globular diatreme	Diatreme	27°27'30.43"S	18°58'44.20"E	TS, WR, µXRF, SEM, SI
039B1	diatreme	Diatreme	27°27'30.43"S	18°58'44.20"E	TS, WR, SI, µXRF
039B2	Carbonatite	Diatreme	27°27'30.43"S	18°58'44.20"E	TS, WR
040A	Diatreme breccia	Diatreme	27°27'24.09"S	18°59'28.46"E	TS, WR, µXRF
040B	Globular diatreme	Diatreme	27°27'24.09"S	18°59'28.46"E	TS, WR, SI, µXRF
040C	Garnet bearing gneiss	Country rock	27°27'24.09"S	18°59'28.46"E	
041A	Garnet bearing gneiss	Country rock/mine	27°27'37.85"S	18°59'47.92"E	WR
041B	Altered diatreme	Diatreme/mine	27°27'37.85"S	18°59'47.92"E	
042A	Dolerite	Dyke	27°27'27.57"S	19°00'11.63"E	TS, WR, µXRF
042B	Diatreme breccia	Diatreme	27°27'27.57"S	19°00'11.63"E	TS, WR, SI, µXRF
042C	Ultramafic	Diatreme	27°27'27.57"S	19°00'11.63"E	TS, WR, µXRF, SEM
042D1	Diatreme breccia	Diatreme	27°27'27.57"S	19°00'11.63"E	TS, WR
042D2	Diatreme breccia	Diatreme	27°27'27.57"S	19°00'11.63"E	TS, µXRF
043	Dolerite	Dyke	27°26'45.35"S	18°57'33.53"E	
043B	Ultramafic	Dyke	27°26'45.35"S	18°57'33.53"E	TS

044A	Carbonatite	Diatreme	27°26'43.53"S	18°57'33.31"E	TS, WR, SI
044B	Diatreme breccia	Diatreme	27°26'43.53"S	18°57'33.31"E	TS, WR, µXRF, SEM
045	Dolerite	Dyke	27°26'39.73"S	18°56'55.91"E	

Appendix 3. Part one of the results from whole-rock analysis conducted on the 35 selected Garub samples

Sample	**25**	**026A**	**026E**	**026F2**	**27**	**028A**	**028C**	**31**	**033B**	**033C**	**035A**	**035B**
(GRB...)	Diatreme	Diatreme	Diatreme	Diatreme	Diatreme	Diatreme	Diatreme	Diatreme	Diatreme	Diatreme	Diatreme	Diatreme
Major elements (wt.%)												
Na_2O	2.95	3.79	2.05	2.60	3.93	1.88	0.06	< 198 PPM	3.92	0.98	3.12	2.96
MgO	9.02	6.22	8.20	9.07	7.80	5.89	6.18	8.04	5.95	6.36	8.06	7.89
Al_2O_3	7.82	7.29	6.50	5.65	6.86	6.46	5.85	5.73	8.15	7.52	6.23	7.44
SiO_2	35.19	31.94	27.76	19.77	28.00	28.85	30.16	24.35	34.20	24.00	26.09	30.91
P_2O_5	1.23	1.27	1.78	0.96	1.27	1.27	1.16	1.16	0.90	1.38	1.08	1.21
K_2O	1.43	0.05	2.97	0.08	0.58	0.08	1.37	0.52	0.93	2.05	0.14	0.92
CaO	13.70	13.86	16.87	18.64	15.13	19.71	17.49	18.06	13.14	16.24	15.79	12.91
TiO_2	3.43	3.64	3.86	3.29	3.60	3.63	3.47	3.30	3.02	3.96	3.24	3.71
Mn_2O_3	0.25	0.23	0.36	0.22	0.23	0.24	0.22	0.22	0.21	0.24	0.24	0.22
Fe_2O_3	12.79	12.81	14.85	12.23	12.91	13.14	11.29	12.63	10.85	13.54	11.43	13.04
LOI	11.08	18.10	13.44	26.10	18.45	17.06	21.89	24.01	18.58	22.55	23.76	17.64
C	2.55	4.97	3.13	7.21	4.98	4.96	5.32	6.23	4.97	5.64	6.64	4.72
S	0.07	0.04	0.10	0.06	0.03	0.21	0.06	0.03	0.03	0.03	0.04	0.03
Total	**99.78**	**99.76**	**99.62**	**99.27**	**99.39**	**99.14**	**99.62**	**98.34**	**100.27**	**99.31**	**99.70**	**99.37**
Trace elements (ppm)												
Li	236	51.8	306	67.3	83.5	277	34.0	107	31.9	56.7	19.3	71.9
Be	8.1	6.5	9.7	1.6	6.3	4.9	2.3	1.2	3.7	8.8	3.5	7.9
Sc	39.8	47.6	66.9	45.6	47.3	49.8	44.8	46.5	43.1	52.5	44.3	50.4
Ti	39543	49351	45693	46815	48020	51224	46909	45540	36570	54415	43869	48821
V	587	580	752	873	596	667	538	561	348	652	488	622
Cr	634	439	329	521	416	574	465	451	456	526	446	528
Mn	3737	3457	5313	3405	3324	3617	3285	3356	3144	3600	3604	3232
Co	96.8	91.0	98.2	91.7	106	97.6	72.3	81.5	72.9	101	83.1	94.6
Ni	237	148	131	144	148	157	122	139	122	167	125	161
Cu	231	235	216	381	234	261	111	8.5	79	226	191	243
Zn	235	249	249	299	212	216	226	278	196	266	161	224
Rb	173.2	3.5	234.5	10.7	48.5	10.3	109.8	43.1	42.0	159	11.5	61.1
Sr	3428	2322	3570	3598	2822	4394	859	553	1634	2758	2504	1991
Y	64.6	64.9	78.1	51.4	60.1	59.9	55.1	55.8	58.5	66.8	60.4	63.1
Zr	745	726	865	417	739	805	715	695	597	867	666	792
Nb	87	290	139	281	257	311	277	261	117	306	249	293
Mo	0.3	0.6	3.0	64.3	0.4	1.0	4.3	3.4	0.8	5.5	1.4	4.6
Ag	0.3	0.2	0.1	0.5	0.2	0.3	0.2	0.1	0.1	0.2	0.1	0.2
Ag	0.2	0.4	0.1	0.7	0.4	0.5	0.3	0.3	0.2	0.4	0.3	0.3
Cd	0.8	0.7	0.7	1.0	0.8	0.9	0.8	1.2	1.2	1.1	0.7	0.8
Sb	2.0	<0.067	<0.067	2.3	<0.067	<0.067	<0.067	<0.067	<0.067	<0.067	<0.067	<0.067
Cs	56.2	0.3	11.9	1.7	3.0	1.7	3.5	0.5	0.4	2.6	0.2	1.6
Ba	2842	1209	3914	363	1310	800	1161	270	806	566	94	1672
Hf	12.5	16.5	14.3	11.8	16.7	18.4	16.6	15.5	13.5	19.9	15.4	18.5
Ta	7.0	18.8	8.4	18.4	17.4	20.3	18.6	17.2	8.7	21.1	16.4	19.4
W	0.6	1.8	0.9	8.3	3.4	1.9	5.1	3.5	2.0	31.8	3.3	1.9
Pb	30.7	13.7	9.5	62.1	13.9	15.1	23.1	21.9	26.6	65.3	9.8	14.5
Bi	0.1	0.1	0.1	0.2	0.1	0.1	0.1	0.1	0.2	0.2	0.1	0.1
Th	34.5	34.3	22.9	27.1	30.8	31.2	28.7	27.8	25.4	35.4	28.7	31.8
U	4.1	10.0	9.3	6.5	5.9	4.7	10.1	8.8	9.2	9.6	6.7	6.5
REE												
La	261	244	222	214	241	253	230	235	198	277	223	243
Ce	496	484	424	408	471	487	443	457	385	537	431	472

Pr	58.7	58.8	50.5	48.3	55.9	57.9	52.9	54.7	46.3	64.2	51.2	56.6
Nd	218	222	189	182	212	217	198	206	175	244	194	212
Sm	37.4	38.6	32.5	30.2	36.6	36.6	33.8	35.0	30.5	41.7	33.6	36.3
Eu	10.0	10.2	9.1	8.0	9.9	10.0	9.5	9.8	7.9	11.5	9.1	9.6
Gd	26.8	27.5	24.1	21.1	26.3	26.2	24.2	25.4	22.3	30.2	24.5	26.1
Tb	3.3	3.4	3.1	2.6	3.3	3.2	3.0	3.1	2.9	3.7	3.1	3.2
Dy	15.8	16.3	16.0	12.8	15.7	15.5	14.4	14.8	14.3	17.6	15.2	16.0
Ho	2.6	2.7	2.9	2.1	2.6	2.6	2.4	2.4	2.4	2.9	2.6	2.7
Er	6.3	6.4	7.6	5.0	6.0	6.0	5.5	5.4	6.1	6.5	6.1	6.4
Tm	0.8	0.8	1.0	0.6	0.7	0.7	0.6	0.6	0.8	0.8	0.8	0.8
Yb	4.5	4.3	5.9	3.4	4.0	4.0	3.6	3.5	4.6	4.3	4.2	4.6
Lu	0.6	0.6	0.8	0.5	0.6	0.6	0.5	0.5	0.6	0.6	0.6	0.7
REE (tot)	**1141**	**1120**	**989**	**938**	**1086**	**1120**	**1023**	**1053**	**896**	**1242**	**999**	**1090**

Appendix 4. Part two of the results from whole-rock analysis conducted on the 35 selected Garub samples

Sample	**035C**	**036A**	**37A**	**037C**	**38**	**039A**	**039B1**	**039B2**	**040A**	**040B**	**042B**	**042C**
(GRB...)	Diatreme	Diatreme	Diatreme	Diatreme	Diatreme	Diatreme	Diatreme	Diatreme	Diatreme	Diatreme	Diatreme	Diatreme
Major elements (wt.%)												
Na_2O	3.48	1.64	< 208 PPM	2.61	2.79	6.07	< 208 PPM	1.33	0.02	0.28	2.79	1.71
MgO	6.61	5.55	8.68	7.26	7.22	2.07	7.35	6.70	6.84	7.25	7.16	6.99
Al_2O_3	6.67	6.11	5.91	7.61	7.62	10.94	6.52	6.28	5.71	5.86	6.80	6.97
SiO_2	29.98	32.06	27.29	34.43	34.69	38.93	29.19	27.39	21.92	25.65	21.19	25.46
P_2O_5	1.17	1.29	1.28	0.92	0.86	0.48	1.58	1.47	1.11	1.22	1.39	1.37
K_2O	0.13	1.48	1.32	2.10	1.87	0.10	1.17	0.84	3.73	3.96	0.08	0.84
CaO	14.46	16.69	14.75	14.22	14.11	14.24	15.00	18.32	20.45	16.87	19.53	18.72
TiO_2	3.55	3.47	4.26	2.90	2.77	2.84	3.98	3.51	3.01	3.11	3.07	3.25
Mn_2O_3	0.21	0.16	0.27	0.19	0.18	0.29	0.26	0.38	0.23	0.23	0.31	0.21
Fe_2O_3	12.39	9.90	14.55	6.95	7.01	8.56	13.49	9.62	10.02	11.63	11.32	14.69
LOI	20.50	20.34	20.93	20.27	20.17	15.01	20.44	23.22	25.24	22.41	24.14	17.64
C	5.34	5.41	5.46	5.33	5.34	3.60	5.00	5.82	6.55	5.91	6.08	4.28
S	0.20	0.02	0.02	0.01	0.01	0.06	0.08	0.09	0.01	0.08	0.15	0.08
Total	**100.07**	**99.03**	**99.57**	**99.84**	**99.66**	**100.08**	**99.45**	**99.65**	**98.62**	**99.12**	**98.44**	**98.64**
Trace elements (ppm)												
Li	23.4	35.3	131	11.5	11.6	8.8	94.6	34.0	24.1	12.7	28.7	123.9
Be	5.1	2.5	8.0	3.8	3.8	1.7	5.8	4.5	3.0	2.0	2.6	4.6
Sc	47.8	49.7	44.2	41.3	44.9	44.0	46.3	47.9	40.8	43.0	46.3	48.1
Ti	47500	46499	57439	36663	34717	36923	54720	50239	39779	39906	39496	34264
V	642	417	624	448	456	182	637	634	328	425	319	606
Cr	492	381	470	327	296	177	408	290	266	271	330	245
Mn	3140	2467	4029	2799	2668	4263	3961	5879	3465	3366	4869	3206
Co	82.4	66.9	90.5	50.3	47.9	99.4	86.0	56.2	62.3	60.7	80.4	99.9
Ni	145	133	179	93	88	111	155	79	69	62	110	118
Cu	232	195	217	28	20	253	246	45	510	157	67	228
Zn	218	237	318	230	222	115	242	105	153	117	420	268
Rb	12.6	72.1	132.1	57.8	51.6	7.8	140	105	202	203	5.8	61.9
Sr	2408	1623	667	1433	1386	425	822	1412	1512	2471	1911	3458
Y	57.1	85.0	61.4	59.9	65.7	54.5	67.8	78.4	61.7	59.6	61.0	66.7
Zr	719	792	649	674	854	437	826	961	643	784	552	622
Nb	309	237	345	179	172	235	333	290	268	259	60	26
Mo	2.7	12.7	5.6	2.4	2.5	15.7	1.0	0.5	2.9	0.8	2.2	0.3
Ag	0.2	0.3	0.2	0.2	0.2	0.3	0.2	0.2	0.1	0.1	0.1	0.2
Ag	0.4	0.4	0.4	0.3	0.3	0.5	0.4	0.3	0.3	0.3	0.1	0.1
Cd	1.1	1.0	1.2	1.0	1.3	0.7	0.9	1.0	0.7	0.9	1.1	0.6
Sb	<0.067	<0.067	<0.067	<0.067	<0.067	<0.067	<0.067	<0.067	<0.067	<0.067	<0.067	<0.067
Cs	0.4	0.3	1.8	0.9	0.9	0.3	2.1	1.1	0.3	0.3	0.3	1.3
Ba	368	330	458	326	309	3610	413	1495	935	1972	171	2507
Hf	17.2	16.8	14.8	18.2	24.3	9.8	17.9	19.1	17.2	17.9	10.5	10.4
Ta	20.0	15.9	24.6	11.7	11.0	16.0	22.6	19.0	16.0	16.0	3.7	2.2

W	3.7	4.6	13.2	8.6	9.4	3.1	1.8	3.0	37.4	26.9	15.0	1.0
Pb	16.4	52.3	47.4	34.7	29.0	42.3	18.5	18.3	16.8	13.9	30.6	28.5
Bi	0.2	0.4	0.1	0.0	0.0	0.4	0.0	0.1	<0.002	<0.002	0.0	0.1
Th	30.0	41.9	39.2	28.9	29.5	34.4	38.1	36.6	28.6	28.8	33.0	34.1
U	7.7	24.3	9.3	8.1	9.7	12.5	10.9	6.7	4.3	3.9	3.6	8.9
REE												
La	233	223	296	200	188	232	306	309	227	235	267	276
Ce	454	436	594	386	361	443	596	610	437	452	502	528
Pr	53.8	52.5	70.7	46.0	42.9	50.1	70.3	71.7	52.7	53.9	59.3	63.2
Nd	203	200	266	172	162	175	263	261	201	205	220	240
Sm	34.9	36.6	44.4	29.4	28.4	25.6	45.3	40.3	34.7	35.1	36.8	40.9
Eu	9.6	11.6	12.1	7.9	7.5	4.5	12.7	10.9	9.6	9.7	10.0	11.1
Gd	24.9	28.1	30.2	21.8	21.5	17.7	31.7	29.6	24.9	25.5	26.9	29.2
Tb	3.1	3.8	3.6	2.8	2.9	2.3	3.8	3.8	3.1	3.2	3.3	3.6
Dy	14.8	19.9	16.9	14.3	14.9	11.9	17.7	19.0	15.4	15.2	15.9	17.1
Ho	2.5	3.5	2.7	2.5	2.7	2.1	2.9	3.2	2.6	2.6	2.6	2.8
Er	5.8	8.7	6.1	6.2	7.1	5.9	6.8	7.6	6.1	6.0	6.2	6.7
Tm	0.7	1.1	0.7	0.8	0.9	0.9	0.8	0.9	0.7	0.7	0.8	0.8
Yb	3.9	6.3	3.7	4.6	5.6	5.8	4.4	5.1	4.1	4.0	4.1	4.5
Lu	0.6	0.9	0.5	0.7	0.8	0.9	0.6	0.7	0.6	0.6	0.6	0.6
REE (tot)	**1044**	**1032**	**1347**	**896**	**846**	**979**	**1362**	**1374**	**1019**	**1048**	**1156**	**1224**

Appendix 5. Part three of the results from whole-rock analysis conducted on the 35 selected Garub samples

Sample	**042D1**	**044A**	**044B**	**026B**	**026C**	**026F1**	**029A**	**036B**	**037B**	**041A**	**042A**
(GRB...)	Diatreme	Diatreme	Diatreme	Limestone	Siltstone	Siltstone	Limestone	"Fenite"	Gneiss	Gneiss	Dolerite
Major elements (wt.%)											
Na_2O	2.58	0.05	0.70	0.00	4.41	8.62	0.32	7.32	1.37	1.77	1.07
MgO	6.37	8.97	9.82	16.20	2.08	3.38	14.34	3.99	1.87	1.83	9.16
Al_2O_3	6.42	6.13	7.16	0.62	8.83	14.43	1.65	13.13	16.33	16.93	16.29
SiO_2	20.63	27.31	19.88	5.72	71.20	53.58	6.81	49.57	70.03	67.19	48.47
P_2O_5	1.35	1.24	1.31	0.02	0.39	0.02	0.04	0.04	0.09	0.11	0.07
K_2O	0.06	1.49	1.11	0.12	0.26	0.05	0.25	0.44	3.87	3.99	0.68
CaO	20.27	15.25	17.25	25.35	6.02	5.42	26.65	8.26	1.00	1.01	11.33
TiO_2	3.10	3.44	3.61	0.02	0.88	0.66	0.05	0.52	1.09	0.95	0.45
Mn_2O_3	0.29	0.32	0.79	0.85	0.06	0.18	1.12	0.12	0.10	0.09	0.18
Fe_2O_3	14.21	12.79	12.12	3.24	2.68	4.34	4.33	3.45	7.26	7.14	10.00
LOI	23.37	21.71	24.69	41.79	7.51	8.98	40.08	12.53	1.74	1.64	0.37
C	6.16	5.81	6.21	11.85	1.98	2.43	11.56	3.49	0.04	0.13	0.07
S	0.03	0.11	0.14	0.02	0.05	0.08	0.05	0.01	0.01	0.11	0.07
Total	**99.16**	**99.43**	**99.75**	**94.07**	**104.79**	**99.92**	**95.96**	**99.53**	**105.06**	**102.98**	**98.43**
Trace elements (ppm)											
Li	39.0	86.1	66.3	6.4	25.5	102.1	9.3	18.0	110	102	22.4
Be	2.2	3.4	2.1	1.2	2.1	3.6	1.5	2.2	14.4	12.5	1.3
Sc	45.6	44.9	48.5	1.5	20.0	23.8	3.7	12.5	34.6	28.1	87.9
Ti	38171	48643	48638	425	8071	8499	914	6810	13237	11991	5993
V	510	589	558	18	83	241	34	132	168	218	445
Cr	218	577	546	8	92	118	10	107	158	147	1102
Mn	4500	4894	11877	13648	770	2620	17386	1742	1249	1267	2747
Co	112	93.0	75.4	6.6	14.5	29.9	13.0	18.3	36.1	39.9	107
Ni	110	219	175	14	27	64	21	26	88	93	404
Cu	217	224	734	4	62	58	18	42	117	117	312
Zn	225	252	464	124	110	183	95	92	183	228	141
Rb	3.2	141	99.7	11.3	19.2	1.2	22.6	24.8	278	345	154
Sr	2474	2985	1384	439	649	826	541	810	197	206	195
Y	67.1	58.0	68.4	14.2	57.3	21.0	25.5	12.8	71.5	58.1	25.2
Zr	640	686	854	13	461	201	26	298	495	461	74
Nb	120	312	308	<0.213	3	23	3	25	41	37	10
Mo	2.4	6.1	4.7	1.4	7.8	41.9	3.2	3.2	2.0	2.9	0.3
Ag	0.1	0.2	0.2	0.3	0.2	0.2	0.0	0.1	0.2	0.2	0.2

Ag	0.2	0.4	0.4	0.3	0.1	0.2	0.1	0.1	0.1	0.2	0.2
Cd	0.7	1.2	2.4	1.4	0.5	0.5	1.8	0.5	0.4	0.4	0.2
Sb	<0.067	<0.067	<0.067	<0.067	<0.067	2.0	<0.067	<0.067	<0.067	<0.067	<0.067
Cs	0.1	1.7	3.8	0.5	0.7	0.3	1.6	1.4	4.2	5.8	3.8
Ba	138	1413	9123	142	2265	91	2160	162	1402	1263	663
Hf	12.1	15.3	17.3	0.4	11.3	5.9	0.7	9.0	14.8	13.6	2.5
Ta	8.7	21.4	20.5	<0.024	<0.024	1.3	<0.024	1.3	2.0	2.8	0.7
W	8.1	3.6	2.8	0.4	1.3	6.1	0.7	1.3	0.5	1.0	0.7
Pb	22.8	55.0	54.0	37.2	44.6	31.6	24.7	52.2	49.1	73.0	8.4
Bi	0.1	0.1	1.1	0.1	0.4	0.2	0.2	0.2	0.1	0.2	0.2
Th	28.8	35.4	36.6	1.4	31.9	13.3	3.0	60.2	49.7	43.6	3.0
U	5.4	9.0	22.6	3.1	6.8	3.5	3.1	5.4	5.2	4.8	1.3
REE											
La	252	276	266	6.1	56.2	57.9	13.1	125	118	98.4	11.2
Ce	479	524	499	13.0	127	112	28.2	271	246	212	26.9
Pr	57.4	61.9	59.3	1.5	15.4	13.8	3.4	34.5	29.9	26.2	3.5
Nd	216	231	220	6.3	61.1	51.8	14.0	131	114	99	14.9
Sm	36.9	38.4	39.5	1.7	13.1	8.9	3.8	24.2	22.6	19.6	4.6
Eu	10.0	10.6	11.3	0.4	2.3	1.5	0.8	2.2	2.9	3.1	1.1
Gd	26.7	26.8	30.2	2.2	12.6	5.7	4.5	13.0	17.9	14.5	4.7
Tb	3.4	3.3	3.8	0.4	1.9	0.8	0.8	1.1	2.6	2.1	0.8
Dy	17.0	15.5	17.7	2.4	11.1	4.2	4.7	3.8	14.4	12.1	4.9
Ho	2.9	2.5	2.9	0.5	2.2	0.8	0.9	0.5	2.9	2.3	1.0
Er	6.9	5.7	6.5	1.3	6.5	2.4	2.5	1.2	8.2	6.7	3.1
Tm	0.8	0.7	0.8	0.2	1.0	0.4	0.4	0.1	1.2	1.0	0.5
Yb	4.6	3.7	4.2	1.1	6.2	2.7	2.2	0.9	7.9	6.3	3.0
Lu	0.6	0.5	0.6	0.2	1.0	0.5	0.3	0.1	1.3	1.0	0.5
REE (tot)	**1114**	**1202**	**1162**	**37.2**	**318**	**264**	**79.6**	**609**	**589**	**505**	**80.7**

Appendix 6. List of samples analysed for stable isotopes, including number of cycles (n) and corresponding $\delta^{13}C_{PDB}$ [‰] and $\delta^{18}O_{SMOW}$ [‰] values, along with their standard deviations (SD)

Sample (GRB...)	**n**	**$\delta^{13}C_{PDB}$ [‰]**	**SD**	**$\delta^{18}O_{SMOW}$ [‰]**	**SD**
026A	10	-3.63	0.06	15.60	0.07
033C	10	-3.17	0.08	17.05	0.13
039A	10	-3.58	0.07	26.34	0.06
039B	10	-0.84	0.06	19.49	0.06
040B	10	-2.20	0.03	19.04	0.06
042B	10	-1.74	0.09	20.43	0.08
044A	10	-4.08	0.05	15.14	0.07

*Communications of the Geological Survey of Namibia, **29** (2026), 43-71*

A global review of the architecture of carbonatite complexes and its implications for melt ascent

Benjamin F. Walter[1] *, R. Johannes Giebel[2,3], Michael A. W. Marks[1] and Gregor Markl[1]

[1] Eberhard Karls University, Scharrenbergstraße 94-96, 72074 Tübingen, Germany
[2] Institute of Applied Geosciences, Technische Universität Berlin, Ernst-Reuter-Platz 1, 10587 Berlin, Germany
[3] Department of Geology, University of the Free State, 250 Nelson-Mandela-Drive, Bloemfontein 9300, South Africa

**corresponding author: <b.walter@uni-tuebingen.de>*

Abstract :- This review analyses the architecture and emplacement characteristics of 551 carbonatite complexes worldwide to address two key questions: (i) how are different geometries linked to each other genetically, e. g. early-stage radial dykes versus late-stage plugs, and (ii) does the architecture of carbonatite complexes contribute to a better understanding of the physicochemical parameters of the melts.

Carbonatite complexes are categorised into volcanic, shallow intrusive, and deep-seated types. Among the 551 studied occurrences, 48% consist primarily of single dykes or dyke swarms, while other geometries such as plugs (20%), cone sheets and ring dykes (11%), and diatreme breccias (8%) are less abundant. The remaining geometries represent various and variable features of lesser importance, such as lenses, sills, etc., which are not further discussed here. Only 20% of carbonatites lack associated alkaline silicate rocks, suggesting a genetic relationship, although exposure bias likely affects these statistics. Notably, geometries such as cone sheets, ring dykes, and plugs occur across different depth levels, limiting their use as reliable indicators of emplacement depth. Similarly, fenite halo development is influenced by local country rock properties rather than emplacement depth.

Field data from key localities, such as Kaiserstuhl (Germany), Oldoinyo Lengai (Tanzania), Palabora (South Africa), and Ardnamurchan (Scotland), illustrate the structural similarities between carbonatitic and silicate systems, including radial dykes, cone sheets, and ring dykes. However, a fundamental difference lies in the high vertical-to-lateral aspect ratios of carbonatite intrusions, which contrast with the horizontally extensive magma chambers typical of silicate magmatism. This distinction arises from the low viscosity, low density, and volatile-rich nature of carbonatite melts, which promote rapid ascent through the crust without significant ponding. Empirical and experimental data suggest that carbonatite magmas can ascend at high velocities and substantially faster than silicate magmas or even kimberlites. Their ascent behaviour closely resembles that of ionic fluids lacking silica polymerisation, which allows for fast and dynamic, jackhammer-like intrusion through the crust. Existing dyke emplacement models support this rapid, unsteady ascent process, involving episodic, self-closing pockets of melt that migrate upward in discrete pulses. These dynamics imply a wide range of vertical carbonatite pocket sizes, from metres to several kilometres, depending on melt volume and crustal conditions.

This review highlights the limitations of geometry alone to infer depth or genesis, given the overprinting effects of erosion and exposure bias. However, the combined structural, petrological, and geophysical data strongly support a dynamic ascent model for carbonatite melts. The refined "jackhammer model" emphasises the unique rheology of carbonatites and their capacity for rapid, transient ascent, without the need for long-lived, crustal magma chambers.

Keywords :- Carbonatite, Geomodel, Deposit model, Architecture, Ascent, Emplacement, Dykes

Introduction

Most carbonatites are igneous rocks that crystallised from carbonate-rich, mantle-derived melts. About 600 occurrences are known world-wide and the majority of them (80 %) is associated with diverse silicate rocks, including nephelinitic-melilititic, trachytic-phonolitic, basaltic-basanitic, aillikitic, kimberlitic and ultramafic compositions (Mitchell, 2005; Woolley and Kjarsgaard 2008; Yaxley *et al*., 2022). Most carbonatites are situated in the vicinity or within continental rift settings or occur along transcrustal-scale lineaments (Woolley and Kjarsgaard, 2008). A recent classification divides carbonatites by their predominant carbonate mineral into calcite/calcio- (sövite and alvikite), dolomite/magnesio- (rauhaugite and beforsite), ankerite-siderite/ferro- and nyererite / natro-carbonatites, with calcite carbonatites being the most common type (Schmidt *et al*., 2024, and references therein). Dolomite and ankerite-siderite carbonatites are much less common, and mostly occur as late-stage dykes or pockets within calcite carbonatites (Tappe *et al*., 2025; Schmidt *et al*., 2024, and references therein). Natro-carbonatite (containing abundant alkali-dominated carbonates, such as gregoryite and nyererite) is exclusively known from today´s only active carbonatite volcano, namely Oldoinyo Lengai (Tanzania) and the neighbouring Kerimasi (Tappe *et al*., 2025, and references therein).

Petrogenetic models for the origin of carbonatites have been recently reviewed in Jones *et al*. (2013), Yaxley *et al*. (2021; 2022), Tappe *et al*. (2025) and Schmidt *et al*. (2024). The two first order processes for the origin of carbonatites are (i) crystallisation from primary carbonatitic melts as a product of low-degree partial melting of carbonate-bearing mantle peridotites and (ii) fractional crystallisation of carbonate-bearing, silica-undersaturated magmas followed by silicate-carbonatite liquid immiscibility. The emplacement of carbonatitic magmas into the crust causes cyclic release of CO_2-H_2O-NaCl (±sulfate, bicarbonate) fluids/brines and variable metasomatic interactions with diverse wall rocks (e. g. Elliot *et al*., 2018; Giebel *et al*., 2019; Walter *et al*., 2021; Vasyukova and Williams-Jones, 2022; Schmidt *et al*., 2024). Published experimental data indicate that crystallisation of calcite, dolomite, ankerite, and siderite at crustal conditions requires alkaline, hydrous carbonate melts with 20 to 25 wt.% $(Na, K)_2CO_3$ + H_2O (Schmidt *et al*., 2024). These authors also suggest that carbonatite rocks, which are poor in these elements, are interpreted as magmatic cumulates. Moreover, based on experimental data, there is a high potential that most carbonatites found in the crust do not have a direct mantle origin (Schmidt *et al*., 2024).

Carbonatite can bear economic ore grades of a variety of commodities which are required for high tech, fertilizer and steel applications (e. g. fluorite, REE, Nb, P, Fe, Zr; Th; Mariano, 1989). Today, some 50-60 carbonatites are either mined or being under advanced exploration, representing ~10% of the known occurrences. However, exploration of carbonatite is challenging because of the complex and variable geometry, mineralogy, micro-textures and general heterogeneity of such deposits (Edahbi *et al*., 2018). Importantly, the true economic value of a carbonatite is not only related to volume and grade, but critically depends on a processable mineralogy and grain size to develop an exploration target into a mining operation. In this context, elucidating the processes responsible for the development of the observed geometry is of both fundamental and economic importance. Outcrop maps and the spatial distribution of alkaline silicate rocks derived from bore hole data and geophysical modelling constitute essential datasets for assessing prospectivity and guiding exploration activities. To secure the future supply of critical raw materials (CRM) from carbonatites, a refined and applicable model of the architecture of carbonatite occurrences based on known ore forming processes is required. This paper provides a global review of carbonatite geometries to answer the following questions:

- What is the genetic link between different carbonatite geometries (e. g. early radial dykes and late stage plugs)?
- What can be learned from carbonatite architecture about the physio-chemical parameters of the involved melts?

To develop comprehensive geomodels for carbonatites, these two problems need to be addressed. Recently, detailed geomodels for alkaline igneous rocks have been published (Beard *et al*., 2023), while a modern geomodel for carbonatites is still lacking. The geometric model of Le Bas (1987) is used for carbonatites worldwide, although it is largely based on observations from carbonatites in the East African rift, exposed at volcanic to subvolcanic levels. Frolov (1971) reviewed many on the known occurrences at that time and interpreted their plan view as representing different exposure levels of subvertical, pipe-like structures, distinguishing erupted and stuck complexes. The stuck ones likely had a sealing, and probably lost much less volatiles than their erupted counterparts (Walter *et al*., 2020, 2021, and references therein). Moreover, Frolov (1971) suggested that mineralisation style as well as the exposed alkaline silicate rock/carbonatite ratio of such structures are depth-dependent - an approach subsequently used and developed further by others (Arzamastsev *et al*., 2000; Giebel *et al*., 2017). A recent review (Simandl and Paradis, 2018) highlighted the role of orebody geometry within carbonatite-alkaline igneous rock complexes for exploration. The outcome of this previous work implies that i) architecture of the complex and alkaline silicate rock/carbonatite ratios depend on crustal depth (e. g. ring dykes as indicators for caldera formation closely above occur only in shallow complexes; Elliot *et al*., 2018) and ii) at a particular depth level, the observed carbonatite architecture can systematically vary (e. g. radial dykes without plugs → radial dykes with plugs → plugs without radial dykes, with increasing depth in a shallow intrusion cluster; Wooley, 1987, 2001, 2019; Kogarko *et al*., 1995). Hence the architecture of carbonatite complexes needs to be reviewed in detail for geomodel refinement which is the scope of this contribution.

Emplacement depth of carbonatites

Carbonatites are exposed at variable crustal levels (Frolov, 1971; Mitchell, 2005), but direct constraints on their emplacement depths are hampered by the general absence of suitable mineral assemblages that would allow for geobarometric determinations. For some occurrences, however, depth estimates have been published based on reconstruction of the eroded overburden at the time of emplacement. For Evate (Mozambique), up to 20 km depth have been estimated (Hurai *et al*., 2021), while for Palabora (South Africa) up to 15 km depth are assumed (Eriksson, 1982), possibly representing the deepest exposed carbonatites known. Based on ductile, synmagmatic deformation including some brittle components, the Swartbooisdrift-Ondoto dyke swarm (Namibia) was likely formed at the brittle-ductile transition zone (Drüppel *et al*., 2006, and references therein) and thus joins the list of deep-seated carbonatite occurences.

An alternative approach uses pressure estimates derived from isochoric projection of microthermometric data of fluid inclusions in primary minerals in carbonatites, such as apatite. This is, however, not straightforward, since such estimates represent the formation depth of the mineral that hosts the fluid inclusion, but not necessarily the emplacement depth of the carbonatite body itself - a problem which is recognised only by few (e. g. Andersen, 1987). For example, the fluid data of Oka (Canada) indicate fluid exsolution from a carbonatitic melt between 0.4-0.8 GPa equivalent to a depth of 14-29 km, which is much deeper than the exposure level of ~1 km, based on extrapolation of the regional geology (Samson *et al*., 1995). Similar problems for other occurrences are discussed in detail by Walter *et al*. (2021), who concluded that isochoric projections may be suitable to specify the formation depth of a particular phase, but can only be used as emplacement monitor for the carbonatite body, if there is evidence for *in situ* crystal growth (e. g. magmatic banding). Thus, knowledge of the emplacement level of carbonatite complexes is very limited and semi-quantitative at best. Accordingly, we distinguish three categories of carbonatite complexes in the following: (i) volcanic carbonatite complexes, (ii) shallow intrusive carbonatite complexes, and (iii) deep-seated carbonatite complexes. Apart from these, a further secondary category comprises complexes that were affected by metamorphism and/or deformation regardless of their emplacement depth.

Volcanic carbonatite complexes

Such occurrences expose effusive (e. g. lavas) and pyroclastic (e. g. lapilli stones) carbonatites, which are in some cases associated with intrusive carbonatite bodies (Fig. 1). Typically, extrusive carbonatites form parts of larger stratovolcanoes (and their eroded subvolcanic centres) that are otherwise dominated by silicate rocks, or they occur as tephra cones, tuff rings, diatremes or maar-type volcanoes (Rosatelli *et al*., 2007; Woolley and Church, 2005; Stoppa *et al*., 2016). Carbonatite-bearing stratovolcanoes eroded to subvolcanic level occasionally expose ring dyke and breccia structures (Elliott *et al*., 2018, and references therein). Important examples include Oldoinyo Lengai (Tanzania), Monte Vulture (Italy), Kaiserstuhl (Germany), Catanda (Angola), Fort Portal (Uganda), Xiluvo (Mozambique), and some Mongolian carbonatites (e. g. Campeny *et al*., 2014; Dawson, 1962; Hay and O'Neil, 1983; Keller and Krafft, 1990; Petrovsky *et al*., 2012; Rapprich *et al*., 2024; Shu and Liu, 2019; Stoppa and Woolley, 1997; Von Knorring and Du Bois, 1961; Woolley and Church, 2005).

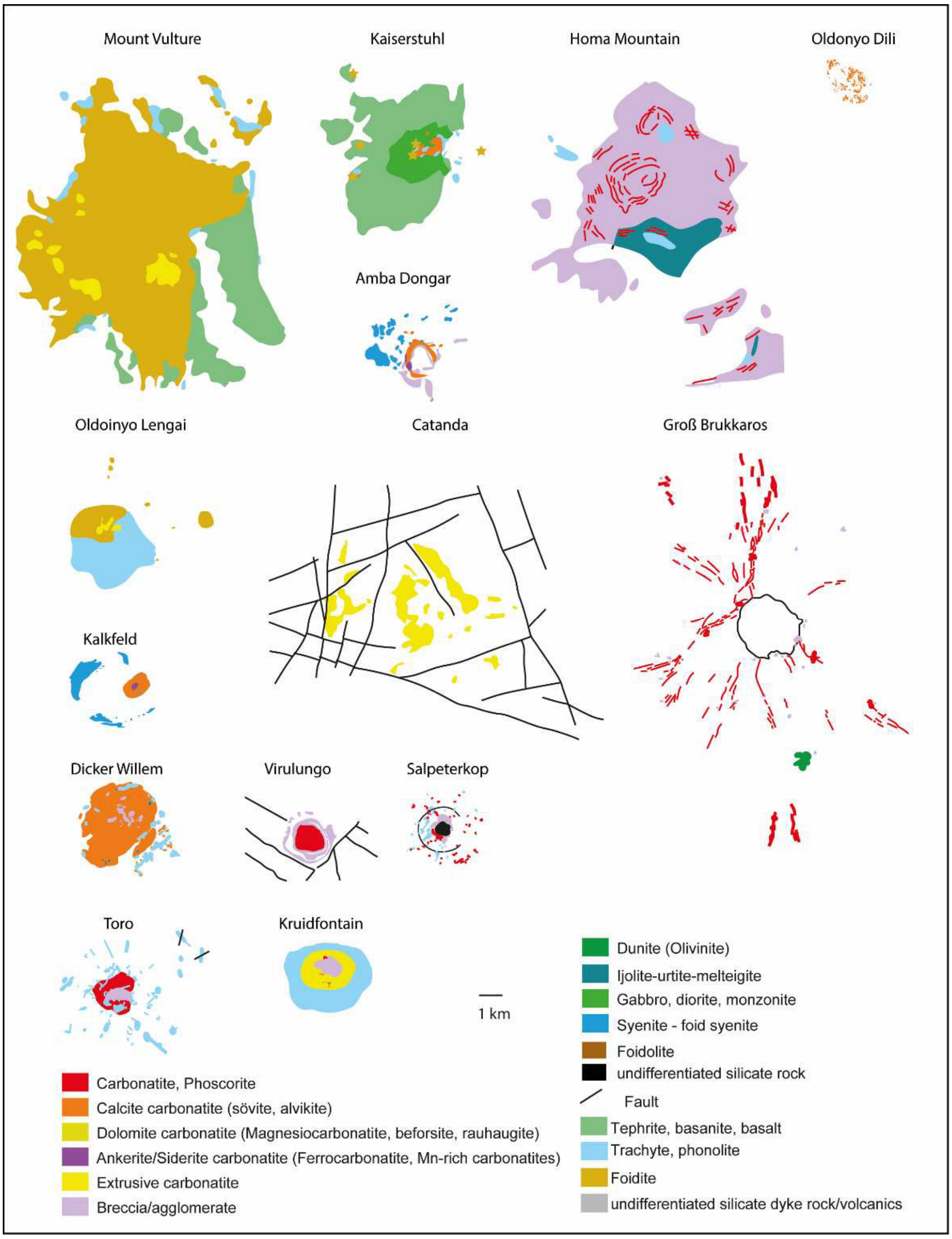

Figure 1. Compilation of exemplary volcanic carbonatite complexes, including the subvolcanic exhumation level (Verwoerd 1967; Braunger *et al*., 018; Walter *et al*., 2018; Woolley 2001, 2019)

Shallow intrusive carbonatite complexes

These complexes typically expose ring dyke/sill structures, cone sheets and radial dyke systems (Fig. 2). Central plug-like carbonatite bodies are locally exposed as well, while extrusive carbonatites are absent. Prominent fenite aureoles are common and in places coarse mafic to ultramafic rocks are associated with the carbonatites. Important examples are Glenover (South Africa), Alnö (Sweden), Fen (Norway), Sokli (Finland), complexes of the Chilwa Province in Malawi (e. g. Kangankunde, Tundulu, Chilwa Island, Songwe Hill), Panda Hill (Tanzania), Siilinjärvi (Finland), Arbarastakh, Seblyavr and Dalbykha (Russia), Dicker Willem and Keishöhe (Namibia) (e. g. Broom-Fendley *et al.*, 2017; Walter *et al.*, 2022; Kogarko *et al.*, 1995; Woolley, 1987, 2001, 2019).

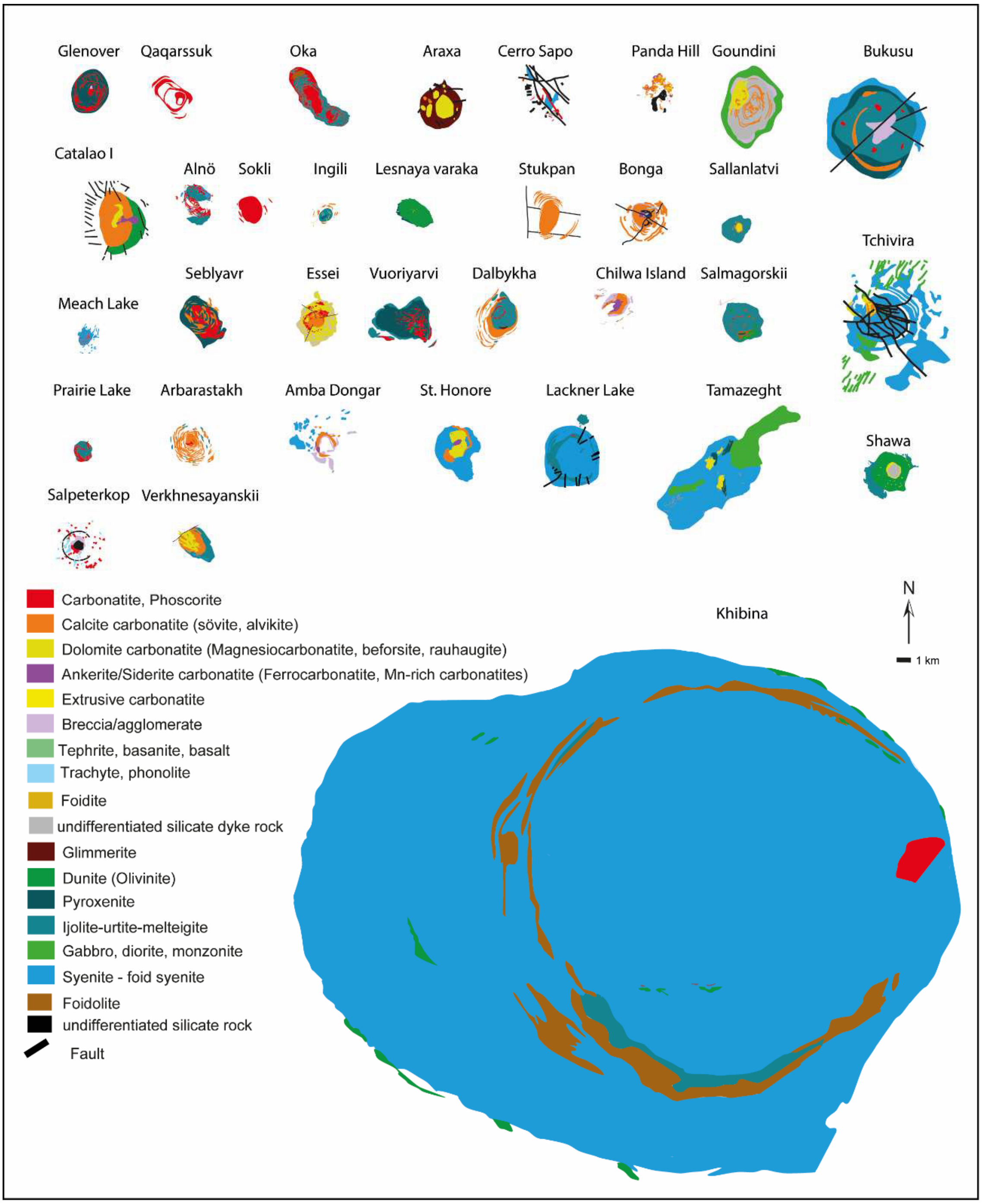

Figure 2. Compilation of exemplary shallow intrusive carbonatite complexes (Kogarko *et al.*, 1995; Woolley, 1987, 2001, 2019)

Deep-seated carbonatite complexes

Intrusive carbonatites emplaced at deeper crustal levels (i. e. >8 km; Fig. 3) are not very common, which is probably an effect of global erosion depths, which are mostly upper crustal. Where they occur, such structures are mainly developed as plugs, while ring dykes, sills, cone sheets and radial dyke systems are generally absent. They often show a well-developed fenite aureole and are typically associated with significant amounts of ultramafic rock (e. g. pyroxenite, dunite) and phoscorites (e. g. Palabora; Giebel *et al.*, 2019a). Important examples of deep-seated carbonatites comprise Mount Weld (Australia), Evate (Mozambique), Palabora (South Africa), and the Kola occurrences including Kovdor and Afrikanda (Russia) (e. g. Epshteyn and Kaban'kov, 1984; Giebel *et al.*, 2019a; Hurai *et al.*, 2021). Moreover, clusters of decimetre- to metre-wide apatitite veins (minor seams of ultramafic rock) from Nolans Bore (Australia) probably represent the root zones of a trans-passing carbonatite melt migrating through the deeper crust (Anenburg *et al.*, 2018).

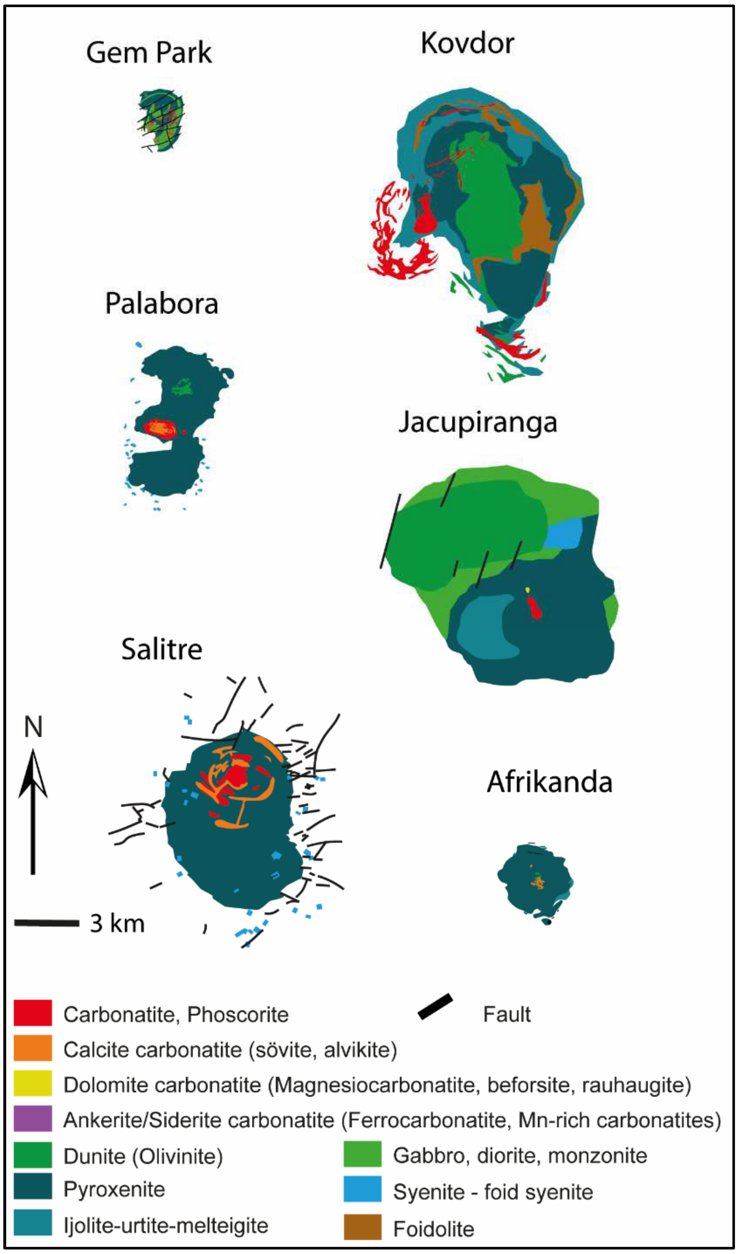

Figure 3. Compilation of exemplary deep-seated carbonatite complexes (Kogarko *et al.*, 1995; Woolley, 1987, 2001, 2019)

<u>Strongly deformed complexes</u>

Deformation of carbonatites is not uncommon and can occur under ductile (e. g. Swartbooisdrift and Otjisazu, Namibia; Ice River, Canada; Bühn *et al*., 2001; Drüppel *et al*., 2006; Mitchell *et al*., 2017) or brittle conditions (Epembe and Glockenberg, Namibia; Bulls Run, South Africa; Walter *et al*., 2022.; Scogings and Forster, 1989) (Figs 4 and 5). Deformation may be related to local or regional faults and lineaments (e. g. Glockenberg and Otjisazu, Namibia; Bühn *et al*., 2001; Walter *et al*., 2022) or to larger-scale regional metamorphism, as at Loe Shilman, Sillai Patti, Koga, Jambil and Jawar in Pakistan (Khan *et al*., 2021), Eureka (Namibia; Broom-Fendley *et al*., 2021), the Maz Complex (Argentina; Casquet *et al*., 2008), the Newania, Sevattur, Jokipatti, Hogenakal, and Munnar complexes in India (Paul *et al*., 2020, and references therein), as well as several occurrences in Northern America (Blue River area, Mount Three Valley Gap carbonatites, Ice River Complex; Millonig *et al*., 2012).

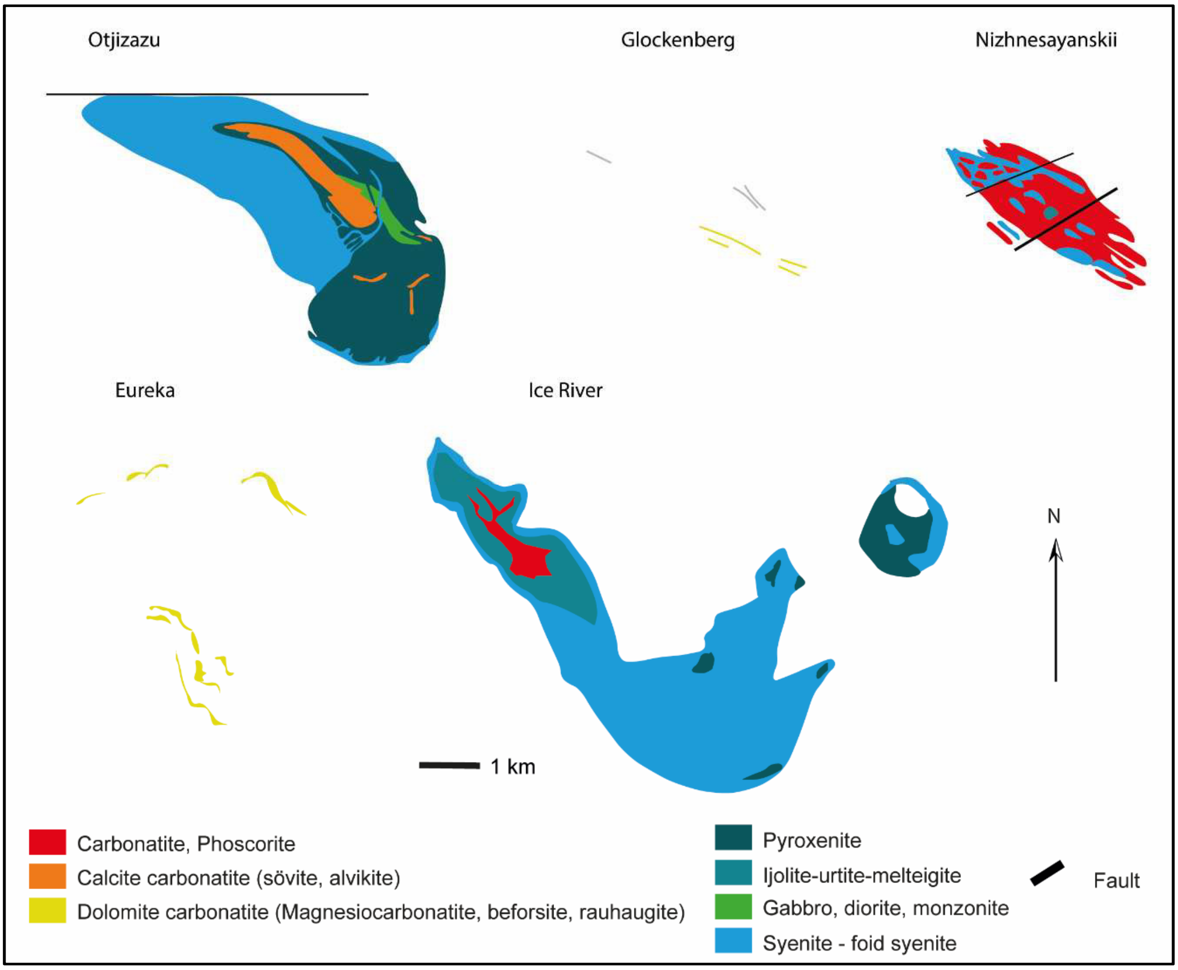

Figure 4. Compilation of exemplary deformed carbonatite complexes (Kogarko *et al*., 1995; Woolley, 1987, 2001, 2019)

3D-shape of intrusive carbonatite bodies

The general architecture of undeformed carbonatite complexes and the shape of intrusive carbonatite bodies are influenced by several factors, including physical parameters of the carbonatite magma itself (e. g. viscosity and density), the rheology of the surrounding country rocks, and the local or regional stress field (Simandl and Paradis, 2018, and references therein). Many vertically elongated and steep carbonatite bodies (plugs) are associated with radial dyke systems, cone sheets and/or ring dykes (Figs 6 and 14; Simandl and Paradis, 2018). The formation of cone sheets and ring dykes, for example, is strongly related to the stress field induced by magma ascent and emplacement. Vertical to subvertical radial dykes or subvertical to outward-dipping, partly crescent-shaped and locally concentric ring dykes, as well as inward-dipping, concentric cone sheets can emplace (Simandl and Paradis, 2018, and references therein). In contrast, in the case of anisotropic regional (tectonic) stress exceeding intrusion-induced stress, regional dyke swarms may form (Simandl and Paradis, 2018, and references therein) that are typically related to regional lineaments and other dominant structures, such as metamorphic foliation (e. g. Lofdal, Namibia), or structures around pre-existing batholiths (e. g. Swartbooisdrift in the vicinity of the Kunene anorthosite). Finally, certain carbonatite geometries are partly influenced by the exposure level of a given carbonatite complex. For example, radial dyke systems seem to be restricted to the top of ascending carbonatite plugs (Richat Dome, Mauritania; Gross Brukkaros, Namibia) at variable depths, whereas cone sheets exclusively occur at subvolcanic emplacement levels (Kaiserstuhl, Germany; Teufelskuppe and Keishöhe, Namibia).

Figure 5. A) Movement on the Okahandja lineament (Namibia) leads to ductile deformation in the Otjisazu Complex on a macro-, meso- and micro-scale; B) the Glockenberg carbonatite dykes (Namibia) intruded into the active Glockenberg mylonitic shear zone and were affected by brittle deformation.

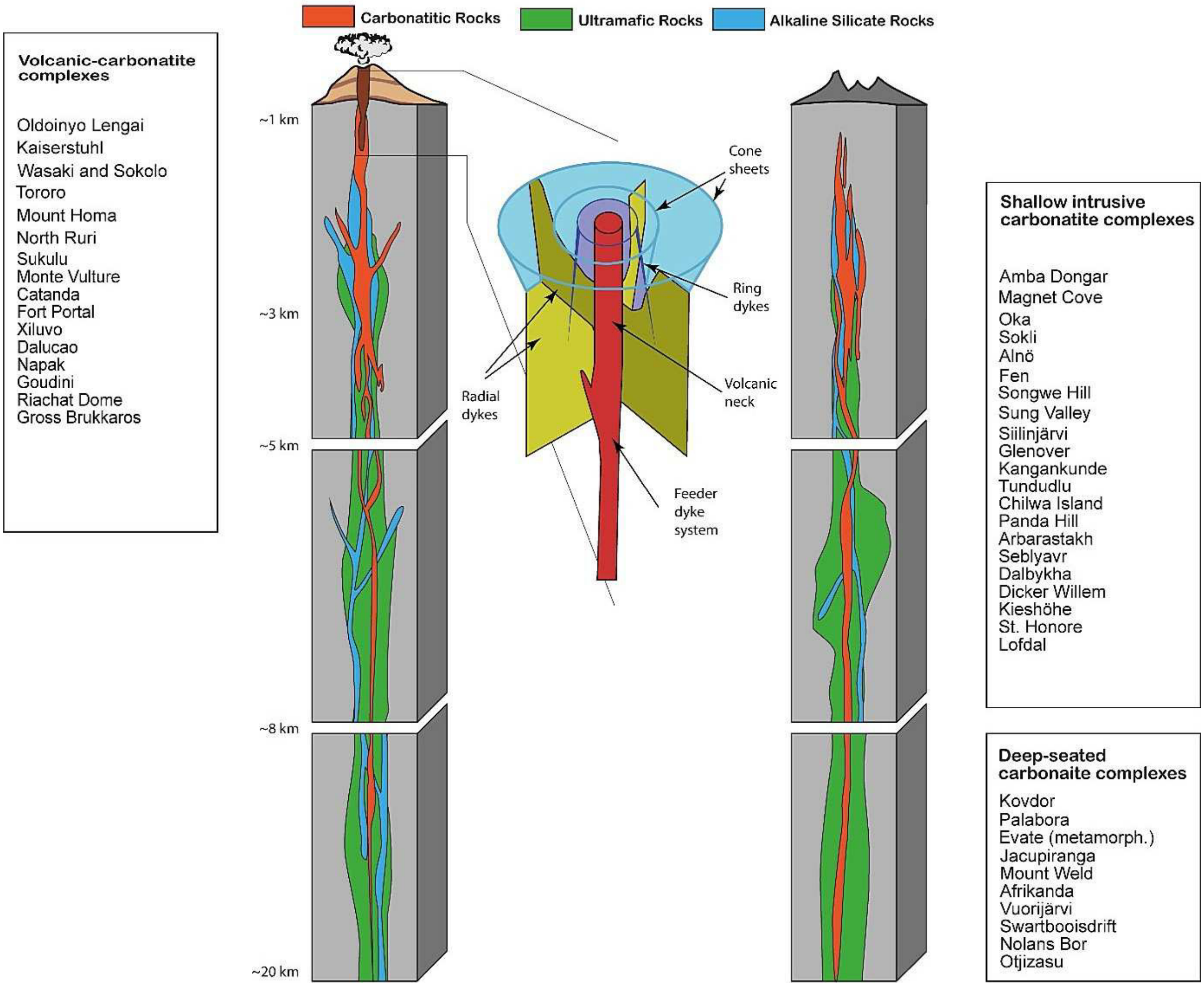

Figure 6. Modified model after Frolov (1971), Simandl and Paradis (2018) and Walter *et al*. (2021), with reference to complexes for which a reliable depth estimation exists

Regional dyke swarms (Type Lofdal)

This group encompasses carbonatite occurrences that consist of single (Fig. 7; e. g. Epembe, Namibia) or multiple carbonatite dykes (e. g. Lofdal, Namibia; Haast River, New Zealand). They lack other geometric elements, such as ring complex structures. The dykes can vary in width, mostly on the centimetre- to metre-scale (e. g. Keikamspoort and Magnet Heights, South Africa; Verwoerd, 1967); rarely they may be up to 500 m wide and traceable for several kilometres along strike (e. g. Vishnevogorskii, Russia, Chernigovskii, Ukraine; Kogaro *et al*., 1995).

Radial dyke systems (Type Gross Brukkaros)

Such localities expose (sub)vertical dyke systems that strike towards a common focal point resembling a central carbonatite plug, which may be actually exposed (e. g. Kaiserstuhl, Germany; Wimmenauer, 2003) or else hidden at deeper levels (e. g. Gross Brukkaros, Namibia; Walter *et al*., 2023). The thickness of such dykes can be variable (decimetres to metres) and may increase towards the magmatic centre (Figs 8 and 9). Well-documented radial dyke systems exposed over hidden carbonatite plugs are rare; the best examples are Gross Brukkaros and Osongombo in Namibia and Richat Dome in Mauritania (Verwoerd, 1967; Matton and Jebrack, 2014; Walter *et al*., 2023). In some cases, the radial dyke system is cut by a younger central carbonatite plug (e. g. Kaiserstuhl) or was destroyed by breccia pipe formation (e. g. Osongombo, Namibia).

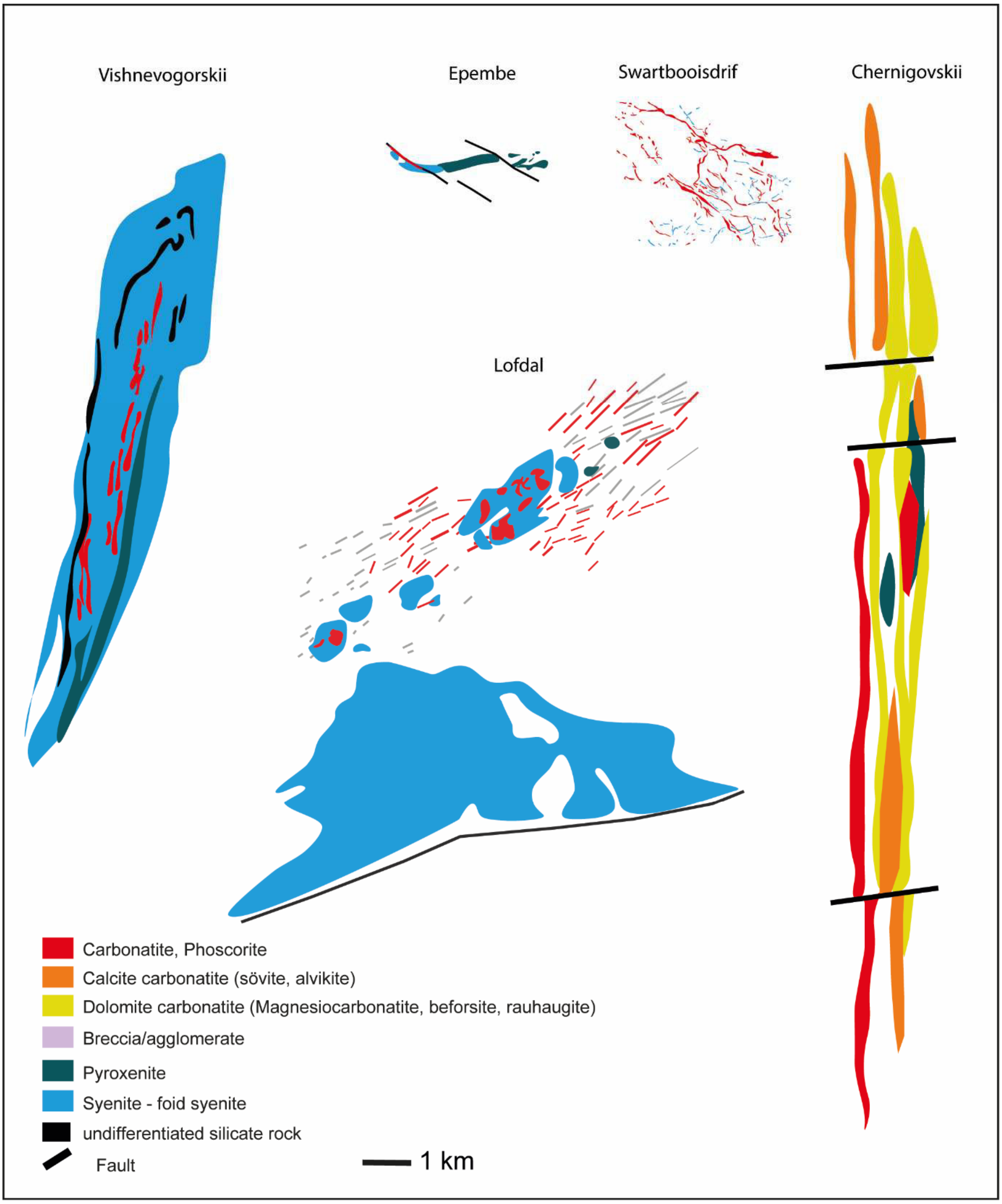

Figure 7. Compilation of occurrences classified as regional dyke swarm (Kogarko *et al*., 1995; Woolley, 1987, 2001, 2019)

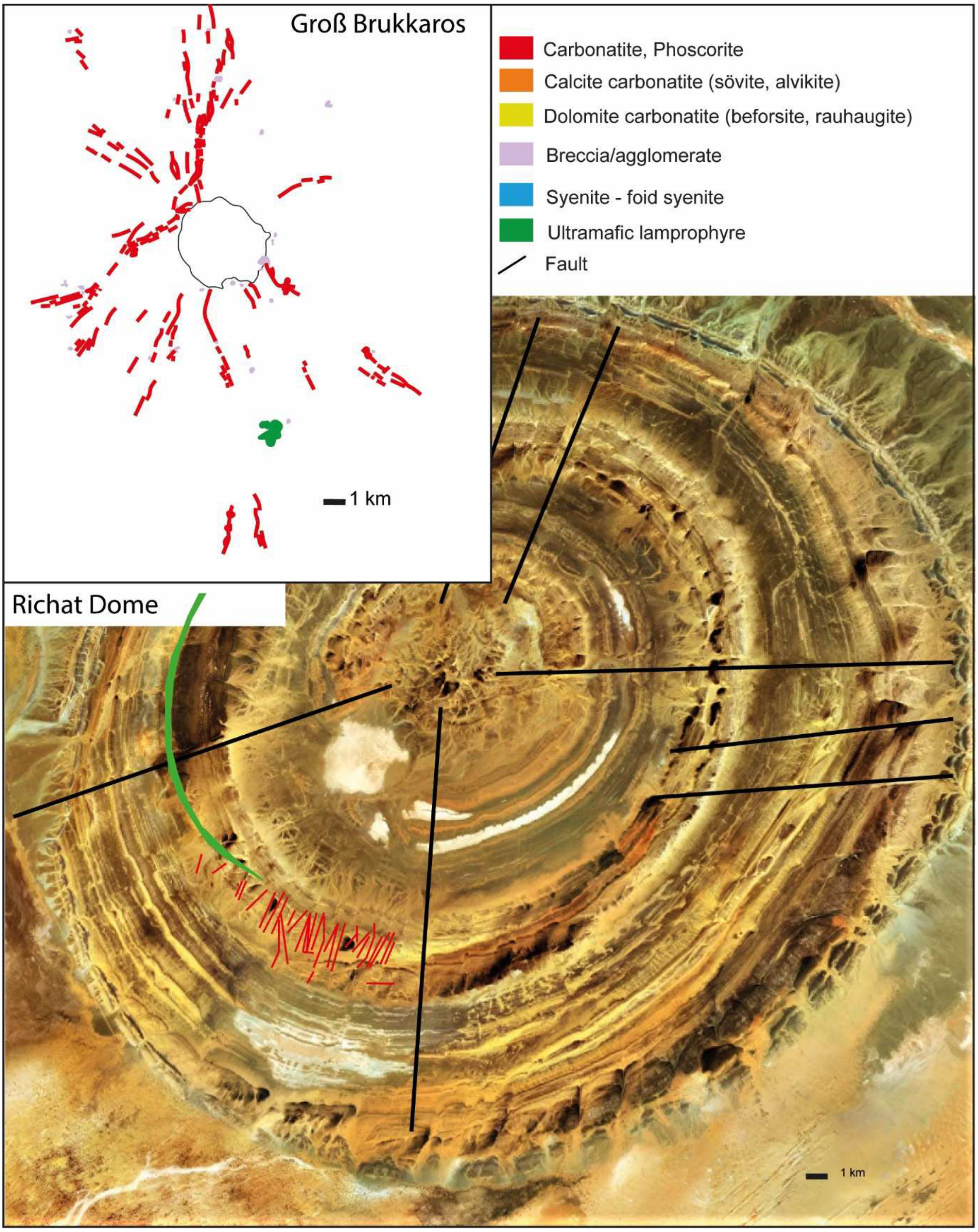

Figure 8. Occurrences classified as radial dyke swarms (Woolley, 2001)

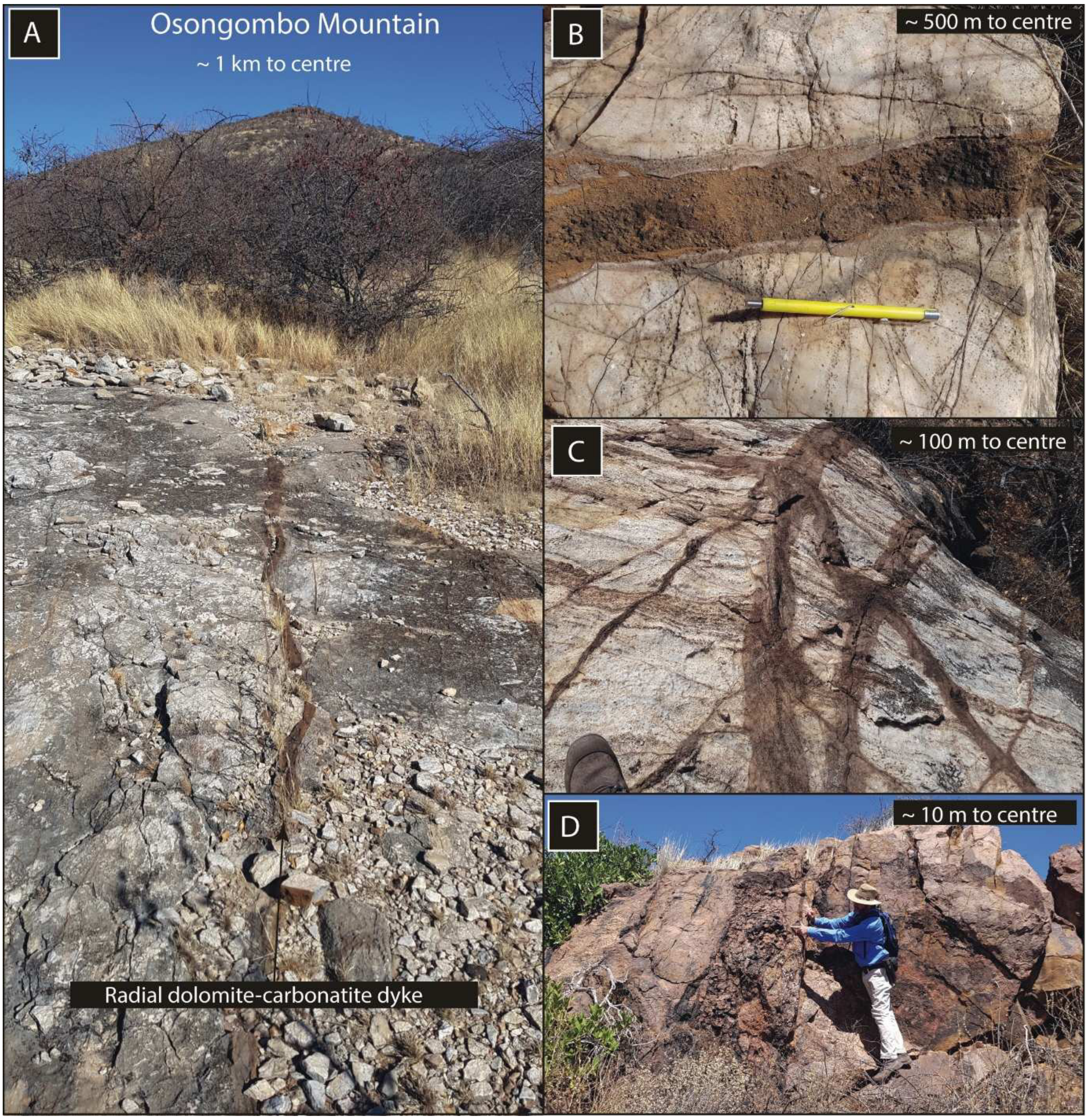

Figure 9. Radial dyke system at Osongombo (Namibia): A) small dykes of <10 cm thickness strike towards the centre (Osongombo Mountain) of the intrusion; B) with decreasing distance to the magmatic centre dyke thickness increases; C) in the direct vicinity of the centre radial dykes become more than a metre thick or form dense networks; D) in the centre of the complex the dykes end up in the root zone of a carbonatite breccia pipe.

Cone sheets and ring dykes/sills (Type Ondurakorume)

Cone sheets and ring dykes may occur at the same locality (Fig. 10). In such cases, ring dyke systems are usually cut by a cone sheet system. Cone sheet and ring dyke systems form continuous or discontinuous single or multiple circular structures of variable carbonatite lithologies, and plutonic as well as (sub)volcanic rocks (Ladisic *et al*., 2025). The width of such dykes/sills varies mostly from the decimetre- to hundreds of metres-scale. Examples of well-documented cone sheet systems include Kaiserstuhl (Walter *et al*., 2018; Giebel *et al*., 2019), Ondurakorume (Namibia; Ladisic *et al*., 2025; Figs 10, 11), Keishöhe (Namibia; Walter *et al*., 2022), Goudini (South Africa; Verwoerd 1967), Homa Mountain (Kenya; Woolley 2001), Chilwa Island (Malawi; Woolley 2001), Alnö (Sweden), Qaqarssuk (Greenland; Wooley 1987) and Arbarastakh (Russia; Kogarko *et al*., 1995). Well-documented ring dyke systems are known from Amba Dongar (India; Chandra *et al*., 2019), Glenover (South Africa; Verwoerd, 1967), Oka (Canada; Wooley 1987), Dicker Willem (Namibia; Woolley 2001) and Gardiner (Greenland; Gudelius *et al*., 2023).

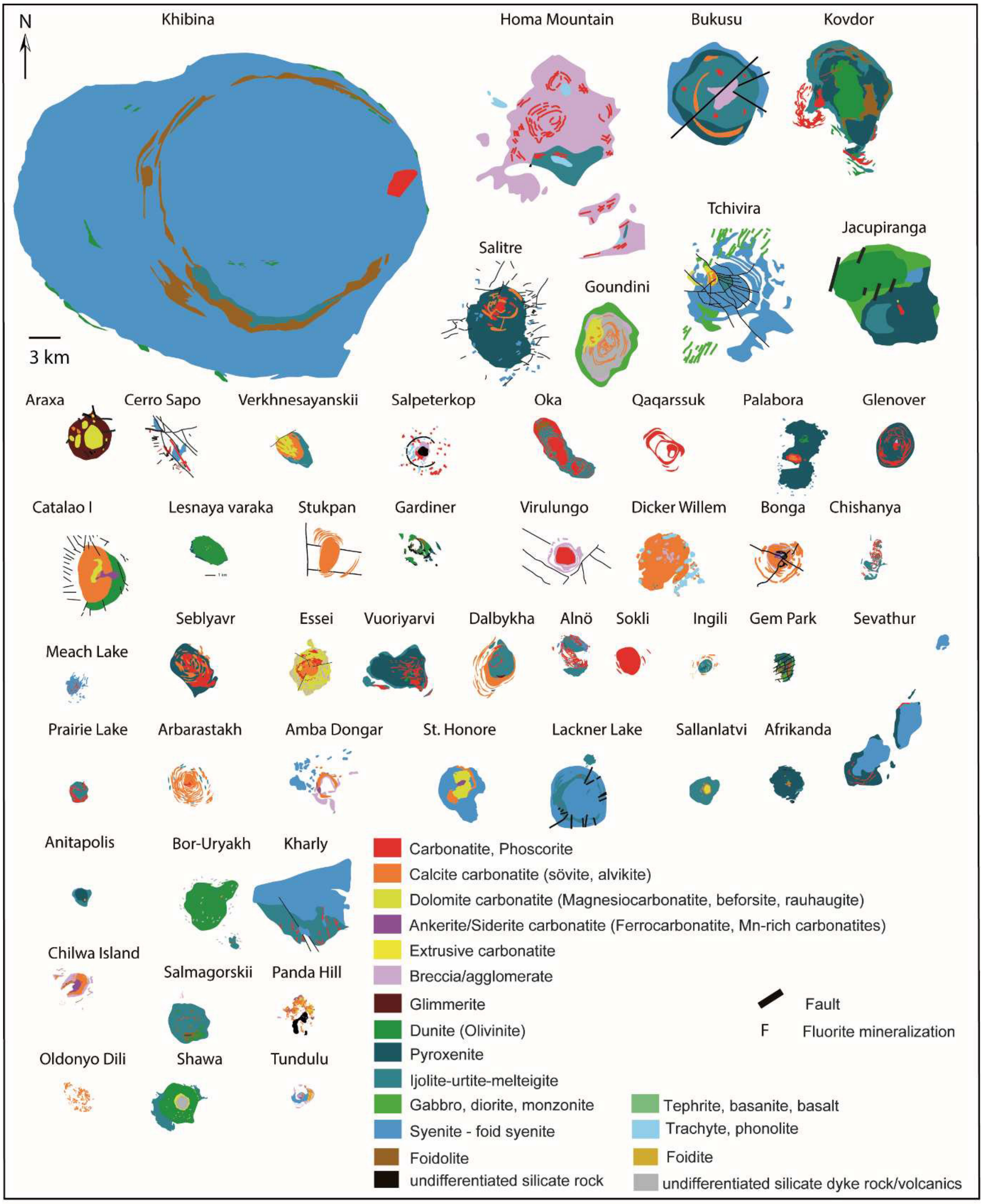

Figure 10. Compilation of occurrences with cone sheet and ring dyke systems (Kogarko *et al*., 1995; Woolley, 1987, 2001, 2019)

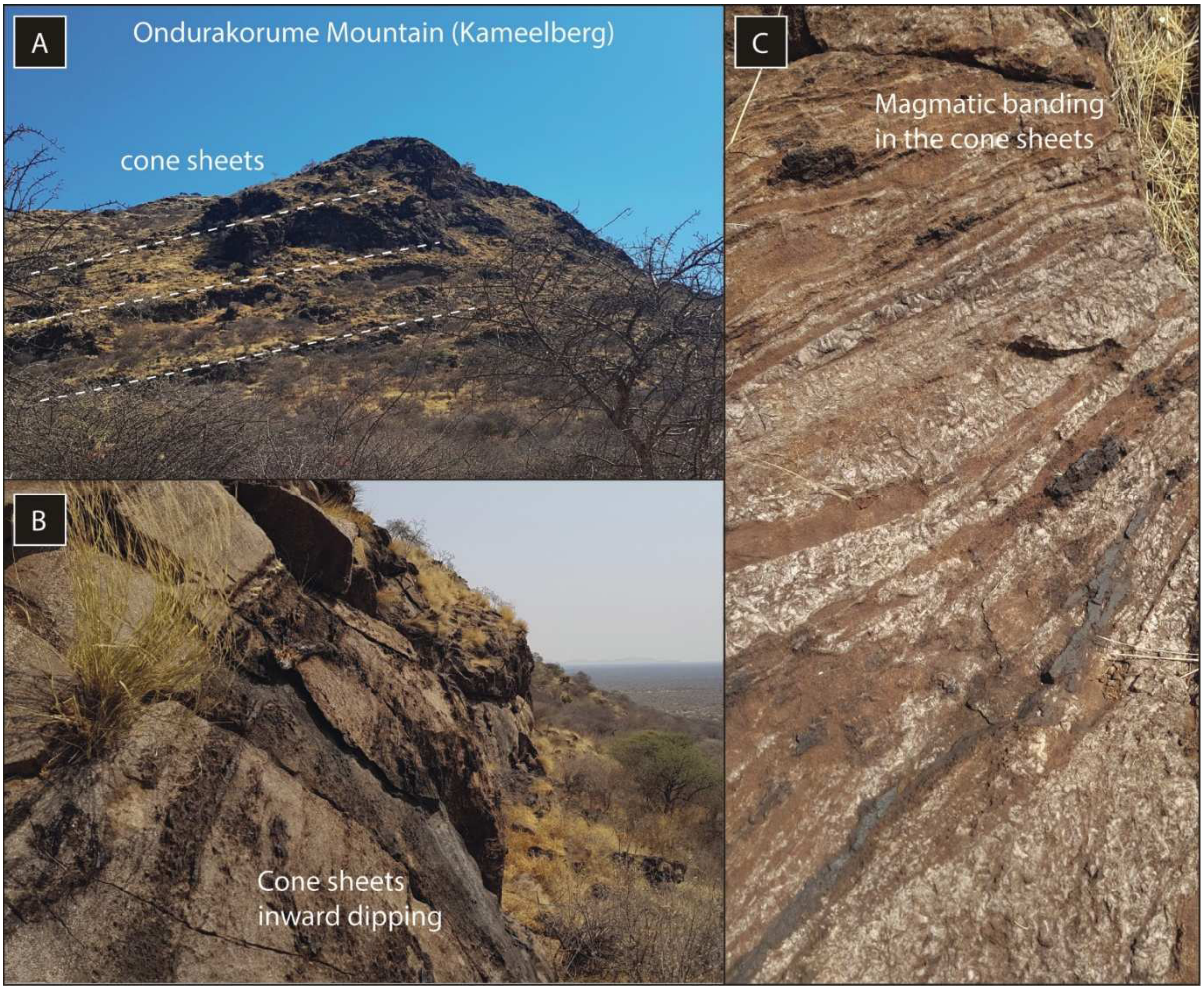

Figure 11. Cone sheets of the Ondurakorume carbonatite, Namibia: A) inward-dipping cone sheets form the entire Ondurakorume Mountain. At least three different cone sheet systems can be differentiated with younger cross-cutting older ones; B and C) calcite carbonatite cone sheet with magmatic banding

Plugs and pipe-like structures (Type Palabora)

Plugs are common features in carbonatite complexes, usually forming the main carbonatite body. Such well-developed, vertically elongated bodies can occur at the junction of transcrustal fault systems (Banks *et al*., 2019) as these represent preferred conduits for melts. In plan view, they are rounded features reaching several hundreds of metres in diameter. Such geometries have been reported from Sokli (Finland; Vartiainen and Paarma, 1979), Kaiserstuhl (Walter *et al*., 2018; Giebel *et al*., 2019), Dicker Willem (Reid *et al.,* 1990), Oka (Canada; Woolley 1987), Palabora and Spitzkop (South Africa; Verwoerd, 1967), Iron Hill (USA; Nash, 1972) and Fen (Norway; Andersen, 1987) (Fig. 12).

Cumulate pockets (Type Nolans Bore)

This group does not reflect a geometry itself, but is mentioned here as a relevant part of a magmatic system. The geometry of the apatite veins at Nolans Bore (Australia) and similar occurrences is strongly linked to a deep (granulite facies) emplacement level (Anenburg *et al*., 2018) and related zones of weakness (Fig. 13). Anenburg *et al*. (2018) interpreted these apatite veins as filter-pressing products of a transpassing carbonatite magma at deep crustal levels. Therefore, the geometry of irregular veins and pockets likely reflects a cumulate fraction generated during the ascent of a carbonatite melt. Further examples are Hoidas Lake (Canada; Pandur *et al*., 2015) and Kasipatnam (India; Choudhuri and Banerji, 1976; Rao, 1976; Panda *et al*., 2015).

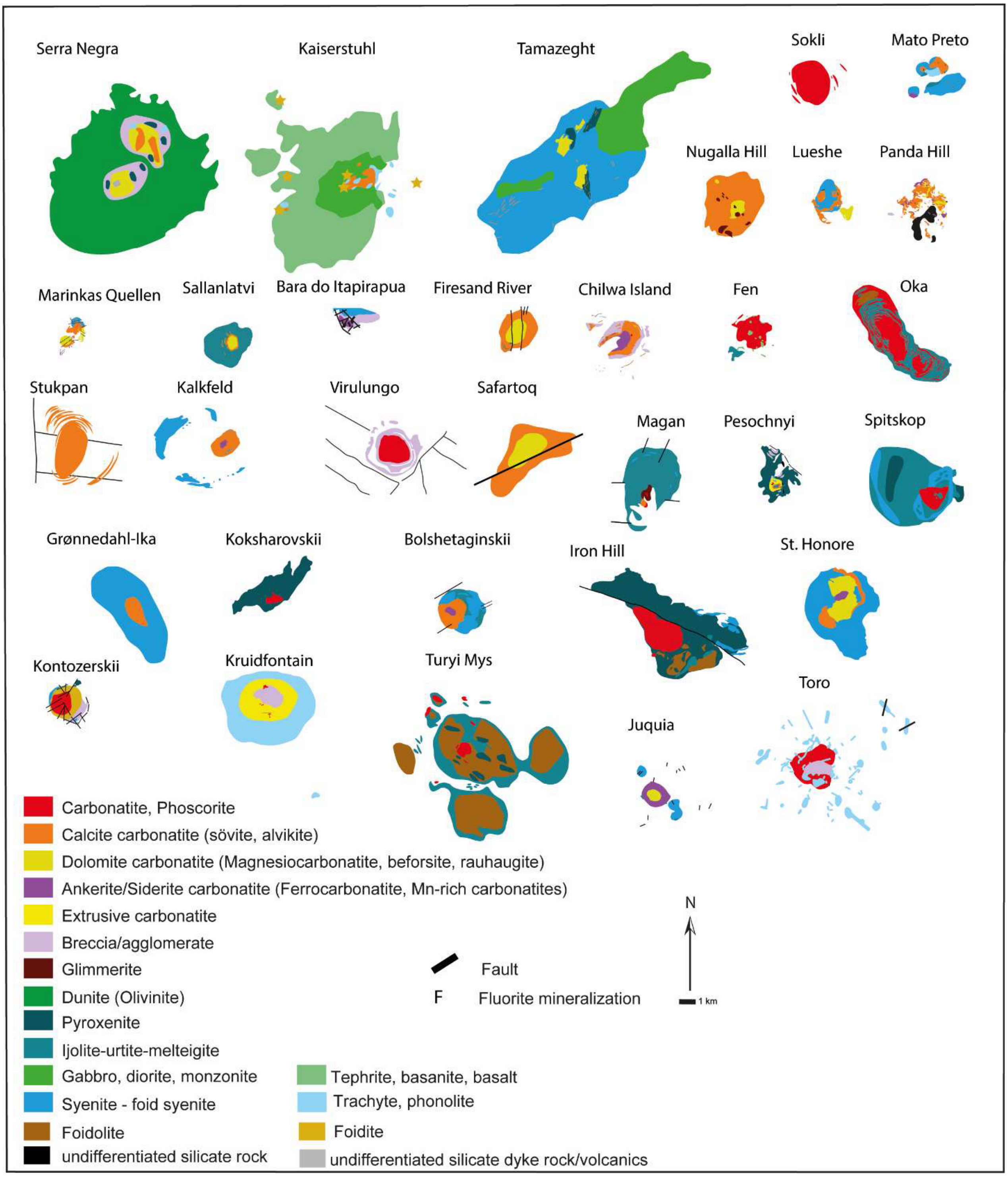

Figure 12. Compilation of occurrences classified as plugs and pipe-like structures (Kogarko *et al*., 1995; Woolley, 1987, 2001, 2019)

Approach

To evaluate the frequency of the various geometric elements described above on a global scale, this review updates the carbonatite lists of Woolley and Kjarsgaard (2008), Wooley (2019), Humphreys-Williams and Zahirovic (2021) and Schmitt *et al*. (2024) based on original and recent descriptions and published maps (supplementary information, Appendices 1 and 2).

About 20% of the 551 known carbonatites are classified as 'strongly deformed'. As deformation may alter or even erase the initial architecture of carbonatites, such bodies are not considered further. The remaining undeformed occurrences (n=459) were categorised into (i) volcanic carbonatite complexes, (ii) shallow intrusive carbonatite complexes, and (iii) deep-seated carbonatite complexes**.** For many of them, plan view maps have been digitised and plotted using the same scale, with consistently labelled lithologies. At each of these localities, the exposed carbonatite bodies were classified as (a) regional dykes swarms, (b) radial dykes, (c) cone sheets, and (d) ring dykes and plugs. It is important to note, that a single location can have more than one geometric feature, e. g. a central plug that is surrounded by a cone sheet system. This compilation provides a statistical base for a quantitative evaluation of the frequency of certain forms and shapes of carbonatite bodies in respect of relative volume and associated alkaline silicate rocks. As one complex can host more than one geometric element, the number of features (and associated lithologies) presented in the following exceeds the number of locations studied.

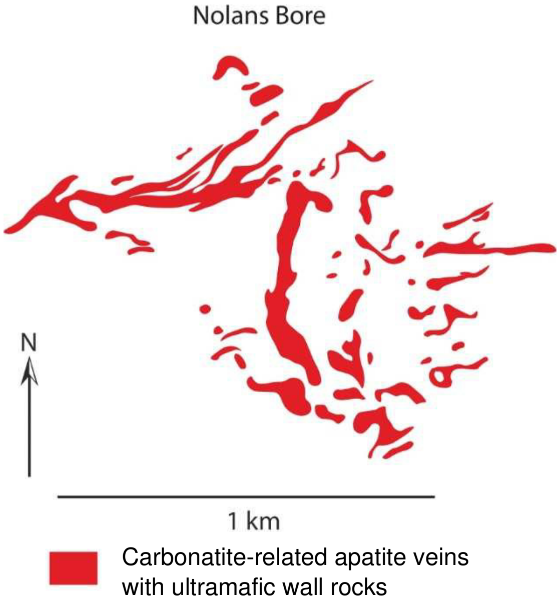

Figure 13. Apatitite pockets at Nolans Bore (Australia) as type locality of cumulate pockets

Results

What is the geometry of a typical carbonatite?

It is important to note that the geometry of carbonatites is independent of their origin (mantle versus crustal source, which is not topic of this paper); therefore, all known occurrences are considered here, not only those identified by Schmidt *et al*. (2024) as "real" carbonatites. After elimination of the deformed complexes (n=110), almost half (48%) of the remaining carbonatite occurrences, for which sufficient information was available (n=459), represent single carbonatite dykes or dyke swarms (n=260), often in association with other geometry types. Plugs are less common (n=110; 20%), followed by cone sheets and ring dykes (n=61; 11%). Sills, with only 14 descriptions (3%), are apparently rare, while subvolcanic, carbonatite-bearing diatreme breccias are described from 44 locations (8%). Occurrences of extrusive carbonatites have been updated from Woolley and Church (2005) and are described from 49 localities.

Only ca. 20% (n=118) of the known carbonatites are apparently not spatially associated with alkaline silicate rocks, which is at least partly influenced by the exposure level. Carbonatites are typically associated with foid syenites (n=171; 32%), syenites and quartz-syenites (n=154; 29%), foidolites (rocks of the melteigite-urtite-ijolite series; n=128; 24%), and ultramafites (pyroxenites-peridotites-dunites; n=156; 29%). Less commonly they occur together with lamprophyres (n=86; 16%), gabbroic rocks (n=72; 13%), phonolites (n=66; 12%), trachytes (n=55; 9%), nephelinites (n=51; 9%), melilitolites/melilites (n=30; 6%), and leucite/pseudoleucite-bearing rocks (n= 23; 4%). Please note that individual complexes can exhibit a variety of rock associations (in addition to a combination of geometries), so that, when grouped according to these criteria, they have been counted twice or more times. Therefore, "n" combined exceeds the total number of known carbonatite complexes.

Discussion

The influence of emplacement depth on carbonatite geometry

The presence of specific geometries (except for lava flows and diatremes) cannot simply be translated into a depth categorisation, since some of the observed geometries (e. g. radial dykes) occur at various depths. Also, while it is true that, for instance, cone sheets are most common in carbonatites emplaced at relatively shallow crustal levels (Elliot *et al*., 2018), this is also the level at which most carbonatite complexes are exposed today. Therefore, interpretations of "carbonatite types" and dominant geometries, and the genesis of carbonatites are probably biased by the typical exposure level of crustal rocks. Today's exhumation situation is clearly pointing towards a dominant erosional cut of the complexes in their roof regions.

Similarly, the intensity of fenite halos surrounding a carbonatite complex cannot be taken as an indicator of emplacement depth, as several parameters are affecting the formation and extent of a fenite halo; chemical gradient to the country rocks, porosity and permeability of the surrounding rocks and fracture networks, to name just a few, can vary significantly among individual complexes at the same emplacement level (e. g. Chilwa Province, Malawi or Damaraland Province, northwestern Namibia), thus influencing alteration of the country rock.

Within the group of surficial to shallow-level carbonatites, volcanic edifices, erosional remnants of volcanoes, and subvolcanic levels of eroded volcanic systems can be observed. These include extrusive carbonatites, such as Kaiserstuhl (Germany), Oldoinyo Lengai (Tanzania) and Monte Vulture (Italy), as well as exposed conduits at locations such as Kaiserstuhl and Napak, where the inferred conduits are represented by intrusive plugs several hundred metres in diameter. Such plugs are, however, not exposed at Gross Brukkaros (Namibia) and Richat Dome (Mauritania), where only a radial dyke system of carbonatites is developed, pointing to slightly lesser (relatively!) erosional exhumation compared, for instance, to Napak (Uganda); at the latter locality a few hundred metres have been removed.

Moreover, cone sheets (Amba Dongar, Ondurakorume and Gardiner) and ring dykes (Tundulu and Homa Mountain; supplementary information, Appendix 3) are common at the same subsurficial level. On the other hand, deeply emplaced complexes like Kovdor and Salitre (Brazil; supplementary information, Appendix 3) show a very well-developed network of cone sheets, dykes and sills as well. Therefore, the architecture of a carbonatite occurrence cannot be used as a tracer for emplacement depth, with exception of ring dykes, which hint at an eroded and collapsed caldera structure.

Are "ring dyke" and "cone sheet" features always of real "dyke" nature?

A further level of complexity is related to recent research on a potential metasomatic origin of associated silicate rocks like ultramafites (Vasyukova and Williams-Jones, 2022). Numerous complexes show "ring dyke- or cone sheet-like" geometries like Kovdor (Russia) and Gardiner (Greenland; Simandl and Paradis 2018; Vasyukova and Williams-Jones, 2022; Gudelius *et al*., 2023). These contain for instance dunites or pyroxenites. It is, however, difficult to imagine that at subvolcanic levels, dunite can be crystallised as a "dyke". Consequently, a metasomatic origin might explain the observed lithologies. In this case, a lining of the ascent channel with ultramafic rocks, as interaction product between the melt and the country rocks (Vasyukova and Williams-Jones, 2022), or associated pre-existing alkaline silicate rocks could produce a similar geometry to such ring structures. If this is true, the evaluation of a shallow emplacement depth by using cone sheet systems as an argument needs to be reconsidered at least for some occurrences. Therefore, much more work has to be carried out to shed light on the process of wall-rock metasomatism and the related geometries and "pseudo-geometries" of alkaline silicate rocks and carbonatites in composite complexes.

Silicate/carbonatite ratio as indicator for relative emplacement depth

An interesting occurrence to illustrate the significance of the model provided by Giebel *et al.* (2017) is Palabora as described in Appendix 1 (see supplementary information). The main Loolekop pipe (central carbonatite intrusion of Palabora)is mined down to ~2 km without evidence of getting thinner with depth. In the southern pit, only pyroxenite was observed down to ~200 m; however, in the new levels of the southern pit, an increasing number of carbonatite dykes can be observed with depth. The same holds true for the nearby Guide Copper mine pyroxenite where carbonatite is only known from drill core. Therefore, at the same emplacement level and the same age, three carbonatites are stuck at different topographic levels. Whereas the Guide Copper mine carbonatite and the southern pit carbonatite at Palabora are stuck ~200 metres below today's land surface, the Loolekop carbonatite at Palabora reached at least the present land surface. Hence, today's level of the southern pit carbonatite records the "stopping" level in the roof zone of an ascending major carbonatite plug. The intense hydrothermal stage developed in the Loolekop carbonatite (Giebel *et al.*, 2017) provides evidence that it did not extrude on to the surface, but was emplaced at a higher crustal level.

The linkage between various geometries as indicators for a pocket-like transcrustal ascent of carbonatite magmas

Radial dyke systems (e. g. Richat Dome, Napak, Gross Brukkaros; Figs 8 and 9) are probably (together with single carbonatite dykes following zones of pre-existing weakness in the country rock) the topmost expressions of carbonatitic magmas ascending through the crust (Fig. 14; Walter *et al.*, 2021), consistent with deformation and updoming of country rocks at these localities (as known from mafic dykes and the experiments of Kavanagh *et al.*, 2018). The radial dyke system of Gross Brukkaros (Namibia) lacks exposed cone sheets, ring dykes, or a major plug. At Alnö (Sweden), a radial dyke system is cut by a cone sheet and ring dyke system. At a slightly deeper level, the Richat Dome (Mauritania) displays a carbonatite radial dyke system, which is cross-cut by a gabbroic ring dyke. In relatively deeper erosional cuts (e. g. Amba Dongar and Oka), well-developed ring dyke systems are exposed, while radial dykes are lacking, as they probably have been eroded (Fig. 14). In numerous complexes, ring dyke systems are cut by plug-like carbonatite bodies (e. g. Dicker Willem, Oka, Kaiserstuhl; (Figs 10 and 14). In some cases, where ring dykes or radial dykes are cut by diatremes or cone sheets (e. g. Keishöhe, Tundulu or Homa Mountain), a volcanic behaviour and eruption of the system is very likely, because ring dykes develop in the context of caldera formation (Simandl and Paradis, 2018).

Because of exposure bias and/or misidentification, the deepest parts of carbonatite magmas ascending through the crust are not well documented. Recent work by Anenburg *et al.* (2018) on Nolans Bore (Australia), which is not a carbonatite *sensu strictu*, provides evidence for a "carbonatitic magma traversing the silicate-dominated middle crust". Thus, it seems likely that exposed carbonatite plugs do not extend through the whole crust, but rather show a pocket-like behaviour, whereas cone sheets and diatremes prove a volcanic behaviour at subvolcanic levels. Ring dykes and radial dykes are the precursors of the following pocket (plugs), and filter-pressed cumulates, as at Nolans Bore and similar occurrences (see supplementary information, Appendix 1), probably mark the deepest parts of an ascent track of a carbonatitic melt batch.

Regional carbonatite dyke swarms (e. g. Lofdal, Jawar, Sillai Patti, Glockenberg, Bulls Run, Eureka and Swartbooisdrift), however, probably belong to a different group of carbonatites (i. e. "post-orogenic carbonatites", Goodenough *et al.*, 2021, and references therein), which follow zones of weakness along suture plains in active orogens; they show a different emplacement behaviour as their geometry is controlled by the metamorphic foliation of the country rocks or the strike and dip of shear zones. Nevertheless, it is not easy to decide if a carbonatite is intruded into a foliation or a pre-existing carbonatite was affected by tectonometamorphic events. Depending on the metamorphic path, the development of a fenite halo can be used as an indicator for pre-, syn- or postorogenic emplacement.

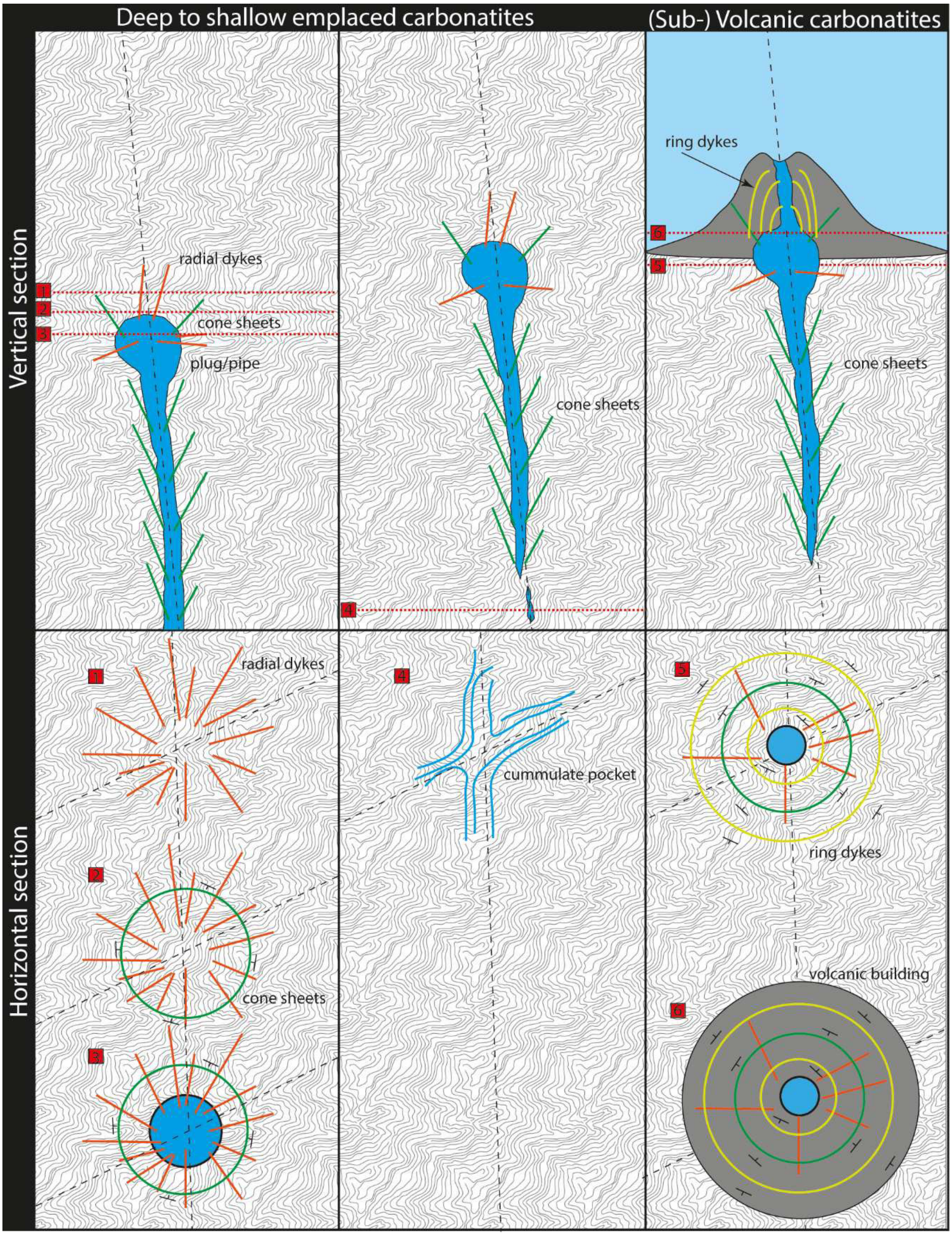

Figure 14. Schematic sketch illustrating the influence of the erosional plain on the carbonatite outcrop situation: depending on the level of erosion various architectural features can be exhumed. 1) Propagating radial dyke systems on top of a melt pocket below; 2) Slighty below the top of the radial system and above the melt pocket, radial dykes and ring dykes occur together; 3) If exhumation cuts the stuck pocket itself, a central plug can be observed on the present surface surrounded by the base of the radial and ring dykes. It is important to note that parts of the ring dyke and radial dyke system in the centre can be lost by the transpassing and emplacing main melt pocket; 4) Below the main melt pocket, the system closes, the melt is transpassing and leaves cumulates of apatite behind (type Nolans Bore). Due to the strong lithostatic forces at depth, pathways below the pockets become filter-pressed; 5) and 6) If the pocket ascends to the land surface, a catastrophic release of the melt leads to rapid emptying of the pocket and caldera breakdown. Associated with the breakdown of the caldera, cone sheet structures develop and locally are filled with the remaining carbonatite melt.

Analogies and differences to silicate systems

Carbonatitic systems exhibit structural similarities to silicate systems, including features such as radial dykes, cone sheets, and ring dykes (Simandl and Paradis, 2018). A compelling example that illustrates this analogy is the Ardnamurchan complex in Scotland, where a shallow (<5 km depth) intrusive network composed of sills, central complexes (England, 1988; Emeleus and Bell, 2005; Magee *et al.*, 2013; O'Driscoll *et al.*, 2006) and regionally extensive NW–SE striking dykes are exposed (Emeleus and Bell, 2005; Magee *et al.*, 2013, and references therein). The cone sheets of Ardnamurchan exhibit a characteristic concentric strike pattern and inward dips ranging from 10° to 70°, steepening towards the central complex, a feature that is also observed in carbonatitic systems (Simandl and Paradis, 2018). Inclined dolerite sheets and NW–SE trending dykes intrude domed country rocks, where sedimentary strata dip outward from the central complex (Magee *et al.*, 2013). These observations suggest that regional tectonic stress regimes play a key role in generating similar intrusive architectures, including cone sheets, ring dykes, and radial dykes, in both carbonatitic and silicate systems.

Despite such similarities, fundamental differences exist in the geometry of carbonatite plugs, as they typically display high vertical-to-lateral aspect ratios compared to the low-ratio magma ponding systems typical of silicate magmatism. This disparity is largely attributed to the physical properties of the respective melts—particularly density and viscosity. The low viscosity and low density of carbonatitic melts makes it impossible to build up horizontally extensive magma chambers as known from silicate systems, as lithostatic pressure will press out the carbonatitic liquids. Carbonatitic systems often lack evidence of substantial magma ponding. Given the physical and chemical characteristics of carbonatite melts—such as density, velocity, and volatile content—the formation of extensive horizontally oriented magma chambers with prolonged ponding is considered unlikely. Instead, carbonatite intrusions typically exhibit steep, semi-circular, pipe-like bodies, similar to kimberlite intrusions. Moreover, some carbonatite occurrences (e. g. Kovdor and Palabora) consist of multiple, misaligned pipe-like intrusions derived from successive pulses of carbonatitic magma, providing further evidence against the existence of a singular, long-lived magma reservoir (e. g. Kogarko *et al.*, 1995; Woolley, 1987, 2001, 2019).

Rapid and turbulent ascent of carbonatite melts is supported by their physical properties. For example, due to the higher density of apatite crystals (3.1–3.2 g/cm³) relative to carbonatite melts (typically <2.8 g/cm³, commonly 2.2–2.6 g/cm³), effective gravitational separation would occur unless ascent rates are sufficiently high (Chakhmouradian *et al.*, 2017; Kono *et al.*, 2014).

As in carbonatitic systems, the ascent dynamics and conduit architecture in silicate systems are also governed by the physical and chemical properties of the melt, including temperature, composition, volatile content, crystallinity, and conduit wall permeability (Browne and Szramek, 2015). These parameters are comparatively well-studied in silicate systems. Key controls on ascent rates include magma viscosity and density, which are, in turn, influenced by compositional and thermal variables. Diffusion modelling based on crystal zoning patterns indicates that magmatic processes, such as magma mixing, can occur over time-scales of approximately 100 days, whereas assimilation and crystal-melt fractionation typically occur over centuries and thousands of years (e. g. Hawkesworth *et al.*, 2016). Therefore, the development of shallow magma chambers in silicate systems likely requires prolonged time-scales relative to the rapid ascent observed in carbonatitic systems. Experimental data suggest a threshold ascent rate of approximately 0.2 m/s is associated with explosive eruption in silicate systems (Browne and Szramek, 2015, and references therein). In contrast, carbonatite melts are modelled to ascend at velocities of up to 65 m/s (Ernst and Bell, 2010; Genge *et al.*, 1995), surpassing even those of kimberlites, for which typical ascent rates range from 0.1 to over 4 m/s (Brett *et al.*, 2015), but which can also reach tens of metres per second (Sparks *et al.*, 2009). Consequently, carbonatite magmas ascend more than two orders of magnitude faster than silicate magmas (Tappe *et al.*, 2025; Walter *et al.*, 2021, and references therein).

Analogy to mafic dyke emplacement

Mafic dyke systems have been studied for their ascent behaviour because they exert an influence on volcanic eruption styles (Caricchi *et al.*, 2014, 2016; Ilyinskaya *et al.*, 2017; Kavanagh *et al.*, 2018). Most dykes do not erupt, as shown by field evidence, gas monitoring, and geophysical methods (Crisp, 1984; Gudmundsson, 2002). The main driver of magma ascent is buoyancy, with dyke migration described as “the release of gravitational potential energy on a planetary scale” (Putirka, 2017; Kavanagh *et al.*, 2018). Kavanagh *et al.* (2018) identified four stages of magma ascent in experiments:

(1) early growth stage: dyke growth starts in the source region, with fluid jets circulating and forming a penny-shaped crack;
(2) pseudo-steady growth: a rapidly up-streaming fluid jet results in equal growth in width and length, with fluid down-welling at dyke margins;
(3) pre-eruption unsteady growth: fluid flow becomes unstable in the central jet, with acceleration towards the surface and thinning of the dyke tail;
(4) eruption stage: eruption occurs as fluid flow moves upwards and outwards, and the dyke closes with an abrupt decrease in strain.

As the experiments of Kavanagh *et al.* (2018) were performed with dyed water having physical properties like carbonatite melt (viscosity of supercritical water: ~ 0.3 Pa s, carbonatite melts: ~ 0.006-0.2 Pa s; Kono *et al.*, 2014), their results and interpretations are used here as an analogue for carbonatite dyke emplacement (Fig. 15). In the context of the observed geometries in all studied carbonatite complexes and the physiochemical properties discussed above, it is probable that carbonatites behave like water-filled pockets, rapidly migrating through the crust, and closing their tail during ascent (Fig. 15). Based on the above carbonatite melt properties and the observed carbonatite/silicate rock ratios, it is possible that, depending on the entire carbonatite melt volume, carbonatite pockets between one metre and several kilometres of vertical extent can occur; smaller pockets must be generated at shallower crustal levels out of an alkaline silicate melt, or they would not have enough energy potential to move through the whole crust. This agrees with the jackhammer ascent model proposed by Walter *et al.* (2021), and therefore represents a refinement of it, in respect of a mobile pocket based on geometric arguments outlined above (Fig. 15).

Structural framework as pathways in the upper crust

Most carbonatites use transcrustal lineaments as pathways for ascent (Banks *et al.*, 2019; Walter *et al.*, 2021). Larger carbonatite occurrences (in particular plugs or ring dyke structures on top of them) may exist on crossings of such lineaments (e. g. Giebel *et al.*, 2019). For example, the Dicker Willem and Keishöhe (Namibia) complexes occur on the transcrustal Kudu lineament (Corner, 2000; Walter *et al.*, 2022). Dicker Willem is emplaced at the crossing of the Glockenberg mylonite shear zone (a Namaqua-age translithospheric shear zone), whereas Keishöhe is positioned at the junction of the Pofadder - Marshall Rocks Shear Zone and the Kudu lineament (Corner, 2000; Walter *et al.*, 2022). The delamination of the orogenic root can also provide access for carbonatite melts into old suture zones, which are steepened during continent-continent collision (Goodenough *et al.*, 2021; Plant *et al.*, 2005). This fits in nicely with the occurrence of DARCs (**D**eformed **A**lkaline **R**ocks and **C**arbonatites; Burke *et al.*, 2003) on such structures. If the ideas presented above are correct, it is possible that carbonatite melts can ascend anywhere, if the mantle reaches fertility and low-degree partial melting occurs; however, only when the melt enters the structure network within the brittle crust, they have a chance to reach the surface.

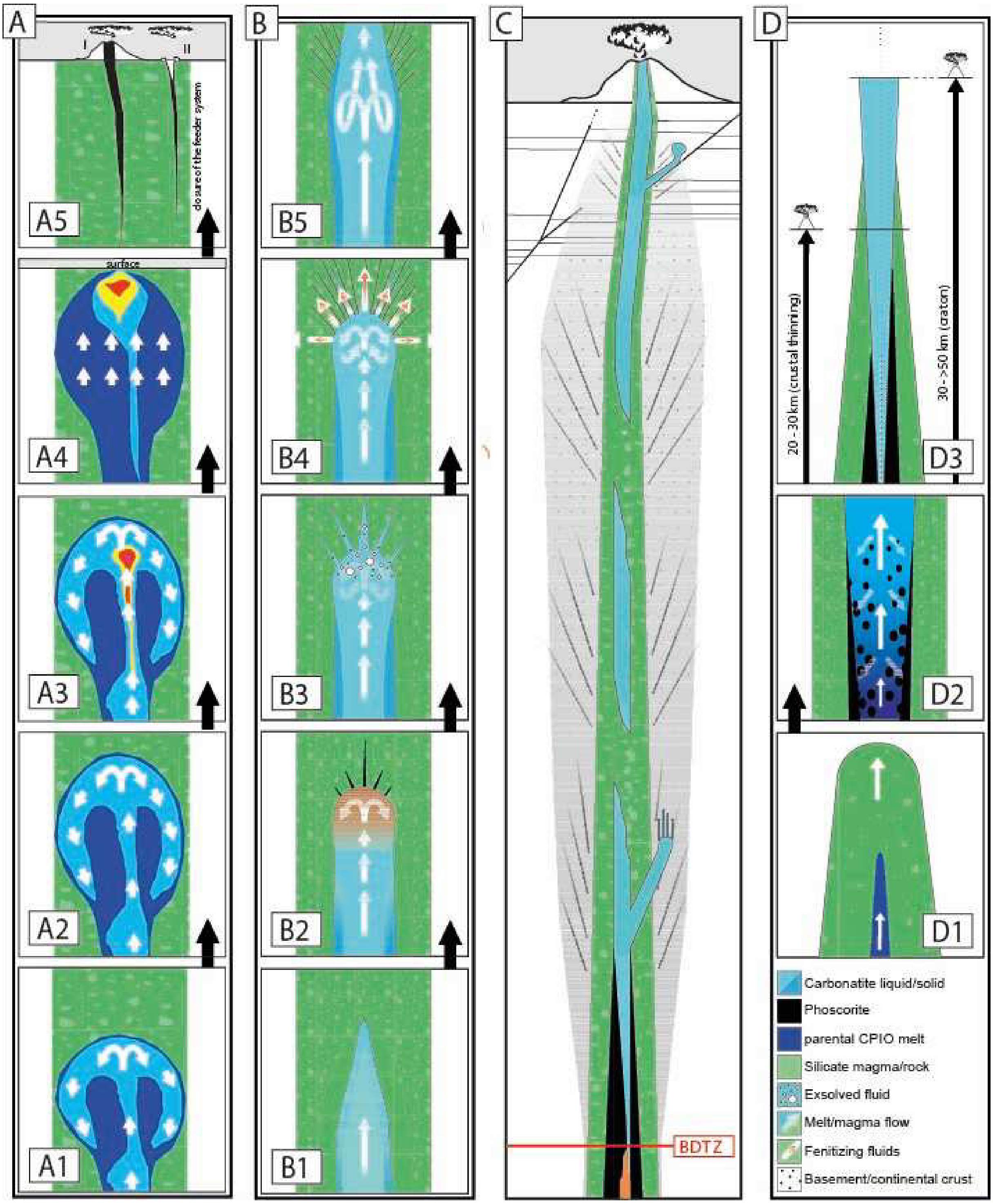

Figure 15. Refined "jackhammer" model adapted from Walter *et al.* (2021) with geometry add-on. (A) Ascent of mafic dykes, based on the model proposed by Kavanagh *et al.* (2018), is presented here as an analogue for carbonatite dyke emplacement. The schematic illustrates the rapid ascent of carbonatitic magmas. (B) Sequence of events constituting the fluid-exsolution-driven "jackhammer" mechanism: (B1) carbonatite magma reaches the terminus of the existing conduit system, forming a bottleneck; (B2) continued influx of ascending carbonatite magma leads to accumulation at the conduit end, generating fluid overpressure and inducing fracturing; (B3) expansion of fractures results in a sudden pressure drop, triggering exsolution of the fluid phase; (B4) consequently, fluids are forcefully injected into the surrounding country rock, promoting progressive expansion of fractures and cracks; (B5) this mechanism may lead to the reactivation of pre-existing fault zones, the breaching of the bottleneck, or the continued propagation of fractures until a new ascent pathway is established or the magma becomes stagnant. (C) Schematic representation of a carbonatite magma ascent

channel traversing the brittle-ductile transition zone (BDTZ): the illustration highlights varying crustal levels, with increased fracturing and enhanced fluid release at shallower depths, promoting intensive fenitisation of the overlying country rocks. The formation of phoscorite is constrained to deeper crustal levels due to its pressure-dependent nature. (D) Conceptual model for carbonatite magma ascent, modified after Giebel *et al.* (2019), which may serve as an initiation mechanism for the "jackhammer" process: (D1) a parental carbonatitic (CPIO) melt ascends along a pre-existing structural weakness utilised previously by an associated silicate magma; (D2) pressure-dependent separation of a phoscorite melt leads to a significant density contrast between the residual carbonatite magma and the exsolved phoscorite phase, resulting in jet-like ascent dynamics; (D3) conceptual depiction of characteristic rock association ratios corresponding to various emplacement levels: as magma differentiation is primarily governed by pressure, these conditions are expected to vary among continental crusts of different thickness. For comprehensive discussion of this model, refer to Giebel *et al.* (2019).

Geometry of carbonatites and their associated silicate rocks in the context of exploration

The analyses above may help to build new deposit models for mineral exploration. The model of Frolov (1971) implies a relationship between commodities and carbonatites reaching the surface and those getting stuck in the crust. His model defines a carbonatite pocket and brings the economic components into a depth relation. We consider it likely, that a carbonatite pocket on a km-scale vertical extension (depending on melt volume and pathways properties) contains apatite-rich rocks (Nolans Bore; Anenburg *et al.*, 2018) at its deepest part, representing early cumulates left behind by a transpassing carbonatite magma batch. Above this level, high alkaline silicate rock/carbonatite ratios (Giebel *et al.*, 2017) are expected, with enrichments in base metals such as copper (e. g. Palabora: Guide Copper mine, Otjisazu) or HFSE (High Field Strength elements) like Zr (e. g. Palabora, Kovdor). The upper parts of the carbonatite pocket, however, are strongly affected by fluid exsolution during ascent (Walter *et al.*, 2020, 2021, and references therein), whereas the jackhammer-like ascent of the pocket leads to crystallisation of Nb, Ta, Sr, Ba, REE-F phases and radionuclides (U and Th). Most of the relatively deep complexes within a hypothetical pocket are low in U and Th, whereas the shallower complexes (upper part of the pockets) often show an elevated radioactivity (Frolov, 1971; Walter *et al.*, 2021, and references therein). Ring dykes and radial dykes are often barren (e. g. Gross Brukkaros), but numerous complexes contain high-grade REE-Nb ores within such structures (e. g. Ondurakorume). This is most likely related to uncertainties defining a circular feature as either ring dyke or cone sheet, which also cannot be resolved by this compilation. If a carbonatite pocket reaches the surface and erupts, most of the volatiles are released and late-magmatic hydrothermal processes are prevented (Walter *et al.*, 2018, 2020, 2021, 2022, 2023; Raza *et al.*, 2025). Therefore, it is very important for mineral exploration to define the relative exhumation level within a carbonatite pocket in order to determine which parts of the pocket are already eroded, and what may be expected at higher levels.

Conclusions

The 3D architecture of a carbonatite complex is the result of external parameters, such as regional stress regime, and intrinsic factors like melt properties (e. g. density and viscosity). The characteristic properties of carbonatite magmas lead to a pocket-like geometry, and such magma pockets can transpass crustal levels very rapidly. The top of the ascending magma pocket is characterised by radial dykes and cone sheets, whereas ring dykes only occur in the volcanic context of caldera formation. The base of a transpassing melt batch is characterised by the closure of the pathway, and filter-pressed cumulates of early magmatic minerals such as apatite are left behind as relic schlieren and veins. The silicate rock/carbonatite ratio of a complex is a depth-related feature, with dominant ultramafic rocks occurring at higher levels. With decreasing depth, i. e. at higher levels, the carbonatite portion increases within a complex. Hence, the geomodel presented here provides a holistic view of the architecture of carbonatite complexes and can be used to identify mineralisation within an individual occurrence.

Acknowledgements

We are thankful to Aylin Polat and Kira Wolpers for their help with producing digital maps. Pete Siegfried, Andreja Ladisic, Saskia Dück, Mohsin Raza and Fadila Adamu are thankfully acknowledged for insightful discussions. Ute Schreiber and Axel Müller are kindly acknowledged for editorial guidance and constructive reviews. This study is supported by DFG (Deutsche Forschungsgemeinschaft) grants WA 3116/3-1, WA 3116/4-1 and WA 3116/15-1 to Benjamin Walter.

References

Andersen, T. 1987. A model for the evolution of hematite carbonatite, based on whole-rock major and trace element data from the Fen complex, southeast Norway. *Applied Geochemistry*, **2(2)**, 163-180.

Anenburg, M., Burnham, A. D. and Mavrogenes, J. A. 2018. REE redistribution textures in altered fluorapatite: symplectites, veins, and phosphate-silicate-carbonate assemblages from the Nolans Bore P-REE-Th Deposit, Northern Territory, Australia. *The Canadian Mineralogist*, **56(3)**, 331-354.

Arzamastsev, A. A., Glaznev, V. N., Raevsky, A. B. and Arzamastseva, L. V. 2000. Morphology and internal structure of the Kola Alkaline intrusions, NE Fennoscandian Shield: 3D density modelling and geological implications. *Journal of Asian Earth Sciences*, **18(2)**, 213-228.

Banks, G. J., Walter, B. F., Marks, M. A. and Siegfried, P. R. 2019. A workflow to define, map and name a carbonatite-or alkaline igneous-associated REE-HFSE mineral system: A case study from SW Germany. *Minerals*, **9(2)**, https://www.mdpi.com/2075-163X/9/2/97

Beard, C. D., Goodenough, K. M., Borst, A. M., Wall, F., Siegfried, P. R., Deady, E. A., Pohl, C., Hutchinson, W., Finch, A., Walter, B. F., Elliot, H. and Brauch, K. 2023. Alkaline-silicate REE-HFSE systems. *Economic Geology*, **118(1)**, 177-208.

Braunger, S., Marks, M. A. W., Walter, B. F., Neubauer, R., Reich, R., Wenzel, T., Parsapoor, A. and Markl, G. 2018. The petrology of the Kaiserstuhl Volcanic Complex, SW Germany: the importance of metasomatized and oxidized lithospheric mantle for carbonatite generation. *Journal of Petrology*, **59(9)**, 1731-1762.

Brett, R. C., Russell, J. K., Andrews, G. D. M. and Jones, T. J. 2015. The ascent of kimberlite: Insights from olivine. *Earth and Planetary Science Letters*, **424**, 119-131.

Broom-Fendley, S., Brady, A. E., Horstwood, M. S., Woolley, A. R., Mtegha, J., Wall, F., Dawes, W. and Gunn, G. 2017. Geology, geochemistry and geochronology of the Songwe Hill carbonatite, Malawi. *Journal of African Earth Sciences*, **134**, 10-23.

Broom-Fendley, S., Siegfried, P. R., Wall, F., O'Neill, M., Brooker, R. A., Fallon, E. K., Pickles, J. and Banks, D. A. 2021. The origin and composition of carbonatite-derived carbonate-bearing fluorapatite deposits. *Mineralium Deposita*, **56(5)**, 863-884.

Browne, B. and Szramek, L. 2015. Rates of magma ascent and storage, 203-214. *In*: H. Sigurdsson, (Ed.), *The Encyclopedia of volcanoes*. Academic Press, Cambridge, Mass., USA.

Bühn, B., Dörr, W. and Brauns, C. M. 2001. Petrology and age of the Otjisazu carbonatite complex, Namibia: implications for the pre-and synorogenic Damaran evolution. *Journal of African Earth Sciences*, **32(1)**, 1-17.

Burke, K., Ashwal, L. D. and Webb, S. J. 2003. New way to map old sutures using deformed alkaline rocks and carbonatites. Geology, **31(5)**, 391-394.

Campeny, M., Mangas, J., Melgarejo, J. C., Bambi, A., Alfonso, P., Gernon, T. and Manuel, J. 2014. The Catanda extrusive carbonatites (Kwanza Sul, Angola): an example of explosive carbonatitic volcanism. *Bulletin of Volcanology*, **76(4)**, 818.

Caricchi, L., Simpson, G. and Schaltegger, U. 2014. Zircons reveal magma fluxes in the Earth's crust. *Nature*, **511(7510)**, 457-461.

Caricchi, L., Simpson, G. and Schaltegger, U. 2016. Estimates of volume and magma input in crustal magmatic systems from zircon geochronology: the effect of modeling assumptions and system variables. *Frontiers in Earth Science*, **4**, https://doi.org/10.3389/feart.2016.00048

Casquet, C., Pankhurst, R. J., Galindo, C., Rapela, C., Fanning, C. M., Baldo, E., Dahlquist, J., Cascado, J. and Colombo, F. 2008. A deformed alkaline igneous rock–carbonatite complex from the Western Sierras Pampeanas, Argentina: Evidence for late Neoproterozoic opening of the Clymene Ocean? *Precambrian Research*, **165(3-4)**, 205-220.

Chakhmouradian, A. R., Reguir, E. P., Zaitsev, A. N., Coueslan, C., Xu, C., Kynický, J., Mumin, H. and Yang, P. 2017. Apatite in carbonatitic rocks: Compositional variation, zoning, element partitioning and petrogenetic significance. *Lithos*, **274**, 188-213.

Chandra, J., Paul, D., Stracke, A., Chabaux, F. and Granet, M. 2019. The origin of carbonatites from Amba Dongar within the Deccan large igneous province. *Journal of Petrology*, **60(6)**, 1119-1134.

Choudhuri, R. and Banerji, K. C. 1976. On the occurrence, emplacement and origin of the apatite deposits of Kasipatnam in Visakhapatnam district, Andhra Pradesh. *Proceedings of the Indian National Science Academy*, **42**, 387-406.

Corner, B. 2000. Crustal framework of Namibia derived from magnetic and gravity data. *Communications of the Geological Survey of Namibia*, **12**, 13-19.

Crisp, J. A. 1984. Rates of magma emplacement and volcanic output. *Journal of Volcanology and Geothermal Research*, **20(3-4)**, 177-211.

Dawson, J. B. 1962. The geology of Oldoinyo Lengai. *Bulletin Volcanologique*, **24(1)**, 349-387.

Drüppel, K., Wagner, T. and Boyce, A. J. 2006. Evolution of sulfide mineralization in ferrocarbonatite, Swartbooisdrif, Northwestern Namibia: constraints from mineral compositions and sulfur isotopes. *The Canadian Mineralogist*, **44(4)**, 877-894.

Edahbi, M., Plante, B., Benzaazoua, M., Kormos, L. and Pelletier, M. 2018. Rare earth elements (La, Ce, Pr, Nd, and Sm) from a carbonatite deposit: Mineralogical characterization and geochemical behavior. *Minerals*, **8(2)**, https://doi.org/10.3390/min8020055

Elliott H. A. L., Wall. F., Chakhmouradian A. R., Siegfried P. R., Dahlgren, S., Weatherley, S., Finch, A. A., Marks, M. A. W., Dowman, E. and Deady, E. 2018. Fenites associated with carbonatite complexes: A review. *Ore Geology Reviews*, **93**, 38–59

Emeleus, C. H., Bell, B. R. and MacGregor, A. G. 2005. *The Palaeogene volcanic districts of Scotland*, **3**. British Geological Survey, Nottingham, UK, 212 pp.

England, R. W. 1988. The early Tertiary stress regime in NW Britain: evidence from the patterns of volcanic activity, 381-389. *In*: A. C. Morton and L. M. Parson (Eds), Early Tertiary Volcanism and the Opening of the NE Atlantic. *Geological Society Special Publications*, **39**, The Geological Society of London, UK.

Epshteyn, Y. M. and Kaban'kov, V. Y. 1984. The depth of emplacement and mineral potential of ultramafic, ijolite, and carbonatite plutons. *International Geology Review*, **26(12)**, 1402-1415.

Eriksson, S. C. 1982. Kimberlites and associated alkaline magmatism, 424-432. *In*: A. J. Tankard, K. A. Eriksson, D. R. Hunter, M. P. A. Jackson, D. K. Hobday and W. E. L. Minter (Eds), *Crustal Evolution of Southern Africa: 3.8 Billion Years of Earth History*. Springer, New York, 524 pp.

Ernst, R. E. and Bell, K. 2010. Large igneous provinces (LIPs) and carbonatites. *Mineralogy and Petrology*, **98(1)**, 55-76.

Frolov, A. A. 1971. Vertical zonation in deposition of ore, as in ultrabasic-alkaline rocks and carbonatites. *International Geology Review*, **13(5)**, 685-695.

Genge, M. J., Price, G. D. and Jones, A. P. 1995. Molecular dynamics simulations of $CaCO_3$-melts to mantle pressures and temperatures: implications for carbonatite magmas. *Earth and Planetary Science Letters*, **131(3-4)**, 225-238.

Giebel, R. J., Gauert, C. D., Marks, M. A., Costin, G. and Markl, G. 2017. Multi-stage formation of REE minerals in the Palabora Carbonatite Complex, South Africa. *American Mineralogist*, **102(6)**, 1218-1233.

Giebel, R. J., Parsapoor, A., Walter, B. F., Braunger, S., Marks, M. A., Wenzel, T. and Markl, G. 2019. Evidence for magma–wall rock interaction in carbonatites from the Kaiserstuhl Volcanic Complex (Southwest Germany). *Journal of Petrology***, 60(6)**, 1163-1194.

Giebel, R. J., Marks, M. A. W., Gauert, C. D. K. and Markl, G. 2019a. A model for the formation of carbonatite-phoscorite assemblages based on the compositional variations of mica and apatite from the Palabora Carbonatite Complex, South Africa. *Lithos*, **324-325**, 89-114.

Goodenough, K. M., Deady, E. A., Beard, C. D., Broom-Fendley, S., Elliott, H. A., Van Den Berg, F. and Öztürk, H. 2021. Carbonatites and alkaline igneous rocks in post-collisional settings: storehouses of rare earth elements. *Journal of Earth Science*, **32(6)**, 1332-1358.

Gudelius, D., Marks, M. W., Markl, G., Nielsen, T. F., Kolb, J. and Walter, B. 2023. The origin of ultramafic complexes with melilitolites and carbonatites: a petrological comparison of the Gardiner (E Greenland) and Kovdor (Russia) intrusions. *Journal of Petrology*, **64(6)**, https://doi.org/10.1093/petrology/egad036

Gudmundsson, A. 2002. Emplacement and arrest of sheets and dykes in central volcanoes. *Journal of Volcanology and Geothermal Research*, **116(3-4)**, 279-298.

Hawkesworth, C. J., Cawood, P. A. and Dhuime, B. 2016. Tectonics and crustal evolution. *GSA Today*, **26(9),** 4-11.

Hay, R. L. and O'Neil, J. R. 1983. Carbonatite tuffs in the Laetolil Beds of Tanzania and the Kaiserstuhl in Germany. *Contributions to Mineralogy and Petrology*, **82(4)**, 403-406.

Humphreys-Williams, E. R. and Zahirovic, S. 2021. Carbonatites and global tectonics. *Elements*, **17(5)**, 339-344.

Hurai, V., Blažeková, M., Huraiová, M., Siegfried, P. R., Slobodník, M. and Konečný, P. 2021. Thermobarometric and geochronologic constraints on the emplacement of the Neoproterozoic Evate carbonatite during exhumation of the Monapo granulite complex, Mozambique. *Lithos*, **380**, https://doi.org/10.1016/j.lithos.2020.105883

Ilyinskaya, E., Schmidt, A., Mather, T. A., Pope, F. D., Witham, C., Baxter, P., Johannsson, T., Pfeffer, M., Barsotti, S., Singh, A., Sanderson, P., Bergsson, B., MacCormmick-Kilbride, B., Donovan, A., Peters, N., Oppenheimer, C. and Edmonds, M. 2017. Understanding the environmental impacts of large fissure eruptions: Aerosol and gas emissions from the 2014–2015 Holuhraun eruption (Iceland). *Earth and Planetary Science Letters*, **472**, 309-322.

Jones, A. P., Genge, M. and Carmody, L. 2013. Carbonate melts and carbonatites. *Reviews in Mineralogy and Geochemistry*, **75(1)**, 289-322.

Kavanagh, J. L., Burns, A. J., Hazim, S. H., Wood, E. P., Martin, S. A., Hignett, S. and Dennis, D. J. 2018. Challenging dyke ascent models using novel laboratory experiments: Implications for reinterpreting evidence of magma ascent and volcanism. *Journal of Volcanology and Geothermal Research*, **354**, 87-101.

Keller, J. and Krafft, M. 1990. Effusive natrocarbonatite activity of Oldoinyo Lengai, June 1988. *Bulletin of Volcanology*, **52(8)**, 629-645.

Khan, A., Faisal, S., Ullah, Z., Ali, L., Ghaffari, A., Nawab, J. and Rashid, M. U. 2021. Pyrochlore-group minerals from the Loe-Shilman Carbonatite Complex, NW Pakistan: implications for evolution of carbonatite system. *Periodico di Mineralogia*, **90(2)**, 277-287.

Kogarko, L. N., Konova, V. A., Orlova, M. P. and Woolley, A. R. 1995. *Alkaline Rocks and Carbonatites of the World - Part Two: Former USSR*. Springer, Dordrecht, Netherlands, 226 pp.

Kono, Y., Kenney-Benson, C., Hummer, D., Ohfuji, H., Park, C., Shen, G., Wang, Y., Kavner, A. and Manning, C. E. 2014. Ultralow viscosity of carbonate melts at high pressures. *Nature communications*, **5(1)**, https://doi.org/10.1038/ncomms6091

Ladisic, A., Marks, M. A., Walter, B. F., Giebel, R. J., Beranoaguirre, A. and Markl, G. 2025. Permo-Triassic magmatism in the Damaraland Igneous Province, NW Namibia: The Ondurakorume alkaline-carbonatite complex. *Geochemistry*, **85(3)**, https://doi.org/10.1016/j.chemer.2025.126287

Le Bas, M. J. 1987. Nephelinites and carbonatites, 53-83. *In*: J. G. Fitton and B. G. J. Upton (Eds), Alkaline Igneous Rocks. *Geological Society Special Publications*, **30**, The Geological Society of London, UK.

Magee, C., Jackson, C. A. L. and Schofield, N. 2013. The influence of normal fault geometry on igneous sill emplacement and morphology. *Geology*, **41(4)**, 407-410.

Matton, G. and Jébrak, M. 2014. The "Eye of Africa" (Richat dome, Mauritania): An isolated Cretaceous alkaline–hydrothermal complex. *Journal of African Earth Sciences*, **97**, 109-124.

Mariano, A. N. 1989. Cathodoluminescence emission spectra of rare earth element activators in minerals. In. Geochemistry and mineralogy of Rare Earth Elements. *Reviews in Mineralog*y, **21**, 339-348.

Millonig, L. J., Gerdes, A. and Groat, L. A. 2012. U–Th–Pb geochronology of meta-carbonatites and meta-alkaline rocks in the southern Canadian Cordillera: a geodynamic perspective. *Lithos*, **152**, 202-217.

Mitchell, R. H. 2005. Carbonatites and carbonatites and carbonatites. *The Canadian Mineralogist*, **43(6)**, 2049-2068.

Mitchell, R., Chudy, T., McFarlane, C. R. and Wu, F. Y. 2017. Trace element and isotopic composition of apatite in carbonatites from the Blue River area (British Columbia, Canada) and mineralogy of associated silicate rocks. *Lithos*, **286**, 75-91.

Nash, W. P. 1972. Apatite-calcite equilibria in carbonatites: chemistry of apatite from Iron Hill, Colorado. *Geochimica et Cosmochimica Acta*, **36(12)**, 1313-1319.

O'Driscoll, B., Troll, V. R., Reavy, R. J. and Turner, P. 2006. The Great Eucrite intrusion of Ardnamurchan, Scotland: Re-evaluating the ring-dike concept. *Geology*, **34(3)**, 189-192.

Panda, N. K., Rao, A. Y., Kumar, K. R., Mohanty, R. and Parihar, P. S. 2015. Anomalous REE concentration in carbonate–phosphate bearing phases from Narasimharajapuram area, Visakhapatnam district, Andhra Pradesh. *Current Science*, **109(5)**, 860-862.

Pandur, K., Ansdell, K. M. and Kontak, D. J. 2015. Graphic-textured inclusions in apatite: Evidence for pegmatitic growth in a REE-enriched carbonatitic system. *Geology*, **43(6)**, 547-550.

Paul, D., Chandra, J. an Halder, M. 2020. Proterozoic alkaline rocks and carbonatites of Peninsular India: a review. *Episodes*, **43(1)**, 249-277.

Petrovsky, M. N., Savchenko, E. A. and Kalachev, V. Y. 2012. Formation of eudialyte-bearing phonolite from Kontozero carbonatite paleovolcano, Kola Peninsula. *Geology of Ore Deposits*, **54(7),** 540-556.

Plant, J. A., Whittaker, A., Demetriades, A., De Vivo, B. and Lexa, J. 2005. The geological and tectonic framework of Europe. *In*: *Geochemical Atlas of Europe*, **Part 1**. Geological Survey of Finland, Espoo, http://weppi.gtk.fi/publ/foregsatlas/article.php?id=4

Putirka, K. D. 2017. Down the crater: where magmas are stored and why they erupt. *Elements*, **13(1)**, 11-16.

Rao, A. T. 1976. Study of the apatite-magnetite veins near Kasipatnam, Visakhapatnam district, Andhra Pradesh, India. *Tschermaks mineralogische und petrographische Mitteilungen*, **23(2)**, 87-103.

Rapprich, V., Walter, B. F., Kopačková-Strnadová, V., Kluge, T., Čejková, B., Pour, O., Hora, J., Kynicky, J. and Magna, T. 2024. Gravitational collapse of a volcano edifice as a trigger for explosive carbonatite eruption? *GSA Bulletin*, **136(5-6)**, 2291-2304.

Raza, M., Giebel, R. J., Staude, S., Beranoaguirre, A., Kolb, J., Markl, G. and Walter, B. F. 2025. The magmatic to post-magmatic evolution of the Nooitgedacht Carbonatite Complex, South Africa. *Geochemistry*, **85(1),** https://doi.org/10.1016/j.chemer. 2025.126249

Reid, D. L., Cooper, A. F., Rex, D. C. and Harmer, R. E. 1990. Timing of post–Karoo alkaline volcanism in southern Namibia. *Geological Magazine*, **127(5)**, 427-433.

Rosatelli, G., Wall, F. and Stoppa, F. 2007. Calcio-carbonatite melts and metasomatism in the mantle beneath Mt. Vulture (Southern Italy). *Lithos*, **99(3-4)**, 229-248.

Samson, I. M., Liu, W. and Williams-Jones, A. E. 1995. The nature of orthomagmatic hydrothermal fluids in the Oka carbonatite, Quebec, Canada: Evidence from fluid inclusions. *Geochimica et Cosmochimica Acta*, **59(10)**, 1963-1977.

Schmidt, M. W., Giuliani, A. and Poli, S. 2024. The origin of carbonatites—combining the rock record with available experimental constraints. *Journal of Petrology*, **65(10)**, https://doi.org/10.1093/petrology/egae105

Scogings, A. J. and Forster, I. 1989. Gneissose carbonatites in the Bull's Run complex, Natal. *South African Journal of Geology*, **92(1)**, 1-10.

Shu, X. and Liu, Y. 2019. Fluid inclusion constraints on the hydrothermal evolution of the Dalucao Carbonatite-related REE deposit, Sichuan Province, China. *Ore Geology Reviews*, **107**, 41-57.

Simandl, G. J. and Paradis, S. 2018. Carbonatites: related ore deposits, resources, foot-print, and exploration methods. *Applied Earth Science*, **127(4)**, 123-152.

Sparks, R. S. J., Brooker, R. A., Field, M., Kavanagh, J., Schumacher, J. C., Walter, M. J. and White, J. 2009. The nature of erupting kimberlite melts. *Lithos*, **112**, 429-438.

Stoppa, F. and Woolley, A. R. 1997. The Italian carbonatites: field occurrence, petrology and regional significance. *Mineralogy and Petrology*, **59(1)**, 43-67.

Stoppa, F., Pirajno, F., Schiazza, M. and Vladykin, N. V. 2016. State of the art: Italian carbonatites and their potential for critical-metal deposits. *Gondwana Research*, **37**, 152-171.

Tappe, S., Beard, C. D., Borst, A. M., Humphreys-Williams, E. R., Walter, B. F. and Yaxley, G. M. 2025. Kimberlite, carbonatite and alkaline magmatic systems: definitions, origins, and strategic mineral resources. EarthArXiv Preprints, https://eartharxiv.org/repository/view/8658/

Vartiainen, H. and Paarma, H. 1979. Geological characteristics of the Sokli carbonatite complex, Finland. *Economic Geology*, **74(5)**, 1296-1306.

Vasyukova, O. V. and Williams-Jones, A. E. 2022. Carbonatite metasomatism, the key to unlocking the carbonatite-phoscorite-ultramafic rock paradox. *Chemical Geology*, **602**, https://doi.org/10.1016/j.chemgeo.2022.120888

Verwoerd, W. J. 1967. The carbonatites of South Africa and South West Africa. *Handbook of the Geological Survey of South Africa*, **6**, Government Printer, Pretoria, South Africa, 452 pp.

Von Knorring, O. And Du Bois, C. G. B. 1961. Carbonatitic lava from Fort Portal area in western Uganda. *Nature*, **192(4807)**, 1064-1065.

Walter, B. F., Parsapoor, A., Braunger, S., Marks, M. A. W., Wenzel, T., Martin, M. and Markl, G. 2018. Pyrochlore as a monitor for magmatic and hydrothermal processes in carbonatites from the Kaiserstuhl volcanic complex (SW Germany). *Chemical Geology*, **498**, 1-16.

Walter, B. F., Steele-MacInnis, M., Giebel, R. J., Marks, M. A. and Markl, G. 2020. Complex carbonate-sulfate brines in fluid inclusions from carbonatites: Estimating compositions in the system H_2O-Na-K-CO_3-SO_4-Cl. *Geochimica et Cosmochimica Acta*, **277**, 224-242.

Walter, B. F., Giebel, R. J., Steele-MacInnis, M., Marks, M. A., Kolb, J. and Markl, G. 2021. Fluids associated with carbonatitic magmatism: A critical review and implications for carbonatite magma ascent. *Earth-Science Reviews*, **215**, https://doi.org/10.1016/j.earscirev. 2021.103509

Walter, B. F., Giebel, J., Marlow, A. G., Siegfried, P. R., Marks, M., Markl, G., Palmer, M. and Kolb, J. 2022. The Keishöhe carbonatites of southwestern Namibia–the post-magmatic role of silicate xenoliths on REE mobilisation. *Communications of the Geological Survey of Namibia*, **25**, 1-31.

Walter, B. F., Giebel, R. J., Siegfried, P. R., Gudelius, D. and Kolb, J. 2023. The eruption interface between carbonatitic dykes and diatremes – The Gross Brukkaros volcanic field Namibia. *Chemical Geology*, **621**, https://doi.org/10.1016/j.chemgeo. 2023.121344

Wimmenauer, W. 2003. Geologische Karte von Baden-Württemberg, 1: 25.000 – Erläuterungen zum Blatt Kaiserstuhl. Landesamt für Geologie, Rohstoffe und Bergbau Baden-Württemberg, Freiburg im Breisgau, Germany, 280 pp.

Wooley, A. R. 1987. *Alkaline rocks and carbonatites of the World. 1. North and South America.* Chapman & Hall, London, UK, 141 pp.

Woolley, A. R. 2001. *Alkaline Rocks and Carbonatites of the World. Part 3: Africa.* The Geological Society of London., UK, 384 pp.

Woolley, A. R. 2019. *Alkaline rocks and carbonatites of the world, Part 4: Antarctica, Asia and Europe (excluding the former USSR), Australasia and Oceanic Islands.* The Geological Society of London, UK, 562 pp.

Woolley, A. R. and Church, A. A. 2005. Extrusive carbonatites: a brief review. *Lithos*, **85(1-4)**, 1-14.

Woolley, A. R. and Kjarsgaard, B. A. 2008. Paragenetic types of carbonatite as indicated by the diversity and relative abundances of associated silicate rocks: evidence from a global database. *The Canadian Mineralogist*, **46(4)**, 741-752.

Yaxley, G. M., Kjarsgaard, B. A. and Jaques, A. L. 2021. Evolution of carbonatite magmas in the upper mantle and crust. *Elements*, **17(5)**, 315-320.

Yaxley, G. M., Anenburg, M., Tappe, S., Decree, S. and Guzmics, T. 2022. Carbonatites: classification, sources, evolution, and emplacement. *Annual Review of Earth and Planetary Sciences*, **50(1)**, 261-293.

*Communications of the Geological Survey of Namibia, **29** (2026), 72-89*

Phengite formation at the contact between carbonatites and muscovite-kyanite schists: Kwaggaspan, northwestern Namibia

Roxanne Steffann[1,2], Benjamin F. Walter[2*], R. Johannes Giebel[3,4], Michael A. W. Marks[2], Andreja Ladisic[2], Lorenz Kemmler[2], Nicolas Schlosser[2], Thomas Binder[2], Felix Reinhard[2], Lukas Mössinger[2], Pascal Löschner[2], Saskia Dück[3] and Gregor Markl[2]

[1] University of Poitiers, Geoscience Department, 6 Rue Michel Brunet - Bât B35, 86073 Poitiers, France
[2] University of Tübingen, Petrology and Mineral Resources, Schnarrenbergstrasse 94-96, 72076 Tübingen, Germany
[3] Technische Universität Berlin, Angewandte Geochemie, Ernst Reuter Platz 1, 10587 Berlin, Germany
[4] University of the Free State, Department of Geology, 250 Nelson-Mandela-Drive, Bloemfontein 9300, South Africa

**Corresponding author: <b.walter@uni-tuebingen.de>*

Abstract :- This study investigates the previously unexamined Kwaggaspan Carbonatite Complex in northwestern Namibia, which intruded into muscovite-kyanite schist and quartzite of the Neoproterozoic Damara Supergroup, providing an ideal natural laboratory for examining the interaction between carbonatitic melts and SiO_2- and Al_2O_3-rich country rocks. A multi-analytical approach is employed, integrating petrographic analysis of thin sections, cathodoluminescence (CL) imaging, micro-X-ray fluorescence (µXRF) mapping, and electron microprobe analysis (EMPA).

Field and petrographic observations reveal that the Kuiseb Formation host schist has been metasomatically altered to quartz-phengite-magnetite rock during interaction with carbothermal brines. The formation of phengite highlights the so far undocumented interaction between a carbonatite melt and carbothermal brine, and a particularly Al-rich country rock. Chemical analyses of three distinct mica generations (F-bearing hydroxy-phlogopite, Fluoro-phlogopit and F-bearing phengite) record progressive alteration, driven by the influx of Al and Si from the surrounding country rock. The carbonatites display a well-defined crystallisation sequence, beginning with two generations of Fe-rich dolomite, followed by two generations of calcite. Metasomatic overprinting of the host rocks produced secondary mineral assemblages with baryte, monazite, pyrite, celestine, strontianite, and clinochlore. Supergene processes during later stages of alteration led to the pervasive development of Fe-oxides and natrojarosite throughout the system.

Keywords :- Carbonatite – country rock interaction, Muscovite-kyanite schist, Phengite, Al-contamination, Brine melt

Introduction

Carbonatites are igneous rocks with >25 vol.% primary carbonates (Tappe *et al.*, 2025) and represent the most silica-poor magmas known (Mitchell, 2005; Woolley and Kjarsgaard, 2008; Jones *et al.*, 2013; Schmidt *et al.*; 2024; Tappe *et al.*, 2025). With about 600 occurrences worldwide, carbonatites include extrusive, intrusive, and carbothermal varieties (Mitchell, 2005), and are classified as calcite-, dolomite-, ankerite- or siderite carbonatites, as well as rare nyerereite carbonatites (Yaxley *et al.*, 2022; Schmidt *et al.*, 2024).

Interactions between diverse silicate country rocks and carbonatite magmas, and the associated possible reactions and interactions driven by the compositional gradients between magma and host rock remain poorly understood (Vasyukova and Williams-Jones, 2022; Anenburg and Walters, 2024). However, during such processes new lithologies may form at the interface between carbonatitic magma and the host rock, generating a progressive reaction front that affects both the country rock (via metasomatic replacement) and the carbonatite magma (Anenburg and Walters, 2024; Giebel *et al.*, 2019; Gudelius *et al.*, 2023; Vasyukova and Williams-Jones, 2022; Walter *et al.*, 2023).

During differentiation and interaction, carbonatitic magma can gradually evolve towards a carbothermal or brine melt stage, characterised by transitional fluid phases exhibiting properties intermediate between aqueous saline fluids and carbonate melts (e. g. Mitchell and Gittins, 2022; Anenburg and Walters, 2024). These solvent-rich fluids can mobilise high-field-strength (HFSE) and large-ion lithophile elements (LILE), including rare-earth elements (REE), Nb, Zr, Ti, Ta, U and Th. Such fluids are frequently associated with magmatic differentiation processes involving liquid immiscibility and exsolution, leading to separation of discrete melt and fluid phases (Walter *et al*., 2020, 2021; Ladisic *et al*., 2025; Raza *et al*., 2025).

The Kwaggaspan Carbonatite Complex in northwestern Namibia, which intruded into the Neoproterozoic Kuiseb schist (muscovite-kyanite schist; Fig. 1), presents a unique opportunity to investigate carbonatitic melt – country rock interaction processes, owing to the specific characteristics of both the host lithologies and the melts. Such metasedimentary rocks provide a valuable natural laboratory for constraining the physico-chemical reactions that may occur when high-temperature carbonatitic melts infiltrate and interact with metapelitic or quartz-rich protoliths (Walter *et al*., 2022, 2023), which is the scope of this contribution. In this context, as detailed below, the host rocks are identified as metapelites and metasandstones notably rich in Al_2O_3 and SiO_2, which exhibit extremely low solubility in carbonatitic melts (Vasyukova and Williams-Jones, 2022; Anenburg and Guzmics, 2023). Emphasis is placed on delineating the processes at the carbonatite – muscovite-kyanite schist/quartzite interface.

Geological setting

The Kwaggaspan Carbonatite Complex is situated some 55 km southeast of the town of Khorixas in the Erongo Region (northwestern Namibia; Fig. 1), which hosts several alkaline and carbonatitic complexes (Harris, 1995; Miller, 2008; Sun *et al*., 2024; Ladisic *et al*., 2025 and references therein). It forms intrusive plugs and dykes within the Neoproterozoic Kuiseb schist (Miller, 2008), which experienced greenschist facies metamorphism and has an estimated stratigraphic thickness of around ten kilometres. The formation is predominantly composed of muscovite-kyanite schist, with intercalated layers of quartzite and dolomite marble. The muscovite-kyanite schist is dominated by quartz, followed by alkali feldspar and muscovite, commonly accompanied by chlorite, kyanite and biotite (Miller, 2008). Deformation and faulting occurred in Pan-African time (535±13 Ma; Goscombe *et al*., 2003).

The five plugs comprising the Kwaggaspan Complex are aligned along a large-scale fold axis; two of them are rich in quartz, hematite, and muscovite, a further two are composed of fine-grained quartz and Fe-rich oxides and the remaining one is a coarse-grained dolomite-calcite carbonatite (Miller, 2008). The latter shows a well-defined outline and has a diameter of about 140 m. The other plugs, however, display a range of carbonatite-wall rock interaction zones, causing transgressive contacts with the country rocks. Coordinates of each sampling location are provided in Table 1.

Sample Name	Latitude (°)	Longitude (°)	Elevation (metres above sea level)
KWG001	-20.780866	15.272881	932
KWG002	-20.781063	15.273947	933
KWG003	-20.785562	15.278503	920
KWG004	-20.785574	15.278862	923

Table 1. Locations of the investigated samples

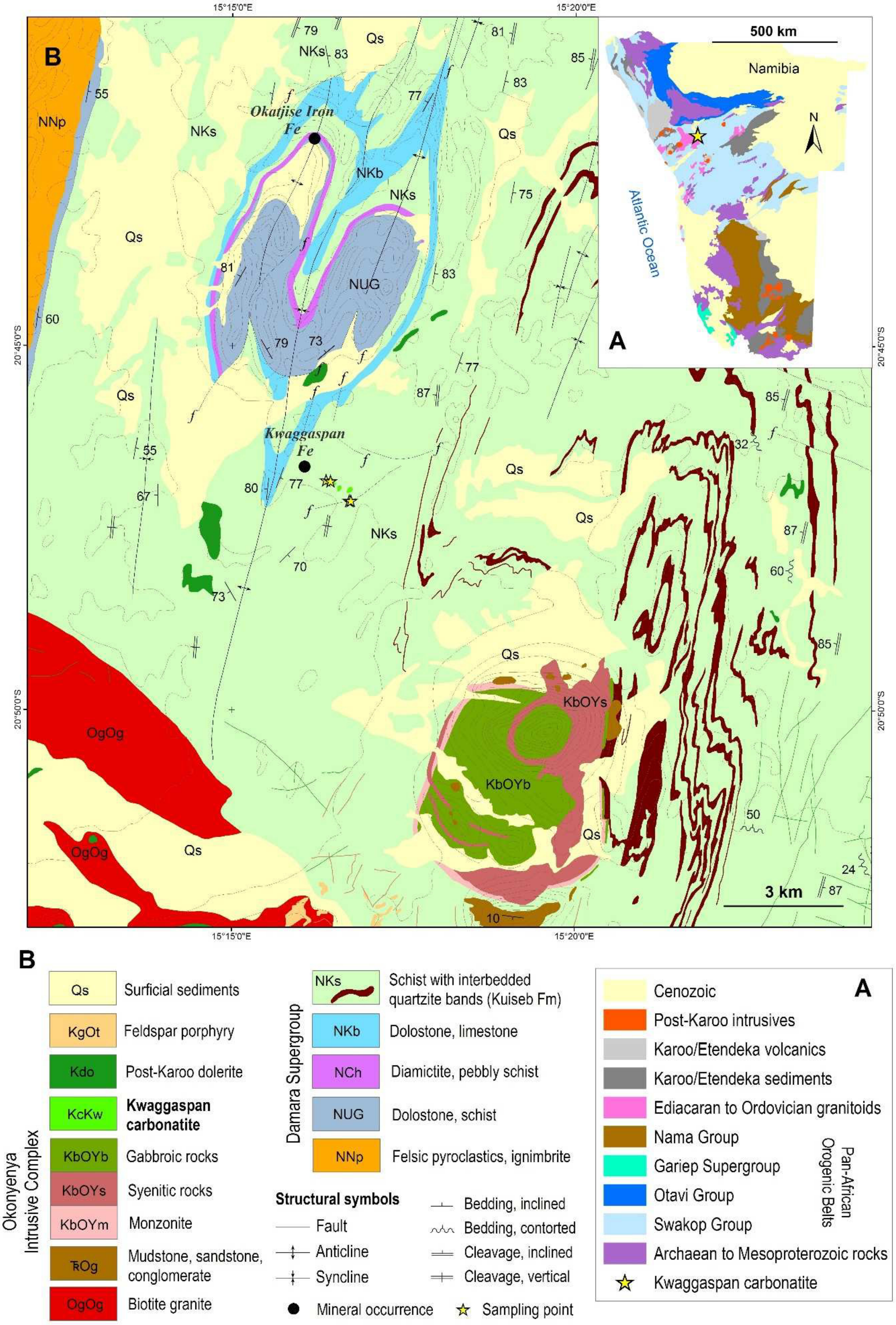

Figure 1. A) Simplified geological map of Namibia after Walter *et al*. (2023); B) Regional geological map showing the location of the Kwaggaspan carbonatites (modified after Geological Survey of Namibia, 2006)

Analytical methods

Thin sections of eleven representative samples from four locations were examined by transmitted and reflected light microscopy. Cathodoluminescence (CL) microscopy using a *Lumic HC6-LM* was performed with a vacuum pressure of 1 Pa, an accelerating voltage of 14 kV and a current of 0.4 mA. Scanning electron microscopy (SEM) was conducted with a *Phenom Tabletop SEM* in low vacuum mode (15 Pa), operating at 15 kV and 10 nA, with a working distance of 7 mm. Three selected polished specimens were analysed using a Bruker *Tornado Micro-X-Ray* system, and run with 50 kV accelerating voltage, 600 nA current, 20 µm beam diameter and 15 or 20 ms exposure time per pixel.

In addition, four thin sections were chosen for mineral chemistry analysis by electron microprobe (EMPA). Two are pure carbonatites and two represent the contact between host rock and carbonatite. The compositional data for micas and carbonates were obtained from an electron probe microanalyser JEOL JXA-8230, using albite (Na and Al), diopside (Mg and Si), sanidine (K), Cr metal (Cr), bustamite (Mn), $SrTiO_3$ (Sr and Ti), hematite (Fe), cryolite (F), tugtupite (Cl), LREE glasses (La, Ce, Pr and Nd), baryte (Ba) and calcite (C and Ca) as standards. Carbon was measured for matrix effects; however, due to carbon coating the content was calculated based on stoichiometric values. An acceleration voltage of 15 kV, a beam current of 20 nA and an electron beam diameter of 10 µm was used. The internal φ(ρz) correction was applied for data reduction. Peak counting times were 16 s for major elements and 30 s for minor elements, with background counting times being half that of peak times. Further details are given in Tables 2 and 3.

Element	Crystal	X-ray emission line	Standard	Peak counting time (s)	Average detection limit (ppm)
Na	TAPL	K_α	Albite	16	200
K	PTEJ	K_α	Sanidine	16	300
Mg	TAP	K_α	Diopside	16	250
Si	TAP	K_α	Diopside	30	250
Sr	PETL	L_α	$SrTiO_3$	16	500
Ba	LIFL	L_α	Baryte	30	700
La	LIFL	L_α	REE	30	850
Pr	LIFL	L_α	REE	30	900
Nd	LIFL	L_α	REE	30	700
Ca	PETJ	K_α	Calcite	16	400
Mn	PETJ	K_α	Bustamite	16	550
Fe	LIF	K_α	Hematite	16	500
Ce	LIF	L_α	REE	30	1400
C	LDE6H	K_α	Calcite	16	700

Table 2. EMPA programme parameters for carbonates

Element	Crystal	X-ray emission line	Standard	Peak counting time (s)	Average detection limit (ppm)
F	LDE1L	K_α	Cryolite	30	250
K	PTEJ	K_α	Sanidine	16	300
Mg	TAP	K_α	Diopside	16	250
Si	TAP	K_α	Diopside	16	200
Al	TAPL	K_α	Albite	16	150
Ba	PETL	L_α	Baryte	30	400
Na	TAP	K_α	Albite	30	200
Ti	PETL	K_α	$SrTiO_3$	30	200
Ca	PETL	K_α	Diopside	16	200
Mn	PETJ	K_α	Bustamite	30	450
Fe	LIF	K_α	Hematite	16	550
Cr	LIF	L_α	Cr	30	400
Cl	PETL	K_α	Tugtupite	30	75

Table 3. EPMA programme parameters for micas

Results

Petrography

A summary of the mineralogical composition of the investigated samples covering carbonatites and variably overprinted country rocks is provided in Table 4. The typical pelitic Kuiseb schist (sample KWG001B3; Figs 2a, b) mainly consists of micas, primarily muscovite I (and minor phlogopite) along with kyanite. The presence of both muscovite and kyanite underscores the high Al and Si content of the Kwaggaspan carbonatite host rocks. A holistic description of the Kuiseb schist is provided by Miller (2008).

<table>
<tr><th colspan="11">SAMPLE</th></tr>
<tr><td>KWG003B</td><td>KWG004A</td><td>KWG001B9</td><td>KWG001A1</td><td>KWG001A2</td><td>KWG001B4</td><td>KWG001A</td><td>KWG001B3</td><td>KWG001B1</td><td>KWG003A1</td><td>KWG003A2</td></tr>
<tr><th colspan="11">LITHOLOGY</th></tr>
<tr><td colspan="2">carbonatite</td><td>carbonatite hosted basement xenolith</td><td>contact zone</td><td colspan="7">overprinted country rock (muscovite kyanite schist)</td></tr>
<tr><th colspan="11">MINERALOGY</th></tr>
<tr><td>mag, phl, dol, cal, hem/goe</td><td>mag, phl, dol, cal, clc/chl, py, mnz</td><td>Kfs, qtz, mag, Fphl-bt, cal, brt, hem/goe</td><td>Kfs, qtz, mag, phen, dol, cal, brt, hem/goe</td><td>Kfs, qtz, ms, mag, brt</td><td>qtz, ms, mag, brt, hem/goe</td><td>qtz, ms, mag, cal, brt, hem/goe</td><td>Kfs, zrn, qtz, ms, mag, cal, kya hem/goe</td><td>qtz, ms, mag, brt, clt, str, mnz, hem/goe</td><td>qtz, ms, mag, mnz, njrs, hem/goe</td><td>qtz, ms, mag, njrs</td></tr>
</table>

Table 4. Modal mineralogy of each sample: a quantification of celestine and strontianite was not possible in all samples. Mineral abbreviations based on Warr (2021): brt – baryte, cal – calcite, clc – clinochlore, clt – celestine, dol – dolomite, hem – hematite, Kfs – K-feldspar, kya – kyanite, mnz – monazite, ms – muscovite, mt – magnetite, njrs – natrojarosite, phl – phlogopite, py – pyrite, qz – quartz, phen – phengite, str – strontianite, zrn – zircon.

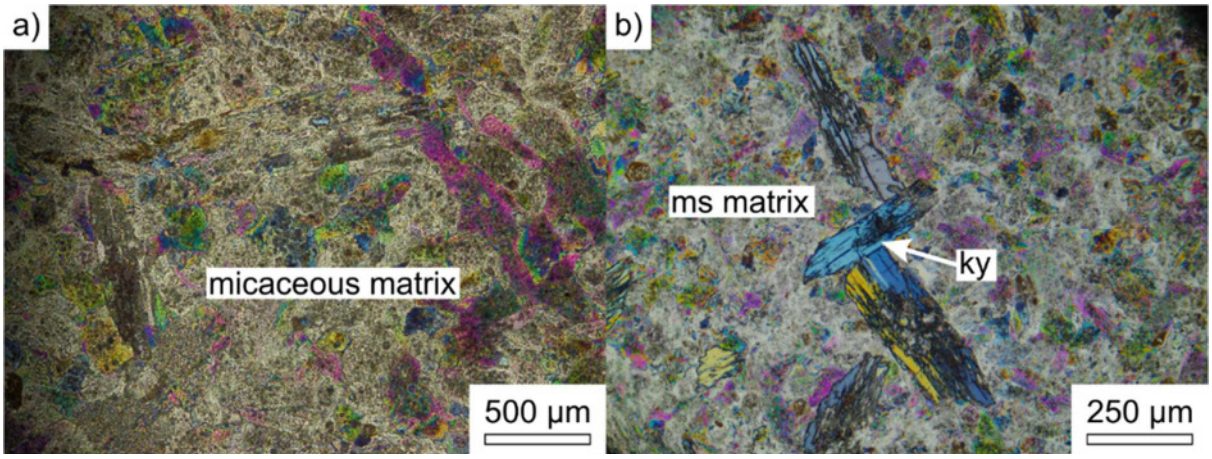

Figure 2. Thin section of sample KWG001B3 under polarised light: a) micaceous matrix with oriented kyanite relics; b) oriented kyanite phenocrysts aligned along foliation within a matrix of muscovite

Carbonatite

Carbonatites (samples KWG003B and KWG004) are composed predominantly of dolomite, which appears as two distinct generations (Fig. 3a, b). The first generation (dolomite I) is anhedral and partly altered to Fe-oxides (often along cleavages). The second generation (dolomite II) overgrows the earlier one, is euhedral and occurs adjacent to minor calcite, which is altered to a dark-brown to black halo of Fe-oxides. Similarly, two generations of calcite (I and II) are observed. Calcite I forms elongated crystals with well-defined chemical zoning, while calcite II is less abundant, finer-grained, and typically lacks the well-defined zoning observed in calcite I (Fig. 3c). Phlogopite occurs frequently and forms platy aggregates. Apatite is small in grain size and very rare. Also, magnetite is scarce in the carbonatites.

Contact zone between carbonatite and country rocks

Very close to the country rock (within a zone of 1-8 cm), xenocrysts of feldspar and quartz are entrained in the carbonatite (e. g. sample KWG001B9; Fig. 3d). In these contact zones, dolomite is typically absent, and calcite is the dominant carbonate together with variable amounts of quartz, altered K-feldspar (in xenoliths and overprinted country rocks), magnetite, phlogopite, and late-stage baryte and hematite. A typical contact zone between carbonatite and country rock (sample KWG001B9) is displayed in Figure 3d, showing the distribution of coarse and acicular calcite I (Sr-rich; Fig. 6c), finer-grained Mn-bearing calcite II, minor dolomite (Mg-rich areas in Fig. 6b), magnetite (Fe-rich areas), and baryte (S-rich areas), which are concentrated close to the contact with the country rock.

Some contact zones show a finer holocrystalline texture and significant alteration (e. g. KWG001A1), with extensive Fe-oxide coatings around minor calcite (Figs 3a, b). Here, the mineralogy is dominated by quartz, remnants of K-feldspar, calcite, baryte, magnetite, and abundant phengite (Figs 3e, f). The latter occasionally displays signs of mechanical stress (Fig. 3e).

Overprinted country rocks

In a decimetres to metres wide zone adjacent to the contact with the carbonatites, the muscovite-kyanite schists (e. g. sample KWG001B5) transition to a fine- to medium-grained magnetite-rich quartzite (Figs 3d, 4b). Two average grain sizes of quartz occur (Figs 4a, c). i. e. ~200 µm and ~50 µm. Cathodoluminescence (blue to red) reveals that both types exhibit polygonal grain contacts; some grains display growth zoning and striations, and luminescence locally changes from blue to orange-brown. Magnetite is abundant (30-250 µm), partly displaying pseudomorphic replacement after hematite or specularite. The samples contain numerous secondary minerals, dominated by baryte, which occurs as two generations: (1) euhedral phenocrysts up to 350 µm, and (2) anhedral pore-filling crystals. Other secondary minerals include pyrite, clinochlore, zircon (only in sample KWG001B-3; Fig. 4f), monazite, strontianite, celestine and natrojarosite (Fig. 4d). The latter is an accessory mineral in sample KWG003A1, but a major phase (with quartz) in KWG003A2. Some country rock samples contain calcite veins (Fig. 4c) with a minor amount of dolomite. At the immediate contact of carbonatite with country rock, K-feldspar is recrystallised to muscovite II (Fig. 7). The complete paragenetic sequence is depicted in Figure 5.

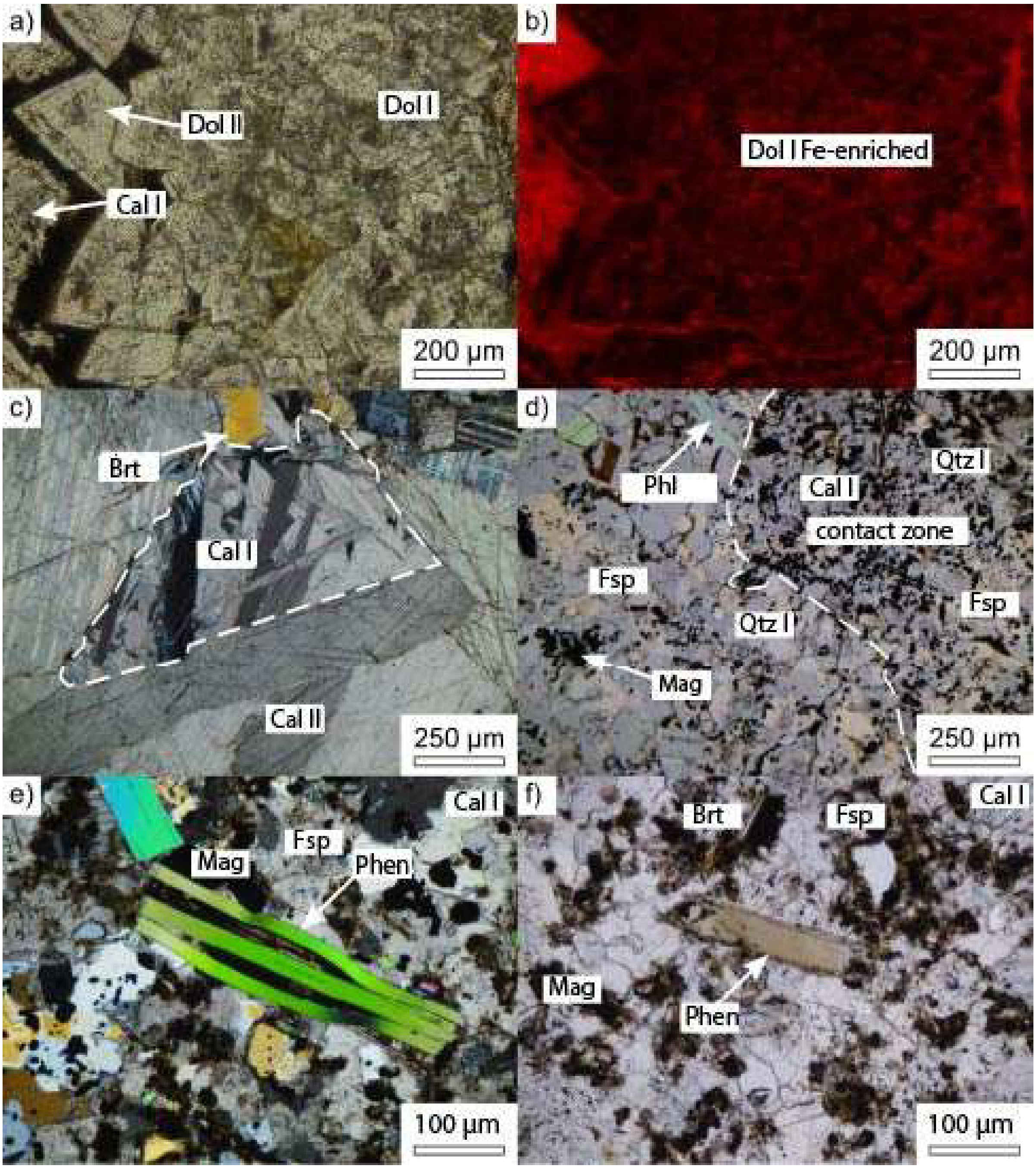

Figure 3. a) KWG003B in PPL (Plane-Polarised Light), two generations of dolomite: The first generation is anhedral and altered, while the second is euhedral and unaltered. An Fe-oxide halo formed around the calcite; b) KWG003B CL: both generations of dolomite are very rich in Fe, causing them to appear almost completely black; c) KWG001B-9 in XPL (Cross-Polarised Light): two generations of calcite differing in size and shape; d) KWG001B-9 in XPL: contact zone between the former carbonatitic melt and the wall rock (left); e) KWG001A-1 in XPL: mechanical stress causes the phengite to split along cleavages. However, no evidence of chemical alteration is observed; f) KWG001A-1 in PPL: phengite has undergone chemical alteration, as shown by a dissolution halo surrounding the grain.

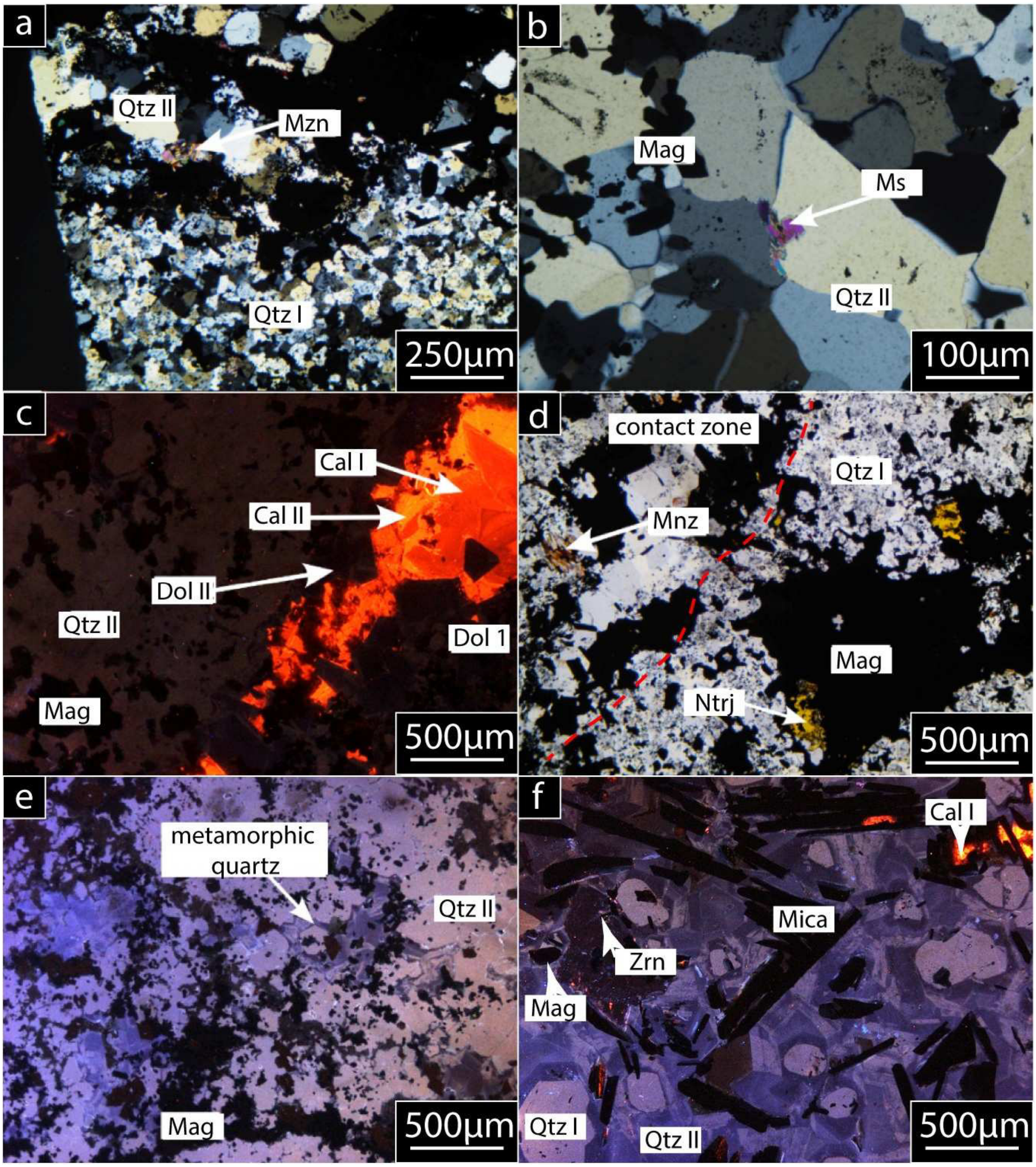

Figure 4. a) KWG001B4 in PPL: two generations of quartz are separated by magnetite. Aggregates of monazite are observed adjacent to magnetite and quartz; b) KWG001B4 in PPL: relicts of muscovite are found between the quartz grains; c) KWG001A CL: two calcite types are observed within the carbonatite vein. The calcite is separated from quartz by dolomite II. Dolomite I is present in much smaller amounts; d) KWG003A1 in PPL: natrojarosite associated with magnetite in altered quartz and accessory monazite; e) KWG001A6 CL: metamorphic and carbothermal quartz; f) KWG001B-3 CL: accessory zircon from the wall rock

Mineral compositions

Carbonates

Carbonates were analysed in carbonatites, contact zones and overprinted country rocks (samples KWG003B, KWG004A, KWG001B9, KWG001A1), with representative analyses given in Table 5. The two texturally distinguished dolomite generations (Figs 3a, 4c) show no discernable compositional differences, with FeO up to 4.7 wt% and MnO up to 0.45 wt%, although Fe increases slightly with evolution (arrow in Fig. 8). Calcite I shows MnO up to 0.2 wt.%, whereas calcite II contains FeO <0.3 wt.% and MnO <2.7 wt.%, also with a slight increase as evolution progresses (arrow in Fig. 8).

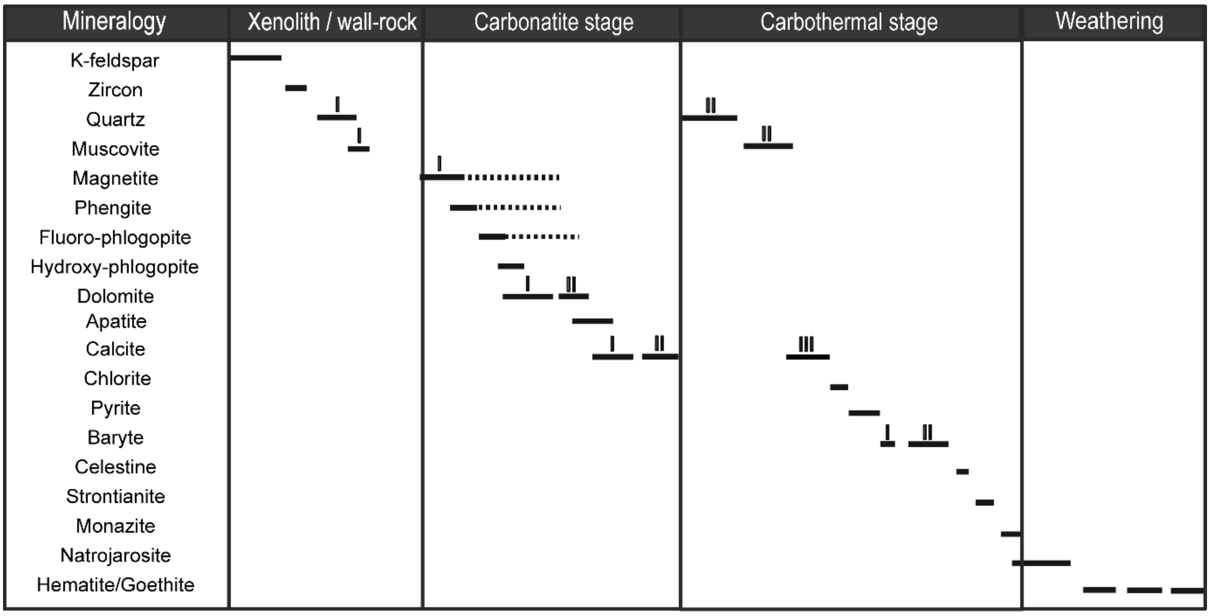

Figure 5. Paragenetic sequence: arrows represent the transformation of one mineral into another

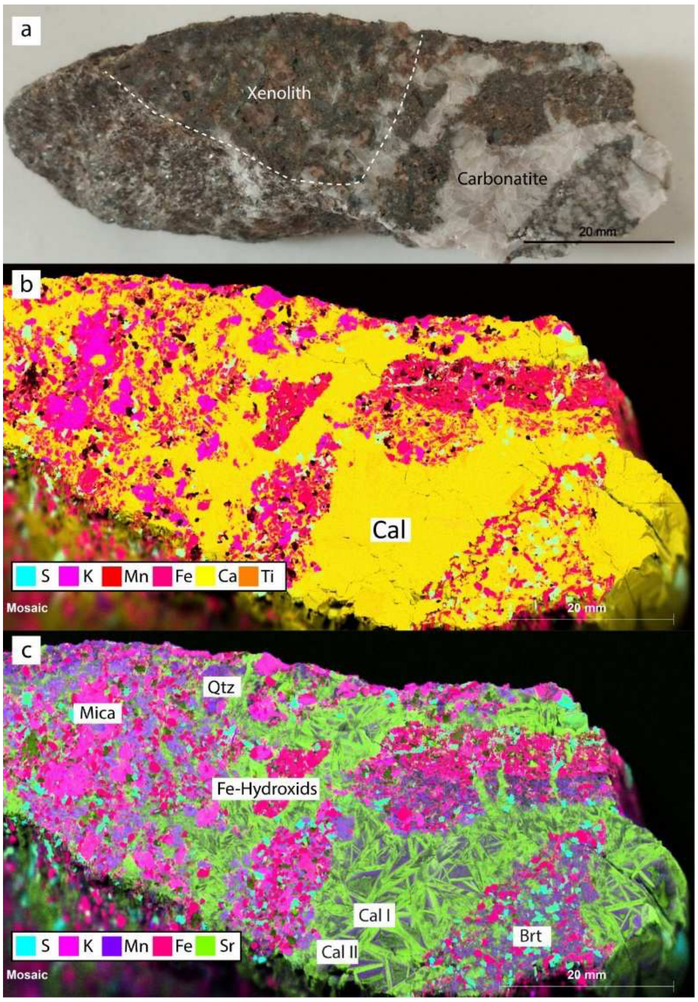

Figure 6. Various chemical maps obtained by µXRF on the polished section of sample KWG001B9 using the Mosaic option and element normalisation: a) Macroscopic photograph of the sample showing two distinct lithological domains: the dark one represents the wall rock and the light one corresponds to the carbonatite; b) elemental distribution map showing Mg, S, K, Ca, Ti, and Fe; c) Elemental distribution map showing S, K, Mn, Fe, and Sr

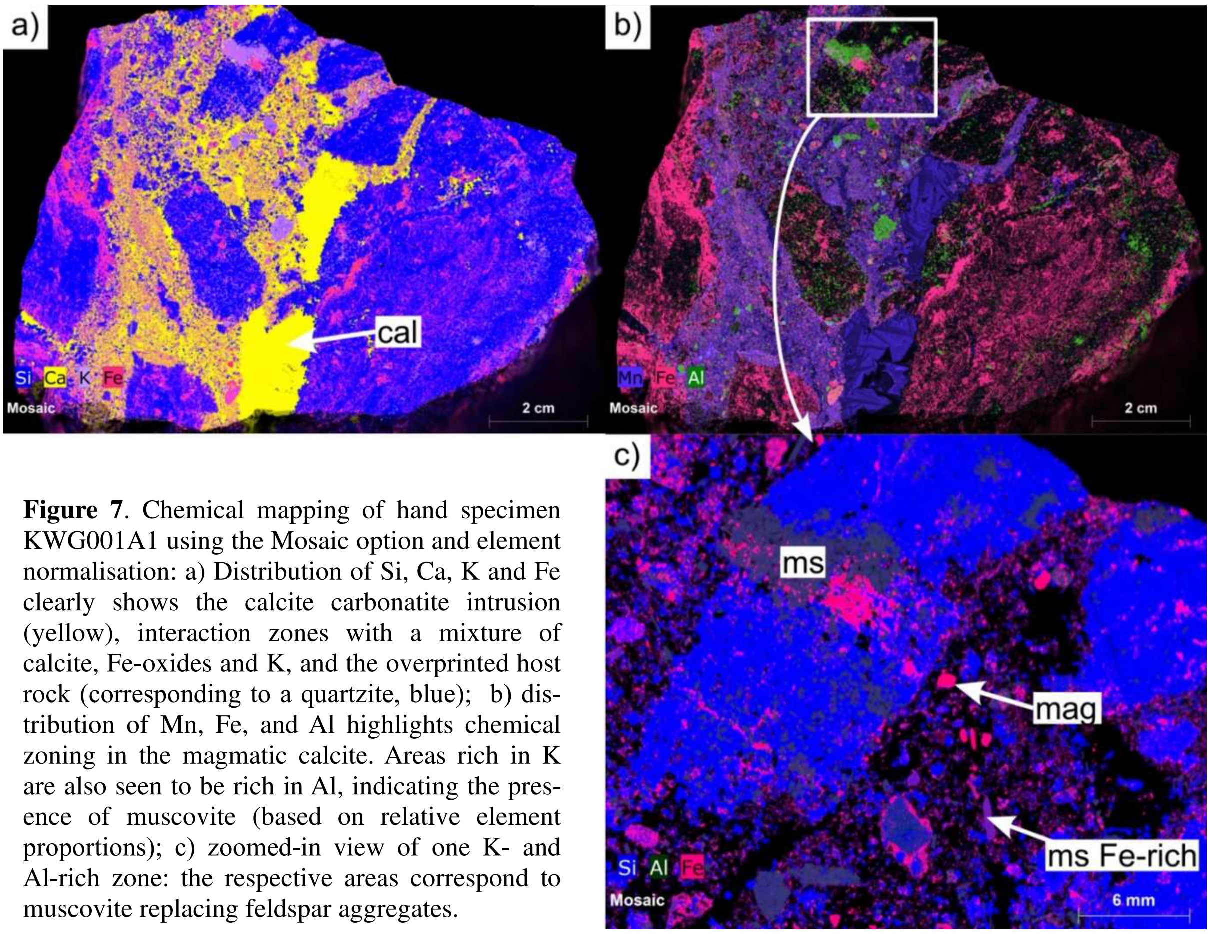

Figure 7. Chemical mapping of hand specimen KWG001A1 using the Mosaic option and element normalisation: a) Distribution of Si, Ca, K and Fe clearly shows the calcite carbonatite intrusion (yellow), interaction zones with a mixture of calcite, Fe-oxides and K, and the overprinted host rock (corresponding to a quartzite, blue); b) distribution of Mn, Fe, and Al highlights chemical zoning in the magmatic calcite. Areas rich in K are also seen to be rich in Al, indicating the presence of muscovite (based on relative element proportions); c) zoomed-in view of one K- and Al-rich zone: the respective areas correspond to muscovite replacing feldspar aggregates.

MINERAL	Fe-bearing dolomite	Ferroan dolomite	Calcite II	Fe-bearing calcite	Calcite II	Calcite I
FeO	2.5	4.66	0.2	0.27	b.d.l.	0.05
MnO	0.33	0.45	0.68	1.55	0.3	0.33
MgO	19.9	18.38	0.1	0.3	0.04	0.04
CaO	29.76	29.11	55.09	55.49	56.07	55.48
SrO	b.d.l.	b.d.l.	0.14	0.07	0.28	0.18
CO_2 calculated	46.88	46.09	43.97	45.06	44.39	43.96
Total	**99.53**	**98.81**	**100.26**	**102.79**	**101.17**	**100.17**
End member proportions						
$CaCO_3$	49.9	49.6	98.5	96.8	99.5	99.4
$MgCO_3$	46.4	43.6	0.2	0.7	0.1	0.1
$(Fe,Mn)CO_3$	3.7	6.8	1.2	2.5	0.4	0.5
Mineral formula						
Ca	0.5	0.5	0.98	0.97	0.99	0.99
Mg	0.46	0.43	>0.01	>0.01	>0.01	>0.01
Mn+Fe	0.04	0.07	0.01	0.03	>0.01	>0.01

Table 5. Exemplary mineral chemistry of carbonates: all analysed chemical elements are listed in their oxide forms, but for the calculation of the structural formula only Ca, Mg, Fe, and Mn were considered. Ba, Na, K, La, Ce, P, and Nd were in all samples below the detection limit and therefore omitted in the table.

Mica

Mica compositions were studied in three samples (KWG003B, KWG001B9 and KWG001A1; Table 6 & Fig. 9), and show distinct differences. Carbonatite (KWG003B) typically contains relatively pure phlogopite, low in both FeO (<2 wt.%) and F (<1.5 wt.%). Closer to the contact with the country rock (sample KWG001B9), phlogopite is higher in FeO (up to 4.6 wt.%) and F (up to 8.8 wt.%), while directly at the contact, within the country rock (KWG001A1), mica occurs as phengite with similar FeO (up to 4.5 wt.%) and F contents (up to 4.3 wt.%), but much higher Al_2O_3 (up to 26.6 wt.%).

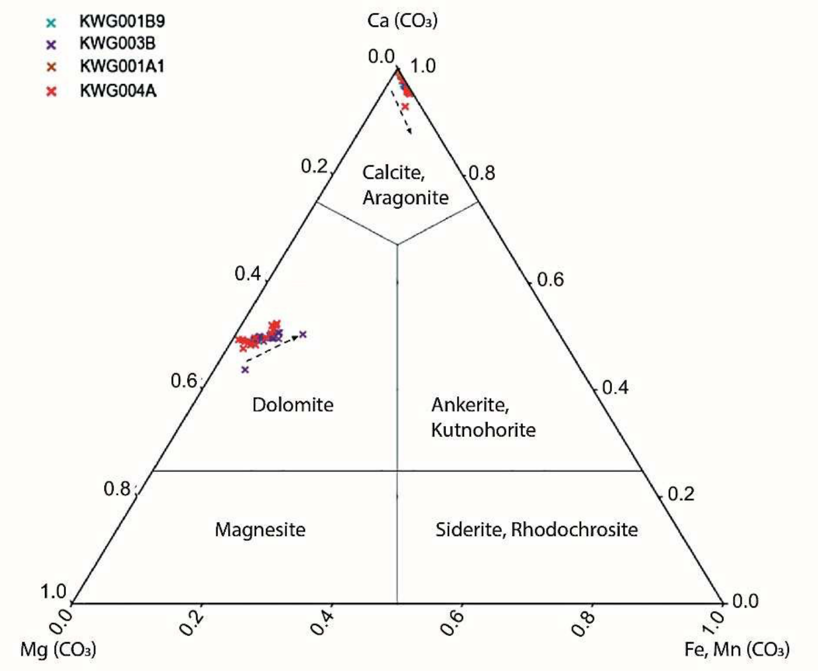

Figure 8. Ternary diagram showing the composition of carbonate; arrows indicate the evolutionary trajectory.

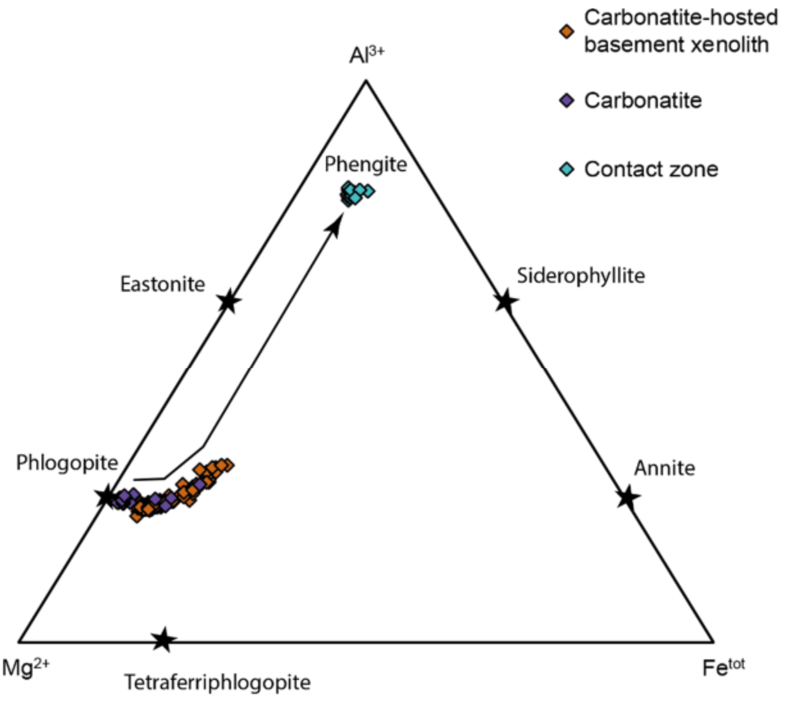

Figure 9. Ternary diagram of the mica mineral chemistry.

SAMPLE	KWG003B		KWG001B9	KWG001A1	KWG001A1	
LITHOLOGY	carbonatite		carbonatite hosted basement xenolith	contact zone	contact zone	
MINERAL	F-bearing hydroxy-phlogopite	F-bearing hydroxy-phlogopite	Fluoro-phlogopite	Fluoro-phlogopite	F-rich phengite	F-rich phengite
SiO_2	43.61	43.58	42.61	41.82	49.57	48.75
TiO_2	0.54	0.45	0.11	0.04	0.32	0.16
Al_2O_3	12.22	12.21	10.93	11.47	25.68	26.70
Fe_2O_3 (calc.)	0.00	0.00	0.06	0.07	0.00	0.00
FeO (calc.)	1.14	1.27	4.21	5.70	3.74	4.69
MgO	27.50	27.49	25.48	24.55	3.44	2.56
Na_2O	0.05	0.05	0.01	0.08	0.21	0.24
K_2O	10.59	10.59	10.85	10.77	11.35	11.22
F	2.53	2.42	8.45	8.29	3.85	3.33
Cl	0.07	0.09	0.03	0.10	0.01	0.01
H_2O (calc.)	2.53	2.63	0.00	0.15	2.59	2.82
$O=F_2,Cl_2$	1.08	1.04	3.56	3.51	1.62	1.4
Total	**99.7**	**99.7**	**99.2**	**99.5**	**99.1**	**99.1**
Si^{4+}	3.06	3.059	3.07	3.02	3.361	3.317
Ti^{4+}	0.028	0.024	0.006	0.002	0.017	0.008
Al^{3+}	1.011	1.01	0.927	0.976	2.052	2.141
Fe^{3+}	0.000	0.000	0.003	0.004	0.000	0.000
Fe^{2+}	0.067	0.075	0.254	0.348	0.211	0.266
Mg^{2+}	2.877	2.876	2.735	2.643	0.348	0.26
Ca^{2+}	0.000	0.000	0.000	0.000	0.000	0.000
Na^+	0.007	0.007	0.002	0.011	0.027	0.032
K^+	0.948	0.948	0.997	0.992	0.982	0.974
Total	**7.998**	**7.999**	**7.994**	**7.996**	**6.998**	**6.998**
F^-	0.561	0.537	1.925	1.893	0.826	0.717
Cl^-	0.009	0.011	0.003	0.012	0.001	0.002
OH^-	1.196	1.231	0.000	0.072	1.173	1.281
$O^{2-}=2-\Sigma(F,Cl,OH)$	0.234	0.221	0.072	0.023	0.000	0.000
Total	**2.000**	**2.000**	**2.000**	**2.000**	**2.000**	**2.000**

Table 6. Exemplary mineral chemistry of mica: Ca, Ba, Cr, and Mn were analysed, but are below the detection limit and therefore omitted in the table.

Discussion

Evolution of the Kwaggaspan Carbonatite Complex

The earliest carbonate phase to crystallise in the carbonatites from Kwaggaspan is ferroan dolomite. The crystals exhibit Fe exsolution at their margins, forming dark Fe-oxide rims that physically separate them from the later crystallised calcite (Figs 3a, b). This sequence represents an inversion of the expected carbonate crystallisation order (Gittins and Harmer, 1997; Woolley and Kjarsgaard, 2008; Mitchell, 2005; Jones *et al*., 2013; Tappe *et al*., 2025), with calcite forming only after the precipitation of ferroan dolomite.

Two non-exclusive hypotheses may explain the observed inversion despite the primary melt's Mg-enrichment. (i) Kinetic control by melt composition and redox conditions: primary carbonatitic melts are typically Mg-rich (Jones *et al*., 2013) and calcite crystallises first due to its higher thermodynamic stability (Schmidt *et al*., 2024). The addition of Fe can shift stability towards hypersolvus Mg/Fe-rich calcite and narrow the dolomite field (or towards Fe-rich carbonates such as ankerite; Schmidt *et al*., 2024). Experimental work shows that Fe/Mg-bearing melts reach dolomite saturation prior to calcite under specific P-T-X(CO_2) conditions (Richert and Schmidt, 2025). (ii) Secondary dissolution and replacement: initial crystallisation starts with calcite, but was followed by subsequent dissolution and replacement by dolomite, possibly through metasomatic processes or fluid-rock interaction during magmatic or post-magmatic stages. The latter has been documented in natural systems (e. g. Chakhmouradian *et al*., 2016; Vasyukova and Williams-Jones, 2022; Gudelius *et al*., 2023), and from sedimentary systems such a replacement is well known (e. g. Mueller *et al.,* 2020; 2022; 2024). Notably, in the investigated samples calcite is more abundant in the contact zones near the host rock, as has been observed also in the Eureka (Namibia) carbonatite (Adamcova, 2025).

Slight enrichment of Fe in dolomite and calcite, as observed in the present study (Fig. 8), is a common feature in evolving carbonatitic systems (Gittins and Harmer, 1997; Woolley and Kjarsgaard, 2008; Mitchell, 2005; Jones *et al*., 2013; Tappe *et al*., 2025). Two interpretations are considered for such a systematic variation. (i) Progressive Fe incorporation during crystallisation: during magmatic differentiation, Fe^{2+} may substitute for Ca^{2+} in calcite as the availability of Ca in the melt diminishes; (ii) post-crystallisation alteration: Fe originally incorporated in calcite could have been leached during later carbothermal alteration, resulting in Fe-depleted, relatively pure calcite. Based on Fe-enrichment along cleavages, post-crystallisation alteration is rather more likely than purely magmatic crystallisation, which would lead to growth zones. Chemical evolution of the different calcite generations observed by µXRF analysis (Fig. 6) provides insights into the crystallisation history of calcite carbonatite. Strontium is preferentially concentrated in the early, elongated calcite crystals, suggesting early and rapid crystallisation from a Sr-rich melt. In contrast, Mn is enriched in more peripheral growth zones, indicating slower crystallisation at a later stage. The partitioning behaviour of these elements is consistent with their ionic properties: Sr^{2+} readily substitutes for Ca^{2+} at elevated temperatures (550–700 °C), while Mn^{2+} incorporation into calcite is more favourable at lower temperatures (250–450 °C) or once Sr saturation is reached (Reeder, 1983). Such development is characteristic of differentiated carbonatites and may also indicate magmatic replenishment or remobilisation by late-stage fluids, potentially of carbothermal origin (involvement of aqueous fluids is indicated by the formation of chlorite and muscovite; Reeder, 1983).

Moreover, a carbothermal stage can be assumed for monazite, which occurs as fine-grained, acicular aggregates dispersed within the carbonatite, the contact zone and the overprinted country rock. Its small grain size and clustered texture are consistent with rapid crystallisation from a probably low-temperature fluid or a brine melt (Anenburg *et al*., 2021). The origin of this mineral is therefore more likely carbothermal than magmatic. The spatial association of monazite with baryte and strontianite also supports precipitation from a REE-enriched carbothermal residue, rather than direct magmatic crystallisation (Walter *et al*., 2022). Monazite formation therefore likely represents low-temperature fluid reaction with country rocks, as has also been described from the Eureka carbonatite in central Namibia (Broom-Fendley *et al*., 2020; Adamcova, 2025).

Mineralogical overprint in the country rock

The overprinted country rocks are predominantly Fe-rich quartzites, marked by the presence of multiple generations of feldspar, magnetite and other Fe-oxides; they also contain muscovite (replacing K-feldspar). The observed mineralogical complexity is interpreted as the result of extensive overprinting due to infiltration of the evolved carbonatite magma/carbothermal residues. Such processes are common in late-stage carbonatitic systems and often lead to the formation of a wide suite of secondary minerals, which will be discussed in the following.

Formation of baryte, strontianite, and natrojarosite

Baryte typically precipitates during the late magmatic to post-magmatic stages of carbonatite evolution (Walter *et al*., 2020, 2021). Upon migration into the surrounding wall rock, these evolved carbonatites/carbothermal residues may encounter chemically and physically distinct environments (often with contrasting pH, redox potential, or ionic activity) leading to baryte precipitation. Baryte is observed in association with pyrite, monazite, hematite and micas in the host rock, further supporting its carbothermal origin. A first generation of well-crystallised baryte likely precipitated under stable conditions at 150-300 °C (Reeder, 1983). A second generation of anhedral baryte fills pore spaces and suggests rapid precipitation from a late-stage or transient carbothermal event.

Under such conditions baryte may crystallise before or concurrently with celestine, provided the fluid is not too highly oxidising. In contrast, celestine forms from interaction between Sr-rich fluids and oxidising, sulfate-rich environments, often within carbothermal veins, or it occurs disseminated in altered carbonates. The required sulfate may originate from the oxidative dissolution of sulfide minerals such as pyrite. This low-temperature mineral assemblage further supports a low-temperature, post-magmatic carbothermal event affecting the country rock.

Most pyrite in the altered country rocks is replaced by natrojarosite, which indicates acidic fluid circulation following carbonatite emplacement under weathering conditions. It may form through either carbothermal alteration, where pyrite oxidation produces SO_4^{2-}-rich, acidic fluids that interact with Na-bearing silicates (mainly feldspars), or via supergene weathering, where oxidised meteoric waters react with sulfide-rich rocks, transforming pyrite into natrojarosite (Desborough *et al*., 2010). In either case, a sulfur-bearing precursor, most likely pyrite, is required. The isometric shapes and spatial distribution of natrojarosite within the rock support its derivation from pyrite. This transformation is common in weathering and hydrothermal systems and marks significant supergene alteration in the Kwaggaspan Complex.

Formation of phengite

The compositional variation of mica in carbonatites has been used to track magma evolution and magma - host rock interaction (e. g. Giebel *et al*., 2019). Typically, mica in carbonatites evolves from phlogopite to eastonite or tetraferriphlogopite and, in the case of wall rock interaction, phlogopite evolves into biotite and subsequently into annite (Giebel *et al*., 2019). In contrast, the present study reveals a distinctly different evolution trajectory from phlogopite to slightly aluminous Fe-rich phlogopite, culminating in the formation of phengite (Fig. 9), and characterised by increasing Fe and Al. This trend is attributed to interaction with the metapelitic, and exceptionally Al-rich country rock (Kuiseb schist), which is notably enriched in muscovite and kyanite (Fig. 2). The high Al-content of the host rock appears to have been a major factor influencing mica composition during interaction.

The mica crystallisation sequence is summarised in Figure 10. Initially, phengite forms within the contact zone during extensive melt – wall rock interaction. The interaction involves Si and Al from the metasedimentary host rock and Fe and F from the infiltrating carbonatitic melt. Subsequently, Fe-rich phlogopite crystallises within the contact zone, reflecting mixed chemical input: Si and Al from the host rock, and Fe, Mg and F from the intruding melt. In the final stage, phlogopite crystallises at lower temperatures, when much of the fluorine has already been incorporated into earlier micas (continuous consumption of fluorine during mica formation). This phase forms at the interface between the melt and host rock and, later, within the melt itself, explaining its restriction to carbonatitic domains.

Emplacement model and evolution of the carbonatitic system

The emplacement of the carbonatitic plugs remains a theoretical reconstruction, inferred primarily from the spatial distribution of sampling points (Figure 1). The curved alignment of these locations, combined with the presence of surrounding fault zones, suggests that the carbonatitic magmas ascended along a zone of structural weakness, possibly the broken axis of a steeply dipping fault. It is proposed that the carbonatitic plugs ascended along this fault system. Since deformation in the area is dated to Pan-African time (535±13 Ma, Goscombe *et al*., 2003), a lower age-limit for the intrusion can be structurally defined. However, a Mesozoic age is more likely due to the adjacent Okenyenye grabbroic intrusion dated at 123.4±1.4 Ma (Milner *et al*., 1993). Nevertheless, Permian and Triassic ages are known from the carbonatites of the Damaraland Igneous Province (Sun *et al*., 2024; Ladisic *et al*., 2025) and therefore the Kwaggaspan Complex could also be part of an earlier carbonatite event. A more specific time frame of intrusion cannot be given at this time.

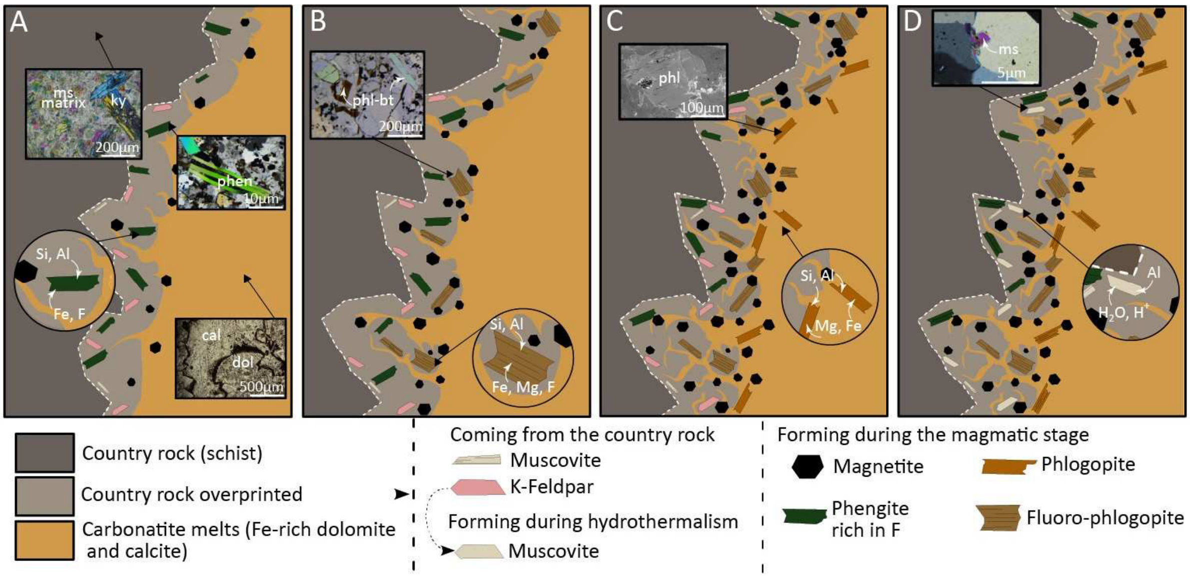

Figure 10. Conceptual diagram of mica evolution and crystallisation: A) Representation of the three different lithologies during the magmatic episode, showing the key minerals inherited from the country rock and the formation of phengite through interaction between the carbonatitic melt and the overprinted country rock; B) at a later magmatic stage, formation of fluoro-phlogopite through continued interaction between the carbonatitic melt and the overprinted country rock occurred close to the carbonatitic melt; C) formation of phlogopite at an even later magmatic stage through interactions between the carbonatitic melt and the overprinted country rock. Formed right at the interface, these minerals, along with part of the magnetite, precipitate directly from the carbonatitic melt; D) during carbothermal alteration, chemical reactions involving feldspar result in muscovite crystallisation.

Upon emplacement, the carbonatites interacted with the surrounding country rock, triggering metasomatic reactions that resulted in the observed mineralogical complexity described above. The strongly overprinted host rock is characterised by quartz, destabilised alkali feldspar, secondary mica and abundant magnetite, underlining the Fe-rich nature of the evolved carbonatites.

The magmatic sequence started with the crystallisation of Fe-rich dolomite, forming first anhedral, then euhedral crystals, with Mg progressively substituted by Fe. Calcite represents the final magmatic phase. Carbothermal activity appears to start during late magmatism, as indicated by the presence of baryte at the carbonatite – country rock interface, reflecting early fluid migration. Carbothermal alteration persists at 250–350 °C, causing quartz recrystallisation, polygonal grain boundaries, and abundant fluid inclusions. Clinochlore begins to crystallise in the carbonatitic units with continued cooling, and is followed by pyrite and two generations of baryte.

Late-stage fluids (200–300 °C) enable the formation of secondary calcite, pyrite, baryte, celestine, strontianite, and monazite. Iron-depleted calcite II forms through alteration of older carbonates. Supergene alteration produces natrojarosite from pyrite, and Fe-oxides (e. g. goethite, hematite) display diverse textures: (i) coarse crystals up to 200 µm; (ii) fine crystals <10 µm; and (iii) spheroidal coatings on pre-existing minerals (e. g. natrojarosite) forming a gossan.

Conclusions

The Kwaggaspan Carbonatite Complex forms several plugs and associated veins, which intruded the Kuiseb schist. Intense interaction between the evolved carbonatites and the host schist produced decimetre-thick, Fe-rich, quartzite-like rocks interpreted as strongly metasomatised country rocks, and led to the formation of phengite. Following this metasomatic overprint, the carbonatitic melt crystallised in a distinctive sequence: two generations of Fe-rich dolomite, succeeded by two generations of calcite. A subsequent carbothermal episode led to the formation of clinochlore, pyrite, baryte, strontianite, celestine, and monazite. Finally, ongoing supergene alteration, in conjunction with the system's Fe-rich character, produced abundant Fe-oxides, such as hematite and goethite. In the course of weathering-related processes, natrojarosite forms through the oxidative alteration of pyrite.

Acknowledgements

This study is supported by DFG (Deutsche Forschungsgemeinschaft) grants (WA 3116/3-1, WA 3116/9-1, WA 3116/28-1; MA 2563/21-1, MA 2135/26-1, GI 1499/11-1, GI 1499/5-1) to Benjamin Walter, Johannes Giebel, Gregor Markl and Michael Marks. Financial support is also provided to the first author by EUR INTREE, the University of Poitiers (France), and the Erasmus+ programme. Tim Langner, Martina Brenn and Simone Schafflick are thanked for their support during sample preparation. Christoph Glotzbach is thankfully acknowledged for trying age dating on the complex. Editors and reviewers are thanked for constructive criticism.

References

Adamcova, A. 2025. Antiskarn formation in the Eureka carbonatite. BSc thesis, Technical University of Berlin, 59 pp.

Anenburg, M., Broom-Fendley, S. and Chen, W. 2021. Formation of rare earth deposits in carbonatites. *Elements,* **17(5)**, 327-332.

Anenburg, M. and Guzmics, T. 2023. Silica is unlikely to be soluble in upper crustal carbonatite melts. *Nature Communications*, **14(1)**, https://www.nature.com/articles/s41467-023-35840-6

Anenburg, M. and Walters, J. B. 2024. Metasomatic ijolite, glimmerite, silicocarbonatite, and antiskarn formation: carbonatite and silicate phase equilibria in the system Na_2O–CaO–K_2O–FeO–MgO–Al_2O_3–SiO_2–H_2O–O_2–CO_2. *Contributions to Mineralogy and Petrology*, **179(5)**, https://doi.org/10.1007/ s00410-024-02109-0

Broom-Fendley, S., Smith, M. P., Andrade, M. B., Ray, S., Banks, D. A., Loye, E., Atencio, D., Pickles, J. R. and Wall, F. 2020. Sulfur-bearing monazite-(Ce) from the Eureka carbonatite, Namibia: oxidation state, substitution mechanism, and formation conditions. *Mineralogical Magazine*, **84(1)**, 35-48.

Chakhmouradian, A. R., Reguir, E. P. and Zaitsev, A. N. 2016. Calcite and dolomite in intrusive carbonatites. I. Textural variations. *Mineralogy and Petrology*, **110(2)**, 333-360.

Desborough, G. A., Smith, K. S., Lowers, H. A., Swayze, G. A., Hammarstrom, J. M., Diehl, S. F., Leinz, R., and Driscoll, R. L. 2010. Mineralogical and chemical characteristics of some natural jarosites. *Geochimica et Cosmochimica Acta*, **74(3)**, 1041-1056.

Geological Survey of Namibia. 2006. *Geological Map of Area 2014 Fransfontein*, 1:250 000 scale series. Ministry of Mines and Energy, Windhoek, Namibia.

Goscombe, B., Hand, M. and Gray, D. 2003. Structure of the Kaoko Belt, Namibia: progressive evolution of a classic transpressional orogen. *Journal of Structural Geology*, **25(7)**, 1049-1081.

Giebel, R. J., Parsapoor, A., Walter, B. F., Braunger, S., Marks, M. A., Wenzel, T. and Markl, G. 2019. Evidence for magma–wall rock interaction in carbonatites from the

Kaiserstuhl Volcanic Complex (Southwest Germany). *Journal of Petrology*, **60(6)**, 1163-1194.

Gittins, J. and Harmer, R.E. 1997. What is ferrocarbonatite? A revised classification. *Journal of African Earth Sciences*, **25(1)**, 159-168.

Gudelius, D., Marks, M.W., Markl, G., Nielsen, T.F., Kolb, J. and Walter, B. 2023. The origin of ultramafic complexes with melilitolites and carbonatites: a petrological comparison of the Gardiner (E Greenland) and Kovdor (Russia) intrusions. *Journal of Petrology*, **64(6)**, https://doi.org/ 10.1093/petrology/egad036

Harris, C. 1995. Oxygen isotope geochemistry of the Mesozoic anorogenic complexes of Damaraland, northwest Namibia: evidence for crustal contamination and its effect on silica saturation. *Contributions to Mineralogy and Petrology*, **122(3)**, 308-321.

Jones, A. P., Genge, M. and Carmody, L. 2013. Carbonate melts and carbonatites. *Reviews in Mineralogy and Geochemistry*, **75(1)**, 289-322.

Ladisic, A., Marks, M.A., Walter, B.F., Giebel, R.J., Beranoaguirre, A. and Markl, G., 2025. Permo-Triassic magmatism in the Damaraland Igneous Province, NW Namibia: The Ondurakorume alkaline-carbonatite complex. *Geochemistry*, **85(3)**, https://doi.org/10.1016/j.chemer.2025.126287

Miller R. McG. 2008. Neoproterozoic and early Palaeozoic rocks of the Damara Orogen. *In*: Miller, R. McG. (Ed.). *The Geology of Namibia*, Vol. **2**, chapter 13, 410 pp. Geological Society of Namibia, Windhoek.

Milner, S. C., Le Roex, A. P. and Watkins, R. T. 1993. Rb-Sr age determinations of rocks from the Okenyenya igneous complex, northwestern Namibia. *Geological Magazine*, **130(3)**, 335-343.

Mitchell, R. H. 2005. Carbonatites and carbonatites and carbonatites. *The Canadian Mineralogist*, **43(6)**, 2049-2068.

Mitchell, R. H. and Gittins, J. 2022. Carbonatites and carbothermalites: A revised classification. *Lithos*, **430-431**, https://doi.org/10.1016/j.lithos.2022.106861

Mueller, M., Igbokwe, O. A., Walter, B., Pederson, C. L., Riechelmann, S., Richter, D. K., Albert, R., Gerdes, A., Buhl, D., Neuser, r., Bertotti, G., and Immenhauser, A. 2020. Testing the preservation potential of early diagenetic dolomites as geochemical archives. *Sedimentology,* **67(2)**, 849-881.

Mueller, M., Jacquemyn, C., Walter, B. F., Pederson, C. L., Schurr, S. L., Igbokwe, O. A., Jöns, N.Richelmann, S., Dietzel, M., Strauss, H., and Immenhauser, A. 2022. Constraints on the preservation of proxy data in carbonate archives–lessons from a marine limestone to marble transect, Latemar, Italy. *Sedimentology*, **69(2)**, 423-460.

Mueller, M., Walter, B. F., Giebel, R. J., Beranoaguirre, A., Swart, P. K., Lu, C., Riechelmann, S., and Immenhauser, A. 2024. Towards a better understanding of the geochemical proxy record of complex carbonate archives. *Geochimica et Cosmochimica Acta*, **376**, 68-99.

Raza, M., Giebel, R. J., Staude, S., Beranoaguirre, A., Kolb, J., Markl, G. and Walter, B. F. 2025. The magmatic to post-magmatic evolution of the Nooitgedacht Carbonatite Complex, South Africa. *Geochemistry*, **85(1)**, https://doi.org/10.1016/j.chemer.2025.126249

Reeder, R. J. 1983. Crystal chemistry of the rhombohedral carbonates. *Reviews in Mineralogy and Geochemistry*, **11(1)**, 1-47.

Richert, P. M. and Schmidt, M. W. 2025. Crustal evolution of carbonatitic melts: Insights from the $CaCO_3$–$MgCO_3$–Na_2CO_3 ternary. Abstracts Goldschmidt 2025 Conference, *6-11 July*, Prague, Czech Republic, https://conf.goldschmidt.info/goldschmidt/2025/meetingapp.cgi/Paper/30031

Schmidt, M.W., Giuliani, A. and Poli, S. 2024. The origin of carbonatites—combining the rock record with available experimental constraints. *Journal of Petrology*, **65(10)**, https://doi.org/10.1093/petrology/egae105

Sun, Y., Galli, A., Szymanowski, D., Guillong, M., Rosskopf, R., Simon, J., Shipandeni, A. and Bachmann, O. 2024. High-precision zircon geochronology and geochemistry of evolved magmatic centres in the Paraná-Etendeka LIP: Temporal placement and tectono-magmatic origin of the Damaraland complexes, Namibia. *Lithos*, **480-481**, https://doi.org/10.1016/j.lithos.2024.107651

Tappe, S., Beard, C. D., Borst, A. M., Humphreys-Williams, E. R., Walter, B. F. and Yaxley, G. M. 2025. Kimberlite, carbonatite and alkaline magmatic systems: definitions, origins, and strategic mineral resources. *EarthArXiv Preprints*, https://eartharxiv.org/repository/view/8658/

Vasyukova, O. V. and Williams-Jones, A. E. 2022. Carbonatite metasomatism, the key to unlocking the carbonatite-phoscorite-ultramafic rock paradox. *Chemical Geology*, **602**, https://doi.org/10.1016/j.chemgeo.2022.120888

Walter, B. F., Steele-MacInnis, M., Giebel, R. J., Marks, M. A. and Markl, G. 2020. Complex carbonate-sulfate brines in fluid inclusions from carbonatites: Estimating compositions in the system H2O-Na-K-CO3-SO4-Cl. *Geochimica et Cosmochimica Acta*, **277,** 224-242.

Walter, B. F., Giebel, R. J., Steele-MacInnis, M., Marks, M. A., Kolb, J. and Markl, G., 2021. Fluids associated with carbonatitic magmatism: A critical review and implications for carbonatite magma ascent. *Earth-Science Reviews*, **215**, https://doi.org/10.1016/j.earscirev.2021.103509

Walter, B. F., Giebel, J., Marlow, A. G., Siegfried, P. R., Marks, M., Markl, G., Palmer, M. and Kolb, J. 2022. The Keishöhe carbonatites of southwestern Namibia–the post-magmatic role of silicate xenoliths on REE mobilisation. *Communications of the Geological Survey of Namibia*, **25**, 1-31.

Walter, B. F., Giebel, R. J., Siegfried, P. R., Gudelius, D. and Kolb, J. 2023. The eruption interface between carbonatitic dykes and diatremes – The Gross Brukkaros volcanic field Namibia. *Chemical Geology*, **621**, https://doi.org/10.1016/j.chemgeo.2023.121344

Warr, L. N. 2021. IMA–CNMNC approved mineral symbols. *Mineralogical Magazine*, **85(3)**, 291-320.

Woolley, A. R. and Kjarsgaard, B. A. 2008. Paragenetic types of carbonatite as indicated by the diversity and relative abundances of associated silicate rocks: evidence from a global database. *The Canadian Mineralogist*, **46(4)**, 741-752.

Yaxley, G.M., Anenburg, M., Tappe, S., Decree, S. and Guzmics, T. 2022. Carbonatites: classification, sources, evolution, and emplacement. *Annual Review of Earth and Planetary Sciences*, **50(1)**, 261-293.

*Communications of the Geological Survey of Namibia, **29** (2026), 90-98*

Integration of Artificial Intelligence at the National Earth Science Museum of Namibia: Enhancing Interactive Exhibits

Albertina Amakali

Geological Survey of Namibia, 6 Aviation Road, Windhoek

<Albertina.Amakali@mime.gov.na>

Abstract :- The integration of Artificial Intelligence (AI) and Machine Learning (ML) in earth science museums is revolutionising the way visitors engage with geological exhibits. By employing AI-driven interactive exhibits and ML-based geological reconstructions, museums can offer immersive and personalised learning experiences going much farther than traditional static displays. This paper explores the transformative impact of AI, its highlighting its relevance in enhancing visitor engagement, improving scientific accuracy, and generally in fostering public interest in the earth sciences. Examples from leading institutions that have successfully implemented AI technologies, on-site observations, digital architectures, benefits and challenges are discussed.

Keywords :- Interactive displays, Artificial intelligence, National Earth Science Museum

Introduction

Museums play a vital role in education, preservation, and public engagement, by providing visitors with insights into history, science, and culture (Kung and Lin, 2024). The National Earth Science Museum of Namibia, like most traditional museums, primarily features static exhibits of fossils, minerals (including the use of various minerals in daily life), models and information on the rich mining history of the country. While these exhibits and showcases effectively present geological and palaeontological knowledge, they lack interactivity, thus limiting visitor engagement and experiential learning, especially with respect to the younger generation.

Although museums have habitually been places of static exhibits and passive learning, science museums, in order to fulfil their role in science communication and education, need to revise and modernise their approach to continue engaging visitor interest. Recent advancements in artificial intelligence (AI) and machine learning (ML) offer innovative solutions to transform static displays into interactive and immersive experiences with reputedly greater learning effect. While AI is the ability of machines to perform tasks that normally require human intelligence, such as learning, reasoning, problem-solving, and understanding language, ML is a branch of AI that enables computers to learn from data provided and improve their performance accordingly over time without reprogramming. In particular, augmented reality (AR), virtual reality (VR), and natural language processing (NLP) are some of the AI-driven technologies employed by museums to enhance visitor engagement, enrich exhibit interpretations, facilitate personalised learning, and provide real-time insights into earth science phenomena (Tseng and Lin, 2024).

In the era of digital transformation, museums worldwide are increasingly utilising information technology to expand their reach and engage broader audiences, as digital initiatives extend their educational influence far beyond their physical boundaries. The digitisation of collections and other material enhances accessibility and fosters public engagement, while promoting life-long learning. Among various digital transformation trends, AI has emerged as a pivotal tool in reshaping museum operations, particularly in enhancing educational practices and visitor interaction (Tseng and Lin, 2024).

VR and AR technologies can be effectively integrated into the context of museum exhibitions to support both storytelling and interaction. While AR overlays digital information on to the real world (for instance by using AR glasses to view dinosaurs moving), VR goes further still to create a fully immersive, computer-generated environment. Viewing content instead of reading or listening to protracted explanations demonstrably enhances the learning experience, as well as increases the probability of retaining information. By means of AR applications, visitors are able to enjoy interactive experiences in which additional content, such as the history and meaning of objects, is digitally added to real artefacts (Spadoni *et al*., 2022). Modern museums have successfully integrated AI with AR and VR to create immersive experiences that reconstruct, for example, historical events, ancient and recent ecosystems and celestial phenomena. At `Dynamic Earth´ (Edinburgh, Scotland), immersive exhibits (Fig. 1) include a virtual meeting with 18th century geologist James Hutton - also known as the `Father of Modern Geology´ - in his study, where he extols his revolutionary theories to captivated audiences.

But AI-powered interactive displays have not only the potential to transform museum experiences by facilitating dynamic reconstructions of past environments or real-time simulations of geological processes; they can also of create responsive virtual guides with the ability of engaging with visitors. ML algorithms can analyse visitor interactions to optimise content delivery, ensuring an adaptive and personalised educational experience. In addition, AI-driven image recognition allows visitors to explore detailed information, for instance about minerals and fossils through interactive kiosks.

This study explores the potential for integrating the various branches of AI at the National Earth Science Museum of Namibia to enhance visitor engagement, interactivity, and learning outcomes. It examines how AI-driven exhibits can provide deeper insights into geological events, simulate ancient ecosystems, and create a bridge between science and public education. By leveraging these technological advancements, the National Earth Science Museum can move beyond static displays, fostering a more immersive and rewarding visitor experience, while advancing scientific literacy in the field of the earth sciences.

Figure 1. Some of the immersive galleries featured at `Dynamic Earth´ dealing with the evolution of our planet (https://dynamicearth.org.uk/)

Interactive and digital exhibitions

Interactive exhibitions are growing in popularity and effectiveness, involving people through different senses and calling them to action. In the development of earth science museums, the application of AI technology has become a significant trend. With its rapid advancement, AI not only enhances the interactivity and personalisation of exhibition content, but also profoundly changes the visitor experience. As museums are crucial institutions for public education, the effective application of new technologies to increase visitor satisfaction has become a focal point both for researchers and practitioners. The application of AI technologies such as computer vision, natural language processing, and machine learning has been pivotal in transforming traditional museum displays into modern interactive galleries. Research conducted by Kung and Lin (2024) identifies essential elements of visitor engagement, including interactivity, educational value, entertainment, and personal satisfaction that are crucial in assessing the effectiveness of AI-driven interactive displays. However, the impact of AI on visitor perception has not yet been methodically studied (Kung and Lin, 2024).

Overlaying digital information on to physical artifacts through AI technologies, enriches the storytelling aspect of exhibits, and notably creates more demonstrative experiences not only for young visitors. Studies have shown that such interactive designs encourage more animated visitor participation, placing the individual at the centre of the learning process (Spadoni *et al*., 2022). Interactive technology also allows people to view objects that could not otherwise be displayed. With the use of AR and VR, buildings, destroyed artifacts or extinct creatures become part of a `life-size´ exhibition. The interactivity of these methods is enhanced by 3D-technology, so that the exhibits can be studied from all angles.

With the rise of AI, museums are increasingly incorporating intelligent systems to present complex scientific information dynamically, and enhance and personalise visitor experiences. The *MusAB* AR application was developed as part of the *MARSS* Project, a research initiative focused on improving science museum experiences through augmented reality. *MusAB* uses machine learning to allow the virtual reconstruction of ancient instruments and artifacts, offering visitors a realistic impression of their original appearance and functionality, while Natural Language Processing (NLP) enables `chatbots´ and virtual assistants to provide real-time explanations, answering visitor queries and adapting responses on the basis of varying knowledge levels. Also, physical panels augmented with additional digital layers, such as animations or 3D models, provide a deeper insight into exhibits (Spadoni *et al*., 2022), as do AI text generators, which produce immersive exhibit descriptions.

Studies on AI-generated content show a growing trend in museum application, with the aim of improving both visitor satisfaction and education. An AI image generation system was developed for an exhibition at the Berlin City Museum, which produces speculative visualisations of potential urban transformation in years to come (Maas, 2024). Conversely, the `Awakening Earth's Majestic Creatures with AI´ project of the Shanghai Natural History Museum (https://www.snhm.org.cn/eg/) uses AI-generated 3D - models and spatial computing to digitally resurrect three extinct iconic species, i. e. the Yangtze River Baiji dolphin, the fin whale, and the mammoth. This initiative combines cutting-edge technology with cultural preservation to create immersive educational experiences (Isaacson, 2024).

AI is also being increasingly applied in mineral identification to enhance efficiency and accuracy. Traditional methods, such as X-ray diffraction (XRD) and Raman spectroscopy, rely heavily on expert knowledge and manual analysis, entailing time-consuming processes and susceptibility to human error. The development of intelligent systems have simplified the process of mineral identification by ML adopting characteristic patterns of mineral samples. AI-driven approaches have been utilised to automate classification, significantly improving speed and precision. AI models have efficiently identified minerals by analysing patterns in data from techniques like Raman spectroscopy (Long *et al*., 2022), refining results and reducing the need for specialised equipment. In addition, AI can process large datasets much more quickly, thus supporting researchers and prospectors in assessing mineral compositions and properties, as well as the geological context of mineral deposits more efficiently. Machine learning methods with applications in interactive museum exhibits contain several mainstream AI models, which are listed and briefly described in Table 1.

Model	**Applications**	**Advantages**	**Shortcomings**
Multilayer Perceptron (MLP)	mineral classification; feature extraction; simple pattern recognition	more effective with smaller data sets (compared to deeper models)	not suitable for complex patterns or large data sets; requires careful regularisation to avoid overfitting; less robust to variations in input data compared to deeper models
Convolutional Neural Network (CNN)	image classification; object detection; mineral identification from images	excellent for image-based classification tasks; robust to transformations like rotation and scaling; automatically extracts relevant features from images; achieves high accuracy in image classification	requires significant computational resources for training; needs large, diverse data sets for effective training; training can be time-consuming
ResNet-18/ResNet-50	deep learning-based image classification with robust feature extraction ability	achieves high accuracy in classification tasks due to robust feature extraction; generalises well across different data sets and tasks	requires significant computational resources for training; needs large data sets for effective training; complex to fine-tune for specific tasks

Table 1. AI Models used in interactive displays (Ahari, 2024)

Approach

To explore the application of AI in the National Earth Science Museum, a qualitative approach, combining case studies, personal observation and interviews with visitors was employed. Case studies of museums that have already integrated AI into their exhibitions provide insights into implementation strategies, AI architectures, benefits, and challenges. These include `Dynamic Earth´, the `Awakening Earth's Majestic Creatures with AI´ project, and AI-powered virtual guides, such as the `Pepper´ robots of the Smithsonian (Washington, USA; https://www.si.edu/newsdesk/releases/smithsonian-launches-pilot-program-pepper-robots), which employ NLP and sentiment analysis to respond to visitor questions. The same institution uses AR to bring its `Bone Hall´ to life by superimposing digital layers over skeletons to reproduce the live animal and their movements (Ahari, 2024), while the Franklin Institute (Philadelphia, USA) employs VR technology that allows visitors, among other exciting options, to explore exotic environments such as the depths of the ocean or outer space (https://fi.edu/en/exhibits-experiences).

Interviews were conducted with visitors of the National Earth Science Museum during guided tours to gather first-hand information on personal experiences and perceptions, as well opinions and feedback regarding the integration of AI in museums, with the aim to of getting a better understanding of the role this technology can play in enhancing the museum experience. Visitor interaction with the various interactive displays were monitored and analysed for an objective assessment of overall user experience. This included tracking how visitors interact with simulations, the duration of their engagement with the respective exhibits, their responses to demonstrations, and their understanding of key concepts.

Findings and discussion

Visitor engagement

The Namibian National Earth Science Museum at present only has three interactive exhibits, i. e. the earthquake display, the fluorescent minerals display and the 'Dino Dig', especially beloved of young visitors. Although Namibia is not prone to severe seismic disturbances, the demonstration of their causes by means of a model of the earth's crust and a seismometer, registering strength of movement along a fault line (Fig. 2), has proved of considerable interest not only to school learners. Similarly, in a darkened cubicle, common minerals such as calcite, fluorite and opal are made to glow in brilliant shades of red, green and blue, depending on their composition, by immersing them in ultraviolet light to visualise the concept of fluorescence (Fig. 3), while at the very popular 'Dino Dig' kids can practise fossil hunting, using trowel and brush to uncover their 'finds' (Fig. 4). The engagement and dwell time at each of these three exhibits clearly indicates their attraction and interest to the museum's visitors (Table 2).

Figure 2. Earthquake interactive exhibit consisting of a simplified model of the earth's crust and a seismometer

The dwell time on interactive displays is about 3 to 7.5 times higher than that of customary, static displays. Moreover, some 90% of visitors in a group engage in conversations on interactive displays, while only 15% of visitors were moved to discuss static displays. This aligns with findings of a University of Twente (Netherlands) study, where interactive exhibits achieved 92% positive engagement ratings versus 67% for static exhibits (Voorde, 2023). These statistics highlight the need for a greater number of attractive, interactive exhibits. However, the study also revealed that reaction to interactive displays is age-related: while over 90% of the younger visitors (e. g. school children) expressed more interest in interactive exhibits, older visitors frequently prefer the more "sober", static displays, as dictated by tradition and authenticity.

Display	**Earthquake**	**Fluorescent minerals**	**\`Dinosaur dig´**	**Static exhibits**
Dwell time [minutes]	5 - 10	5	10 - 15	1.5 - 2
Group conversation [%]	60	75	90	15

Table 2. Time spent on interactive versus static displays at the National Earth Science Museum

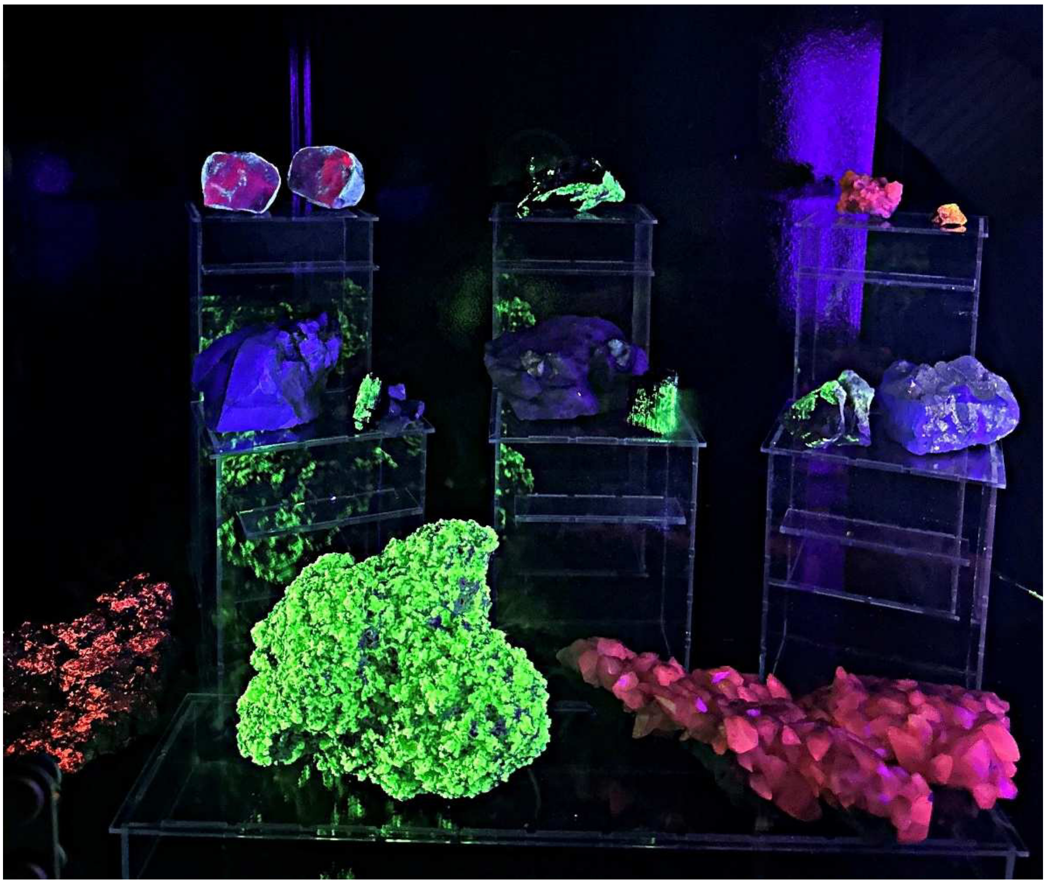

Figure 3. Fluorescent minerals display

Figure 4. 'Dinosaur dig' and model of *Massospondylus* at the National Earth Science Museum

Interactive display for Animatronics

While specific examples of animatronics in earth science museums are less common, they have been successfully adopted and are used to create interactive storytelling experiences. This technology can bring historical figures or extinct species to life (Fig. 5), or realistically reproduce natural processes, such as volcanic eruptions, thus improving the narrative and educational value of exhibits (e. g. Lava Dome – Deutsches Vulkanmuseum, Mendig, Germany, https://www.lavadome.de/en/lava-dome/; Natural History Museum, London, UK, with its T. Rex display, https://www.nhm.ac.uk/events/t-rex-show-with-teach-rex.html; Dynamic Earth; Gondwana Praehistorium). Integrating animatronics with AR or VR further enhances the immersive experience, as it allows visitors to view and interact with life-like models of ancient creatures or experience geological processes. 'Multi-Layered Interaction Engines' combines considered, autonomous, and reactive AI systems to simulate natural behaviours in animatronics.

Interactive displays in mineral identification

Interactive displays can be designed to allow visitors to scan minerals and receive real-time information about their chemical and physical properties. This includes AR overlays that highlight specific features or provide educational content about a mineral. AI-powered apps analyse images of adequate resolution or data of specimens and, by comparing them with a set of training data, return more or less detailed information and identifications. The architecture of AI-based mineral identification is shown in Figure 6.

Figure 5. *Tyrannosaurus rex* in his natural environment at the `Gondwana Praehistorium´ natural history museum (Schiffweiler, Germany*;* https://gondwana-das-praehistorium.de/en/home-en)

Model architectures used in interactive museum display

ResNet50 is a deep convolutional neural network (CNN) architecture that serves as a powerful base network for feature extraction. The model requires a minimum of 10 000 images for accurate training. The learning rate (LR) determines how well a model can make predictions on a new sample, based on the data it has previously been exposed to. This system of AI-powered image recognition tools has been used in mineral and fossil exhibits to allow for more immersive and informative exploration, increasing visitor curiosity and participation (Cha, 2024). Once the model is trained and tested, museum visitors, small-scale miners and other users can apply it to identify unknown minerals.

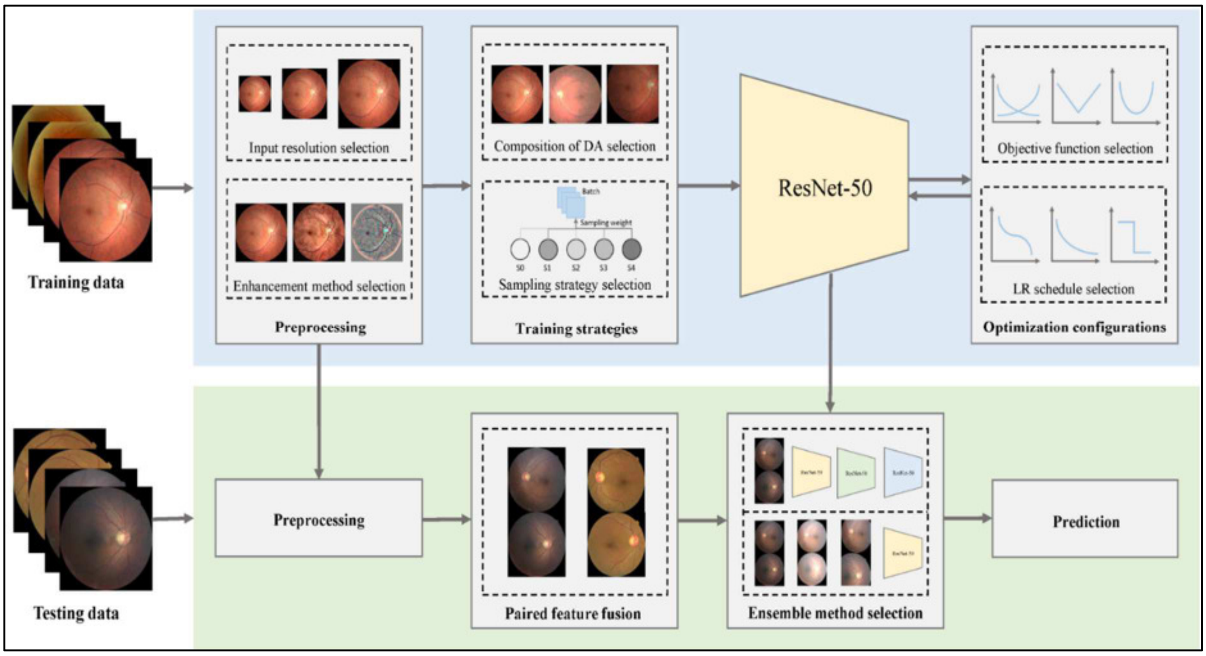

Figure 6. Architecture of AI-based mineral identification (ResNet-50; Huang *et al*., 2023)

In addition, transformer-based `chatbots´ have been adopted by several museums including the Field Museum in Chicago (USA), the Centre Pompidou in Paris (France), and the Milan House Museums (Case Museo di Milano, Italy) to support visitor engagement. Their systems use NLP and deep learning (DL) to answer visitor questions, provide guided tours, and enable interactive storytelling experiences.

Figure 7 illustrates the architecture of an AI-based chatbot. The User Interface (UI) serves as the front end of this architecture. `Input Processing´ is the initial gatekeeper, organising user inputs and preparing them for analysis. The chatbot employs NLP components to interpret user intention. The processed information is subsequently fed into the Dialogue Management System, the chatbot's decision-making hub. Responses are generated based on the conversation context, accumulated knowledge, and past interactions, ensuring relevant and meaningful interaction.

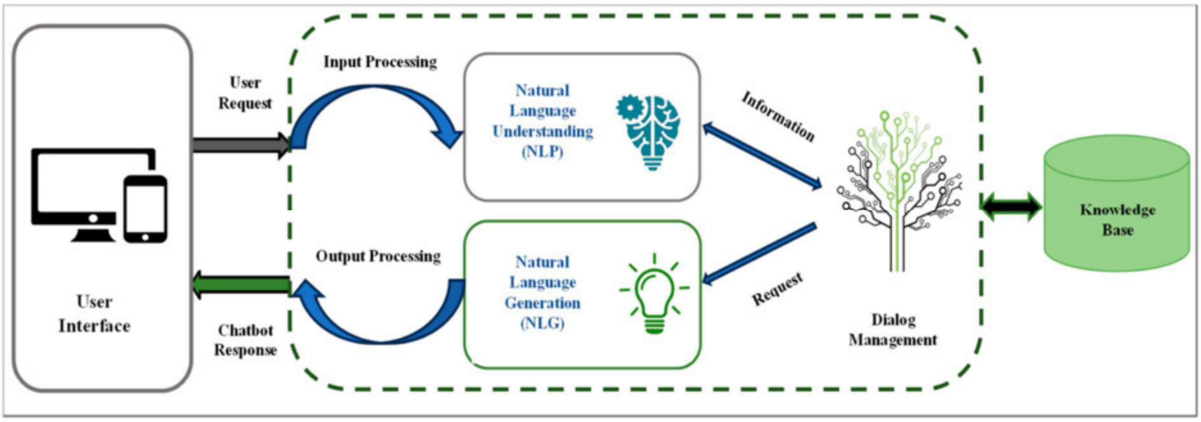

Figure 7. Transformer-based chatbots using NLP (Izadi and Forouzanfar, 2024)

Conclusions

AI-driven interactive museum displays represent significant improvements in visitor engagement and educational outcomes. Museums which have implemented AR and VR technologies report increased knowledge retention and deeper understanding of scientific concepts. Applications, such as ChatGPT offer a variety of ways to modernise and improve performance and visitor satisfaction (e. g. curatorial assistance, personalised exhibition guides, real-time translation services and interactive storytelling; Charr, 2024). While the technology obviously still has limitations, for instance accuracy, bias and copyright issues (Charr, 2024), not to mention implementation and maintenance cost, the above-mentioned benefits clearly outweigh initial challenges.

The adoption of advanced AI technologies at the Namibian National Earth Science Museum are believed to significantly enhance its educational and engagement capabilities, increase visitor numbers and interest, and in general make earth sciences more understandable to a diverse audience.

References

Ahari, H. D. 2024. A review of AI for mineral identification. *ISERDAR*, **2(2)**, 8–20. https://doi.org/10.5281/zenodo.13631172

Cha, V. 2024. *Demystifying Artificial intelligence for mineral exploration*. https://wearevuka.com/insights/smart-city/demystifying-artificial-intelligence-for-mineral-exploration/

Charr, M. 2024. *How Museums Can Use ChatGPT to Transform Their Operations in 2025*. https://www.museumnext.com/article/how-museums-can-use-chatgpt-to-transform-their-operations-in-2025/

Huang, Y., Lin, L., Cheng, P., Lyu, J., Tam, R. and Tang, X. 2023. Identifying key components in ResNet-50 for diabetic retinopathy grading from fundus images: Asystematic investigation. *Diagnostics*, **13(10)**, https://doi.org/10.3390/diagnostics13101664

Isaacson, A. 2024. Lenovo and Shanghai Natural History Museum resurrecting Earth's majestic creatures with VR and AI. https://thevrcollective.com/lenovo-and-shanghai-natural-history-museum-resurrecting-earths-majestic-creatures-with-vr-and-ai/

Izadi, S. and Forouzanfar, M. 2024. Error correction and adaptation in conversational AI: A review of techniques and applications in chatbots. *AI*, **5(2)**, 803-841, https://doi.org/10.3390/ai5020041

Kung, C.-H. and Lin, P.-S., 2024. A study on the application of artificial intelligence in interactive museum displays and visitors perception. *International Journal of Organisational Innovation*, **17(2)**, 155-167.

Long, T., Zhou, Z., Hancke, G., Bai, Y. and Gao, Q. 2022. A review of artificial intelligence technologies in mineral identification classification and visualization. *Journal of Sensor and Actuator Networks*, **11(3)**, https://doi.org/10.3390/jsan11030050

Maas, C. 2024. Using AI Image Generation for Museum Exhibitions. https://www.aureka.ai/aureka-blog/using-ai-image-generation-for-museum-exhibitions

Spadoni, E., Porro, S., Bordegoni, M., Arosio, H., Barbalini, L. and Carulli, M. 2022. Augmented reality to engage visitors of science museums through interactive experiences. *Heritage*, **5(3)**, 1370-1394.

Tseng, J.-L. and Lin, C.-C. 2024. Leveraging Artificial intelligence in Museum Education: Innovations and challenges for promoting sustainable development goals. *Taiwan Education Review Monthly*, 1**3(11)**, 19-32.

Voorde, B. T. 2023. *Exploring engagement in Science Museums: A comparative study of static and interactive exhibitions*. BA thesis, University of Twente, Enschede, Netherlands, 30 pp.

Communications of the Geological Survey of Namibia, ***29*** *(2026), 99-105*

UNESCO Global Geoparks – What do they mean for Namibia?

Josephine Uushona

Geological Survey of Namibia, 6 Aviation Road, Windhoek

<Josephine.Uushona@mime.gov.na>

Abstract :- Namibia is built upon more than 2600 million years of geological history, encompassing ancient cratons, rifted continental margins, spectacular desert landforms, volcanic remnants, and some of the oldest fossils on earth, to name but a few of its varied aspects. The country tells a compelling story of earth's evolution, yet much of this geological heritage remains known primarily to scientists, its wider value for education, communities, and sustainable development not being fully appreciated. It is within this context that the concept of geoparks, and more specifically UNESCO Global Geoparks, becomes increasingly relevant for Namibia. They are an opportunity to turn Namibia's landscapes into living classrooms that connect science, people, and national development.

Keywords :- Geopark, Earth science education, Sustainable development, Economic growth

Introduction

A geopark is a clearly defined geographical area that contains sites of geological significance. These sites are managed in a holistic way to achieve three main goals: conservation, education, and sustainable development (UNESCO, 2015). More importantly, geoparks are not only about protecting and preserving geological heritage, they are also about understanding how earth works and how people interact with their environment. Geoparks promote a living relationship between people and earth, where geological heritage supports learning, cultural identity, and local livelihoods (Herrera-Franco *et al*., 2021).

While geoparks can be developed at national or regional levels, international experience has shown that the greatest long-term impact is achieved, when they are embedded within a recognised global framework. Globally, geoparks have demonstrated how geological heritage can be transformed into opportunities for education, geotourism, scientific research, and community development (Drinia *et al*., 2023). UNESCO Global Geoparks represent the highest standard of geopark development, combining scientific credibility, strong governance, community participation, and international visibility (Rodrigues *et al*., 2025).

For Namibia, pursuing UNESCO Global Geopark designation provides not only global recognition of its geological heritage, but also access to international networks, expertise, and best practice in education, conservation, and sustainable development.

UNESCO Global Geoparks

The concept of geoparks emerged in Europe during the late 1980s as an approach to integrate the protection of geological heritage with sustainable regional development (Henriques *et al*., 2017). Germany established the first geopark in 1989, followed by the creation of the European Geoparks Network in 2000 (Henriques *et al*., 2017). This model subsequently expanded beyond Europe, resulting in the formation of the Global Geoparks Network in 2004 and, ultimately, the formal recognition of UNESCO Global Geoparks in 2015 (Herrera-Franco *et al*., 2021).

UNESCO, as the only United Nations agency concerned with geoscience through the International Geoscience and Geoparks Programme (IGGP), plays a central role in promoting international scientific cooperation related to sustainable resource management, disaster risk reduction, and the conservation of geoheritage (Adiyaman *et al*., 2018). Currently, there are 229 UNESCO Global Geoparks worldwide, spread across 50 countries, with the highest concentration found in Europe and China (UNESCO, 2015).

UNESCO Global Geoparks are built

upon three closely connected pillars. *Conservation,* focusing on safeguarding significant geological sites and landscapes to ensure their preservation for future study and enjoyment. *Education and public awareness,* seeking to improve understanding of earth processes and related issues, such as climate change, natural hazards, and the exploitation of natural resources, through educational initiatives, including school programmes, museum exhibits, guided tours, and community outreach. *Sustainable development,* connecting geological heritage to income-generating activities, like geotourism, guiding services, crafts, and local enterprises, with the aim to enable local communities to benefit directly from the responsible use of their natural heritage. Together, these pillars ensure that geological heritage is protected, understood, and used responsibly. However, this requires strong community commitment, robust partnerships, long-term political and public support, and a comprehensive strategy that balances community goals with the preservation of geological heritage.

Geoparks and National Parks: Understanding the Difference

Although the definitions of geoparks and UNESCO Global Geoparks are clear, the use of the word "park" may create confusion. Geoparks are frequently misunderstood as a form of national park, but the two concepts differ significantly in their objectives, management approaches, and roles in conservation and development.

National parks prioritize biodiversity protection and control human activities within strict legal frameworks. Access and land use are usually reserved primarily for conservation purposes (National Policy on Community Based Natural Resource Management, 2013), while management often is based on top-down governance structures headed by government authorities.

Geoparks, on the other hand, focus on geological heritage and people. They encourage community involvement, education, and legal economic activities without creating new protected status. They recognize that communities living within these landscapes and their knowledge, culture, and livelihoods are integral to heritage management (UNESCO, 2015). It is important to note that "Geopark" is a designation, not a restricted fenced off area like traditional National Parks.

Similarly, a distinction exists between national geoparks and UNESCO Global Geoparks. While national geoparks are recognized at country level, UNESCO Global Geoparks meet internationally agreed standards and undergo regular evaluation by UNESCO. The UNESCO designation brings global visibility, credibility, and opportunities for international collaboration, while still respecting national laws and local governance.

In addition to the Geopark designation, UNESCO recognises several other categories of natural and cultural heritage protection through various international programmes. *World Heritage Sites* identify places of outstanding cultural or natural value; Namibia currently has two such sites, which are the Namib Sand Sea and the Twyfelfontein Prehistoric Reserve with its ancient rock engravings. In contrast, *biosphere reserves* focus on promoting a balanced relationship between conservation and the sustainable use of natural resources; so far Namibia doesn't boast a biosphere reserve. Together, these UNESCO designations celebrate and protect the world's cultural, biological, and geological diversity, while supporting sustainable economic development.

Why UNESCO Global Geoparks in Namibia?

Namibia has an exceptional geological heritage, including some of the oldest rocks on earth, iconic desert landscapes, world-class fossil sites, and mineral resources that have shaped both the country's history and its economy. UNESCO Global Geoparks provide an opportunity to recognise and showcase this heritage beyond mineral exploration, by placing equal emphasis on education, conservation, and community development. Through geoparks, geological landscapes are transformed into learning spaces that benefit students, researchers, local communities, and visitors alike.

UNESCO Global Geoparks are particularly relevant in the Namibian context, because they align closely with the country's long-standing approach to community-based natural resource management (CBNRM). This approach is grounded in the principle that communities, who have recognised rights in the use, management, and benefit from natural resources, have a vested interest to conserve them sustainably (National Policy on Community Based Natural Resource Management, 2013). The participatory and bottom-up nature of geoparks reinforces local ownership, respects traditional knowledge, and promotes shared benefits. As such, UNESCO Global Geoparks can complement existing conservancies and heritage initiatives, strengthening rather than replacing Namibia's current conservation and development frameworks.

Beyond conservation, UNESCO Global Geoparks offer a strategic framework for linking geological heritage to national development priorities. They encourage diversification of rural economies, promote geotourism, and enhance public understanding of earth processes, climate change, and natural resources. In doing so, geoparks contribute to both sustainable livelihoods and informed decision-making.

The Geopark Initiative in Namibia

Namibia has been pursuing the establishment of a geopark since 2004 through an ongoing initiative led by the Ministry of Industries, Mines and Energy via the Geological Survey of Namibia. Over the past two decades, this effort has gained increasing national and international attention, reflecting growing recognition of Namibia's exceptional geological heritage, not only in the scientific community, and its potential to support education, geotourism, and sustainable development. As a result, two priority geopark initiatives have been identified, i. e. the Gondwanaland Geopark in central Namibia (Fig. 1) and the Nama–!Garib Geopark along the border with South Africa. These proposed geoparks represent some of the country's most significant geological landscapes and are viewed as strong candidates for future inclusion within the UNESCO Global Geoparks framework.

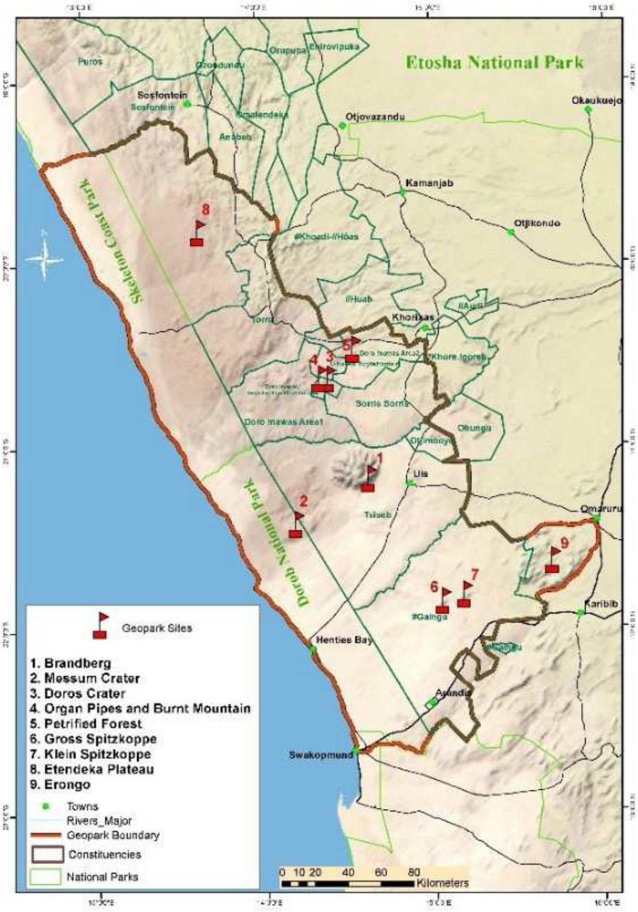

Figure 1. Locality map of the Gondwanaland Geopark and indicating geosites

Gondwanaland Geopark

The Gondwanaland Geopark is located in central western Namibia, along the Atlantic coast, and covers parts of the Kunene and Erongo Regions, totalling some 60,000 km² in area. It contains a remarkable collection of geological sites, including Brandberg (Fig. 2), Spitzkoppe and Erongo, granite massifs of both geological and archaeological significance, the Messum and Doros craters, actually mafic intrusions related to the break-up of Gondwana, the Etendeka Plateau, part of the Parana-Etendeka Iarge igneous province, Vingerklip, an erosional remnant of ancient river terraces, the Petrified Forest, which hosts the biggest accumulation of large petrified logs in southern Africa, and the Twyfelfontein area of World Heritage fame (Fig. 3; Schneider and Schneider, 2004). The Gondwanaland Geopark tells the remarkable story of a time, when today's southern continents were joined together in a giant supercontinent called Gondwana, as well as its eventual break-up. The landscapes and rocks found within the geopark record hundreds of millions of years of earth history, showing how continents collided, mountains rose, oceans opened, and life evolved.

Figure 2. The Brandberg granite massif contains Namibia's highest peak, the Königsstein (2573 m).

Figure 3. The rock engravings of Twyfelfontein also merited UNESCO World Heritage status.

The rocks of the Gondwanaland Geopark formed deep within the earth and at its surface during dramatic geological events. Powerful forces pushed landmasses together, creating mountain belts, while volcanic activity and molten rock shaped the crust from below. Over time, these ancient mountains were worn down by wind and water, leaving behind the striking scenery we see today. One of the most important stories preserved in the geopark is the break-up of Gondwana. As the supercontinent slowly pulled apart, new oceans formed and Africa began to drift toward its present position. Rivers, deserts, and coastal environments developed, leaving clear evidence in layers of sandstone, volcanic rock, and fossil-rich sediments.

However, the Gondwanaland Geopark is not only about rocks, but also about people and nature. Human communities have lived in and adapted to this landscape for thousands of years, developing strong cultural ties to the land. This is showcased at the Damara Living Museum at Twyfelfontein (Fig. 4), a unique place to learn about the culture, traditional practices and language of the Damara people.

Figure 4. Cultural dance at the Damara Living Museum at Twyfelfontein

Today, the area supports diverse ecosystems, from arid zones to river corridors, hosting unique plant and animal life. Through conservation and sustainable development, the Gondwanaland Geopark aims to protect this shared natural and cultural heritage. It offers visitors a chance to walk through deep time, where the story of drifting continents is written into the land itself, connecting earth's ancient past to the lives and landscapes of today.

Nama-!Garib Geopark

The Nama-!Garib Geopark is located in southern Namibia in the ǁKaras Region, covering 2,918 km² along the northern bank of the Orange River (Fig. 5). The area offers a rare glimpse into earth's deep geological past. The rocks tell a story that began more than a billion years ago, when earth's continents were joined together in a supercontinent known as Rodinia.

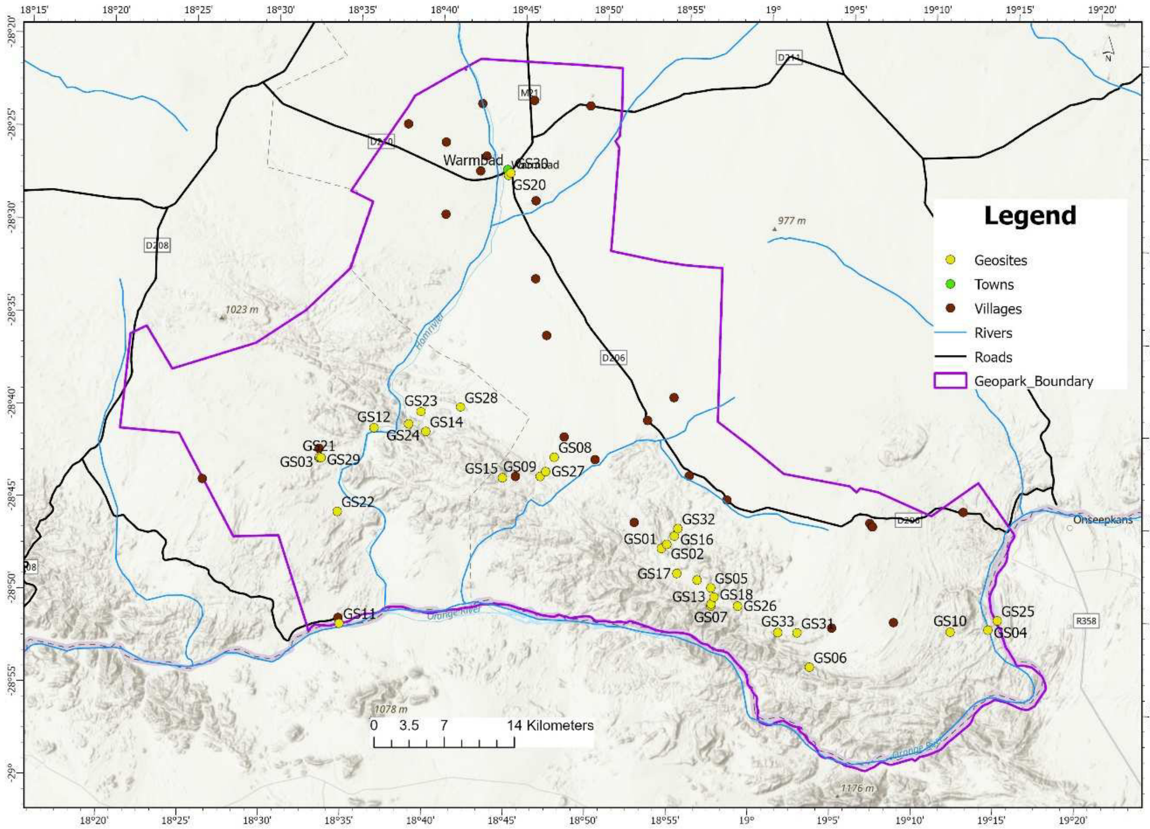

Figure 5. Locality map of the Nama-!Garib Geopark indicating geosites

Geologically, the area lies within the Namaqua–Natal Metamorphic Province, a broad belt of ancient rocks that formed along the edge of one of Africa's oldest landmasses. Over millions of years, powerful earth movements squeezed, stretched, and heated the crust, welding pieces of the continent together. By the end of this process, the land had stabilised to form the Kalahari Craton, an important building block of the Rodinia supercontinent.

What makes the Nama–!Garib geopark special is that these ancient processes can still be seen in the rocks of today. Huge layers and slabs were pushed over one another along major thrust zones (Fig. 6), and long scars in the earth's crust mark where rocks slowly slid past each other deep underground. Molten rock forced its way into cracks created by this movement, later cooling to form striking bands of lighter-coloured rock. The Orange River has since carved its bed into this landscape, to reveal some of these features in even more spectacular natural outcrops.

Beyond its geological importance, the area is rich in living heritage. The indigenous Nama people have a deep cultural connection to the land and possess generations of knowledge that has enabled them to survive in this harsh environment. The Nama-!Garib Geopark is also home to remarkable biodiversity, especially rare and endangered succulent plants, and forms part of the unique Orange River–Karoo ecosystem.

Today, conservation initiatives in the area are helping to restore natural landscapes, protect wildlife (Fig. 7), and support local communities. Together, the rocks, cultures, and ecosystems of the Nama–!Garib Geopark make it a formidable example of how earth's ancient history continues to shape life and landscapes today, making it an excellent candidate for a UNESCO Global Geopark.

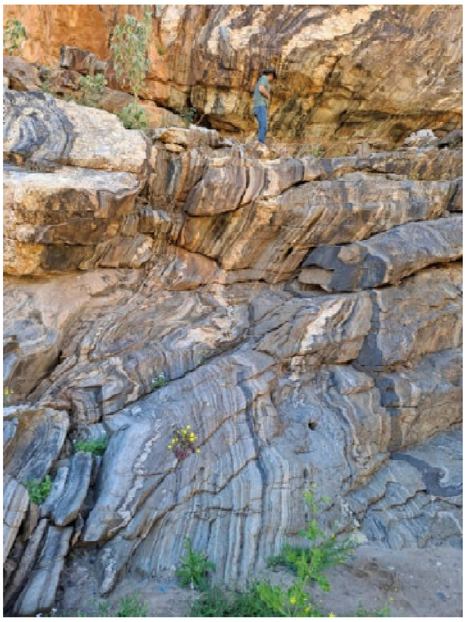

Figure 6 (left). One of the proposed geosites features an exposed thrust zone of late Namaqua-age (~1000 Ma).

Figure 7 (above). The geopark is also home to a variety of wildlife.

Benefits of Geoparks in Namibia

The establishment of Geoparks in Namibia, as has been seen in other countries, is expected to deliver wide-ranging social, economic, and environmental benefits. By promoting geotourism, geoparks can support sustainable economic growth in rural areas that have traditionally been underdeveloped, creating employment opportunities and encouraging new, local-based businesses. Moreover, geoparks strengthen local communities. Communal conservancies gain the ability to protect, manage, and promote their own natural heritage, generating income through activities such as campsites, guided experiences, and craft production - revenues which can be reinvested into community priorities, including education, infrastructure, and social development projects. Geoparks also serve as important platforms for learning and discovery. They support educational programmes for schools (Fig. 8), universities, and the public, while also providing valuable opportunities for scientific research. Through these activities, geoparks help raise awareness of the earth sciences, environmental stewardship, and sustainable land use (Fig. 9).

Internationally, recognition as part of the UNESCO Global Geopark Network would significantly enhance Namibia's profile as a destination for earth heritage tourism, attracting visitors interested in landscapes, culture, and deep-time history. At their core, geoparks treat the landscape as an open-air museum, where ancient rocks tell the story of earth's evolution while simultaneously supporting modern livelihoods. For scientists, geoparks offer more than research sites, they provide spaces for long-term data collection and management, collaboration across disciplines, and meaningful engagement with the public. Research undertaken within geoparks may directly yield educational materials and local exhibitions, as well as initiate community dialogue, thereby helping to bridge the gap between science and society.

For local communities, geoparks create practical economic opportunities, including guiding, cultural storytelling, crafts, and small businesses linked to heritage interpretation. Training, skills development, and local employment are central to the geopark approach, ensuring benefits remain within the community and are not reaped by outside investors. Perhaps most importantly, geoparks nurture a sense of pride and ownership. People who recognise the global importance of their local landscapes, become committed custodians of that heritage, actively contributing to its protection and sustainable use. UNESCO Global Geoparks therefore offer Namibia a powerful opportunity to rethink how geological heritage is valued and shared. By bringing together science, culture, education, and community development, geoparks can transform ancient landscapes into living classrooms and drivers of sustainable growth, ensuring that the stories written in stone continue to benefit society for generations to come.

Figure 8. Earth science education at schools is one of the main aspects of geoparks.

Figure 9. Crop farming at the proposed Nama-!Garib Geopark

References

Adiyaman, O., Neirman, K., Patzak, M. and McKeever, P. 2018. *International Geoscience Programme, in service of the society since 1972*. Paper presented at the 8th International Conference on UNESCO Global Geoparks, 16-20 May, 2018, Madonna di Campiglio, Italy.

Drinia, H., Voudouris, P. and Antonarakou, A. 2023. Geoheritage and Geotourism Resources: Education, Recreation, Sustainability II. *Geosciences*, **13(11)**, https://doi.org/10.3390/geosciences13110350

Henriques, M. H., Brilha, J. 2017. UNESCO Global Geoparks: a strategy towards global understanding and sustainability. *Episodes*, **40(4)**. http://dx.doi.org/10.18814/epiiugs/2017/v40i4/017036

Herrera-Franco, G., Montalván-Burbano, N., Carrión-Mero, P., Jaya-Montalvo, M., Gurumendi-Noriega, M. 2021. Worldwide Research on Geoparks through Bibliometric Analysis. *Sustainability*, **13(3)**, https://doi.org/10.3390/su13031175

National Policy on Community Based Natural Resource Management. 2013. Directorate of Parks and Wildlife Management, Ministry of Environment and Tourism, Windhoek, Namibia. https://www.npc.gov.na/wp-content/uploads/2022/06/National-Policy-on-Community-Based-Natural-Resources-Management-March-2013.pdf

Rodrigues, J., Costa e Silva, E. and Pereira, D. I. 2025. The landscape of science communication and public engagement in UNESCO Global Geoparks. *International Journal of Geoheritage and Parks*, **13(4)**, 547-560.

Schneider, G. I. C and Schneider, M. B. 2004. Gondwanaland Geopark - A proposed Geopark for Namibia. Proposal, 91 pp. https://www.scribd.com/document/44363141/Gondwana-Park-Sm

UNESCO. 2015. Statutes of the International Geoscience and Geoparks Programme and Operational Guidelines for UNESCO Global Geoparks. https://unesdoc.unesco.org/ark:/48223/pf0000391354

Communications of the Geological Survey of Namibia, ***29*** *(2026), 106-127*

Namibia Palaeontology Expedition May - June 2025

Martin Pickford[1]*, Brigitte Senut[1], Dominique Gommery[2], Helke Mocke[3] and Albertina Amakali[3]

[1] *Centre de Recherche en Paléontologie - Paris (CR2P/ UMR 7207 : MNHN-CNRS-SU), Muséum national d'Histoire naturelle, Paris, France*
[2] *Centre de Recherche en Paléontologie - Paris (CR2P/ UMR 7207 : MNHN-CNRS-SU), Sorbonne Université, Paris, France*
[3] *Geologial Survey of Namibia, 6 Aviation Road, Windhoek, Namibia*

**Corresponding author: <martin.pickford@mnhn.fr>*

Abstract :- The aim of the field survey by the Namibia Palaeontology Expedition in May-June 2025, was to prospect for fossils in the Miocene deposits in the Sperrgebiet (Phase 1, Fig. 1) and in the Miocene to Pleistocene karstic deposits of the Otavi Mountainland (Phase 2, Fig.1) in order to throw light on their geological and palaeoenvironmental contexts and ages. The work of the expedition, which has been operating since 1991, is authorised by the National Commission on Research, Science and Technology and the National Heritage Council of Namibia.

Keywords :- Palaeontology, Otavi Mountainland, Sperrgebiet, Miocene, Pleistocene, Fossils

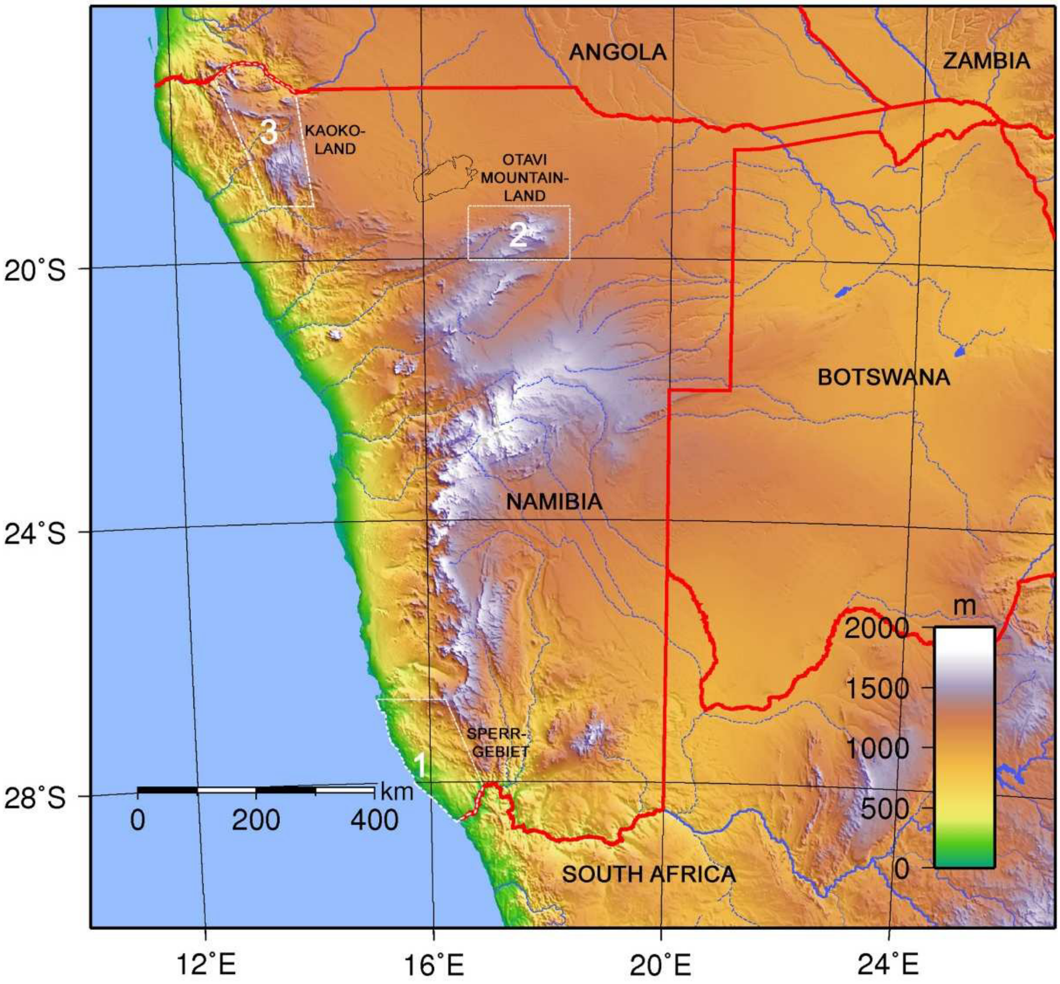

Figure 1. The three main areas in which the Namibia Palaeontology Expedition currently has permits to survey: 1) Sperrgebiet in the southwest, 2) Otavi Mountainland in north central Namibia, and 3) Kaokoland in the north-west

Phase 1: Sperrgebiet

In the Sperrgebiet, detailed prospecting for fossils was carried out at Langental, Neue Anlage, Grillental, Elisabethfeld and Glastal (Fig. 2). At the National Earth Science Museum, Windhoek, the fossil frog remains from the Sperrgebiet were assembled and photographs were taken of all the material, comprising over a hundred specimens. This was undertaken as a preliminary phase of a detailed study of the collection by A. Lemierre to be carried out in the near future.

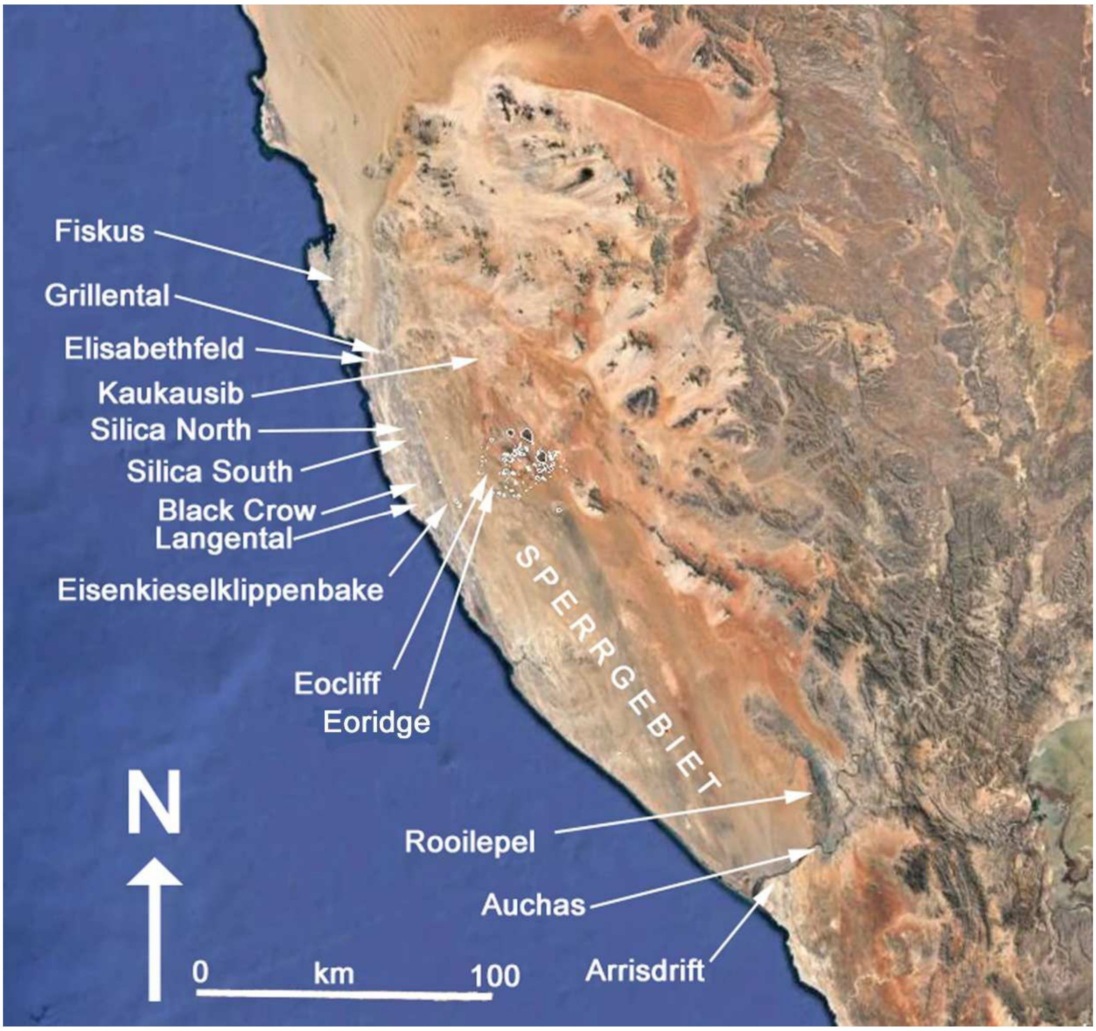

Figure 2. Fossiliferous localities in the Sperrgebiet, Namibia. The 2025 survey focussed on Elisabethfeld, Grillental and Langental as well as Neue Anlage close to Langental and Glastal between Eisenkieselklippenbake and Langental.

Elisabethfeld

Two days of survey at Elisabethfeld resulted in the collection of over 28 fossils among which are a well-preserved pedal phalanx of the extinct miniature ostrich *Struthio coppensi* (Fig. 3) and some associated skeletal remains of the small hypsodont macroscelidid *Myohyrax oswaldi* (Fig. 4). One of the palates of the latter taxon contains all the cheek teeth, including the tiny canine and anterior premolars, which are relatively poorly represented in previous collections due to their tiny dimensions.

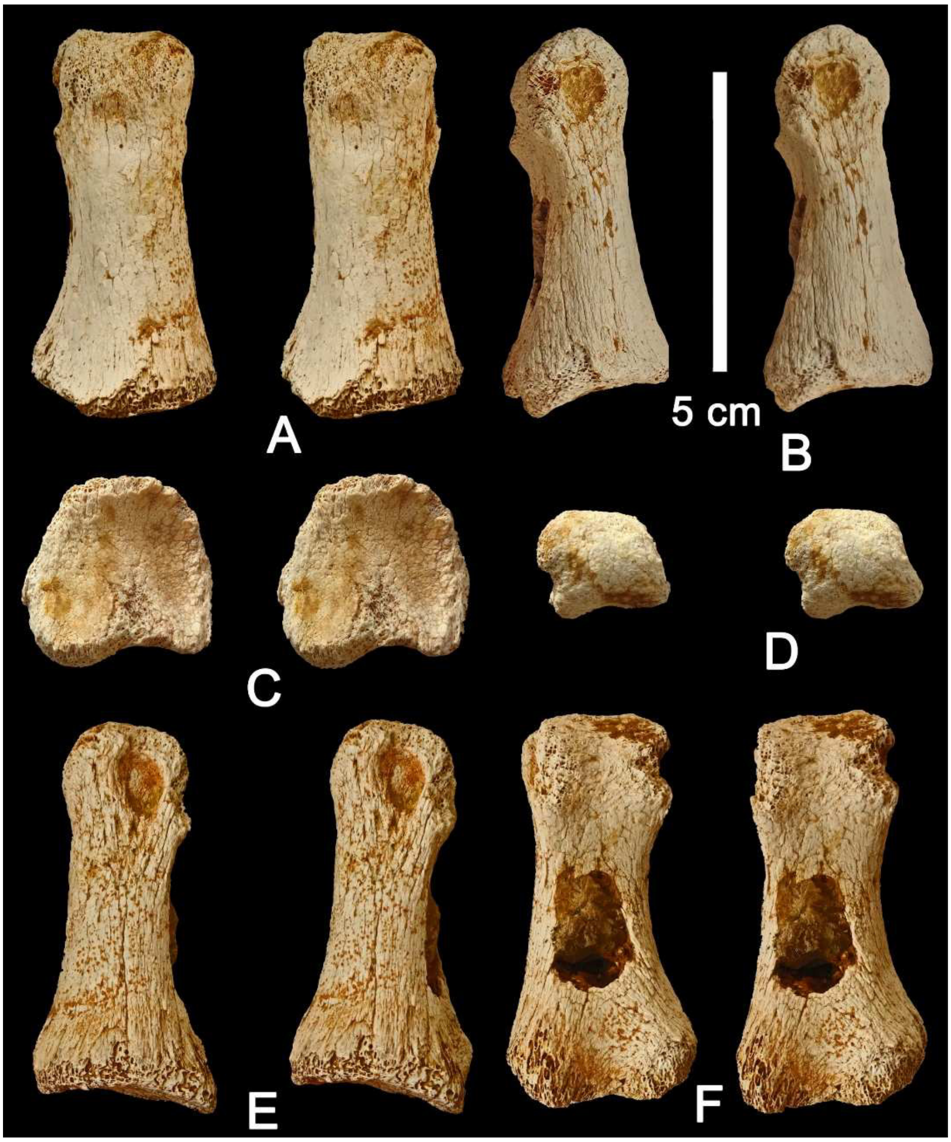

Figure 3. Stereo images of EF 3’25, pedal phalanx of *Struthio coppensi* from Elisabethfeld. A) dorsal view, B) abaxial view, C) proximal view, D) distal view, E) axial view, F) plantar view

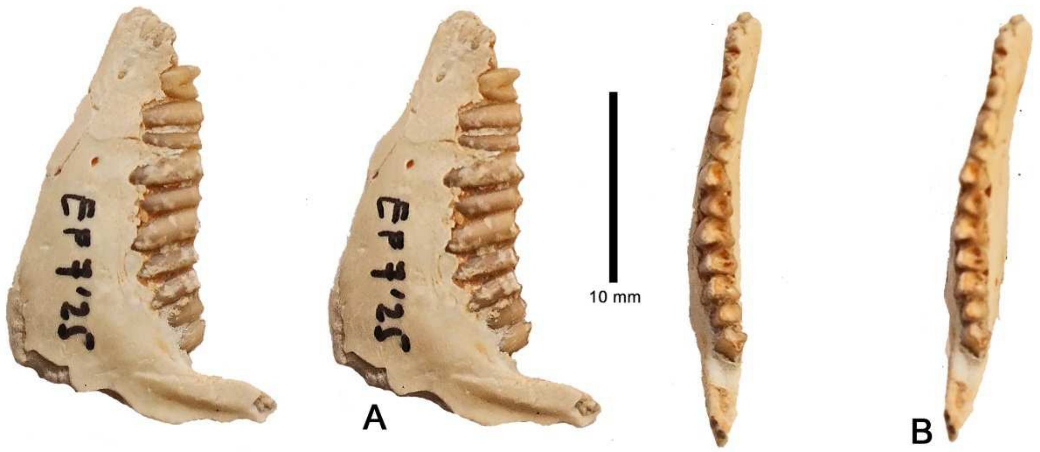

Figure 4. Stereo images of EF 7’25, left mandible of *Myohyrax oswaldi* from the Early Miocene red clays of Elisabethfeld, Namibia. A) buccal view, B) occlusal view.

Grillental

In 2023 and 2024 much of the eastern part of Grillental VI was covered by a large dune (Fig. 5), but by 2025 it had migrated northwards sufficiently far to expose the underlying sediments again (Fig. 6). 128 entries were made in the Grillental faunal catalogue. The specimens collected include the remains of a tiny species of macroscelidid that is new to science. Excellent samples of *Myohyrax* (Fig. 7) and *Protypotheroides* (Fig. 8) were found as well as abundant rodents (Fig. 9), some frogs, birds and medium-sized mammals (Fig. 10). A tiny carnivoran maxilla was collected at Grillental Borrow Pit, the carnassial measuring 1.4 mm in mesio-distal length (Fig. 11).

Figure 5. Large dune covering the Grillental VI anthracothere site in 2023. Note the tilted slab of sandstone, a local landmark (arrow).

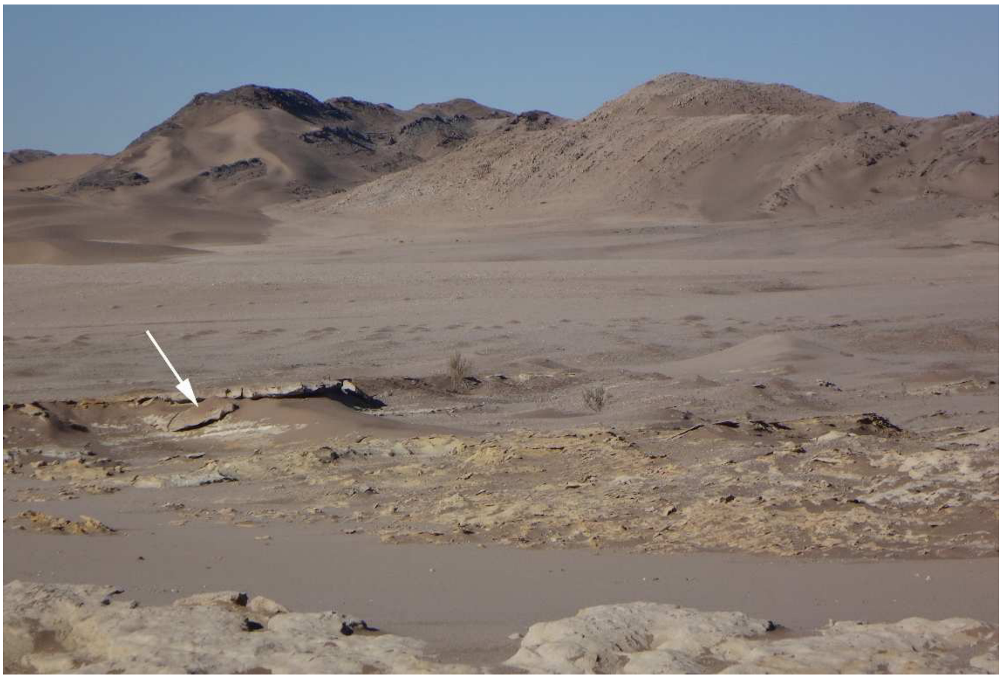

Figure 6. Grillental VI anthracothere site in 2025, the dune that covered it in 2023 having migrated northwards out of the depression. Arrow shows the tilted slab of sandstone below the low cliff, a local landmark.

Figure 7. Stereo images of GT 59'25, left and right mandibles of *Myohyrax oswaldi* from the Early Miocene green clays of Grillental VI (Knoll Site); top row - occlusal views of left and right mandibles, Middle row - lingual and buccal views of right mandible, bottom row - lingual and buccal views of left mandible

Figure 8. Stereo images of GT 16'25, left mandible of *Protypotheroides beetzi* from Grillental VI. A) buccal view, B) occlusal views, C) lingual view

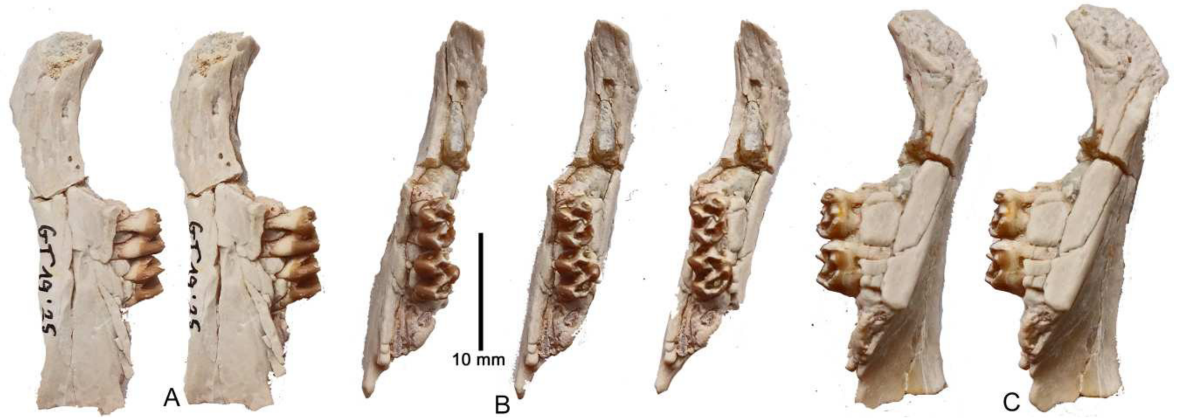

Figure 9. Stereo images of GT 19'25, left mandible of *Diamantomys luederitzi* from Grillental VI. A) buccal view, B) occlusal views, C) lingual view

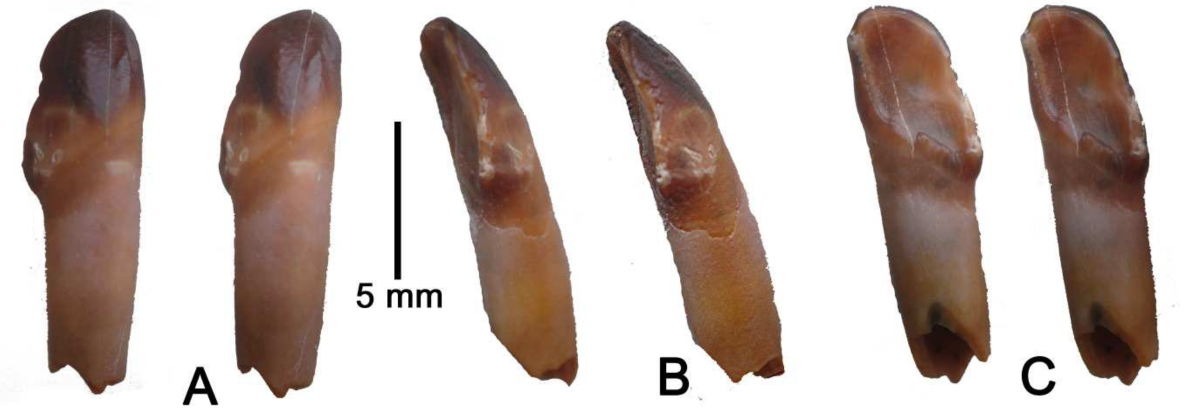

Figure 10. Stereo images of GT 91'25, left I1/ of *Diamantohyus africanus* from Grillental Carrière. A) labial view, B) distal view, C) lingual view

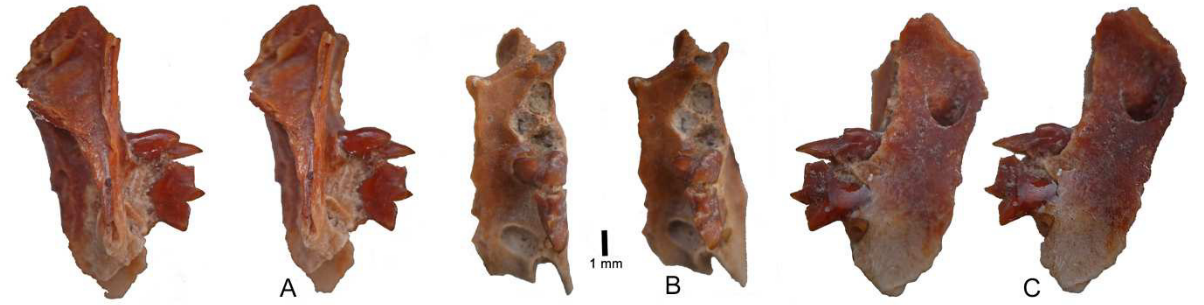

Figure 11. Stereo images of GT 98'25, left maxilla with P4/ of a minuscule carnivoran from Grillental Borrow Pit. A) lingual view, B) occlusal view, C) buccal view

An interesting find at Grillental VI was that of a talus of a small tragulid, which reveals that the species concerned is *Afrotragulus parvus* (Fig. 12). Previously, the small tragulid remains from Grillental were attributed to *Afrotragulus moruorotensis*, but it is now considered to be more likely that the taxon concerned is *Afrotragulus parvus* which is slightly larger than *A. moruorotensis*. *A. parvus* is well represented in Early Miocene localities in Kenya and Uganda, dating from ca 18-17 Ma. *Afrotragulus moruorotensis*, in contrast, is known in East Africa only from localities younger than 17 Ma.

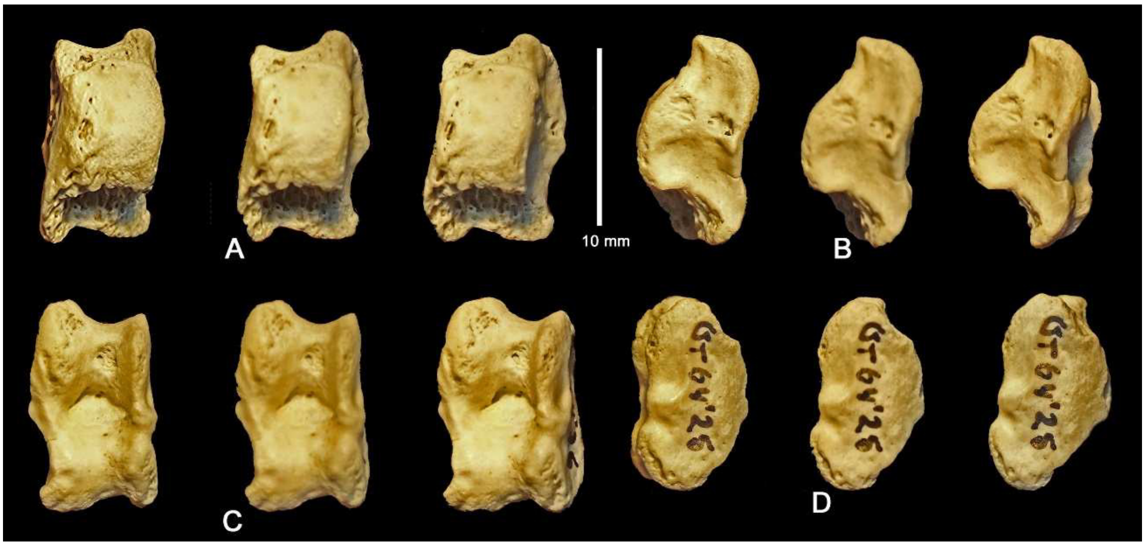

Figure 12. Stereo images of GT 64'25, right talus of *Afrotragulus parvus* from GT VI. A) caudal views, B) lateral views, C) cranial views, D) medial views

The rains in 2023 and 2024 flooded the depressions at Grillental, depositing clays and silts in their floors, thereby obscuring much of the fossiliferous deposits. Nevertheless, many fossils were collected from GT VI, especially from the knoll site. In the eastern branch of the valley at GT VI, the rains exposed a series of large footprints most of which had hitherto been obscured under a thin layer of aeolian sand (Figs 13-15). Mapping of the footprints reveals that they were likely made by a graviportal mammal, probably a proboscidean such as *Eozygodon* or *Progomphotherium*, both of which are known to occur in the Early Miocene deposits of the Sperrgebiet.

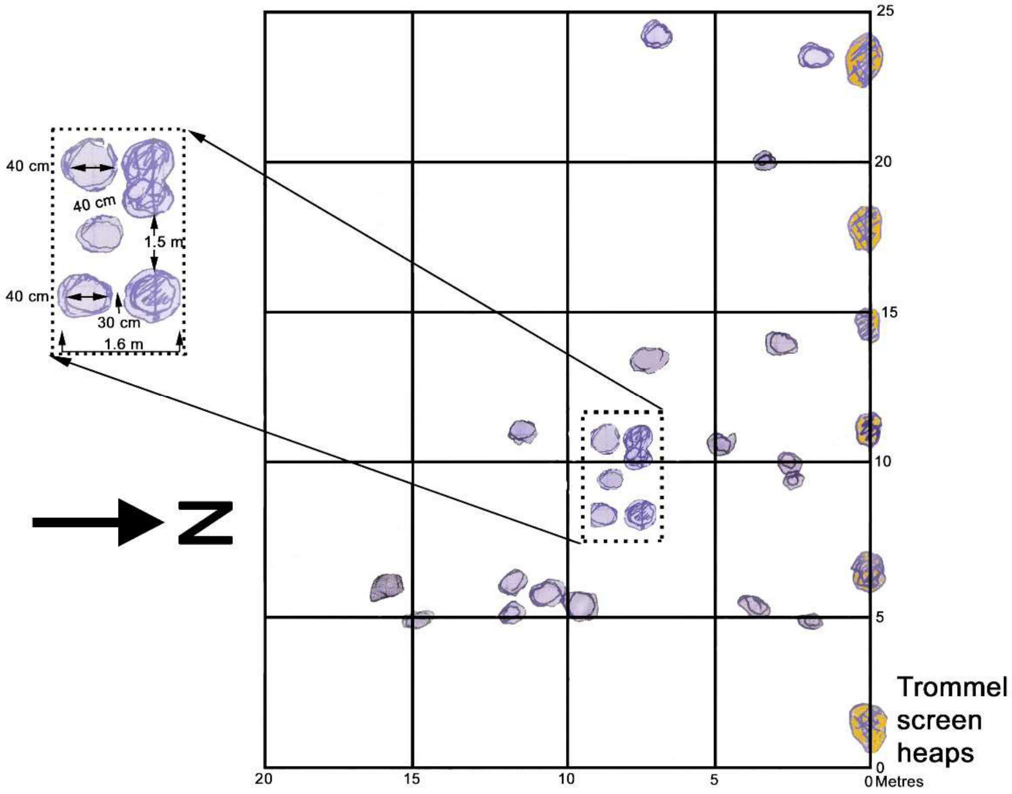

Figure 13. Field sketch map of 23 footprints of a large graviportal mammal, most likely a proboscidean, at Grillental VI, northern Sperrgebiet. The feet of this individual were ca 40 cm in diameter, and the distance between the front and hind feet was ca 1.5 metres.

Figure 14. Overview of the proboscidean footprints at Grillental VI. Note the lines of small trommel screen heaps (right of image) evidence of prospecting activities during the 1920's (view westwards).

Figure 15. Close-up view of some of the proboscidean footprints at Grillental VI. Note the raised margins of the prints where the soft sediment squidged upwards round the foot of the track maker. The feet of this individual were ca 40 cm in diameter. The small track close to the main print (bottom of figure) is a demi-print, made when the animal rested the anterior part of its hind foot on the surface close to the front foot, but without putting its full weight on it.

Close examination of the coarse grits that overlie the green silts and clays of Grillental (Figs 16, 17), indicate that they were transported and deposited by highly energetic flood events. The presence of a tooth of the white rhino (*Ceratotherium*) in the grits indicates a latest Miocene or Plio-Pleistocene age for these deposits. Until now, these grits have remained without a precise name and were not correlated to any other rock units in the Sperrgebiet. Herein they are called the GT Grits. It is possible that they represent the lateral equivalents of the Gemsboktal Conglomerates which are widespread in the Central Sperrgebiet, between the Klinghardt Mountains and the coast. The Gemsboktal unit comprises widespread but generally thin layers of coarse conglomerate forming hamadas on the relatively planar inner Namib. At Kalkrücken, there is an aeolianite bed (the Terrassenfeld Aeolianite) intercalated between the two main horizons of Gemsboktal Conglomerate. The GT Grits in contrast, are interpreted to represent the downstream equivalents of the hamada deposits where the finer fractions transported by flash floods were eventually confined to valleys such as the Grillental, where they rapidly accumulated as thick masses of trough-cross-bedded grits. The scale of the trough cross-bedding and the coarseness of the grits indicates that the flash floods were highly energetic. The sand, silt and clay fractions transported by the floods were probably deposited in the Atlantic Ocean.

Figure 16. Trough cross-bedded coarse grits at Grillental 1

Figure 17. Trough cross-bedded coarse grits exposed at locality GT 1, that overlie Early Miocene green silts and clays. The scale of the troughs and the cross-bedding indicate transport by highly energetic floodwaters which were overloaded with sediment (height of cliff: ca. 2 m).

Similar deposits form today in arid areas such as the sub-Atlas zones of the Maghreb when sporadic but violent storms occur in hilly or mountainous areas. Conglomeratic hamadas accumulate in the flatter ground at the edges of the mountains, often as overbank flood debris, and the grits, sand and finer fractions are carried downstream where they eventually end up in valleys closer to the coast or in inland water bodies such as ephemeral lakes.

The stratigraphic correlation between the Gemsboktal Conglomerates on the one hand, and the GT Grits on the other, provides food for thought concerning Latest Miocene to Plio-Pleistocene climatic conditions in the Sperrgebiet, and it potentially throws light on the geomorphological development of parts of the drainage system of the region (Fig. 18). It is possible that clasts such as agates and diamonds that were present in the drainages prior to flood events, could have been flushed out into the ocean by these vigorous palaeo-flood events.

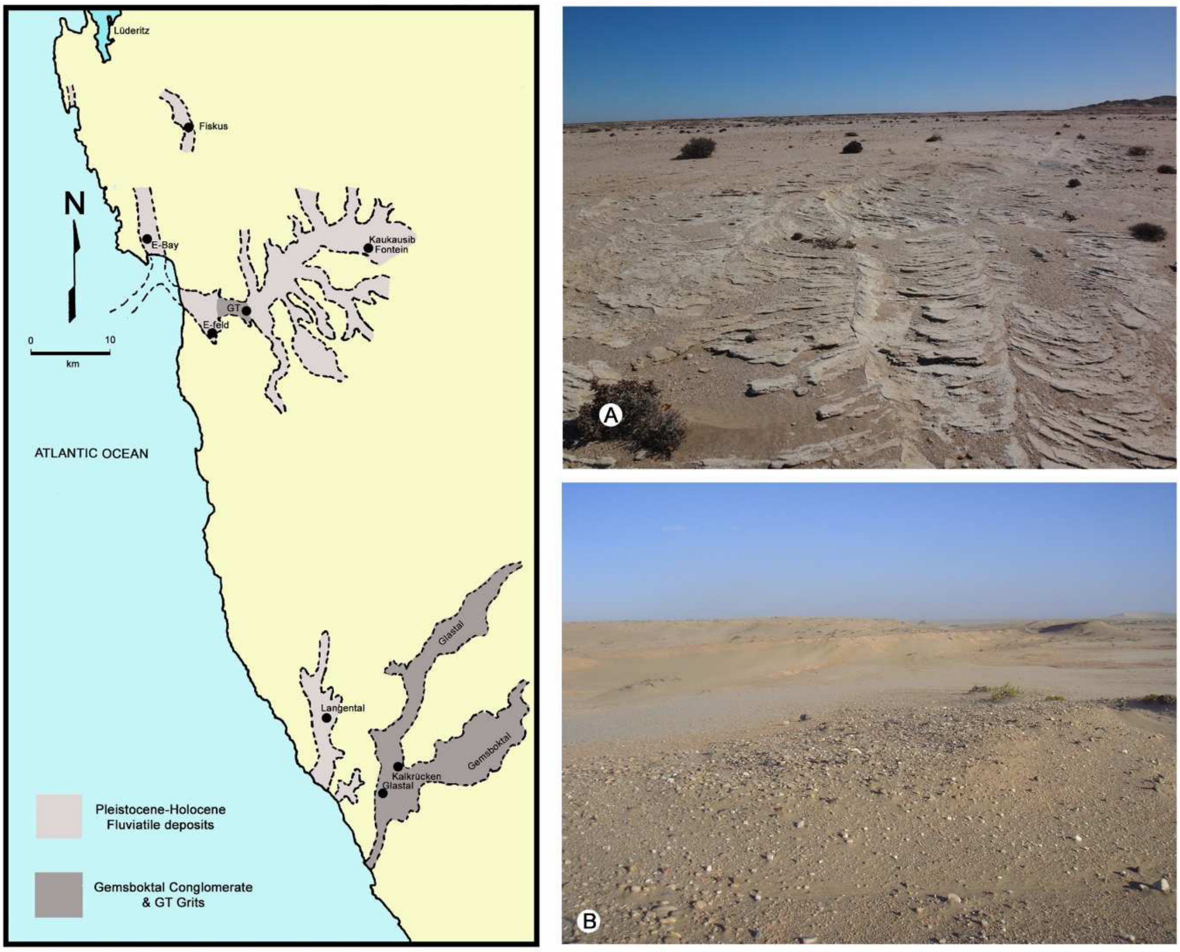

Figure 18. Distribution of the Gemsboktal Conglomerates and GT Grits (dark grey) and Pleistocene to Recent fluviatile deposits (light-grey) in the Sperrgebiet. A) Late Miocene to Plio-Pleistocene GT Grits at Grillental 1, B) Two layers of Gemsboktal Conglomerate at Kalkrücken, with the late Miocene Terrassenfeld Aeolianite intercalated between them

Langental

It rained at Langental during the 2025 survey, and it was noted that, in addition to surface drainage of the waters that eroded and transported quantities of silt and clay, there was also underground drainage via micro-pipes (Fig. 19). In the latter situation small cracks in the Early Miocene sediment were slightly enlarged by water flowing into them gently. The cracks at the surface continue underground, and much of the water in the depressions drained away via these subterranean channels. The important point to note is that these cracks are large enough that small fossils and lithic clasts can fall into them. By this means fossils and even recent bones can be reworked locally into deposits older than their original depositional context. Diamonds and agates can also fall into the cracks and thus be reburied after lying on the surface for extended periods of time.

Figure 19. Erosion and transportation of fine-grained sediment at Langental Miocene Site following light but prolonged rainfall on the 20th May, 2025. Top row: surface flow features, lower row: emptying of depressions via drainage into micro-pipes with subterranean flowage

47 entries were made in the Langental faunal catalogue. Informative specimens of the burrowing rodent *Bathyergoides* (Figs 20, 21), the large macroscelidid *Protypotheroides*, and the dassie *Prohyrax* (Fig. 22) were collected, as well as the usual crop of ruminants (Fig. 23), sanitheres, a species of frog, a chelonian and other microfauna.

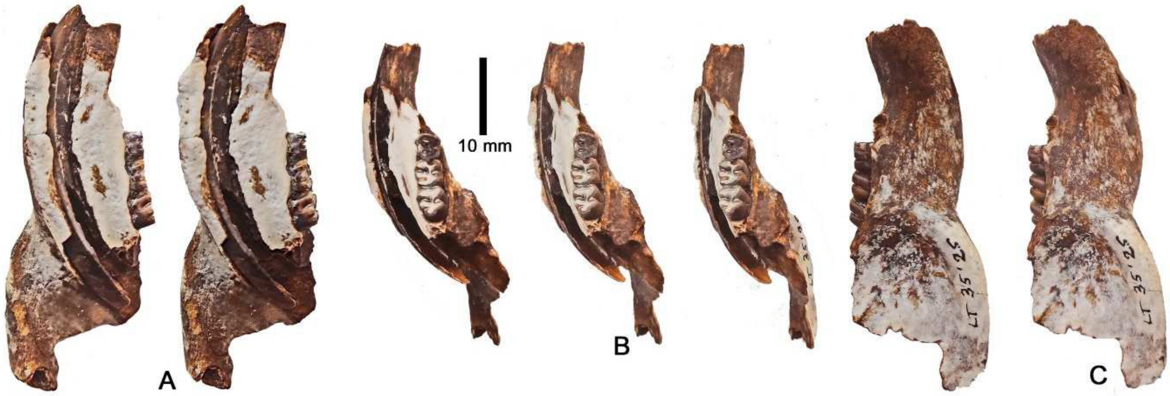

Figure 20. Stereo images of LT 35’25, right mandible of *Bathyergoides neotertiarius* from Langental.A) lingual view, B) occlusal views, C) buccal view

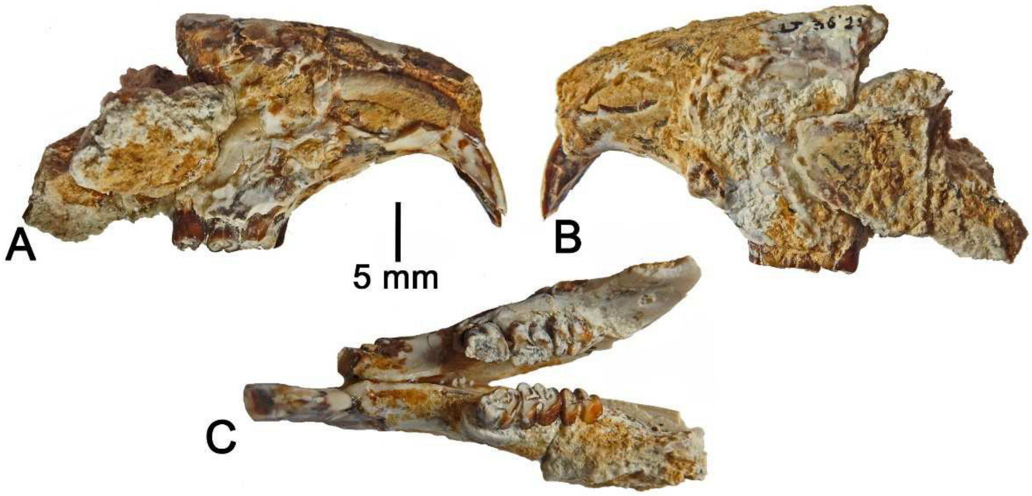

Figure 21. LT 36'25, skull of *Bathyergoides neotertiarius* from Langental. A-B) right and left lateral views of cranium, C) dorsal view of mandible

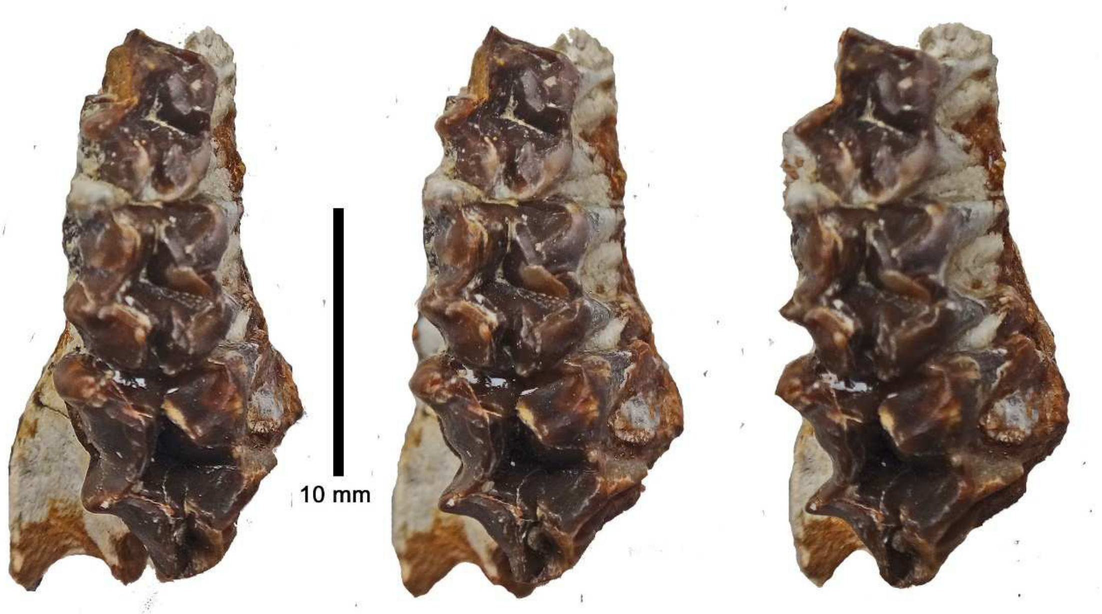

Figure 22. Stereo occlusal images of LT 1'25, right maxilla of *Prohyrax tertiarius* from Langental

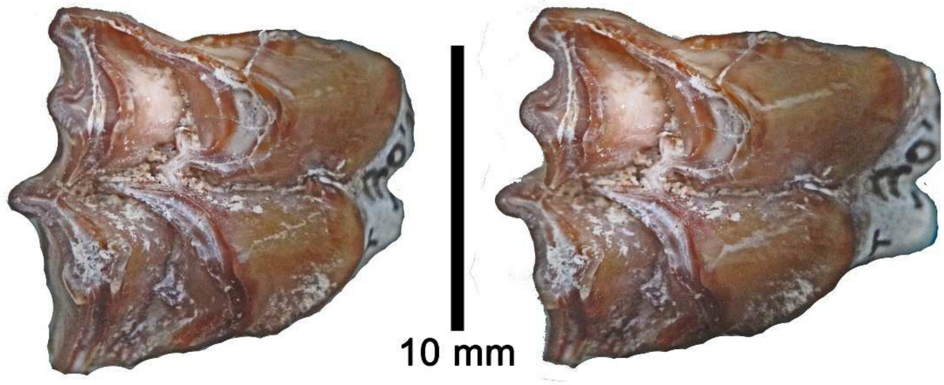

Figure 23. Stereo occlusal view of LT 30'25, right upper molar of a pecoran ruminant from Langental

In addition to arranging and studying the Langental fossils at the National Earth Science Museum, Windhoek, work was started on the cleaning of a fossil anthracothere neurocranium (LT 147'09) that was collected in 2009. The specimen is enclosed in hard siltstone which is best removed using a micro-engraver. The time available for this cleaning was limited, so only one side of the skull was partly prepared and consolidated, the fossil having been slightly crushed and twisted prior to fossilisation. Nevertheless, the specimen yields precious information about the identity of the species, hitherto represented at Langental by two small enamel fragments of upper molars. It is now clear that the species concerned is *Rusingameryx aequatorialis* (Fig. 24), which is known mainly from Early Miocene deposits in Kenya and Uganda (20-16.5 Ma). The following images are of the partly cleaned fossil.

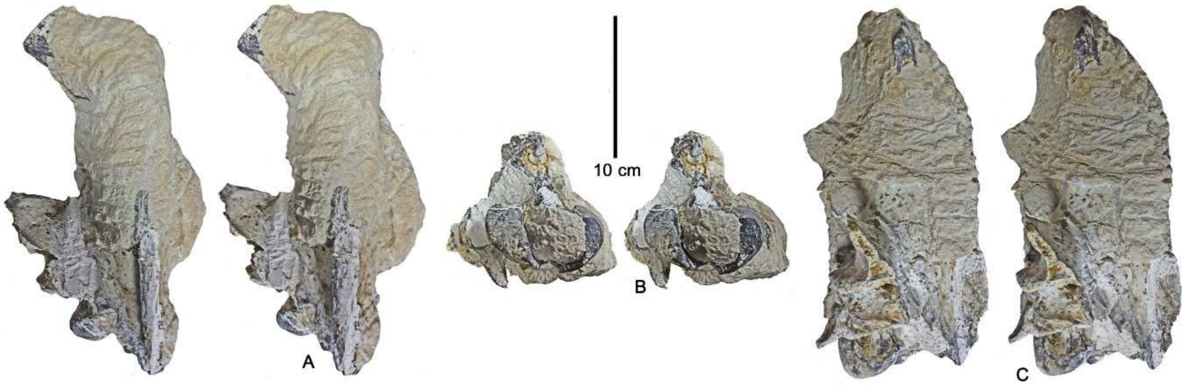

Figure 24. Stereo images of LT 147'09, partly prepared neurocranium of *Rusingameryx aequatorialis* from Langental. A) dorsal view, B) distal view, C) left lateral view

Glastal

A brief survey of the Early Miocene deposits at Glastal yielded a single specimen of the land snail *Dorcasia*, a genus that today is a denizen of summer rainfall, steppic to savannah areas of Namibia.

Neue Anlage

An hour was spent looking for fossils at Neue Anlage, a site that used to be known as the Langental Shark Site. Over 100 shark teeth were collected, along with crab claws, bivalve shells (oysters) and fragments of coral. A poorly preserved mammal tooth was also found, but it is unidentifiable, although it shows some features of sirenians. Further searches are recommended as there could be additional mammalian specimens in the deposits.

Phase 2: Otavi Mountainland (Project Geo-Pal Namibia)

In 2025, the Otavi Mountainland survey was focussed on the sites Kombat E-900, Harasib 3a and Gross Otavi situated in the southern part of the area between the mining towns of Kombat and Tsumeb (Fig. 25).

Harasib 3a

One day was devoted to investigating the Harasib 3a karst breccias (Figs 26, 27). Thirty-five blocks of fossiliferous breccia were collected, containing rodents (Fig. 28) and other microfauna. These blocks require digestion in acid in order to liberate the fossils.

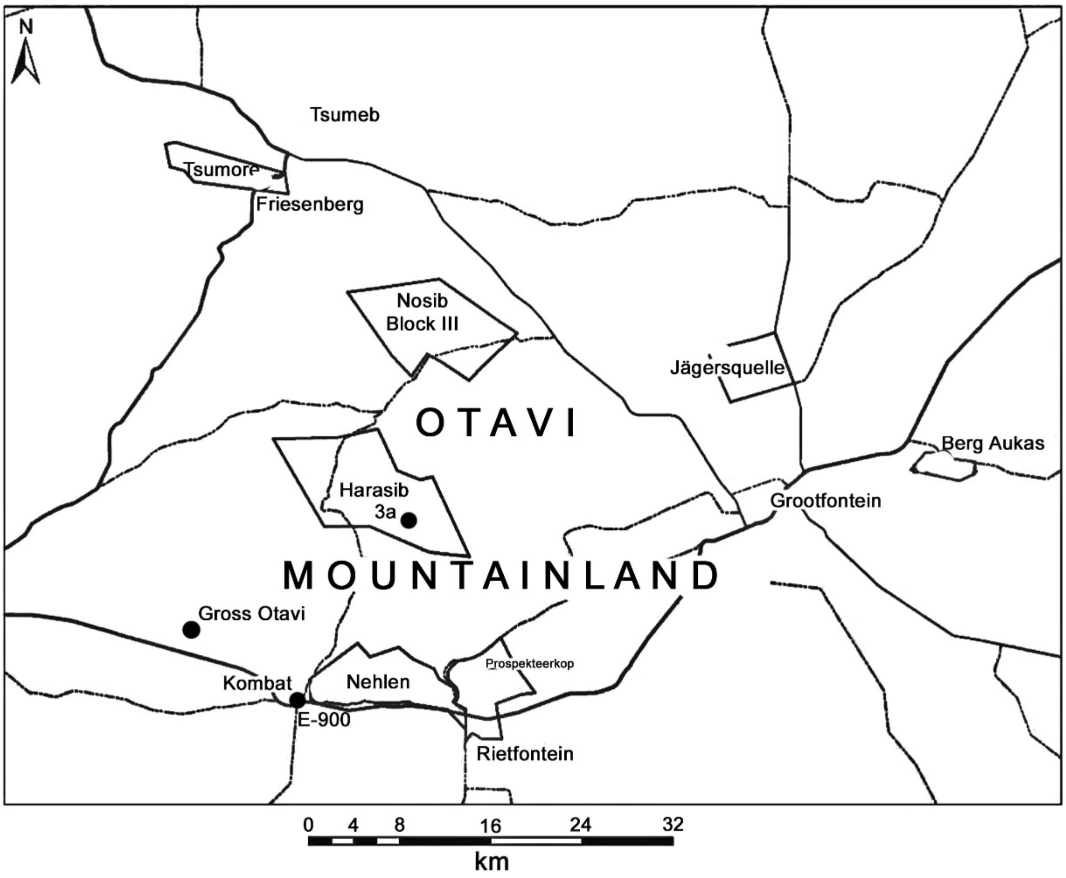

Figure 25. Fossiliferous localities in karst breccias of the Otavi Mountainland, Namibia

Figure 26. The glory hole at Harasib 3a, from which the bright red fossiliferous breccia was extracted during mining operations

Figure 27. Examining breccia blocks in the mine dumps at Harasib 3a, Otavi Mountains, Namibia

Figure 28. Small rodent palate *in situ* in a block of breccia from Harasib 3a, Otavi Mountains, Namibia

While studying the old collections from Harasib, a colobine incisor (Fig. 29) was noticed in a small box labelled ‘non-rodent’. This specimen is compatible in dimensions with the other colobine teeth from the site attributed to the basal Late Miocene genus *Microcolobus,* known mainly from Vallesian equivalent deposits (ca 11-10 Ma) at Ngerngerwa and Nakali, in the Gregory Rift Valley, Kenya.

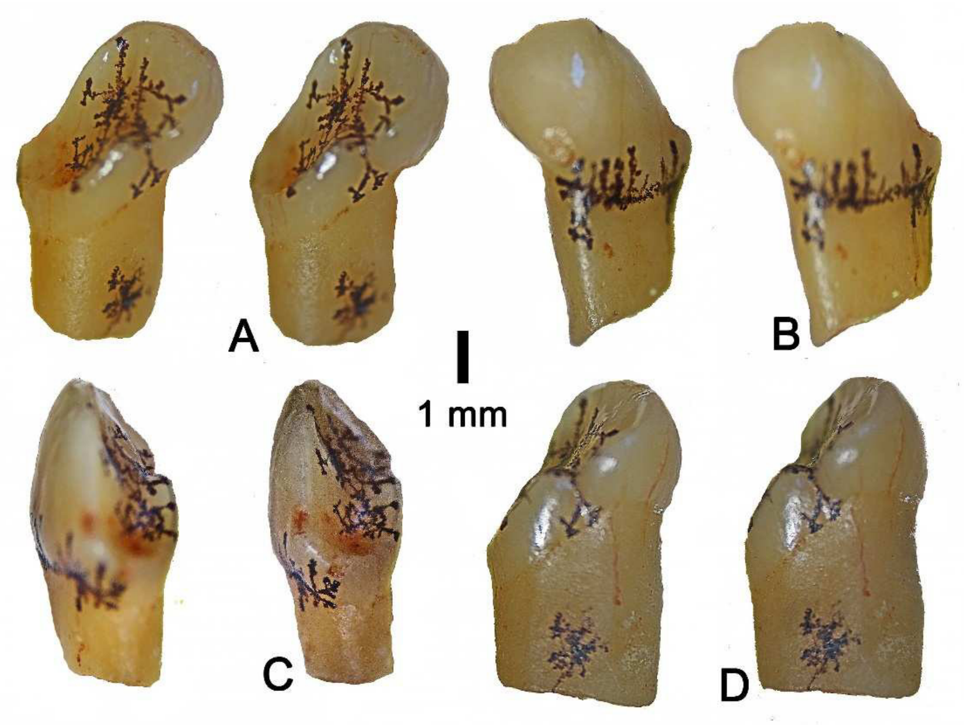

Figure 29. Stereo images of HA 1'25, right upper lateral incisor of *Microcolobus* sp. from the basal Late Miocene breccias at Harasib 3a, Otavi Mountainland, Namibia. A) lingual view, B) labial view, C) distal view, D) mesial view

Gross Otavi

A survey of the mineral prospecting pits at Gross Otavi revealed the presence of abundant *in situ* epikarst breccia in fissures, and loose blocks of breccia in the dumps (Fig. 30), but no fossils were observed.

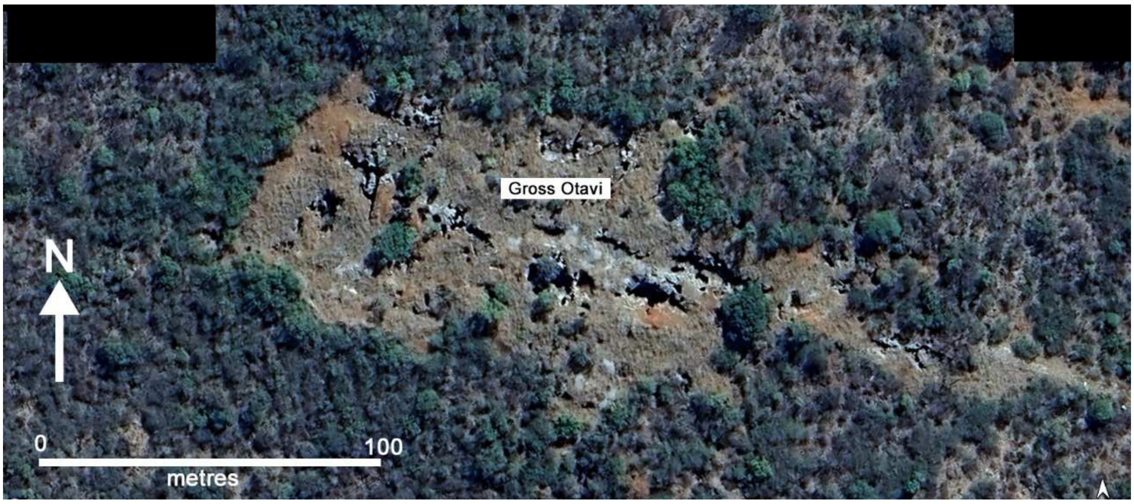
[redacted] [redacted]

Figure 30. The mineral prospecting pits at Gross Otavi, Northern Namibia. The brown tones are epikarst breccia deposits, often containing descloizite, copper oxides and copper carbonates, but lacking in fossils.

Kombat E-900

Screening of the decalcified fissure filling at Kombat E-900 was continued (Figs 31, 32), with 55 sacks treated. The fractions greater than 2 mm were picked through on site and at the lodge. The faunal catalogue runs to 171 entries, and includes abundant ruminants, hyracoids, macroscelidids, lagomorphs and rodents, as well as a few birds, snakes and lizards (Figs 33-38). Among the mammals, the presence of the extinct springbok, *Antidorcas bondi*, suggests a Pleistocene age for the infilling. Substantial quantities of infilling remain to be treated at the site.

Figure 31. Dry screening of the sediment infilling at the Kombat E-900 ‘A’ fissure. The dark-brown infilling is richly fossiliferous, yielding abundant bones and teeth that are impregnated with copper salts, which give them a blue to green interior colouration.

Figure 32. Wet screening of fossiliferous sedimentary infilling from Kombat E-900 ‘A’ on Farm Felsenquell

Fractions of the Kombat sediments coarser than 2 mm were picked through and yielded over 150 specimens. The fractions finer than 2 mm remain to be examined in detail, but they will undoubtedly yield abundant specimens of micromammals and other vertebrates.

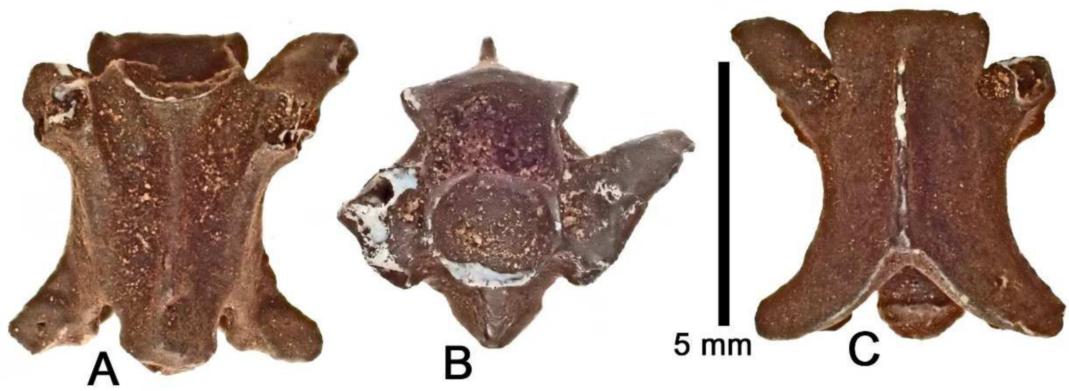

Figure 33. KOM 128'25, vertebra of a small lacertilian from Kombat E-900 'A' fissure. A) ventral view, B) cranial view, C) dorsal view

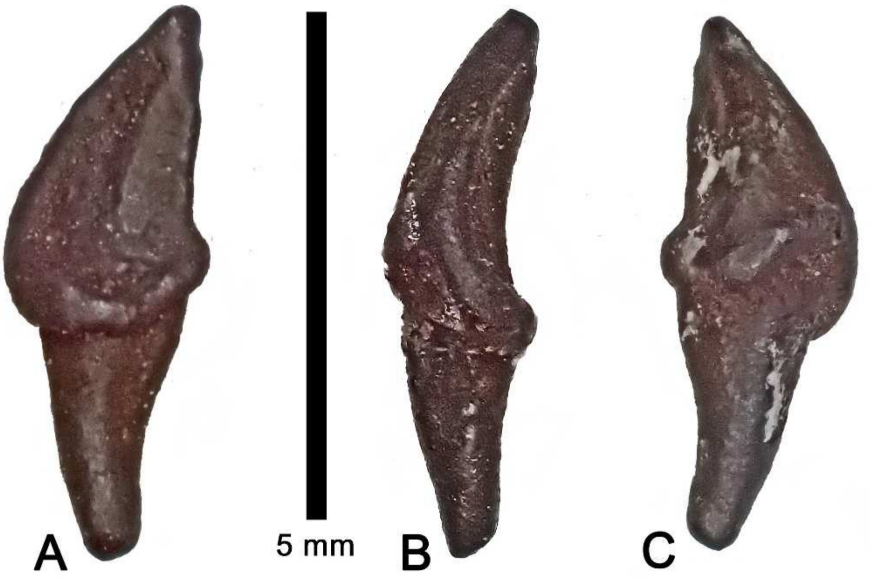

Figure 34. KOM 91'25, chiropteran canine from Kombat E-900 'A' fissure

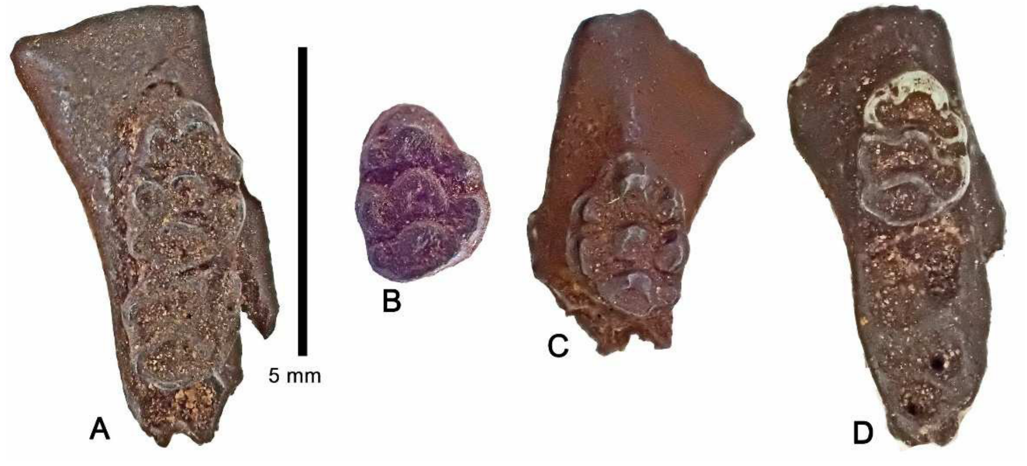

Figure 35. Occlusal views of upper dentognathic remains of *Micaelamys* sp. from Kombat E-900 'A' fissure. A) KOM 104'25, left maxilla with M1/ and M2/, B) KOM 114'25, left M1/, C) KOM 132'25, right maxilla with M1/, D) KOM 59'25, left maxilla with M1/

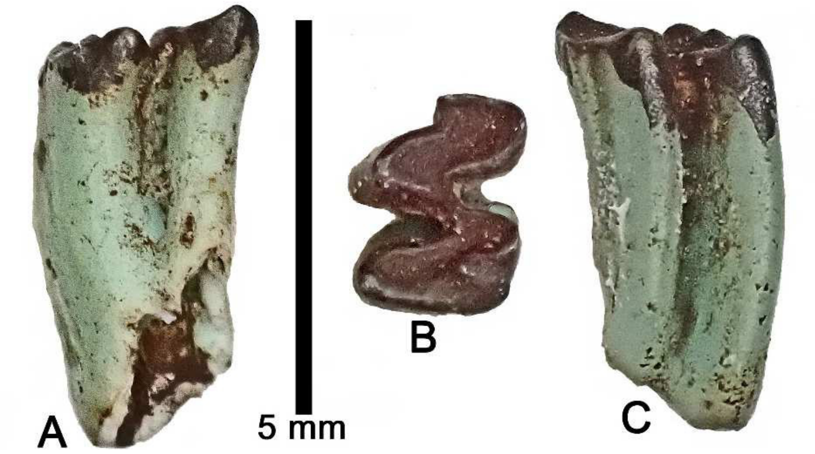

Figure 36. KOM 138'25, left p/4 of *Petromus* sp. from Kombat E-900. A) lingual view, B) occlusal view, C) labial view

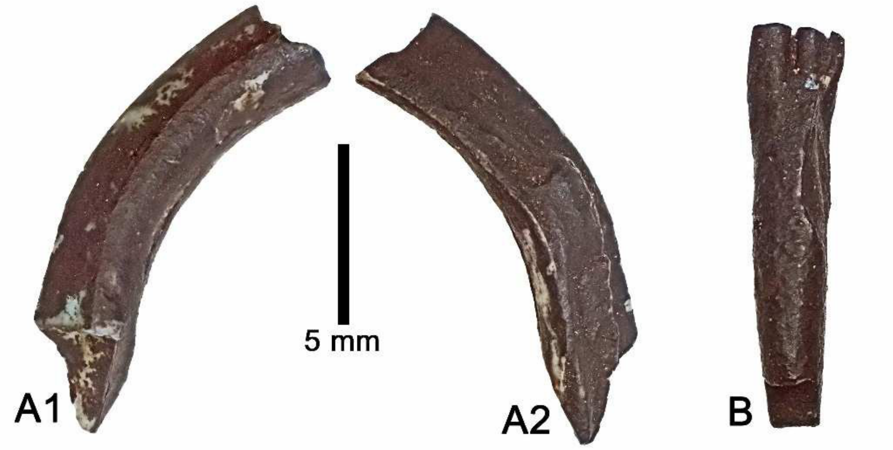

Figure 37. Incisors of *Procavia capensis welwitschii* from Kombat E-900 'A' fissure. A and B) KOM 60'25, mesial and distal views of male right I1/, B) KOM 61'25, lingual view of right i/1

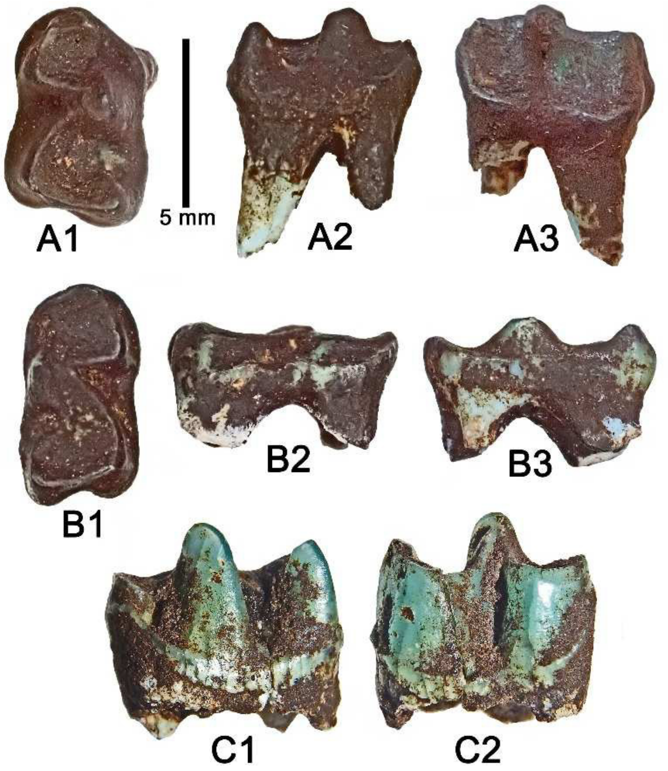

Figure 38. Lower cheek teeth of *Procavia capensis welwitschii* from Kombat E-900 'A' fissure. A) KOM 137'25, left p/4, A1 - occlusal view, A2 - lingual view, A3 - buccal view, B) KOM 56'25, right p/3, B1 - occlusal view, B2 - buccal view, B3 - lingual view, C) KOM 22'25, right m/1, C1 – lingual view, C2 - buccal view

The southern wall of the E-900 fissure consists of dolomite coated with a thin layer of calcified breccia. The latter deposit contains a few fossils (ruminant talus, bone flakes) *in situ* in the breccia. Of interest is the presence of root casts, especially one long, thick root cast which indicates that the fissure had a tree growing at its surface, with roots penetrating deeply into the fissure (Fig. 39). Although the plant species is not identifiable, it is noted that the root casts are similar in dimensions to those of fig trees (*Ficus*) and other large plants such as Moringa, that today grow on the edges of fissures in the Otavi Mountains.

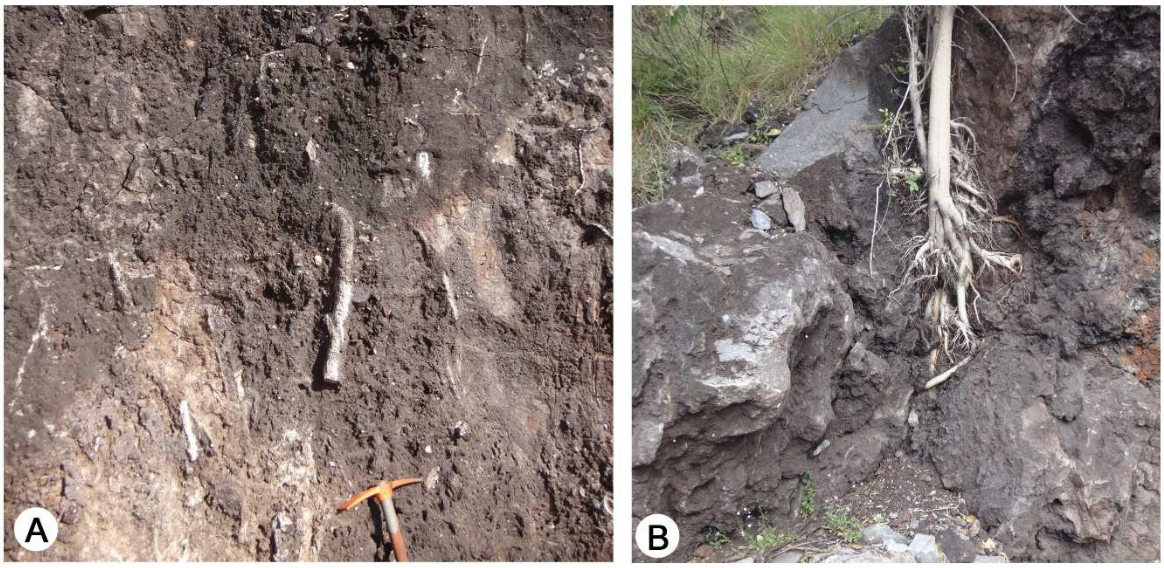

Figure 39. A) fossil root casts in the wall of the Kombat E-900 'A' fissure (pick for scale), B) Moringa tree growing in a fissure close to the E-900 fossil occurrence with tap roots of similar diameter to the fossil in 'A'

Discussion and conclusions

Both phases of the 2025 palaeontological field survey in Namibia were productive, with numerous fossils collected from the Sperrgebiet and the Otavi Mountains.

In the Sperrgebiet, in addition to the usual crop of taxa, some new occurrences were found, including jaws and post-cranial elements of a tiny macroscelidid that is new to science, and some footprints of proboscideans in the Early Miocene deposits of Grillental. Associated skeletal remains of *Myohyrax oswaldi* were found at Grillental and Elisabethfeld, a finding that removes doubt about which postcranial elements go with which cranio-dental ones.

Examination of the coarse fluviatile grits that occur widely in the Grillental in the Northern Sperrgebiet, led to the conclusion that they probably accumulated at the same time as the Gemsboktal Conglomerates, which are widespread in the Central Sperrgebiet between the Klinghardt Mountains and the coast. As such the grits and the conglomerates likely represent different facies of the same overall geological processes related to sporadic but violent rainstorms during the late Neogene that occurred in the hinterland which, at the time, was generally arid to hyperarid. The conglomerates are the proximal facies that accumulated on the relatively flat ground near the foot of the escarpment and mountains of the Inner Namib, often as overbank deposits, whereas the grits were transported by highly turbulent waters (flash floods) and were deposited further downstream within valleys traversing the Inner Namib and the Trough Namib. As such they are characterised by large-scale trough-crossbedding. The even finer facies (sand, silt, clay) were probably flushed out into the Atlantic Ocean. Even though the two units are poorly fossiliferous, they have yielded a few palaeontological remains (a tooth of the white rhinoceros, *Ceratotherium*, and eggshell fragments of *Diamantornis laini*) indicative of deposition sometime during the latest Miocene to Plio-Pleistocene periods.

The sediment infilling at Kombat E-900 'A' fissure in the Otavi Region, yielded abundant remains of ruminants and small mammals, including jaws and teeth of a species of lagomorph, probably *Pronolagus*. The presence of the extinct springbok *Antidorcas bondi* in the deposits, suggests that they are of Pleistocene age. Several dentognathic remains of the small dassie *Procavia capensis welwitschii* were collected, along with remains of a bat and some insectivores.

While examining fossils from Harasib 3a that are curated at the National Earth Science Museum of the Geological Survey of Namibia, an upper incisor of a small colobine monkey was recognised in a box labelled 'non-rodent'. This brings to five the quantity of teeth of *Microcolobus* recovered from the site. Breccia blocks from the same site contain abundant remains of basal Late Miocene rodents and macroscelidids, suggesting an age of ca 11-10 Ma for the breccias.

A survey of rock outcrops at Gross Otavi revealed the presence of abundant epikarst breccias associated with fissures and shallow caverns, but no fossils were observed in them.

Acknowledgements

For administrative help, the NPE thanks the French Embassy in Namibia (Mme Cécile Vigneau), the Muséum National d'Histoire Naturelle, Paris (S. Colas), and UMR 7207 of the CNRS (Dr S. Charbonnier, A. Bastos). The Namibian National Commission on Research, Science and Technology is thanked for the issuance of research visas and the Namibian National Heritage Council issued excavation permits. The Geological Survey of Namibia helped with logistics and provided access to fossil collections in its care. Funding was provided by the ATM project PalPrim Namibie (Paléobiodiversité des primates du Néogène et du Quaternaire en Namibie) (MNHN) and the Prix Del Duca. Financial and logistic support was provided by Namdeb.

In Windhoek, Ms Gloria Simubali of the Geological Survey of Namibia provided help and encouragement. Thanks to Erica Ndalikokule, Lucia Namushinga and Edith Stanley of the Namibian National Heritage Council for arranging authorisation to excavate for fossils in Namibia.

Namdeb staff in Lüderitz (Hugo Du Toit) and Oranjemund (Jürgen Jacob, Gottfried Grobbelaar, Cindy Andrews, Renee Strauss, Hugh-Reece Boer) are thanked for providing logistic and administrative help for the survey in the Sperrgebiet, as are the staff of Sperrgebiet Diamonds, Lüderitz (Claudine Losper).

Land owners in the Otavi Mountains (Sarel Lacante, Dag Kullmann, Ms M. Du Toit) are thanked for permitting access to their land. Thanks are also due to Faan Van de Merwe (Grootfontein) for information about Otavi Mountainland history.

Recent Publications by members of the NPE

Gheerbrant, E., Billet, G. and Pickford, M. 2024. New data on the earliest known arsinoitheriid embrithopod (Mammalia, Paenungulata), *Namatherium* Pickford, Senut, Morales, Mein & Sanchez, 2008, from the middle Eocene of Namibia. *Geodiversitas*, **47(8)**, 343-368.

Godinot, M., Senut, B. and Pickford, M. 2023. An upper molar of *Namadapis* (Primates, Adapiformes, Middle Eocene, Namibia). *Abstr. 29th Colloquium of African Geology*, 26-29 Sept., Windhoek, Namibia, 30.

Mocke, H., Pickford, M., Senut, B. and Gommery, D. 2023a. Fossil Evidence of a Death Trap at Ozombindi, Northwestern Namibia. *Abstr. 29th Colloquium of African Geology*, 26-29 Sept., Windhoek, Namibia, 28-29.

Mocke, H., Pickford, M., Senut, B. and Gommery, D. 2023b. Hominoids from Berg Aukas, Middle Miocene, Namibia - Revision of dental measurements. *Communications of the Geological Survey of Namibia*, **26**, 34-38.

Mocke, H., Pickford, M., Senut, B. and Gommery, D. 2023c. A note on Plio-Pleistocene insect cocoons from Prospekteerkop, Rietfontein, Northern Namibia. *Communications of the Geological Survey of Namibia*, **26**, 66-76.

Mourer-Chauviré, C., Pickford, M., Mocke, H.

and Nduutepo, A. 2023a. Early Miocene Lovebird from Namibia *Abstr. 29th Colloquium of African Geology*, 26-29 Sept., Windhoek, Namibia, 25-26.

Mourer-Chauviré, C., Pickford, M., Mocke, H. and Nduutepo, A. 2023b. Small birds (Psittaculidae, Galliformes and Passeri) from the Early Miocene of Namibia. *Communications of the Geological Survey of Namibia*, **26**, 10-20.

Mourer-Chauviré, C., Pickford, M. and Senut, B. 2023c. New remains of *Struthio coppensi*, Early Miocene, Namibia. *Communications of the Geological Survey of Namibia*, **26**, 21-33.

Pickford, M. 2023a. Revision of the timing of accumulation of the raised beach deposits of the central Sperrgebiet, Namibia. *Abstr. 29th Colloquium of African Geology*, 26-29 Sept., Windhoek, Namibia, 112.

Pickford, M. 2023b. Revision of the timing of accumulation of the raised beach deposits of the central Sperrgebiet, Namibia. *Communications of the Geological Survey of Namibia*, **26**, 1-9.

Pickford, M. 2023c. Kaokoland Cascade Tufa Survey - 2023 Research. *Communications of the Geological Survey of Namibia*, **26**, 39-65.

Pickford, M. 2024. Taxonomic revision of the extinct avian oospecies *Diamantornis karingarabensis* (Senut *et al*., 1998) from the Latest Miocene of Namibia. *Communications of the Geological Survey of Namibia*, **27**, 66-71.

Pickford, M., Morales, J., Mocke, H., Gommery, D. and Senut, B. 2024. Bat-eared fox (Canidae, *Otocyon*) from the Pleistocene of northern Namibia. *Communications of the Geological Survey of Namibia*, **27**, 47-65.

*Communications of the Geological Survey of Namibia, **29** (2026), 128-133*

A New Tetrapod from Southern Africa: Spectacular Find at Gai-As, Northwestern Namibia

Helke Mocke[1]* and Sibusiso Mtungata[2]

[1]Geological Survey of Namibia, 6 Aviation Road, Windhoek
[2]Iziko South African Museum, Cape Town, South Africa

**Corresponding author: <Helke.Mocke@mime.gov.na>*

Abstract :- *Gaiasia jennyae,* named after its place of discovery, Gai-As, in northwestern Namibia and palaeontologist Jennifer Clack, is a salamander-like predator which lived during the Permian period – at a time when southern Africa was still getting over the extensive Dwyka glaciation. Over two metres long and in possession of a massive head, it was a formidable hunter in those cold waters, and the largest of its kind known to date. Its discovery sheds new light on the evolution and distribution of tetrapods (four-legged vertebrates), hitherto only known from ancient equatorial sites with a tropical climate, in North America and Europe.

Keywords :- Permian, Tetrapods, Gai-As, Excavation, Preparation

Introduction

Tetrapods are animals that have legs, or animals with ancestors that had legs, such as whales, bats, snakes, birds and frogs (Clack, 2009). Palaeontologists have long been interested in finding fossils of earliest tetrapods the better to understand the evolution of land-dwelling animals, from aquatic tetrapods which migrated from water to on to dry land. The earlier transition from fish to tetrapod is postulated to have happened at the end of the Devonian (Clack, 2009). However, theories abound suggesting that such organisms could not have thrived in the southern hemisphere during the Carboniferous period, as climatic conditions were too harsh with glaciers and ice sheets covering much of the land. Therefore, a sampling bias resulted, and the majority of tetrapod finds arose from targeted field sampling campaigns carried out in northern hemisphere localities.

Previous geological work and palaeontological done in the Gai-As Formation of the Karoo-age Huab Basin (northwestern Namibia) uncovered several fossils of fishes, such as *Namaichthys* and *Atherstonia,* molluscs (*Leinzia similis)* and disarticulated bones of larger animals initially identified as amphibians (mastodonsauroids or matoposaurids; Stollhofen *et al*., 2000). The mainly clastic, reddish to purplish sediments (shales, siltstones, sandstones) of the Gai-As Formation reflect the existence of an enclosed, isolated lake which, according to Crossley (1984), Tiercelin (1991) and Baltzer (1991), can be compared to the lakes of the present day Rift Valley of East Africa (e. g. Lake Tanganyika, Lake Malawi).

Renewed fieldwork in the Gai-As area in 2014 and 2015 resulted in the discovery of a new, large tetrapod that would challenge old theories and will shift the search for these primitive tetrapods to the neglected southern hemisphere. *Gaiasia jennyae* was named after its place of discovery, Gai-As, in northwestern Namibia, and palaeontologist Jennifer Clack by its finders (Marsicano *et al*., 2024). Most popular articles have described it as a salamander-like predator, which lived in the cold swamps of Gondwana around 280 million years ago and predated the dinosaurs by millions of years. During this time southern Africa was situated at a much higher latitude than today (~55º S) and still recovering from the widespread Dwyka glaciation of the Carboniferous period. With an overall length of ca. 2.5 m and a large, flat head of a length of 60 cm, it was a fearsome hunter in the dark, murky waters of Lake Gai-As. It is the largest tetrapod of its kind known to date. The description of the animal is based on four incomplete specimens, i. e. one holotype, two paratypes and a specimen found in the early 2000s (Marsicano *et al*., 2024).

Discovered in 2015 by Prof. Roger Smith of the Iziko Museum, Cape Town, South Africa, and his team on occasion of a field trip to Namibia, *Gaiasia* caused a minor sensation around the world, when its existence was first publicised online in July 2024 in an article in *Nature* (Marsicano *et al*., 2024). At the same time, various international newspapers and science magazines reported on this important find, among them The Guardian (UK), New Scientist (UK), Westdeutsche Allgemeine Zeitung (Germany), New York Times (USA), Washington Post (USA) and Gazeta Brasil to name but a few.

Excavation at Gai-As

During initial exploration of the red hills of Gai-As some fossils were found scattered on the slopes, which had already been eroded out of their sediment cases, making them easily recognisable (Fig. 1).

Figure 1. Finding tetrapod bones on the hillside at Gai-As (in front: Sibusiso Mtungata, left and Roger Smith, right; at the back: Claudia Marsicano)

Elsewhere, it took careful observation and a good eye to discover a hint of a bone, jaw or tooth embedded within the rock, with the rest of the skeleton deeply buried. Once a bone fragment or tooth was identified, large blocks of rock containing parts of the fossil skeleton had to be carefully prised loose of the matrix to avoid damage, and carried downhill on a makeshift stretcher made from hessian cloth, wooden poles and rope. Individuals with strong arms, shoulders and backs thus transferred the precious cargo to the field vehicle for its journey to the National Earth Science Museum in Windhoek and further preparation (Fig. 2).

Figure 2. Sibusiso Mtungata (left) and Leandro Gaetano (right) carrying *Gaiasia jennyae* downhill on a makeshift stretcher

Preparation at Iziko South African Museum in Cape Town

For preparation and further studies, *Gaiasia jennyae* was brought to the Iziko South African Museum in Cape Town, where it remained for a period of three years. With the arrival of this interesting specimen some alterations were effected at the Iziko Karoo Palaeontology Laboratory, which mostly works on Late Permian to Early Triassic fossils, to meet slightly different challenges posed by the rock matrix. In addition - because of the importance and uniqueness of this find and ongoing reconstruction work at the museum lab - special arrangements were made (such as installation of extra dust extractors and allocation of dedicated workstations) to avoid all possibility of contamination in the preparation room (Fig. 3).

Preparation of the palatal fangs was especially crucial and important, as scientists can deduce a lot of information aiding in the identification of the animal from the features of the palate (Fig. 4). This painstaking work - which takes a steady hand - was carried out with a suitable scribe, i. e. the Paleo Tools Micro Jack 3.

The sedimentary rock covering the bone surface *of Gaiasia jennyae* was approximately 10 cm in thickness, hence the long time it took to chisel it out of its “tomb”, where it had rested for eons. Special caution also had to be taken during preparation, as *Gaiasia* shows some unique morphological features resulting in the probe encountering fossil bone in unexpected places, while removing the surrounding rock matrix – a job requiring infinite patience, painstaking precision and diligence. Moreover, the zigzag patterned ornamentation on the skull roof (Fig. 5) posed further challenges to the preparator because of its variable angles and floating osteoderms.

Figure 3. Sibusiso Mtungata preparing *G. jennyae* at the Iziko South African Museum in Cape Town

Figure 4. Meticulous preparation of the palatal fangs of *G. jennyae*

Figure 5. *G. jennyae* skull after complete preparation, showing the osteoderms with the zigzag patterned ornamentation

Return of the Gai As tetrapod to the National Earth Science Museum

On 5 July 2019 the *Gaiasia jennyae* material was returned to the National Earth Science Museum, but the COVID 19 pandemic, which started soon afterwards, temporarily put a halt to plans for its exhibition. However, after the publication of *Gaiasia*'s discovery in *Nature* and the attendant worldwide publicity, the museum received many enquiries and requests, both from locals and the travelling public, expressing interest in this spectacular specimen which, since its arrival back in Windhoek five years ago, had dwelt ignominiously in its backrooms. Accordingly, priority was given to planning and designing a display appropriate to its prominence and fame, which will allow visitors to view both the actual fossil remains and a reconstruction of what *Gaiasia* (most likely) looked like, when it was haunting and hunting the swamps around Lake Gai-As in Permian times (Fig. 6).

Figure 6. The new *Gaiasia jennyae* display at the National Earth Science Museum, Windhoek

References

Baltzer, F. 1991. Late Pleistocene and recent detrital sedimentation in the deep parts of northern Lake Tanganyika (East African Rift). *In*: Anadón, P., Cabrera, L., and Kelts, K. (eds), Lacustrine Facies Analysis. *International Association of Sedimentologists (IAS) Special Publications,* **13**, 147-173.

Clack, J.A. 2009. The Fish–Tetrapod Transition: New Fossils and Interpretations. *Evolution: Education and Outreach*, **2(2)**, 213-223.

Crossley, R. 1984. Controls of sedimentation in the Malawi Rift Valley, Central Africa. *In*: Jansa, L. and Burollet, F. (eds), IAS Basin Analysis Volume. *Sedimentary Geology*, **40**, 33-50.

Marsicano, C.A., Pardo, J.D., Smith, R.M.H., Mancuso, A.C., Gaetano, L.C. and Mocke, H. 2024. Giant stem tetrapod was apex predator in Gondwanan late Palaeozoic ice age. *Nature*, **631**, 577-582.

Stollhofen, H., Stanistreet, I.G., Rohn-Davies, R., Holzförster, F. and Wanke, A. 2000. The Gai-As lake system, northern Namibia and Brazil. *In*: Gierlowski-Kordesch, E.H. and Kelts, K. (eds), Lake basins through space and time. *AAPG Studies in Geology*, **46**, 87-108.

Tiercelin, J.-J. 1991. Natural resources in the lacustrine facies of the Cenozoic rift basins of East Africa. *In*: Anadón, P., Cabrera, L., and Kelts, K. (eds), Lacustrine Facies Analysis. *International Association of Sedimentologists (IAS) Special Publications,* **13**, 3-37.

Communications of the Geological Survey of Namibia, **29** (2026), 134-136

Editor's note: The Thompson Field Forum coming to Namibia

Thompson Field Forums, named in honour of geology researcher James B. Thompson Jr., and organised by the Geological Society of America, deal with earth and planetary science topics under current investigation and active debate (such as *Age and Craving of the Grand Canyon*, *The Geology of Cuba*, and *Melt Segregation and Transfer Mechanisms in the Lower Crust*, to name but a few of the subjects and worldwide destinations of the Forum). To encourage individual and collaborative research, field forums are interdisciplinary, bringing together experts from all over the world to exchange current knowledge and theories. They consist of several days to a week of workshops, discussions and site visits, for which reason they are usually held in a field setting.

This year's Field Forum:
"How to build complex life: Understanding Ediacaran-Cambrian environmental change and the emergence of animals"

will once again (after 2004) take place in southern Africa. The late Proterozoic to Cambrian Nama Group and its spectacular crop of fossil organisms, whose unique place in the evolution of life has earned them a place among the IUGS "Second 100" Geological Heritage Sites (Schreiber and Mocke, 2024), makes Namibia an ideal venue for fruitful insights and discussions of this exciting topic. During the transition from the Neoproterozoic era to the Cambrian period many significant changes took place in the development of our planet (Rose *et al.*, 2019), with rising oxygen levels causing dramatic environmental changes, only one of them. To investigate and document this period in earth's history the international *Geological Research through Integrated Neoproterozoic Drilling* (GRIND) progamme was called into being with drilling sites in Brazil, China and Namibia to produce a worldwide network and archive of time-calibrated cores for sharing and research (Rose *et al.*, 2019).

Reconstruction of the late Neoproterozoic palaeoenvironment depicting a shallow sea teeming with new life forms (drawing by C. Marais)

Field Forum Programme

Talks and discussions at the University of Namibia's Southern Campus in Keetmanshoop (25- 29 May 2026) will cover the following subjects, highlighted by keynote speakers, lightning talks and poster sessions:

- Geochronology (Ediacaran–Cambrian age constraints)
- Geochemistry (palaeoenvironmental conditions and oxygenation across the Ediacaran-Cambrian boundary)
- Palaeontology (early animal evolution and biostratigraphy)
- Palaeomagnetism and Palaeogeography (palaeomagnetic signals and global reconstructions)

View from Swartpunt stratigraphically below the Ediacaran - Cambrian boundary (Photo: F. Bowyer)

Following the indoor sessions, a two-day field trip (31-31 May 2026) will take up to 40 participants to key locations of the lower and middle Nama Group (Kuibis and Schwarzrand Subgroups) on farms Swartpunt, Swartkloofberg and Sonntagsbrunn near the township of Aus in southern Namibia, to discuss sedimentology and trace fossil record at the visited sites, and the regional placement of the Ediacaran-Cambrian boundary. The event will conclude with a visit of the National Earth Science Museum in Windhoek, which houses a collection of Ediacaran fossils, and a workshop on GRIND-ECT drill cores (1-2 June) at the Geological Survey of Namibia.

Leaders and conveners will be renowned geology researchers

Emmy Smith, Johns Hopkins University, Baltimore, Maryland, USA
Catherine Rose, University of St Andrews, St Andrews, Scotland, UK
Francis Macdonald, University of California, Berkeley, USA

Nama fossils at the National Earth science Museum, Windhoek (photos: M. Meyer)

For more information visit:

https://www.geosociety.org/GSA/Events/Thompson/GSA/thompson/current.aspx?hkey=020e5771-aeb9-4c08-8c5f-8b34208cd3a1For

References

Rose, C. V., Prave, A. R., Bergmann, K. D., Condon, D. J., Kasemann, S.A., MacDonald, F. A., Hoffmann, K.-H., Trindade, R. I. F. and Zhu, M. 2019. Project Report: Grinding Through the Ediacaran-Cambrian Transition. *Communications of the Geological Survey of Namibia*, **21**, 1-14.

Schreiber, U. M. and Mocke, H. 2024. Namibia's IUGS Geological Heritage Sites. *Communications of the Geological Survey of Namibia*, **27**, 115-119.